Study the combustion ash reactivity of biomass mixtures

Emile Atallah

THÈSE

Pour obtenir le grade de

DOCTEUR DE L'UNIVERSITE GRENOBLE ALPES

Spécialité: 2MGE : Matériaux, Mécanique, Génie civil, Electrochimie.

Arrêté ministériel : 25 mai 2016

Présentée par

Emile Atallah

Thèse dirigée par **Alexander Pisch**
Et codirigée par **Capucine Dupont** et **Françoise Defoort**

Préparée au sein du Laboratoire Réacteurs et Procédés (LRP), Département Thermique Conversion et Hydrogène (DTCH), LITEN, CEA Grenoble

Et du Laboratoire Science et Ingénierie des Matériaux et Procédés (SIMaP), CNRS, Grenoble INP, Université Grenoble Alpes (UGA)

Etude de la réactivité des cendres des mélanges de biomasses en combustion
Study the combustion ash reactivity of biomass mixtures

Thèse soutenue publiquement le 9 Juin 2022
Devant le jury composé de:

Monsieur Michael Muller
Directeur de recherché HDR, FZ Jülich, Rapporteur
Monsieur Hervé JEANMART
Professeur HDR, Université catholique de Louvain, Rapporteur
Monsieur Gerard Mortha
Professeur HDR, Université Grenoble Alpes, Président
Madame Rian Visser
Docteure en science, The Netherland's Organisation of Applied Scientific Research, Examinatrice
Monsieur Marc Lomello Tafin
Professeur HDR, Université Savoie Mont Blanc, Examinateur
Monsieur Olivier Dezellus
Maitre de conférence HDR, Université Claude Bernard Lyon 1, Invite
Monsieur Matthieu Campargue
Ingénieur, RAGT Energie, Invite
Monsieur Alexander Pisch
Charge de recherche HDR, Université Grenoble Alpes, Directeur de thèse
Madame Capucine Dupont
Professeur HDR, IHE Delft Institute for Water Education, codirectrice de thèse
Madame Françoise Defoort
Docteur, CEA Grenoble, Encadrante de thèse

THIS RESEARCH WAS FUNDED BY THE INSTITUTE CARNOT ENERGY FOR THE FUTURE

Acknowledgments

It is now the end. Time to move on and turn the pages for a new adventure and a new chapter of my life. Three years ago, I arrived by bus in a sad-weather town, called “Grenoble”. I was anxious since the weather was cold and the sky was dark. However, the next day, the sun came out and the temperatures went up. I traveled and worked in three different countries. However, my Ph.D. experience in France was the toughest of them. I thought I reached the end several times, but I never lost hope. I always kept coming again and again. What QUEEN said totally summarizes my feelings now, and there are no words that can describe it better than some lyrics of his song ‘we are the Champions”:

I've paid my dues
Time after time
And bad mistakes
I've made a few
I've had my share of sand
Kicked in my face
But I've come through
And we mean to go on and on and on and on
I thank you all
But it's been no bed of roses
No pleasure cruise
We (I) are (am) the champions, my friends
And we'll keep on fighting till the end
No time for losers

And now, before I go, I have to thank many people for their help, support, and some of them for just their presence.

First of all, I want to thank my family, who stood beside me during all these stages. I also want to more than thank my Ph.D. colleagues, especially Victor Vastra, Florent Thevenon, Elvira Rodriguez, Lucie Matricon, Hala Braidy, Chancel Muwalala, and many more with whom I crossed path. Girls and guys, “mes pots”, you really made my day. Whenever I needed you, you were always there to support me emotionally and practically. I am honestly out of words. Our discussions, our laughs, our jokes, our going-outs, our pauses and lunches, and even our nagging…It was my pleasure to get to know all of you. The mark of each one of you will never leave me. You were, are, and will always be family to me.

I want to thank deeply and enormously my thesis supervisor Alexander Pisch and the head of my laboratory Laurent Bedel. Honestly, without your support, I do think that I would never have gone this far. Alex, I have wanted to work with you since day 1, and I am thrilled that I had the chance to pass a couple of months learning from you at SIMaP. It was a life-changing experience. You were the one who pushed the most to choose me for the position, and the one who listened to me and supported me all the way through. I hope that I did not let you down, and I promise you that I will never do. I want to thank my encadrante Francoise Defoort, for all her guidance all along these three years. Working together was not always easy, but I learned a lot from you, and I developed personal qualities that I think I will need in my career. I cannot forget to also thank my co-supervisor Capucine Dupont. You were indeed, far in distance but always close in presence.

Big thanks to Matthieu Campargue for all his support in conducting the pilot scale experiments. In addition, his presence as an active member of my thesis and CSI was crucial in helping me to see the end of the line. I would never forget his guidance and his support. I also want to thank SNOOP and Sebastien Thierry for their support in doing the experiments. Claude Chabrol, thank you for all your support and the rich discussions! If I keep counting, I will never stop. I apologize if I have missed someone. Hence, I want to thank all the people that contributed to this work explicitly and implicitly, directly and indirectly. Without all of you, there won’t be Dr. Emile Atallah.

After three years of tough work, long overtime night writing and researches, thorough analysis and studies, more than 120 experiments, two schools, many and many conferences and presentations, and much more… I am overjoyed to present to you my Ph.D. thesis manuscript. I hope that it will guide you and answer many of your questions.

As the KING QUEEN also said, “the show must go on” and it will.

I wish you all the best, deep from my heart. I hope that you achieve all your goals and dreams, as I currently did, do, and will do.

One last thing I want to tell you from experience: In the end, the shadow is only a passing thing. Even darkness must pass. A new day will come. And when the sun shines, it will shine out the clearest, the strongest! You might have several chances to turn back. Just don’t! Hold on to your dreams! Fight for them! And be sure, there is always something “Good” in this world. And this good will get to you, sooner or later. Never lose HOPE!

Wish you all the best.

MAVERICK

Contents

Figures

Tables

Short Summary (English Version)

Mixing biomasses has a good potential to solve operational problems related to ash behavior in thermochemical valorization processes. Chemical reactions within the ash of the blend, and not only a mixing effect without reaction, need to take place to form new solid phases in the mixture at the expense of getting rid of the problematic liquid phase to decrease the slagging tendency. In addition, instead of random/proportion mixing, process simulation approaches based on thermodynamic calculations can provide good capabilities to predict the ash behavior of biomasses and their mixtures.

The present work had three main objectives. First, it focused on validating the presence of a chemical reaction in comparison with a simple mixing effect within the ash of biomass mixtures. Then, it aimed to assess the capabilities of thermodynamic approaches to predict the ash behavior of biomass and their blends, compared with experimental data; and to highlight possible improvements. Finally, several thermodynamic properties were investigated and improvements to the thermodynamic database were proposed.

Various oak barks, wheat straws, and their mixtures were used in combustion laboratory furnaces and pilot scale reactors (boilers and fluidized bed). The operating conditions were varied in laboratory furnaces to study their effects on the reactivity of the ash within the mixtures. For thermodynamic calculations and simulations, two commercial thermodynamic databases, FToxid and GTOX, were used with the FactSage Gibbs energy minimization software.

The mixing without reaction effect was more evident when biomass pellets were used on both laboratory and pilot scales. In this case, the simple mixing rule was roughly able to simulate the general ash behavior of biomass mixture. However, chemical reactions effect was dominant when mixtures of compressed ash of biomass were used. Solid crystalline phases $K_2Ca_2Si_2O_7$ and $K_2Ca_6Si_4O_{15}$ were the direct products of these chemical reactions. Their relative proportion was inversely proportional to the problematic amorphous phase in the final ash produced. Once the reactor cools down, this phase, which contains ash in the molten liquid phase, solidifies and blocks the combustion furnaces. These two compounds were mostly stable at 1000°C, at which equilibrium was reached after 6 h. However, they existed at a lower proportion at 850 °C and disappeared at 1200 °C.

The developed laboratory pellet test was able to predict efficiently the pilot ash behavior of both individual biomasses and their mixture in terms of crystalline and amorphous mineralogical composition in a quantitative way along with agglomeration distribution. The phase diagram approach also showed good capabilities in predicting the physical state of the ash (solid, liquid, or solid-liquid mixture) using both databases. Global simulations using the FToxid database showed better prediction capabilities for single biomass ash than the ones using the GTOX database. In the case of blends, global simulations using the FToxid dataset were significantly limited; and those using the GTOX dataset did not give satisfactory results. Both databases showed correct volatilization prediction capabilities but failed to forecast the characteristic temperatures of the solidus and liquidus.

To improve the thermodynamic database, three ternary compounds $K_2Ca_2Si_2O_7$, $K_2Ca_6Si_4O_{15}$, and $K_4CaSi_3O_9$ were synthesized. Their melting points and enthalpies of formation were measured. The Cp of the stoichiometric intermediate compounds in the binary K_2O-SiO_2 were also remodeled based on the 3rd generation CalPhad Einstein model using experimental and DFT calculated heat capacities. An updated and more accurate version for the calculated K_2O-SiO_2 phase diagram (solid only) was presented.

Short Summary (French version)

Les mélange des biomasses ont un bon potentiel pour résoudre les problèmes opérationnels liés au comportement des cendres dans les procédés de valorisation thermochimique. Des réactions chimiques au sein des cendres du mélange, et pas seulement un effet de dilution, doivent avoir lieu pour former de nouvelles phases solides dans le mélange pour éliminer la phase liquide problématique. De plus, au lieu d'un mélange aléatoire/proportionnel, les approches de simulation de processus basées sur des calculs thermodynamiques peuvent fournir de bonnes capacités pour prédire le comportement des cendres des biomasses et de leurs mélanges.

Le présent travail avait trois objectifs principaux. Dans un premier temps, il s'est attaché à valider la présence d'une réaction chimique par rapport à un simple effet de dilution au sein des cendres des mélanges de biomasse. Ensuite, il s'agissait d'évaluer les capacités des approches thermodynamiques à prédire le comportement des cendres de la biomasse et de leurs mélanges, par rapport aux données expérimentales ; et de mettre en évidence les améliorations possibles. Enfin, plusieurs améliorations liées à la base de données thermodynamique ont été proposées.

Diverses écorces de chêne, pailles de blé et leurs mélanges ont été utilisés dans des fours de laboratoire à combustion et des réacteurs pilotes (chaudières et lit fluidisé). Les conditions opératoires ont été variées dans des fours de laboratoire pour étudier leurs effets sur la réactivité des cendres au sein des mélanges. Pour les calculs et les simulations thermodynamiques, deux bases de données thermodynamiques commerciales, FToxid et GTOX, ont été utilisées avec le logiciel de minimisation d'énergie FactSage Gibbs.

L’effet de dilution était plus évident lorsque les granulés de biomasse étaient utilisés à la fois à l'échelle du laboratoire et à l'échelle pilote. Dans ce cas, la règle de mélange était à peu près capable de simuler le comportement général des cendres. Cependant, l'effet des réactions chimiques était dominant lorsque des mélanges de cendres comprimées de biomasse étaient utilisés. Les phases cristallines solides $K_2Ca_2Si_2O_7$ et $K_2Ca_6Si_4O_{15}$ sont les produits directs. Leur proportion relative était inversement proportionnelle à la phase amorphe problématique. Ils étaient stables à 1000°C, à laquelle l'équilibre a été atteint après 6h. Cependant, ils existaient en moindre proportion à 850°C et disparaissaient à 1200°C.

Le ‘pellet test’ sur des granules de biomasses a pu prédire le comportement des cendres a échelle pilote. L'approche du diagramme de phase a également montré de bonnes capacités de prédiction de l'état physique des cendres (solide, liquide ou mélange solide-liquide) en utilisant les deux bases de données. Les simulations globales utilisant la base de données FToxid ont montré de meilleures capacités de prédiction pour les cendres de biomasse unique que celles utilisant la base de données GTOX. Dans le cas des mélanges, les simulations globales utilisant l'ensemble de données FToxid étaient considérablement limitées ; et ceux utilisant la base de données GTOX n'ont pas donné de résultats satisfaisants. Les deux bases de données ont montré des capacités de prédiction de volatilisation correctes mais n'ont pas réussi à prévoir les températures caractéristiques du solidus et du liquidus.

Pour améliorer la base de données thermodynamique, trois composés ternaires $K_2Ca_2Si_2O_7$, $K_2Ca_6Si_4O_{15}$ et $K_4CaSi_3O_9$ ont été synthétisés. Plusieurs de leurs propriétés thermodynamiques ont été mesurées. Les composés intermédiaires stœchiométriques dans le binaire K_2O-SiO_2 ont également été remodelés par le modèle CalPhad Einstein de 3eme génération en utilisant des capacités thermiques expérimentales et calculées par DFT. Une version mise à jour et plus précise du diagramme de phase K_2O-SiO_2 calculé (solide uniquement) a été présentée.

Résumé de la thèse (en Français)

La demande énergétique mondiale ne cesse d'augmenter avec la croissance démographique et économique, et devrait atteindre environ 250 000 TWh en 2040 (Bhaskar and Pandey 2015). La biomasse, lorsqu'elle est utilisée comme combustible dans des processus de conversion thermique tels que la combustion ou la gazéification, a le potentiel de satisfaire plus de 60 % de cette demande énergétique croissante (Scarlat et al. 2015). Cependant, ces combustibles se caractérisent par leur teneur élevée en cendres et une large gamme de compositions de cendres qui induit divers problèmes lorsqu'ils sont appliqués dans des procédés de conversion thermochimique (Vassilev, Baxter, and Vassileva 2013; 2014).

Le comportement des cendres des résidus agricoles pose plusieurs problèmes opérationnels. Beaucoup d'entre eux, comme la paille de blé, sont caractérisés par des teneurs élevées en silicate alcalin qui abaissent le point de fusion de la cendre résultante et conduisent à l'apparition de cendre en phase liquide, même à des températures relativement basses (c'est-à-dire 800 °C) (Boström et al. 2012). Ainsi, ils peuvent former des agglomérats dans le réacteur à lit fluidisé (FBR), c'est-à-dire des cendres en phase liquide qui collent ou réagissent avec les matériaux du lit, ou induire des effets de frittage dans les chaudières, c'est-à-dire des cendres en phase liquide qui collent au fond du réacteur ou ses murs. Cela peut entraîner le blocage, l'encrassement, le colmatage du réacteur ainsi que l'arrêt de l'instrument, une mauvaise dégradation par la réaction de combustion et une augmentation des coûts d'exploitation (Öhman et al. 2000); la cendre en phase solide est préférée dans ce cas. Contrairement aux cas du chaudière et du lit fluidisé, les cendres en phase liquide sont fortement nécessaires dans un réacteur à flux entraîné (EFR) pour contrôler la température et le flux de cendres sur les parois (Ma et al. 2013; Froment et al. 2015).

Contrairement aux résidus agricoles, les cendres de la biomasse de bois sont riches en silicates de calcium qui produisent des cendres en phase solide, même à des températures élevées (c'est-à-dire 1300°C) (Vassilev, Baxter, and Vassileva 2013). Cela en fait de bons candidats pour la chaudière et le FBR, mais pas pour l'EFR. Par conséquent, l'utilisation d'un type de biomasse peut produire des cendres en phase solide ou liquide, ou même parfois produire un mélange de phases liquide-solide, posant ainsi plusieurs limitations sur le procédé appliqué.

Le mélange de biomasse s'est avéré être une solution pour lutter contre le décrassage et l'agglomération en termes de coût et d'efficacité (Fournel et al. 2015) et a suscité l'intérêt de nombreux chercheurs au cours des trente dernières années (Boström et al. 2012; P. Thy et al. 2010; Zeng et al. 2018; 2016; Peter Thy et al. 2006; Rodríguez et al. 2020). Le mélange de biomasses avec différentes teneurs en cendres et compositions à divers ratios modifie la composition chimique et les propriétés physiques de la matière première. Ensuite, lors du chauffage, des réactions chimiques au sein des cendres peuvent avoir lieu pour former de nouvelles phases solides dans le mélange et réduire ainsi le pourcentage de la phase liquide. Cependant, un mélange sans interaction peut également avoir lieu, bloquant les réactions chimiques et renforçant la phase problématique.

Au lieu d'essais et d'erreurs ou d'un mélange proportionnel systématique de 0 à 100, un outil de prédiction peut être développé pour adapter le type et la composition du mélange de biomasse

au processus appliqué. Comme environ 90 % en poids des cendres de la biomasse sont formées de silicate, de potassium et de calcium (Vassilev et al. 2010), un outil thermodynamique basé sur le système $CaO-K_2O-SiO_2$ peut prédire le comportement des cendres dans les processus réels.

Cette thèse a démarré le 5 juin 2019 et a été financé par l'institut Carnot Energie du Futur. Elle consistait à étudier la réactivité des cendres des mélanges de biomasse avec trois objectifs majeurs :

1- Vérifier la présence, puis étudier la réaction chimique au sein des cendres (et pas seulement la dilution de phase) dans les procédés de combustion (FB, chaudière) lors du mélange de différentes matières premières à l'échelle laboratoire et pilote.
2- Évaluer les capacités de l'outil thermodynamique (à l'équilibre) pour prédire le comportement des cendres des mélanges de biomasse, en mettant en évidence les principales pistes d'amélioration.
3- Appliquer les améliorations nécessaires à l'outil de prédiction.

L'écorce produit des cendres en phase solide (extrême solide), tandis que la paille produit des cendres en phase liquide (extrême liquide). Par conséquent, un mélange 50-50 écorce de chêne-paille de blé a été choisi comme mélange principal dans ce travail. Les objectifs majeurs sont détaillés dans le programme suivant :

<u>Objectif 1 :</u>

1. Étudier l'effet des conditions d'opération (température, temps de séjour, vitesse de refroidissement) sur la réactivité des cendres d'un mélange 50-50 écorce-paille à l'échelle laboratoire ("ash test [pastilles comprimées de cendre de biomasse]" et "pellet test [pastilles comprimées de biomasse]"), en vérifiant la présence d'une réaction chimique par rapport à une dilution de phase.
2. Vérifier l'existence d'une réaction chimique au sein des cendres d'un mélange 50-50 écorce-paille à l'échelle pilote (Boiler, FB) en étudiant les cendres collectées (Sieving, P-XRD, SEM).
3. Vérifier si différents types (c'est-à-dire différentes teneurs en cendres et compositions) de la même matière première (paille 1, paille 2, paille 3, écorce 1, écorce 2, écorce 3) conduiront à des résultats différents en étudiant les cendres collectées du "ash test" (P - DRX, SEM).

<u>Objectif 2 :</u>

1. Mettre en évidence l'amélioration de la base de données en comparant la plus récente (FToxid 7.3, 8.0 et 8.1) avec l'ancienne (GTOX 2018) sur des diagrammes de phases ternaires calculés et des simulations de combustion de cendres de biomasse.
2. Vérifier la fiabilité des prédictions de la base de données thermodynamique actuelle dans FactSage en comparant ses résultats aux résultats expérimentaux pour prédire :
   a. Le comportement à l'équilibre des cendres comprimées comme matériaux de départ (condition favorisant l'équilibre), c'est-à-dire "ash test", vs calculs FactSage.

b. Le comportement du procédé (peut ou non être à l'équilibre) en utilisant des granulés de biomasse, c'est-à-dire "pellet test", vs calculs FactSage.

Objectif 3:

1. Synthétiser des phases ternaires importantes qui existent dans le diagramme CaO-K_2O-SiO_2 et mesurer leurs propriétés thermodynamiques (Cp, point de fusion, ΔH_f, etc.).
2. Évaluer la stabilité des phases ternaires présentes dans le diagramme de phase.
3. Remodeler le diagramme de phase binaire K_2O-SiO_2.

Ce manuscrit a été divisé en 6 chapitres principaux. Chacun de ces chapitres peut être résumé comme suit.

Chapitre 1

Dans le premier chapitre, une revue bibliographique approfondie autour de la biomasse utilisée et des techniques de valorisation thermochimique (avec un accent sur la combustion) a été réalisée. En outre, l'importance du mélange de la biomasse a également été soulignée et la limitation des outils de prédiction thermodynamique actuels a été débattue.

Les cendres des biomasses de bois (telles que l'écorce de chêne) avaient un point de fusion élevé et une faible tendance au frittage en raison de leur composition élevée en oxydes de terre. En revanche, les cendres de résidus agricoles (en particulier la paille de blé) ont présenté une forte tendance au frittage et à la scorification en raison de leur teneur élevée en silicates alcalins. Leurs émissions étaient également riches en HCl et SOx. Leurs techniques actuelles de scorification et de contrôle des émissions se sont révélées limitées, d'où la nécessité de proposer des solutions plus efficaces. L'une des solutions proposées dans la littérature était l'application des additifs. Cependant, leur contrôle du comportement des cendres s'est avéré encore limité, affecté par le coût élevé, les émissions toxiques secondaires et la dépendance à l'égard des cendres de la matière première.

Mélanger différentes biomasses (écorces avec paille dans ce cas) s'est avéré être une solution plus adaptée que les additifs pour lutter contre le décrassage et l'agglomération en termes de coût et d'efficacité. La plupart des travaux de la littérature dans ce domaine ont évité de parler de réactions chimiques ou d'interactions inorganiques au sein des cendres des mélanges de biomasse. Ils avaient plutôt tendance à lier l'effet du mélange à plusieurs facteurs affectant les cendres et leurs comportements. Par exemple, l'augmentation de la fraction de résidus agricoles dans le mélange paille-écorce (bois) a augmenté la tendance à la scorification et réduit les émissions (K, Cl et S retenus dans les scories) dans les appareils de laboratoire et pilotes. De plus, l'augmentation du niveau de frittage a diminué les émissions. Cependant, en fonction de la composition des résidus agricoles, il existe une fraction seuil de mélange, à partir de laquelle les émissions et les scories augmentent en même temps.

En termes de test de prédiction, les différents tests de prédiction à l'échelle laboratoire se sont révélés très limités, de même pour les indices. En parallèle, la littérature a mis en évidence le besoin d'améliorations supplémentaires dans l'approche de prédiction de simulation de procédé basée sur l'équilibre thermodynamique. La base de données thermodynamique autour du système CaO, K_2O et SiO_2 nécessite encore des investigations supplémentaires et des mesures

des propriétés thermodynamiques. De plus, le système binaire K_2O-SiO_2 nécessitait une révision.

Chapitre 2

Dans le deuxième chapitre, les différentes matières premières utilisées dans ce travail, telles que les biomasses, leurs cendres et ainsi que les composés purs, ont été présentées. En outre, les procédures expérimentales et les configurations utilisées pour mener les expériences nécessaires sur la biomasse et leurs cendres à différentes échelles et celles appliquées pour synthétiser les composés ternaires purs d'intérêt ont été discutées. Les instruments et les méthodes d'analyse ont également été discutés en détail. De plus, les approches de calcul et de simulation thermodynamiques ont été présentées ainsi que les logiciels nécessaires et les bases de données thermodynamiques qui y ont été utilisées.

Chapitre 3

Dans le troisième chapitre, les deux approches de prédiction thermodynamique proposées dans ce travail ont été examinées, mettant en évidence les différences dans les résultats prédits à l'aide des différentes bases de données. Les calculs utilisant la base de données FToxid ont fourni un diagramme de phase CaO-K_2O-SiO_2 contenant plus de composés ternaires par rapport à GTOX, en particulier après l'ajout de $K_2Ca_6Si_4O_{15}$ et $K_2Ca_2Si_2O_7$ à sa base de données. Les approches de simulations globales du diagramme de phase et du test de cendres ont montré le même comportement. Cependant, des différences apparentes entre l'approche du diagramme de phase (=simulation du 'ash test') et la simulation du test des granulés ('pellet test') étaient présentes, d'autant plus que le mélange devenait plus riche en écorce.

Dans l'approche de simulation globale, des différences significatives étaient évidentes dans les phases condensées et les volatilisations prévues entre les deux ensembles de bases de données à des températures et des fractions de poids d'écorce variables dans les mélanges. Certains éléments inorganiques se sont avérés déstabiliser certaines phases prédites. Par exemple, P, Cl et Mg ont déstabilisé $K_2Ca_2Si_2O_7$. De plus, l'application du slag B dans les simulations plutôt que le slag A a déstabilisé plusieurs phases majeures riches en K. D'autre part, effet insignifiant sur les résultats prévus pour l'ajout de la base de données FTsalt à l'ensemble de bases de données FToxid.

Chapitre 4

Dans le quatrième chapitre, la présence d'une réaction chimique ou d'un mélange sans effets d'interaction était investiguée. L'effet des réactions chimiques était dominant lorsque les mélanges de cendres (c'est-à-dire le 'ash test') étaient utilisés. Mais, l'influence de la règle de mélange était la plus importante lorsque les mélanges de biomasse étaient appliqués à la fois à l'échelle laboratoire (c'est-à-dire le 'pellet test') et à l'échelle pilote, avec seulement une petite réactivité chimique trouvée dans ces deux cas. Les réactions chimiques étaient plus complexes dans le réacteur à lit fluidisé en modes gazéification et combustion. Les éléments inorganiques réagissaient avec les matériaux du lit au lieu les uns des autres. Ainsi, en termes de tests, la réactivité des cendres du mélange BCWC (50% écore de bois BC et 50% paille de blé WC) peut être classée dans l'ordre décroissant comme suit : ash test > pellet test > chaudières pilotes.

De plus, les effets des conditions d'opération sur la réactivité des cendres des mélanges de biomasse ont été évalués en détail. La température puis le temps de séjour ont eu des effets plus importants sur la réactivité des cendres que la vitesse de refroidissement et le taux de compression des granulés. $K_2Ca_6Si_4O_{15}$ et $K_2Ca_2Si_2O_7$ étaient les principaux produits des réactions chimiques dans les mélanges 50-50 écorce (BC)-paille (WC) biomasses et cendres. Ils étaient absents dans les cendres des biomasses seules, mais très stables à 1000 °C et 6 h dans le mélange dans le 'ash test', conditions dans lesquelles l'équilibre a été expérimentalement atteint. Leur apparition ainsi que leurs proportions croissantes ont conduit à une diminution de la proportion amorphe.

De plus, le test de granulés 'pellet test' à l'échelle laboratoire a pu prédire le comportement du brûleur pilote en termes de proportions cristallines et amorphes ainsi que la distribution d'agglomération pour les biomasses individuelles et les mélanges de biomasse. Par conséquent, l'utilisation du ce test avant toute opération de brûleur pilote a le potentiel de réaliser des économies et de réduire les problèmes opérationnels liés au comportement des cendres dans les réacteurs à l'échelle industrielle.

Chapitre 5

Dans ce chapitre, les capacités de prédiction des deux approches thermodynamiques, présentées au chapitre 3, ont été minutieusement évaluées par rapport aux résultats expérimentaux sur des échantillons de cendres. L'approche du diagramme de phase a montré de bonnes capacités à prédire l'état des cendres (solide ou liquide) en utilisant les deux bases de données, avec des limitations pour les biomasses et les mélanges situés dans la partie supérieure (partie solide) du diagramme.

D'autre part, en utilisant l'approche de simulation globale, les simulations utilisant l'ensemble de base de données FToxid ont offert de bonnes prédictions qualitatives et quantitatives pour la cendre de biomasse unique. Il est également montré des capacités de prédiction qualitative décentes pour les mélanges de cendres loin de la section centrale du diagramme ternaire. Cependant, la prédiction de la phase cristalline/liquide à l'aide de l'ensemble de données GTOX n'a pas bien marché. De plus, les calculs utilisant les deux bases de données ont montré d'excellentes capacités de prédiction de la volatilisation. Néanmoins, ils n'ont pas réussi à prévoir les températures caractéristiques des transitions de phase.

En fin de compte, la prédiction du comportement des cendres dans le 'pellet test' des granulés utilisant les deux ensembles de données était moins bonne qu'avec le 'ash test' en raison du manque de réactivité dans le premier mélange. Dans le cas d'un seul granulé de biomasse, la même capacité de prédiction a été obtenue pour les cendres ou les granulés.

D'autres corrections et améliorations sont encore nécessaires, en particulier dans la partie centrale du diagramme. La mesure des propriétés thermodynamiques de $K_2Ca_2Si_2O_7$ et $K_2Ca_6Si_4O_{15}$ au lieu des estimations, et la suppression du composé K_2CaSiO_4 de ce système peuvent améliorer considérablement les capacités de prédiction.

Chapitre 6

Dans le cadre des améliorations de la base de données thermodynamiques, les conditions optimales de synthèse des composés ternaires $K_2Ca_2Si_2O_7$, $K_2Ca_6Si_4O_{15}$ et $K_4CaSi_3O_9$ ont été discutées en détail. Leurs mesures d'enthalpie de formation (par calorimétrie en solution) et de points de fusion (par DSC) ont également été présentées. Une enquête approfondie autour de la stabilité du quatrième composé ternaire dans le diagramme de phase CaO-K_2O-SiO_2 entre 800 °C et 1200 °C, K_2CaSiO_4, a été délibérée. Plusieurs mélanges de CaO, K_2O et SiO_2 positionnés autour de K_2CaSiO_4 dans le diagramme ternaire ont été formulés et analysés après recuit. Cependant, K_2CaSiO_4 n'a jamais été trouvé. Néanmoins, une nouvelle phase non identifiée était présente. D'autre part, la section d'équilibre CaO-Ca_2SiO_4-$K_2Ca_6Si_4O_{15}$ et la ligne d'équilibre CaO-$K_2Ca_2Si_2O_7$ ont été confirmées.

De plus, une contribution à la modélisation du diagramme binaire K_2O-SiO_2 a également été présentée. Par conséquent, tous les propriétés thermodynamiques des composés stœchiométriques intermédiaires dans ce binaire ont été examinés de manière critique. Des données expérimentales fiables ont été utilisées pour la minimisation de Gibbs à l'aide du modèle CalPhad Einstein de 3eme génération avec plusieurs températures d'Einstein et des corrections anharmoniques. Pour la première fois dans la littérature sans valeurs estimées, une combinaison de mesuré (dans la littérature) et calculée (par DFT) a été proposée pour ré-modéliser les composés stœchiométriques dans ce binaire. De plus, pour la première fois dans la littérature, des propriétés thermodynamiques précises de K_4SiO_4 et $K_6Si_2O_7$ ont été fournies au lieu d'estimations.

Au final, la capacité calorifique des trois composés ternaires synthétisés n'a pas été mesurée pour déterminer leur Cp sur toute la gamme de température, en raison de contraintes de temps. De plus, la stabilité de K_2CaSiO_4 nécessite des investigations supplémentaires. De plus, la section liquide du diagramme binaire K_2O-SiO_2 est toujours absente de ce travail et nécessite une étude et un examen plus approfondi.

References

Bhaskar, Thallada, and Ashok Pandey. 2015. “Advances in Thermochemical Conversion of Biomass—Introduction.” In *Recent Advances in Thermo-Chemical Conversion of Biomass*, 3–30. Elsevier. https://doi.org/10.1016/B978-0-444-63289-0.00001-6.

Boström, Dan, Nils Skoglund, Alejandro Grimm, Christoffer Boman, Marcus Öhman, Markus Broström, and Rainer Backman. 2012. “Ash Transformation Chemistry during Combustion of Biomass.” *Energy & Fuels* 26 (1): 85–93. https://doi.org/10.1021/ef201205b.

Fournel, Sébastien, Joahnn H. Palacios, Stéphane Godbout, and Michèle Heitz. 2015. “Effect of Additives and Fuel Blending on Emissions and Ash-Related Problems from Small-Scale Combustion of Reed Canary Grass.” *Agriculture* 5 (3): 561–76. https://doi.org/10.3390/agriculture5030561.

Froment, K., J. M. Seiler, J. Poirier, and L. Colombel. 2015. “Determining Cooling Screen Slagging Reactor Operating Temperature.” *Energy & Fuels* 29 (8): 5069–77. https://doi.org/10.1021/acs.energyfuels.5b00744.

Holubcik, Michal, Jozef Jandacka, Matej Palacka, and Peter Vician. 2016. “Additives Application to Wheat Straw to Increasing the Ash Fusion Temperature.” *AIP Conference Proceedings* 1768 (1): 020014. https://doi.org/10.1063/1.4963036.

Link, Siim, Patrik Yrjas, and Leena Hupa. 2018. “Ash Melting Behaviour of Wheat Straw Blends with Wood and Reed.” *Renewable Energy*, SI: Waste Biomass to Biofuel, 124 (August): 11–20. https://doi.org/10.1016/j.renene.2017.09.050.

Ma, Charlie, Fredrik Weiland, Henry Hedman, Dan Boström, Rainer Backman, and Marcus Öhman. 2013. “Characterization of Reactor Ash Deposits from Pilot-Scale Pressurized Entrained-Flow Gasification of Woody Biomass.” *Energy & Fuels* 27 (11): 6801–14. https://doi.org/10.1021/ef401591a.

Mack, Robert, Daniel Kuptz, Claudia Schön, and Hans Hartmann. 2019. “Combustion Behavior and Slagging Tendencies of Kaolin Additivated Agricultural Pellets and of Wood-Straw Pellet Blends in a Small-Scale Boiler.” *Biomass and Bioenergy* 125 (June): 50–62. https://doi.org/10.1016/j.biombioe.2019.04.003.

Öhman, Marcus, Anders Nordin, Bengt-Johan Skrifvars, Rainer Backman, and Mikko Hupa. 2000. “Bed Agglomeration Characteristics during Fluidized Bed Combustion of Biomass Fuels.” *Energy & Fuels* 14 (1): 169–78. https://doi.org/10.1021/ef990107b.

Rodríguez, Juan Luis, Xana Álvarez, Enrique Valero, Luis Ortiz, Natalia de la Torre-Rodríguez, and Carolina Acuña-Alonso. 2020. “Design of Solid Biofuels Blends to Minimize the Risk of Sintering in Biomass Boilers.” *Journal of the Energy Institute* 93 (6): 2409–14. https://doi.org/10.1016/j.joei.2020.07.015.

Scarlat, Nicolae, Jean-François Dallemand, Fabio Monforti-Ferrario, and Viorel Nita. 2015. “The Role of Biomass and Bioenergy in a Future Bioeconomy: Policies and Facts.” *Environmental Development* 15 (July): 3–34. https://doi.org/10.1016/j.envdev.2015.03.006.

Thy, P., B.M. Jenkins, R.B. Williams, C.E. Lesher, and R.R. Bakker. 2010. “Bed Agglomeration in Fluidized Combustor Fueled by Wood and Rice Straw Blends.” *Fuel Processing Technology* 91 (11): 1464–85. https://doi.org/10.1016/j.fuproc.2010.05.024.

Thy, Peter, Bryan M. Jenkins, Charles E. Lesher, and Sidsel Grundvig. 2006. “Compositional Constraints on Slag Formation and Potassium Volatilization from Rice Straw Blended Wood Fuel.” *Fuel Processing Technology* 87 (5): 383–408. https://doi.org/10.1016/j.fuproc.2005.08.015.

Vassilev, Stanislav V., David Baxter, Lars K. Andersen, and Christina G. Vassileva. 2010. "An Overview of the Chemical Composition of Biomass." *Fuel* 89 (5): 913–33. https://doi.org/10.1016/j.fuel.2009.10.022.

Vassilev, Stanislav V., David Baxter, and Christina G. Vassileva. 2013. "An Overview of the Behaviour of Biomass during Combustion: Part I. Phase-Mineral Transformations of Organic and Inorganic Matter." *Fuel* 112 (October): 391–449. https://doi.org/10.1016/j.fuel.2013.05.043.

———. 2014. "An Overview of the Behaviour of Biomass during Combustion: Part II. Ash Fusion and Ash Formation Mechanisms of Biomass Types." *Fuel* 117 (January): 152–83. https://doi.org/10.1016/j.fuel.2013.09.024.

Wang, Chang'an, Lei Zhao, Ruijin Sun, Yueyi Hu, Guantao Tang, Wufeng Chen, Yongbo Du, and Defu Che. 2019. "Effects of Silicon-Aluminum Additives on Ash Mineralogy, Morphology, and Transformation of Sodium, Calcium, and Iron during Oxy-Fuel Combustion of Zhundong High-Alkali Coal." *International Journal of Greenhouse Gas Control* 91 (December): 102832. https://doi.org/10.1016/j.ijggc.2019.102832.

Yao, Xiwen, Haodong Zhou, Kaili Xu, Qingwei Xu, and Li Li. 2019. "Evaluation of the Fusion and Agglomeration Properties of Ashes from Combustion of Biomass, Coal and Their Mixtures and the Effects of K2CO3 Additives." *Fuel* 255 (November): 115829. https://doi.org/10.1016/j.fuel.2019.115829.

Zeng, T., A. Pollex, N. Weller, V. Lenz, and M. Nelles. 2018. "Blended Biomass Pellets as Fuel for Small Scale Combustion Appliances: Effect of Blending on Slag Formation in the Bottom Ash and Pre-Evaluation Options." *Fuel* 212 (January): 108–16. https://doi.org/10.1016/j.fuel.2017.10.036.

Zeng, T., N. Weller, A. Pollex, and V. Lenz. 2016. "Blended Biomass Pellets as Fuel for Small Scale Combustion Appliances: Influence on Gaseous and Total Particulate Matter Emissions and Applicability of Fuel Indices." *Fuel* 184 (November): 689–700. https://doi.org/10.1016/j.fuel.2016.07.047.

Introduction

The world demand for energy is continuously increasing with time. For instance, the International Energy Outlook 2013 (IEO2013) projects an increase in the world energy demand by 56% between 2010 and 2040 (Bhaskar and Pandey 2015). In addition, it is forecasted to rise from 630 quadrillions Btus ($1.8x10^8$ GWh) in 2020 to 820 quadrillions Btus ($2.4x10^8$ GWh) in 2040 (Bhaskar and Pandey 2015).

To satisfy this increasing energy demand, the international energy agency (IEA) shows that the world depends heavily on fossil fuels i.e., coal, petroleum, and natural gas. World coal consumption rises at an average rate of 1.3% per year, expected to reach 220 quadrillions Btus ($6.4x10^7$ GWh) in 2040 (Bhaskar and Pandey 2015). Comparatively, petroleum (Chen, Suzuki, and Lackner 2017) and natural gas (Chen, Suzuki, and Lackner 2017) are also used due to their low capital costs and high heating contents.

However, two main drawbacks exist in front of the application of fossil fuels to satisfy the increasing energy demand. First, their price is constantly increasing with their demand, and is expected to reach more than 200 dollars per barrel by 2035 (Chen, Suzuki, and Lackner 2017). Second, new policies and regulations limiting their application are constantly emerging. Such regulations mainly aim to reduce Greenhouse Gas (GHG) emissions by 30% by 2030 and by 80-90% by 2050 (Scarlat et al. 2015; EC 2011a), by hindering the use of such a toxically emission fuel.

In parallel, the world is suffering from serious waste generation problems. For instance, in a recent study published by the World Bank (The world bank 2019), 50% of the two billion tons of waste generated worldwide is organic (food, green, and wood). This amount is expected to double by 2050. Unfortunately, 33% of this organic waste is disposed of in open dumps, 29% landfilled, and 11% incinerated (The world bank 2021). Due to such waste disposal technique and based on the volume of waste generated, its composition, and its management, more than 1.6 billion tons of carbon dioxide (CO_2) was generated yearly during the last 3 years (The world bank 2021). Solid waste-related emissions are anticipated to increase to 2.38 billion tons of CO_2 by 2050 if no improvements are made in this sector (The world bank 2021).

Thermochemical treatment techniques are widely used to recover energy from organic materials and provide an efficient disposition technique (Chen, Suzuki, and Lackner 2017). The word thermochemical can be divided into thermal, i.e. use of temperature, and chemical, i.e. chemical or elemental components. Hence, thermochemical valorization techniques use high

temperatures (200℃-1200℃) to degrade the fuel into its main elemental constituents and form new products that have more proficient use and are more ecofriendly (Chen, Suzuki, and Lackner 2017; Richardson et al. 2015; Speight 2011). When burnt, organic wastes are considered to close the carbon cycle since the CO_2 absorbed from nature during photosynthesis is released back to it along with a certain amount of energy (Chen, Suzuki, and Lackner 2017).

As a result, thermochemical valorization of bioenergy feedstock has the possibility to:

1. Increase the share of renewable sources in energy production.
2. Efficiently face the increasing price of fossil fuels by providing an alternative solution.
3. Decrease the total CO_2 emissions by closing the carbon cycle.
4. Support the green economy set of goals.
5. Solve the waste disposal problems.

Thermochemical valorization techniques can be divided into dry and wet depending on the fuel. Combustion and gasification are more preferably used to treat dry fuel. Since its early beginning, combustion pursues human history, where mainly wood is combusted to produce heat (Luo and Zhou 2012). Coal combustion started with the mining industry and continued during the world wars (Suárez-Ruiz and Ward 2008). However, the coal and wood preliminary cofiring concept was introduced during World War I and II to satisfy the increasing need for energy, but they remained limited. As a result, new combustion and gasification reactors with improved efficiency and universality were invented later in the same era. They included improved solid fuels burners, staged combustors with moving grates, bubbling, and circulating fluidized bed reactors (Miles and Miles 1996).

The oil crisis and the clean air act in the 1970s pushed the energy market to find new eco-friendly sources, introducing the wood gasification and combustion concept (Miles and Miles 1996; Arvelakis et al. 1999). Wood started to be mixed with coal or applied alone in the reactor chambers more efficiently (Bhaskar and Pandey 2015). Wood trials became successful, and this bioenergy feedstock was widely used later as a highly suitable feedstock, especially for furnaces and fluidized beds (Bhaskar and Pandey 2015; Richardson et al. 2015). Early research in 1973 started cofiring wood with small quantities of agricultural processing residues, such as straw, nuts, peat, etc. (Miles and Miles 1996). Early trials with these types of blends were not successful until 1995, when researchers found that 20% of agricultural waste at most can be blended with wood to secure an efficient reactor operation (Miles and Miles 1996).

The ash behavior of agricultural residues introduces several operational problems. Many of them, such as wheat straw, are characterized by high alkali-silicate contents that lower the melting point of the resulting ash and lead to the occurrence of liquid phase ash, even at relatively low temperatures (i.e. 800 °C) (Boström et al. 2012). Hence, they can form agglomerates in fluidized bed reactor (FBR), i.e. ash in the liquid phase that sticks or reacts with the bed materials, or induce sintering effects in furnaces, i.e. ash in the liquid phase sticking to the bottom of the reactor or its walls. This can lead to blocking, fouling, clogging the reactor, instrument shutdown, poor degradation by combustion reaction, and increased operational costs (Öhman et al. 2000); ash in the solid phase is preferred in this case. Contrary to the cases of the furnace and the fluidized bed, ash in the liquid phase is highly needed in an entrained flow reactor (EFR) to control the temperature and flow of ash on the walls (Ma et al. 2013; Froment et al. 2015).

In contrast with agricultural residues, ash of wooden biomass is rich in calcium-silicates that produce ash in the solid phase, even at high temperatures (i.e. 1300°C) (Vassilev, Baxter, and Vassileva 2013). This makes them good candidates for furnace and FBR but not for EFR. Consequently, using one type of biomass can yield ash in either the solid or the liquid phases, or even sometimes produce a mixture of liquid-solid phases, hence posing several limitations on the applied process.

Additives, a set of various compounds added to the initial feedstock (such as Kaolin), were widely used to decrease agglomeration and sintering levels. However, their cost is high, and each has its problem (Mack et al. 2019; Holubcik et al. 2016; Wang et al. 2019; Yao et al. 2019). On the other hand, biomass mixing proved to be a more suitable solution than additives to fight slagging and agglomeration in terms of cost and effectiveness (Fournel et al. 2015) and triggered the interest of many researchers during the last thirty years (Boström et al. 2012; P. Thy et al. 2010; Zeng et al. 2018; 2016; Peter Thy et al. 2006; Rodríguez et al. 2020). Mixing biomasses with different ash contents and compositions at various ratios modifies the feedstock's chemical composition and physical properties. Then upon heating, chemical reactions within the ash can form new solid phases in the mixture and reduce the percentage of the liquid phase (Boström et al. 2012; Defoort et al. 2019). However, mixing without interaction can also take place, hindering the chemical reactions and enhancing the problematic phase.

Instead of trial-and-error or systematic proportional mixing from 0 to 100, a prediction tool can be developed to adapt the type and composition of the biomass mixture to the applied process. Empirically derived indices proved their limitations in this domain in the case of biomass, while

experimental laboratory tests were time-consuming and costly (Rodríguez et al. 2020; Link, Yrjas, and Hupa 2018). Consequently, since around 90 wt.% of the biomass ash comprises silicate, potassium, and calcium (Vassilev et al. 2010), a thermodynamic tool based on the CaO-K_2O-SiO_2 system can predict the ash behavior in real-life processes.

As a result, this project started on June 5th, 2019, and was funded by the "Carnot Energy du Future." It consisted of studying the ash reactivity of biomass mixtures with three major objectives:

1- Check the presence, then study the chemical reaction within the ash (and not just phase dilution) in combustion processes (FB, boiler) when mixing different feedstock at laboratory and pilot scales.

2- Assess the thermodynamic tool (at equilibrium) capabilities to predict the ash behavior of biomass mixtures, highlighting the major rooms for improvements.

3- Apply the needed improvements to the prediction tool.

Bark produces ash in the solid phase (solid extreme), while straw produces ash in the liquid phase (liquid extreme). Hence, a 50-50 oak bark-wheat straw mixture was picked as the major blend in this work. The first two objectives are detailed in the following program:

Objective 1:

1. Study the effect of operating conditions (temperature, residence time, and cooling rate) on the ash reactivity of a 50-50 mixture bark-straw at a laboratory scale («ash test» and «pellet test»), verifying the presence of a chemical reaction compared to a phase dilution.
2. Check the existence of a chemical reaction within the ash of a 50-50 mixture of bark-straw at a pilot scale (Boiler, FB) by studying the collected ashes (Sieving, P-XRD, SEM).
3. Check if different types (i.e. different ash contents and compositions) of the same feedstock (straw1, straw2, bark1, bark2) will lead to different results («ash test» and «pellet test») by studying the collected ashes (P-XRD, SEM).

Objective 2:

1. Highlight the database improvement by comparing the predicted results using two sets of databases (FToxid 7.3/8.0/8.1 + FactPS + FTsalt vs GTOX 2018 + FactPS) on calculated ternary phase diagrams and biomass ash combustion simulations.

2. Check the prediction reliability of the current thermodynamic database versions (FToxid, FactPS, FTsalt, GTOX) in FactSage by comparing its findings with experimental results to predict:
    a. The equilibrium behavior of a 50-50 mixture bark-straw using compressed ash chips as initial materials (condition favoring equilibrium), i.e. “ash test”, vs equilibrium calculations.
    b. The process behavior (may or may not be at equilibrium): laboratory “pellet” and pilot-scale tests (Boiler, FB) using biomass pellet vs equilibrium calculations.

Objective 3:

1. Synthesis of the important ternary phases in the $CaO\text{-}K_2O\text{-}SiO_2$ and measure their thermodynamic properties (such as Cp and Δh_f) along with their constitutional properties (such as melting point).
2. Assess the stability of the present ternary phases in the phase diagram.
3. Remodel the thermodynamic properties of the stoichiometric intermediate compounds in the binary phase diagram $K_2O\text{-}SiO_2$ and recalculate it.

The manuscript is organized as follows.

In chapter 1, a thorough literature review of the used biomass, the thermochemical valorization techniques, and the prediction tools will be presented. In this chapter, the importance of biomass mixing will also be highlighted, and the limitation of the current thermodynamic prediction tools will be discussed.

In chapter 2, the used raw materials along with the experimental setups and the analysis techniques and instruments used in this work will be presented.

In chapter 3, the thermodynamic prediction approaches proposed in this work will be examined, highlighting the differences in the predicted results using the various databases.

In chapter 4, the presence of a chemical reaction or a mixing without interaction effects (i.e. phase dilution) within the ash of biomass mixtures will be assessed compared to experimental findings at both laboratory and pilot scales. In this chapter, the effects of operating conditions on the ash reactivity of biomass mixtures will be also evaluated in details. An optimum

experimental equilibrium condition will be presented, and a laboratory prediction test will be discussed.

In chapter 5, the prediction capabilities of the thermodynamic approaches, presented in chapter 3, will be thoroughly assessed with respect to experimental results on ash samples. As a result, all the needed database improvements will be highlighted.

In chapter 6, as part of the improvements to the thermodynamic database, the synthesis of several ternary compounds along with their thermodynamic properties measurements will be discussed. In addition, a contribution to the modeling of the binary diagram K_2O-SiO_2 will also be presented.

The major conclusions will be presented in a final chapter at the end of this work, and several perspectives will be proposed.

References

Arvelakis, S., C. Sotiriou, A. Moutsatsou, and E. G. Koukios. 1999. “Prediction of the Behaviour of Biomass Ash in Fluidized Bed Combustors and Gasifiers.” *Journal of Thermal Analysis and Calorimetry* 56 (3): 1271–78. https://doi.org/10.1023/A:1010189919655.

Bhaskar, Thallada, and Ashok Pandey. 2015. “Advances in Thermochemical Conversion of Biomass—Introduction.” In *Recent Advances in Thermo-Chemical Conversion of Biomass*, 3–30. Elsevier. https://doi.org/10.1016/B978-0-444-63289-0.00001-6.

Boström, Dan, Nils Skoglund, Alejandro Grimm, Christoffer Boman, Marcus Öhman, Markus Broström, and Rainer Backman. 2012. “Ash Transformation Chemistry during Combustion of Biomass.” *Energy & Fuels* 26 (1): 85–93. https://doi.org/10.1021/ef201205b.

Chen, Wei-Yin, Toshio Suzuki, and Maximilian Lackner, eds. 2017. *Handbook of Climate Change Mitigation and Adaptation*. 2nd ed. Springer International Publishing. https://www.springer.com/gp/book/9783319144085.

Defoort, Françoise, Matthieu Campargue, Gilles Ratel, Hélène Miller, and Capucine Dupont. 2019. “Physicochemical Approach To Blend Biomass.” *Energy & Fuels* 33 (7): 5820–28. https://doi.org/10.1021/acs.energyfuels.8b04169.

EC. 2011a. “A Road Map for Moving to a Competitive Low Carbon Economy in 2050.” COM(2011)112 final, Brussels.

Fournel, Sébastien, Joahnn H. Palacios, Stéphane Godbout, and Michèle Heitz. 2015. “Effect of Additives and Fuel Blending on Emissions and Ash-Related Problems from Small-Scale Combustion of Reed Canary Grass.” *Agriculture* 5 (3): 561–76. https://doi.org/10.3390/agriculture5030561.

Froment, K., J. M. Seiler, J. Poirier, and L. Colombel. 2015. “Determining Cooling Screen Slagging Reactor Operating Temperature.” *Energy & Fuels* 29 (8): 5069–77. https://doi.org/10.1021/acs.energyfuels.5b00744.

Holubcik, Michal, Jozef Jandacka, Matej Palacka, and Peter Vician. 2016. “Additives Application to Wheat Straw to Increasing the Ash Fusion Temperature.” *AIP Conference Proceedings* 1768 (1): 020014. https://doi.org/10.1063/1.4963036.

Link, Siim, Patrik Yrjas, and Leena Hupa. 2018. “Ash Melting Behaviour of Wheat Straw Blends with Wood and Reed.” *Renewable Energy*, SI: Waste Biomass to Biofuel, 124 (August): 11–20. https://doi.org/10.1016/j.renene.2017.09.050.

Luo, Zhongyang, and Jingsong Zhou. 2012. “Thermal Conversion of Biomass.” In *Handbook of Climate Change Mitigation*, edited by Wei-Yin Chen, John Seiner, Toshio Suzuki, and Maximilian Lackner, 1001–42. New York, NY: Springer US. https://doi.org/10.1007/978-1-4419-7991-9_27.

Ma, Charlie, Fredrik Weiland, Henry Hedman, Dan Boström, Rainer Backman, and Marcus Öhman. 2013. “Characterization of Reactor Ash Deposits from Pilot-Scale Pressurized Entrained-Flow Gasification of Woody Biomass.” *Energy & Fuels* 27 (11): 6801–14. https://doi.org/10.1021/ef401591a.

Mack, Robert, Daniel Kuptz, Claudia Schön, and Hans Hartmann. 2019. “Combustion Behavior and Slagging Tendencies of Kaolin Additivated Agricultural Pellets and of Wood-Straw Pellet Blends in a Small-Scale Boiler.” *Biomass and Bioenergy* 125 (June): 50–62. https://doi.org/10.1016/j.biombioe.2019.04.003.

Miles, T. R., and Jr Miles. 1996. “Experience with Biomass Fuel Blends in Combustion Systems,” 1996 international joint power generation conference, Houston, TX (United States). https://www.osti.gov/biblio/427867.

Öhman, Marcus, Anders Nordin, Bengt-Johan Skrifvars, Rainer Backman, and Mikko Hupa. 2000. “Bed Agglomeration Characteristics during Fluidized Bed Combustion of Biomass Fuels.” *Energy & Fuels* 14 (1): 169–78. https://doi.org/10.1021/ef990107b.

Richardson, Yohan, Martin Drobek, Anne Julbe, Joël Blin, and François Pinta. 2015. “Biomass Gasification to Produce Syngas.” In *Recent Advances in Thermo-Chemical Conversion of Biomass*, 213–50. Elsevier. https://doi.org/10.1016/B978-0-444-63289-0.00008-9.

Rodríguez, Juan Luis, Xana Álvarez, Enrique Valero, Luis Ortiz, Natalia de la Torre-Rodríguez, and Carolina Acuña-Alonso. 2020. “Design of Solid Biofuels Blends to Minimize the Risk of Sintering in Biomass Boilers.” *Journal of the Energy Institute* 93 (6): 2409–14. https://doi.org/10.1016/j.joei.2020.07.015.

Scarlat, Nicolae, Jean-François Dallemand, Fabio Monforti-Ferrario, and Viorel Nita. 2015. “The Role of Biomass and Bioenergy in a Future Bioeconomy: Policies and Facts.” *Environmental Development* 15 (July): 3–34. https://doi.org/10.1016/j.envdev.2015.03.006.

Speight, James G. 2011. *An Introduction to Petroleum Technology, Economics, and Politics: Speight/An Introduction*. Hoboken, NJ, USA: John Wiley & Sons, Inc. https://doi.org/10.1002/9781118192528.

Suárez-Ruiz, Isabel, and Colin R. Ward. 2008. “Chapter 4 - Coal Combustion.” In *Applied Coal Petrology*, edited by Isabel Suárez-Ruiz and John C. Crelling, 85–117. Burlington: Elsevier. https://doi.org/10.1016/B978-0-08-045051-3.00004-X.

The world bank. 2019. “Solid Waste Management.” https://www.worldbank.org/en/topic/urbandevelopment/brief/solid-waste-management.

———. 2021. “WHAT A WASTE 2.0, A Global Snapshot of Solid Waste Management to 2050, Trends in Solid Waste Management.” https://datatopics.worldbank.org/what-a-waste/trends_in_solid_waste_management.html.

Thy, P., B.M. Jenkins, R.B. Williams, C.E. Lesher, and R.R. Bakker. 2010. “Bed Agglomeration in Fluidized Combustor Fueled by Wood and Rice Straw Blends.” *Fuel Processing Technology* 91 (11): 1464–85. https://doi.org/10.1016/j.fuproc.2010.05.024.

Thy, Peter, Bryan M. Jenkins, Charles E. Lesher, and Sidsel Grundvig. 2006. “Compositional Constraints on Slag Formation and Potassium Volatilization from Rice Straw Blended Wood Fuel.” *Fuel Processing Technology* 87 (5): 383–408. https://doi.org/10.1016/j.fuproc.2005.08.015.

Vassilev, Stanislav V., David Baxter, Lars K. Andersen, and Christina G. Vassileva. 2010. “An Overview of the Chemical Composition of Biomass.” *Fuel* 89 (5): 913–33. https://doi.org/10.1016/j.fuel.2009.10.022.

Vassilev, Stanislav V., David Baxter, and Christina G. Vassileva. 2013. “An Overview of the Behaviour of Biomass during Combustion: Part I. Phase-Mineral Transformations of Organic and Inorganic Matter.” *Fuel* 112 (October): 391–449. https://doi.org/10.1016/j.fuel.2013.05.043.

Wang, Chang’an, Lei Zhao, Ruijin Sun, Yueyi Hu, Guantao Tang, Wufeng Chen, Yongbo Du, and Defu Che. 2019. “Effects of Silicon-Aluminum Additives on Ash Mineralogy, Morphology, and Transformation of Sodium, Calcium, and Iron during Oxy-Fuel Combustion of Zhundong High-Alkali Coal.” *International Journal of Greenhouse Gas Control* 91 (December): 102832. https://doi.org/10.1016/j.ijggc.2019.102832.

Yao, Xiwen, Haodong Zhou, Kaili Xu, Qingwei Xu, and Li Li. 2019. “Evaluation of the Fusion and Agglomeration Properties of Ashes from Combustion of Biomass, Coal

and Their Mixtures and the Effects of K2CO3 Additives." *Fuel* 255 (November): 115829. https://doi.org/10.1016/j.fuel.2019.115829.

Zeng, T., A. Pollex, N. Weller, V. Lenz, and M. Nelles. 2018. "Blended Biomass Pellets as Fuel for Small Scale Combustion Appliances: Effect of Blending on Slag Formation in the Bottom Ash and Pre-Evaluation Options." *Fuel* 212 (January): 108–16. https://doi.org/10.1016/j.fuel.2017.10.036.

Zeng, T., N. Weller, A. Pollex, and V. Lenz. 2016. "Blended Biomass Pellets as Fuel for Small Scale Combustion Appliances: Influence on Gaseous and Total Particulate Matter Emissions and Applicability of Fuel Indices." *Fuel* 184 (November): 689–700. https://doi.org/10.1016/j.fuel.2016.07.047.

1. Chapter 1. State of the art

In this chapter, the state of the art on ash reactivity of biomass mixtures will be thoroughly discussed. In the first section, the definitions of biomass will be presented, and its different classifications, inorganic contents, and families will be elaborated. Then, in section 2, the thermochemical conversion techniques will be discussed, emphasizing combustion. In section 3 the various reactors used in the thermochemical conversion techniques will be presented, highlighting their advantages and disadvantages. In section 4, the effect of each inorganic element in the biomass on the combustion behavior of each section of the ash will be dissected in detail. Section 5 is considered the most important in this chapter. It will contain a discussion on the effect of woody biomass, agricultural residues, and their blends on the combustion ash behavior of biomass on both laboratory and industrial scales, with an emphasis on oak bark, wheat straw, and their blends. A critical assessment of the importance of biomass blending in controlling the operational problems related to the ash will be presented in section 5.4. A prediction tool for the ash behavior of biomass blends is another pillar of this work. Hence, the prediction methods used in the literature will be assessed and presented in section 6.

1. Biomass

Biomass is the core of this work. Hence, in this section, biomass is defined, classified, and then its inorganic constituents are presented in detail. For further information about the subject, a comparison between biomass and coal is presented in Appendix A.

1.1. Biomass definition and classifications

The European environmental agency defined biomass as "the biodegradable fraction of products, waste and residues from agriculture (including vegetal and animal substances), forestry and related industries, as well as the biodegradable fraction of industrial and municipal waste" (European Environmental Agency 2022). In parallel, Chen et al. (W.-Y. Chen, Suzuki, and Lackner 2017) defined biomass as "all the matter on earth's surface of recent biological origin". Vassilev et al. (Vassilev et al. 2010) also designated biomass as "the contemporaneous (non-fossil) and complex biogenic organic–inorganic solid product generated by natural and anthropogenic (techno-genic) processes. Vakkilainen et al. (Vakkilainen 2021) elucidated biomass as "a material that originates from plants and animals i.e. has a recent biological origin". Biomass includes (W.-Y. Chen, Suzuki, and Lackner 2017):

1. Forest resources (also called woody biomass), such as forest growth residues, urban wood residues, forest products industry wastes, and fuelwood.
2. Agricultural resources, such as wheat, straw, rice, corn, hay, peat, miscanthus, etc.
3. Aquatic plants, such as algae.

They can also be divided into natural or derived materials; and subdivided into agricultural waste, forest products, and energy crops (Vassilev et al. 2010).

1.2. Biomass inorganic contents

Biomass is mainly formed of organic elements that consist of 70 wt.% to 95 wt.% of its total weight and include C, O, H, N, and S. However, they are out of the scope of this work (more details are given in Appendix A). In addition to their organic fraction, biomass contains an inorganic portion that mainly consists of Calcium (Ca), Silica (Si), Potassium (K), Magnesium (Mg), Sodium (Na), Phosphorous (P), Iron (Fe), and Chlorine (Cl). They are present in the fuel in the form of oxides, sulfates, carbonates, etc. Table 1.1 shows the inorganic contents of typical fuels analyzed by Vassilev et al. (Vassilev, Baxter, and Vassileva 2013) using ICP-MS (inductively coupled plasma spectroscopy – mass spectrometry). According to Vassilev et al. (Vassilev, Baxter, and Vassileva 2013), in general, the inorganic contents of biomass can be ranked as follow, depending on its type:

- Woody and animal biomass: Ca > Si > K > Mg > Al > P.
- Agricultural residues, such as straws and grass: Si > K > Ca > Mg > P > Al.
- Shells and husks: K > Si > Ca > P > Mg > Al.

Inorganic compounds can also be divided into 8 different families (Vassilev et al. 2010):

1. Oxides and hydroxides, such as $Mg(OH)_2$, $Ca(OH)_2$, and Fe_2O_3.
2. Silicates, such as SiO_2, Ca-silicates, and aluminosilicates.
3. Sulfates and sulfides, such as $CaSO_4$ and K_2SO_4.
4. Phosphates, such as Ca-phosphates, Ca-Mg-phosphates, and K-phosphates.
5. Carbonates, such as $CaCO_3$ and $CaMg(CO_3)_2$.
6. Chlorides, such as KCl and K-Ca-chloride.
7. Nitrates, such as KNO_3 and Ca-nitrates.
8. Other inorganic matter such as metals.

Table 1.1: Oxide (ash) contents of typical biomasses(Vassilev, Baxter, and Vassileva 2013)

Biomass group and sub-group	SiO_2	CaO	K_2O	P_2O_5	Al_2O_3	MgO	Fe_2O_3	SO_3	Na_2O	TiO_2	Sum	Mn	Samples
1. Wood and woody biomass (WWB)													
Mean	22.22	43.03	10.75	3.48	5.09	6.07	3.44	2.78	2.85	0.29	100.00	1.32	28
Minimum	1.86	5.79	2.19	0.66	0.12	1.10	0.37	0.36	0.22	0.06		0.08	28
Maximum	68.18	83.46	31.99	13.01	15.12	14.57	9.54	11.66	29.82	1.20		3.57	28
2. Herbaceous and agricultural biomass (HAB)													
Mean	33.39	14.86	26.65	6.48	3.66	5.62	3.26	3.61	2.29	0.18	100.00	0.13	44
Minimum	2.01	0.97	2.29	0.54	0.10	0.19	0.22	0.01	0.09	0.01		0.02	44
Maximum	94.48	44.32	63.90	31.06	14.60	16.21	36.27	14.74	26.20	2.02		0.46	44
2.1. Grasses (HAG)													
Mean	46.18	11.23	24.59	6.62	1.39	4.02	0.98	3.66	1.25	0.08	100.00	0.31	10
Minimum	8.73	2.98	2.93	3.14	0.67	1.42	0.58	0.83	0.09	0.01			10
Maximum	84.92	44.32	53.38	20.33	2.59	8.64	1.73	9.89	6.20	0.28			10
2.2. Straws (HAS)													
Mean	43.94	14.13	24.49	4.13	2.71	4.66	1.42	3.01	1.35	0.16	100.00	0.09	9
Minimum	7.87	2.46	12.59	0.98	0.10	1.67	0.41	1.18	0.16	0.02		0.02	9
Maximum	77.20	30.68	38.14	10.38	5.57	14.10	2.82	4.93	3.52	0.33		0.28	9
2.3. Other residues (HAR)													
Mean	24.47	16.58	28.25	7.27	4.90	6.62	4.84	3.80	3.05	0.22	100.00	0.16	25
Minimum	2.01	0.97	2.29	0.54	0.11	0.19	0.22	0.01	0.12	0.01		0.02	25
Maximum	94.48	44.13	63.90	31.06	14.60	16.21	36.27	14.74	26.20	2.02		0.46	25
3. Animal biomass (AB)													
Mean	2.90	49.04	7.67	28.17	1.69	2.75	0.35	3.91	3.50	0.02	100.00	0.05	2
Minimum	0.02	41.22	3.16	15.40	1.01	1.38	0.25	3.59	0.60	0.01		0.01	2
Maximum	5.77	56.85	12.19	40.94	2.37	4.11	0.45	4.24	6.41	0.03		0.09	2
4. Mixture of biomass (MB)													
Mean	44.19	17.48	6.00	5.72	10.82	3.52	6.34	2.66	2.53	0.74	100.00	0.16	4
Minimum	34.75	11.51	3.11	1.08	9.77	2.31	4.19	1.88	1.25	0.52			4
Maximum	57.83	25.70	7.76	18.07	11.35	4.77	10.44	4.62	3.18	0.95			4
5. Contaminated biomass (CB)													
Mean	35.73	18.30	3.45	3.64	15.41	3.60	9.78	3.45	1.90	4.74	100.00	0.15	8
Minimum	3.39	7.63	0.16	0.20	3.08	1.57	0.82	0.99	0.54	0.32		0.02	8
Maximum	60.10	26.81	9.70	15.88	53.53	6.45	22.18	10.55	4.06	27.58		0.23	8
All varieties of biomass (AVB)													
Mean	29.76	25.27	17.91	5.71	5.51	5.42	4.00	3.28	2.48	0.66	100.00	0.75	86
Minimum	0.02	0.97	0.16	0.20	0.10	0.19	0.22	0.01	0.09	0.01		0.01	86
Maximum	94.48	83.46	63.90	40.94	53.53	16.21	36.27	14.74	29.82	27.58		3.57	86
Natural biomass													
Mean	29.14	25.99	19.40	5.92	4.49	5.60	3.41	3.27	2.54	0.24	100.00	0.81	78
Minimum	0.02	0.97	2.19	0.54	0.10	0.19	0.22	0.01	0.09	0.01		0.01	78
Maximum	94.48	83.46	63.90	40.94	15.12	16.21	36.27	14.74	29.82	2.02		3.57	78
Aquatic biomass (A)													
Marine macroalgae	1.65	12.39	15.35	9.76	0.85	12.50	1.87	25.74	19.88	0.01	100.00	0.03	11
Solid fossil fuels													
Peat	37.53	9.97	1.12	2.75	20.14	2.14	13.83	12.11	0.10	0.31	100.00	0.08	1
Lignite (mean)	44.87	13.11	1.48	0.20	17.11	2.50	10.80	8.64	0.48	0.81	100.00	0.07	5
Sub-bituminous coal (mean)	54.74	7.05	1.67	0.08	22.86	2.14	5.30	4.07	1.09	1.00	100.00	0.05	10
Bituminous coal (mean)	56.14	4.90	1.61	0.22	24.82	1.55	6.68	2.16	0.77	1.15	100.00	0.05	22
Coal (mean)	54.06	6.57	1.60	0.50	23.18	1.83	6.85	3.54	0.82	1.05	100.00	0.05	37
Coal (minimum)	32.04	0.43	0.29	0.10	11.32	0.31	0.79	0.27	0.09	0.62		0.02	37
Coal (maximum)	68.35	27.78	4.15	1.70	35.23	3.98	16.44	14.42	2.90	1.61		0.18	37

2. Thermochemical conversion techniques

The word thermochemical can be divided into thermal, i.e. use of temperature, and chemical, i.e. chemical or elemental components. Hence, thermochemical conversion techniques use

temperature (200℃-1600℃) to degrade the fuel into new products that are more ecofriendly and have more proficient applications (W.-Y. Chen, Suzuki, and Lackner 2017; Richardson et al. 2015; Speight 2011). In addition, these conversion techniques can recover the chemical energy that already exists in organic materials (Luque, Campelo, and Clark 2011; J. Zhang and Zhang 2019). For instance, when burnt, biomass is considered to close the carbon cycle since the CO_2 absorbed from the atmosphere during photosynthesis is released back to it along with a certain amount of energy (W.-Y. Chen, Suzuki, and Lackner 2017). To support this idea, the heating values of the primary biomass wastes (i.e. bioenergy feedstock) are shown in Table 1.2 (W.-Y. Chen, Suzuki, and Lackner 2017). It can be seen from this table that the gross heating values of these typical biomasses (i.e. the amount of heat produced by the complete combustion of a unit quantity of fuel (Engineering Toolbox 2019)) is significant. Hence, their conversion provides a good energy source.

Thermochemical conversion techniques can be divided into dry and wet, depending on the fuel (J. Zhang and Zhang 2019). Wet techniques, such as hydrothermal carbonization, liquefaction, and gasification, are applied to degrade biomass with a moisture content higher than 60 wt.% (Zhao et al. 2014; Libra et al. 2011; Ubando, Felix, and Chen 2020; Nirmala et al. 2022). However, they are out of scope in this work. On the other hand, dry techniques, such as torrefaction, pyrolysis, combustion, and gasification, are used for biomass that has moisture contents lower than 60 wt.% (as received basis) (The Bioenergy Association in New Zealand and Australia 2019; G. Cruz et al. 2018; Orang and Tran 2015; Nasir Ani 2016; Gebgeegziabher et al. 2013; Rentizelas 2016).

Torrefaction, pyrolysis, and gasification are out of the scope of this work. However, some details about gasification are presented in Appendix A. On the other hand, combustion is considered a worldwide and well-established commercial technology with applications not only in industrialized countries, but mostly in developing ones, due to its low cost and high reliability.

Table 1.2: Main bioenergy feedstock with their heating values (W.-Y. Chen, Suzuki, and Lackner 2017).

Component	Heating value (gross) (GJ/MT unless otherwise mentioned)
Bioenergy feedstocks	
Corn stover	17.6
Sweet sorghum	15.4
Sugarcane bagasse	18.1
Sugarcane leaves	17.4
Hardwood	20.5
SoftWood	19.6
Hybrid poplar	19.0
Bamboo	18.5–19.4
Switchgrass	18.3
Miscanthus	17.1–19.4
Arundo donax	17.1
Giant brown kelp	10.0 MJ/dry kg
Cattle feedlot manure	13.4 MJ/dry kg
Water hyacinth	16.0 MJ/dry kg
Pure cellulose	17.5 MJ/dry kg
Primary biosolids	19.9 MJ/dry kg
Liquid biofuels	
Bioethanol	28
Biodiesel	40
Fossil fuels	
Coal (low rank; lignite/subbituminous)	15–19
Coal (high rank; bituminous/anthracite)	27–30
Oil (typical distillate)	42–45

The combustion process consists of multiple exothermic reactions in which the carbon is oxidized into carbon dioxide and the hydrogen into water. The simplified combustion reaction is as follows:

$$C_nH_mN_kO_l + (n+m/4-l/2)O_2 \text{ or Air} \rightarrow nCO_2 + (m/2)H_2O + (k/2)N_2 + \text{heat} \quad (A)$$

The major products of combustion are heat, H_2O, and CO_2. However, this formula is incomplete since it does not account for the inorganic metals in the ash, the moisture contents in the feedstock, and the numerous pollutants, such nitrous oxides (NO_x).

In combustion, the fuel burns at a temperature ranging between 800 °C and 1000 °C with excess oxygen. It has three main requirements to happen: fuel, air, and heat. If any of these factors is

absent, burning can stop or be incomplete. The excess air ratio, denoted by lambda (λ), is a key factor in any combustion process. Its formula is as follows:

$$\lambda = \frac{real\ air\ or\ O2\ pumped\ into\ the\ system}{stoichiometric\ air\ or\ O2} \quad (1)$$

The excess air ratio is higher than the stoichiometric amount and the locally available combustion air, ranging between 1 and 2.3 (Royo et al. 2019).

The decomposition of the organic section of the biomass by combustion occurs via a sequence of steps in parallel or sequentially. First, it starts by heating or drying the fuel to get rid of all the moisture contents (Abuelnuor et al. 2014). Then, the organic decomposition follows and happens between 200 °C and 800 °C (volatilization, pyrolysis, tars and char decomposition, etc.) (Strzalka, Erhart, and Eicker 2013). More details are provided in Appendix A, despite that the combustion of the organic section of the biomass is out of the scope of this work.

The most important combustion step related to this work is ash oxidization. This step is much slower than the other ones and encompasses around 20% of the total combustion time (Strzalka, Erhart, and Eicker 2013). The inorganic contents, which already exist in the parent biomass (section 1.2), are oxidized in the combustion mode. It concentrates inside the reactor or is emitted with the gaseous output. Both ways, it creates several operational and emissions problems, as will be discussed later on.

3. Applied reactors

Various types of reactors can be used in thermochemical conversion techniques, specifically combustion, such as furnace, fluidized bed, and entrained flow reactors. Each type of these reactors is defined, and its operational mode is discussed in Appendix A. A comparison summary for the key point parameters is presented in Table 1.3.

From Table 1.3, a furnace is used in small-scale appliances and has the simplest design along with the easiest operation compared to the other two types of reactors. However, the produced tar, ash, and char quantities are high, making the ash operational problems significant in a furnace compared to the other two reactors. The other two reactors provide good fuel mixing and efficient heat and mass transfers, leading to high carbon conversion and low tar and char production. Nevertheless, they suffer from ash operational problems, and their operation is complicated and comes at a higher cost than in furnaces.

Table 1.3: Key points comparison between the furnace, fluidized bed, and entrained flow reactors based on literature in combustion shown in Appendix A.

	Furnace	**Fluidized bed**	**Entrained flow reactor**
Design	simple	complicated	complicated
Reactor scale	Small capacities	Medium-size units	Large capacities
Capacity	kW	MW	GW
Operation	easy	moderate	hard
Performance	reliable	high	moderate
Reactor pressure	low	high	very high
Reactor chamber temperature (°C)	800-1200	800–1000	>1200
Homogeneous temperature distribution	low	high	moderate
Oxidant requirements	Low	Moderate	High
Operational and investment cost	low	moderate	high
Controlling the operating conditions	easy	easy	moderate
Fuel type applied	dry biomass	wet or dry biomass	dry biomass
Tolerance for fines	Limited	Good	Excellent
Heat and mass transfer	low and non-uniform	high	moderate
Fuel mixing	low	high	moderate
Carbon conversion	low	high	high
Tars, ash and chars quantity	large	small	small
Nature of ash produced	Dry	Dry	Slagging
Ash problematic complications	high	low	moderate

4. Interactions between the inorganic elements that affect the ash behavior

Ash comes from the inorganic materials that already exist in the biomass (section 1.2), and remains in the reactor after combustion. These inorganic elements follow different chemical reactions depending on the operating temperature, the oxidizing or reducing gas atmosphere (air/O_2 in combustion), the total pressure inside the reactor, and the surrounding materials (bed material, metallic or refractory reactor walls). To understand the biomass ash behavior, which composition varies a lot and affects its behavior, the types and forms of interactions between the inorganic elements behind it should be well understood. As a result, in this section, the interactions between the inorganic elements in ash each division will be discussed in detail.

4.1. Ash inorganic constituents families and stabilities

The main constituents of the ash can be divided into 5 main families (Vassilev et al. 2010):

1. Alkaline earth metals, such as Ca and Mg, which have very high melting temperature in the oxide forms.
2. Alkali metals, such as K and Na, which have low melting temperature.
3. Other metals, such as Al, Fe, and Mn.

4. Nonmetals, such as P, S, and Cl.
5. Metalloids, such as Si.

Na and K belong to the same periodic group, so their functional role is similar. Na concentration in the biomass is generally lower than K. Hence Na behavior can be approximated by K behavior (Boström et al. 2012; Royo, Canalís, and Quintana 2020). Similarly, Mg behavior can be approximated by Ca behavior (Boström et al. 2012; Royo, Canalís, and Quintana 2020). Al can play an important role in the ash transformation mechanism. However, it originates from external mineral matters included in the fuel matrix, such as sand or kaolin (Boström et al. 2012). Hence, it will be omitted from the discussion.

In combustion mode, the mutual affinity of the ash-forming element to oxygen in relation to the oxygen affinity to the carbon-hydrogen matrix of the fuel is a core factor for ash transformation. After calculating Gibbs free energy for different oxides at various temperatures in Figure 1.1, Bostrom et al. (Boström et al. 2012) ranked the oxides stability in this increasing order: $K_2O < Na_2O < SO_2 < H_2O/P_2O_5 < CO_2 < CO < SiO_2 < MgO < CaO$. Hence, under a high amount of oxygen, such as combustion mode, SiO_2, MgO, and CaO will stay mainly as oxides, while P_2O_5, SO_2, Na_2O, and K_2O will easily volatilize and react.

Bostrom et al. (Boström et al. 2012) went on and divided the primary oxides into acidic ($P_2O_5 > SO_2/SO_3 > HCl > SiO_2 > CO_2 > H_2O$) and basic ($KOH > NaOH > CaO > MgO > H_2O$), with decreasing reactivity. Bostrom et al. (Boström et al. 2012) defended the concept that the reactions within the ash will move on upon an acid-base reaction mechanism between the basic (KOH and NaOH similar, and CaO and MgO similar) and the acidic components, and following the order of reactivity:

$$P_2O_5\,(g) + 2KOH\,(g) \leftrightarrow 2KPO_3\,(l,g) + H_2O\,(g) \quad (B)$$

$$SO_3\,(g) + 2KOH\,(g) \leftrightarrow K_2SO_4\,(l,g) + H_2O\,(g) \quad (C)$$

$$HCl\,(g) + KOH\,(g) \leftrightarrow KCl\,(g,l) + H_2O\,(g) \quad (D)$$

$$SiO_2\,(s) + 2KOH\,(g) \leftrightarrow K_2SiO_3\,(l) + H_2O\,(g) \quad (E)$$

$$CO_2\,(g) + 2KOH\,(g) \leftrightarrow K_2CO_3\,(l,g) + H_2O\,(g) \quad (F)$$

$$P_2O_5\,(g) + 3CaO\,(s) \leftrightarrow Ca_3P_2O_8\,(s) \quad (G)$$

$$SO_3\,(g) + CaO(s) \leftrightarrow CaSO_4\,(s,l) \quad (H)$$

$$2HCl\,(g) + CaO(s) \leftrightarrow CaCl_2\,(g,l) + H_2O(g) \quad (I)$$

$$SiO_2\,(s) + CaO\,(s) \leftrightarrow CaSiO_3\,(s) \quad (J)$$

$$CO_2\,(g) + CaO\,(s) \leftrightarrow CaCO_3\,(s) \qquad (K)$$

$$K_2SiO_3\,(l) + CaO\,(s) \leftrightarrow K\text{-}Ca\text{-silicate}\,(l) \qquad (L)$$

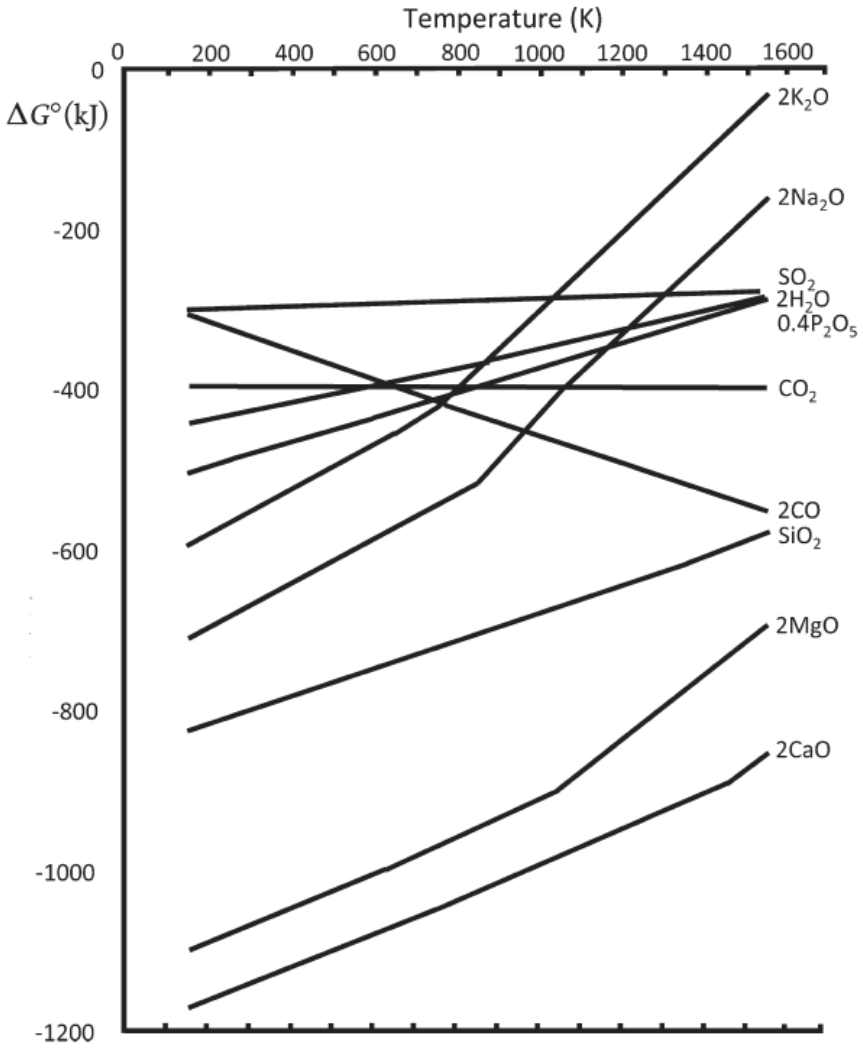

Figure 1.1: Stability diagram of the major ash-forming oxides (Boström et al. 2012).

Consequently, K-phosphates (or Na) will first form, then K-sulfates followed by chlorides according to the acidic order. Silicates and carbonates are usually formed in later stages and are congregated in the bottom ash. It should be noted that carbonates are favored over all other compounds when basic metals (i.e. K, Ca, Mg) are in surplus over the acidic ones (i.e. P, S, Si, Cl) (Boström et al. 2012).

4.2. Elemental interaction in the bottom ash

Bottom ash is considered the part of the ash that concentrates in the bottom of the reactor. Bottom ash speciation, partition, and transformation are highly dependent on the process operating conditions and ash composition (Boström et al. 2012; Díaz-Ramírez et al. 2012). Temperature and oxygen contents (oxygen partial pressure) play a major role in affecting the ash transformation. The interactions between Si, Ca, and K can significantly affect the bottom ash behavior.

Si exists in the original biomass either in the amorphous SiO_2-H_2O (i.e. silica gel) form or as a dissolved $Si(OH)_4$ in the silica gel. Si has a higher affinity to oxygen than hydrogen or carbon. It also has several refractory characteristics. Consequently, during combustion, H_2O will evaporate. Then, SiO_2 will be liberated as small silica (SiO_2) particles, which will form a silicate matrix and react with the other remaining elements in the bottom ash, especially alkali and alkaline earth metals.

Ca is originally present as oxalate in the dissociated form Ca^{2+} and can be transferred during combustion via the intermediates $Ca(OH)_2$, $CaCO_3$, and CaO to different silicates, carbonates, and phosphates (Höfer and Kaltschmitt 2017). Due to the very high stability of the calcium-oxygen compounds, it will probably be first liberated as small micrometered-sized particles during thermochemical conversion of biomass. These particles will increase the CaO refractory character; hence, most of it will remain in the solid oxide form. Due to their small size, a part of these liberated CaO particles will compete with the rest of the inorganic compounds (especially with alkali metals) for a place on the silicate matrix or react with them on this matrix. This is the exact same case for Mg.

It should be noted that Fe could be found in the dissociated form Fe^{2+} in biomass and forms amorphous structures in biomass ash (Höfer and Kaltschmitt 2017). Mn can also be found as MnO in CaO or MgO, the remainder as MnO_2 (Höfer and Kaltschmitt 2017).

4.2.1. Sintering formation

Ash sintering is a common problem in a furnace and any grate reactor. It is directly related to the interaction between the alkaline earth and alkali metals on the silica matrix. The tensile strength and the adhesion force of silica gradually increase between 400 °C and 700 °C (Tsukada, Yamada, and Kamiya 2003). Once it starts capturing K on its matrix, alkali-silicate compounds start to form. The alkali-silicate system, especially K-Si, has a low eutectic

temperatures that can be as low as 600 °C (Rodríguez et al. 2020). This makes the formation of a molten phase much easier.

Depending on the ash composition of the fuel, in the case of the high availability of K and Si, the density of molten K-silicate particles increases significantly. But as the fuel particles are burning out due to carbon loss (between 350 °C and 450 °C) along with K, S, and Cl volatilization (between 400 °C and 600 °C), it shrinks, and the ash particles approach each other with an increased opportunity of contact (Boström et al. 2012; Rebbling et al. 2020; Tsukada, Yamada, and Kamiya 2003). This will lead to an aggregation of the molten K-silicate particles, which will form larger droplets and initiate slag formation (Alam et al. 2021; Tsukada, Yamada, and Kamiya 2003). The liquid phase forms a bridge between the ash particles to promote ash adhesion on all the surfaces in the reactor and with the bed materials (Tsukada, Yamada, and Kamiya 2003). Cl acts as a facilitator of the reaction between alkali metals and Si that yields alkali metal silicates with melting temperature below 800 °C (Arvelakis et al. 1999). Luan et al. (Luan, You, and Zhang 2014) have also found that sintering temperature decreased with the basic/acidic ash ratio increase.

Rebbling et al. (Rebbling et al. 2020) discussed in more details the reason for liquid ash phase (i.e. slag) intensification. Close to the burning of the fuel bed, three reactions compete with each other:

$$2KOH\,(g) + 4SiO_2\,(s) \leftrightarrow K_2Si_4O_9\,(l, s) + H_2O\,(g) \qquad (M)$$

$$KOH\,(g) + HCl\,(g) \leftrightarrow KCl\,(g,s) + H_2O\,(g) \qquad (N)$$

$$2KOH\,(g) + SO_3\,(g) \leftrightarrow K_2SO_4\,(s) + H_2O\,(g) \qquad (O)$$

If the fuel is highly rich with silicates, which is the case of most agricultural wastes, for example, the first reaction (reaction M) is favored. Consequently, KOH in the gaseous phase will react with the silicate matrix and intensify slag formation, forming low melting compounds such as $K_2Si_4O_9$. As a result, Si rich fuel can decrease fly ash and alkali release and lower particulate matter (PM) and corrosion by K entrapment in the silicate matrix but at the expenses of slag formation (Rebbling et al. 2020). Consequently, decreasing corrosion and Alkali release are convoyed with increasing slag formation.

It should be noted that the K-phosphates formed in the first reaction (reaction B) is molten, so they can easily react with alkaline earth and/or aluminum oxides to form ternary compounds. In this case, they become saturated in the bottom ash due to incorporating alkaline earth metals.

4.2.2. Agglomeration in the fluidized bed

Bed agglomeration is widely seen in biomass combustion in the fluidized bed reactor. Bed materials (i.e. silica, olivine, etc.) are used to enhance mixing and temperature distribution inside the reactor. However, bed agglomeration can take place and freeze the bed circulation (Balland et al. 2017). This in turn restricts the heat transfer inside the reactor and limits the fuel conversion.

In the first mechanism of bed agglomeration, high temperature molten or partially molten sulfates, carbonates, and especially silicates bond/react with the bed particles (Visser, van Lith, and Kiel 2008; Öhman et al. 2000; P. Thy et al. 2010). Consequently, large chunks of bed materials-ash particles solid mixtures, called agglomerate, form. This mechanism is often referred to as "coating induced agglomeration" (Visser, van Lith, and Kiel 2008). Firing temperature, fuel composition, and additives can all affect it (Skrifvars et al. 1999).

Agglomeration in a fluidized bed reactor can also occur in a second mechanism because of the partial melting of the ash over the operating temperature range (700 °C-1000 °C) (Öhman et al. 2000). This mainly occurs in the fuel rich in alkaline (K, Na), like wheat straw. The K and Na rich ash particles will melt down at low temperatures and entrap bed materials within (Visser, van Lith, and Kiel 2008). This will form agglomerates. In contrast with the first mechanism, no interaction between the ash and bed materials occurs here. This mechanism is often referred to as "melt-induced agglomeration" (Visser, van Lith, and Kiel 2008).

4.2.3. Controlling sintering and agglomeration

Possible ways can be applied to decrease corrosion and alkali release while keeping slag formation low. First, phosphate will always compete with silicate in the bottom ash matrix. Slag formation can be hindered by high phosphate contents in the fuel since P prevents K from attacking the surface of the quartz bed grains (Boström et al. 2012). Second, fuels, such as woody biomasses, which are concentrated with sand and clay, are highly rich in aluminosilicates. These compounds are highly stable and can increase the melting temperature of ash (Boström et al. 2012). Third, preheating the oxidizing agent has the potential to increase the amorphous matter fraction via a liquid phase ash formation (Royo, Canalís, and Quintana 2020), so no-preheating is favored. Fourth and most importantly, the K-silicates compounds, such as $K_2Si_4O_9$, that has a low melting temperature (Rebbling et al. 2020; Santoso et al. 2020a), can encounter the alkaline earth oxides that are mostly concentrated in the bottom ash. Competition between the alkaline earth metals (Ca, Mg) and K on the active sites of the silicate matrix lead to a substitution of K in this matrix by Ca and Mg. A reaction between the two on

the same matrix can also happen. This incorporation of alkaline earth metals into the agglomerates, due to the high affinity of silicate melts to alkaline earth metals (Boström et al. 2012), increases the melting temperature of ash and decreases the agglomeration propagation. Rebbling et al. (Rebbling et al. 2020) showed several reaction pathways for this incorporation leading to more stable compounds seen in several studies in biomass combustion. The reactions are as follows:

$$CaO\ (s) + SiO_2\ (s) \leftrightarrow CaSiO_3\ (s) \quad (P)$$

$$2CaSiO_3\ (s) + K_2Si_4O_9\ (l,s) + 3SiO_2\ (s) \leftrightarrow Ca_2K_2Si_9O_{21}\ (s,l) \quad (Q)$$

$$CaO\ (s) + 4K_2Si_4O_9\ (l,s) \leftrightarrow CaK_8Si_{10}O_{25}\ (s,l) + 6SiO_2\ (s) \quad (R)$$

Consequently, choosing a fuel rich in Si and Ca / Mg is important since high Si will capture the alkali metals and decrease particulate matter emissions and corrosion, and high Ca counteracts low temperature melts by inhibiting the silicate matrix and increasing the melting temperature of the slag.

4.3. Elemental interactions in the fly ash

The Encyclopedia of Energy defines fly ash as “the finest ash particles, transported from the combustion chamber by exhaust gases, and formed from the mineral matter in the fuel along with a small amount of carbon that remains from incomplete combustion”.

From Figure 1.1, alkali metals (i.e. K and Na) are the least stable oxides and may be reduced to metal vapor by the carbon-hydrogen fuel matrix. In the gaseous phase, they will primarily react with water vapor to form a relatively more stable volatile potassium hydroxide (KOH) and sodium hydr°oxide (NaOH). These alkali metals are less reactive than P, S, and Cl due to the low volatility of their host compounds (Boström et al. 2012). However, they will be highly volatile in the hydroxide (KOH / NaOH) and chloride (KCl / NaCl) forms, and will be easily released in the fly ash.

S is also highly volatile. It can easily combine with alkali metals to form deposits on the reactor walls and convective surfaces (Miles and Miles 1996). It can also react with CaO to form $CaSO_4$ in the gas form (Shi et al. 2022). In addition, S has a lower affinity to oxygen than to carbon and hydrogen, hence it will be released in the form of S_2 gas or H_2S. Then, it will further oxidize in the presence of excess oxygen between 820 °C and 1000 °C to form SO_2 and SO_3 in the gas.

Cl, which is considered an unstable oxide, will easily volatilize in the form of Cl_2 and HCl vapor due to their low stability bonds with oxygen. At low temperatures, KOH and HCl can

react to form KCl (Höfer and Kaltschmitt 2017). KCl is considered the direct and major cause of corrosion (Luan, You, and Zhang 2014). In parallel, SO_3 can also react with KCl and water to form K_2SO_4 (Höfer and Kaltschmitt 2017). These sulfates deposit on the reactor walls and react with it to start corrosion (Miles and Miles 1996; Arvelakis et al. 1999). In addition, the sulfates act as collectors of fly ash and aerosols to increase the size of deposits (Arvelakis et al. 1999). Sulfates volatilize at moderate temperature, while chlorides will always be directly released to the gas phase.

Fly ash can be formed by two different pathways: condensation or entrainment (Royo, Canalís, and Quintana 2020; Höfer and Kaltschmitt 2017).

Condensation: Due to their high volatilization, alkali metals, chlorides, sulfates, and hydroxides easily vaporize. Upon contact with the reactor walls far from the reactor core, these particles start to cool down (condense). Then, they deposit on the heating surfaces of the reactor as chlorides (corrosion), sulfates, and carbonates. This deposition happens by direct condensation or after forming aerosols by thermophoresis or turbulent diffusion (Royo, Canalís, and Quintana 2020). More specifically, due to their low melting point, alkali metals compounds (K, Na) form a sticky layer to which other condensed elements adhere (Miles and Miles 1996; Royo et al. 2019).

Entrainment: Silicates, aluminosilicates, phosphates, oxides, carbonates, sulfates, and hydroxides of Mg, Si, Ca, and Fe leave the bottom ash by inertial impact and adhere to the sticky layer on the reactor surface (Royo, Canalís, and Quintana 2020). Hence, they form fly ash and aerosols.

Most of the fly ash coming from condensation are Cl, S, K, and Na based compounds. Their percentage decreases as the excess air ratio (λ) increases (Royo, Canalís, and Quintana 2020). Ca, Mg, and Al come from the entrainment effect, originating from the bottom ash, and increasing with the increase in excess air ratio (Royo, Canalís, and Quintana 2020).

4.4. Elemental interaction in the particulate matter emissions

The United States Environmental Protection Agency defines TPM or total particulate matter as “the general term used to describe solid particles and liquid droplets found in the air” (United States Environmental Protection Agency 2014). They are formed of organic and inorganic compounds of the fuel, especially of volatile and semi-volatile ash-forming elements such Al, Ba, Ca, Cd, Cr, Cu, Fe, K, Mg, Mn, Na, Ni, Pb, Sr, V, and Zn (Zeng et al. 2016; Yatkin and Bayram 2007; Lamberg et al. 2013). The key difference between fly ash and particulate matter

is that the first stick to the reactor walls while the second exits the reactor with the gaseous product (Lamberg et al. 2013). This is mainly due to the small particle size (usually <10 µm) of the latter (Lamberg et al. 2013).

TPM comprises alkali metals sulfates, chlorides, and carbonates (Lamberg et al. 2013). K is the most abundant element in aerosols, so its concentration in the mother fuel plays a crucial role in the particulate matter emissions (Lamberg et al. 2013). Depending on K interactions with Cl and S, K compounds such as K_2SO_4, KCl, KOH, and K_2CO_3 are all released to the gas phase (Zeng et al. 2016). These compounds are widely found in the TPM of combusted biomass. Fuels rich in S tend to form more alkali sulfates than alkali chlorides. This will increase Cl emissions in the TPM in the form of HCl (Lind et al. 2006). Zn is also found in the TPM as ZnO and $ZnCl_2$ (Lamberg et al. 2013).

TPM emission is highly dependent on combustion reactor and fuel types, specifically bed temperature and fuel ash composition (Knudsen, Jensen, and Dam-Johansen 2004; Zeng et al. 2016). TPM are usually emitted at a fuel bed temperature between 795°C and 1088°C (Zeng et al. 2016). For instance, the sum of K, Na, Cl, and S in the fuel is linearly related to TPM emissions (Sippula et al. 2007). K_2SO_4 consist around 80-90 wt.% of biomass TPM (Höfer and Kaltschmitt 2017). Phosphate-rich fuels also proved to generate a larger amount of total particulate matter than silicate-rich fuels (Díaz-Ramírez et al. 2012). This was mainly related to the lower sintering temperature (slag phase can retain some of the TPM) of the latter than the former (Díaz-Ramírez et al. 2012).

5. Biomass ash behavior (with an emphasis on bark and straw)

The previous section detailed the general interactions between the inorganic elements that can exist in each biomass ash division in combustion mode. However, biomass ash composition is more heterogeneous, leading to more complicated ash interactions that highly depend on the feedstock ash contents and compositions. As a result, the key literature findings around the combustion ash behavior in woody biomass and agricultural residues will be discussed, focusing on oak bark and wheat straw in furnaces and fluidized beds (sections 5.1 and 5.2). In section 5.3, the capability of additives to be a typical solution for ash problematics will be assessed, highlighting their limitations. Then, in section 5.4, blending will be presented as an alternative that renders the application of both wood and agricultural residues possible in the various types of reactors with minimal ash problematics. Section 5.4 will be the most important part of this chapter as fuel blending is the main topic of this work. For further information, the

ash behavior in coal and coal-biomass combustion were presented in Appendix A, underlining the limitations and environmental problematics of this approach.

5.1. Woody biomass

As introduced in section 1.1, woody biomass includes all the forest resources that exist in nature, such as forest growth residues, urban wood residues, forest industry wastes, and fuelwood. Woody biomasses have the lowest total ash contents among all the families of biomass, hitting as low as 1 wt.% in the case of wood (Vassilev, Baxter, and Vassileva 2013; Royo et al. 2019; Alam et al. 2021; Porbatzki, Stemmler, and Müller 2011). Hence, their ash-related problems are usually easily controllable (Miles and Miles 1996). As shown in Table 1.2, their ash are characterized by high Ca/K and Ca/Si ratios. Consequently, they will present high melting temperature, which can go as high as 1500 °C (Royo, Canalís, and Quintana 2022; Díaz-Ramírez et al. 2012; Rizvi et al. 2015; Vassilev, Baxter, and Vassileva 2014). In addition, woody biomass have low S and Cl contents (Rodríguez et al. 2020). Hence, their corrosion and emissions-related problems are limited.

5.1.1. Bottom ash behavior in woody biomasses

Bottom ash contents of woody biomasses are concentrated with Si, Ca, Mg, Al, and P. Si exists mainly in the form of quartz (SiO_2) and feldspars ($(K,Na)AlSi_3O_8$) (Boström et al. 2012). The Al contents in the biomass ash are considered to originate from soil contamination as external mineral matter, such as feldspars or clay minerals (Siim Link, Yrjas, and Hupa 2018). Ca and Mg are present in the form of carbonates and silicates, such as $CaCO_3$ and $CaSiO_3$ (Boström et al. 2012; Defoort et al. 2019). The major part of P is also located in the bottom ash of woody biomasses in the form of apatite ($Ca_5(PO_4)_3OH$) and whitlockite ($Ca_3(PO_4)_2$) (Boström et al. 2012).

Alkaline earth oxides can react with the alkali-silicate slag (Rebbling et al. 2020; Defoort et al. 2019). As a result, ternary compounds of alkaline-earth-silicates will be formed in the bottom ash of biomass, decreasing the slag formation tendency (Rebbling et al. 2020; Defoort et al. 2019). However, Bostrom et al. (Boström et al. 2012) reported that they were never found in woody biomasses. One possibility is their precipitation in the slag with the temperature decreasing as the reactor cools down (Boström et al. 2012). Another possibility is the reaction of alkaline earth metals with the silicate matrix instead of the alkali-silicate compounds, replacing the alkali metals on the first and pushing them towards the gaseous phase (Boström et al. 2012; Rebbling et al. 2020). The probability of the second possibility is enhanced by the high Ca concentration in the woody biomasses at the expense of low K contents (Table 1.2).

5.1.2. Fly ash and TPM behavior in woody biomasses

Fly ash is rich in alkali sulfates and chlorides, especially K_2SO_4, $K_3Na(SO_4)_2$, and KCl. This is due to the high volatility of alkali metals and the incorporation of the alkaline earth metals into the silicate matrix in the bottom ash (Boström et al. 2012). For instance, Ca-sulfides were approximately absent since most of Ca and the heavy metals were retained in the bottom ash (Porbatzki, Stemmler, and Müller 2011). In addition, most K migrates into the gas phase in the form of KCl. Hence, the low Cl contents in wooden ash hinder K passage to the gaseous phase (Royo et al. 2019). At the same time, if S contents are high in the wooden ash, K-sulphates will be easily formed (Royo et al. 2019).

Similarly, particulate matters of woody biomass are abundant with alkali sulfates and KCl, while carbonates are almost absent (Boström et al. 2012). At a temperature above 900°C, the equilibrium between HCl and KCl shifts towards alkali chlorides, and then KCl emissions significantly increase (Porbatzki, Stemmler, and Müller 2011). This might be directly related to the increasing water partial pressure with the temperature increase, shifting the $2KCl + H_2O = 2HCl + K_2O$ reaction towards the left. TPMs are also poor with phosphates retained in the bottom ash (Porbatzki, Stemmler, and Müller 2011). S emissions are less problematic in wooden residues than in other biomasses due to their high Ca/S ratio. For example, Hu et al. (Hu et al. 2020) characterized the ash behavior in a 30 MW biomass-fired power plant emissions. They have found that bark emitted coarse particles (1-10 µm) with negligible and low-moderate S contents (Hu et al. 2020).

5.1.3. Parameters affecting the ash behavior of woody biomasses

Ash composition of woody biomass can affect their behavior. For instance, Bostrom et al. (Boström et al. 2012) found that the high $(K_2O+Na_2O+CaO+MgO)/SiO_2$ in woody biomasses hindered slag formation. Hence, high alkali metals contents increased particulate matter formation instead of slag formation (Boström et al. 2012). High Si contents and hence low (Ca+K)/Si ratio led to higher retention of alkali and alkaline earth (heavy) metals in the bottom ash and decreased the TPM emissions (Porbatzki, Stemmler, and Müller 2011). Porbatzki et al. (Porbatzki, Stemmler, and Müller 2011) analyzed the slag in the bottom ash and found that it consisted mainly of silicates and phosphates.

The operating conditions can also affect the ash behavior. Royo et al. (Royo et al. 2019; Royo, Canalís, and Quintana 2022) studied the effect of air flow rate, temperature, and excess air ratio (λ) on ash sintering and deposition of wood, barley straw, corn, and their blends in laboratory fixed bed reactor in combustion mode. In the case of pure woody biomasses, the entrainment

effect is more abundant than volatilization due to the lower sintering tendency of this single biomass. Hence, as λ increased, the excess alkaline earth metals in the residual ash and the small alkali metals contents passed to the fly ash (Royo et al. 2019; Royo, Canalís, and Quintana 2022). This decreased the bottom ash proportion and increased the fly ash emissions (Royo et al. 2019; Royo, Canalís, and Quintana 2022; Porbatzki, Stemmler, and Müller 2011). In parallel, the increase in temperature enhanced emissions but had a minor effect on slag formation due to the small concentration of alkali metals in this type of biomass (Royo et al. 2019; Porbatzki, Stemmler, and Müller 2011). According to Porbatzki et al. (Porbatzki, Stemmler, and Müller 2011), the release time decreased with the increasing temperature (Porbatzki, Stemmler, and Müller 2011).

In conclusion, in the literature, the ash of woody biomasses presents a high melting point and a low sintering tendency due to their high alkaline earth oxides composition. However, their emissions highly depend on their S and Cl concentrations.

5.2. Agricultural biomass

Agricultural residues consist of a wide range of natural agricultural wastes, such as wheat, straw, rice, corn, hay, peat, miscanthus, etc. (Vassilev, Baxter, and Vassileva 2013). Ash concentration in agricultural biomasses is 5 to 20 times higher than in woody biomasses (Boström et al. 2012; Alam et al. 2021). Moreover, the composition of agricultural fuel is more heterogeneous than the latter, with higher concentrations of K, Si, S, and Cl (Vassilev et al. 2010; Vassilev, Baxter, and Vassileva 2013; Royo, Canalís, and Quintana 2020; Zeng et al. 2016; Alam et al. 2021). Hence, their bottom and fly ash behaviors will differ from those of the woody biomasses.

5.2.1. Bottom ash behavior of agricultural residues

As discussed in section 4, the presence of K-silicates will always lower the ash melting temperature of the feedstock and promote slagging (Rebbling et al. 2020; Díaz-Ramírez et al. 2012). On the other hand, Cl presence enhances corrosion (Rebbling et al. 2020; Díaz-Ramírez et al. 2012). Consequently, ash problems related to sintering and agglomeration, along with corrosion (KCl and HCl) and toxic emissions (SO_x) are more prominent when agricultural biomasses are applied (Díaz-Ramírez et al. 2012).

In one of the first researches in this domain, Arvelakis et al. (Arvelakis et al. 1999) tried to predict the combustion ash thermal behavior using a DSC on three configurations of wheat straw (untreated wheat straw, fractioned wheat straw, and leached wheat straw), the agricultural residue used in the current work. The ash of wheat straw yielded three endotherms: the first two

endotherms at 150℃ and 250℃ were attributed to water evaporation, while the third endotherm that started at 700℃ until around 1000℃ was related to ash melting behavior (Arvelakis et al. 1999). The DSC analysis showed a sharper curve due to the increase in sintering degree resulting from the substitution of Ca by K in the silicate matrix (Arvelakis et al. 1999). According to the preliminary reaction pathway of the alkali-silicate metals proposed by Arvelakis et al. (Arvelakis et al. 1999), the large quantities of alkali metals in the straw were first oxidized. Then, they reacted with the silica matrix and initiated low melting temperature slag formation (Arvelakis et al. 1999). This mechanism was adapted and developed by several subsequent researchers in the domain (Boström et al. 2012; Royo, Canalís, and Quintana 2022; Rebbling et al. 2020; Zeng et al. 2016; Alam et al. 2021; Tsukada, Yamada, and Kamiya 2003). Xiaoping et al. (Xiaoping et al. 2020) argued that the alkali metals sulfidation reaction (KCl reaction with sulfur oxide) is responsible for the molten phase forming on the reactor walls, while the alkali metals react with the silicates to form the bottom ash slag. The ash of straw was recently reported to melt completely at 1300 °C (Zhai et al. 2022).

5.2.2. Fly ash and TPM behavior in agricultural residues

Agricultural residues with high K contents will favor fly ash and particulate matter emissions (Boström et al. 2012). SO_x emissions are also enhanced when these fuels are used (Boström et al. 2012). For instance, deposits and TPM from agricultural residues combustion are rich in K-sulfates, K-chlorides, and K-phosphates if the original biomass is rich in P (Díaz-Ramírez et al. 2012; Zhai et al. 2022). The oxides can react with S to produce a minor amount of sulfates in the solid phase (dissolved in the slag), but a major one in the gas phase (Arvelakis et al. 1999). This behavior enhances fly ash deposition (Arvelakis et al. 1999). Similarly, alkali metal chlorides can vaporize between 770℃-900℃ (Arvelakis et al. 1999). This vaporization also facilitates the gas phase reactions, which lead to fly ash and TPM formations (Arvelakis et al. 1999).

5.2.3. Slagging and emissions relationship in the ash of agricultural residues

Slagging and emissions in agricultural residues are directly related. These biomasses are rich in K, which is the core element affecting both sintering and emissions at the same time (Vassilev, Baxter, and Vassileva 2013). The majority of this K will react with Si to form slags, while the rest will be emitted with the gaseous effluent. Generally, around 30 wt.% of the total ash of the agricultural residues is emitted as TPM or fly ash (Jamian et al. 2020). The rest is slag. In addition, Cao et al. (Cao et al. 2021)found that the release of K in wheat straw samples started at 700 °C and reached 60% (from its initial contents) at 1000 °C in a

laboratory scale combustion furnace. This K fractionation was due to the ashes of agricultural residues that have less tendency to entrain and more tendency to sinter and increase the bottom ash proportion (Royo et al. 2019). This is directly related to their high Si and K contents, especially in the case of wheat straw (Royo et al. 2019). Then, the molten ash will entrap the volatile K, Cl, and S compounds, increasing the carbon conversion in the gaseous phase (Zhai et al. 2022). In addition, the surplus of Si in the agricultural residues enhances the sintering effect of alkaline earth metals, so sintering becomes more affluent beyond 900°C (Royo et al. 2019).

In conclusion, higher slagging leads to lower emissions but more operational problems in the literature.

Several researchers in the literature presented the inverse relation between slagging and emissions in agricultural residues. Zeng et al. (Zeng et al. 2018; 2016) studied the slagging behavior, particulate emissions, and gaseous emissions of pure wood, pure miscanthus, pure wheat straw, and their blends in a commercial boiler of 30KW in combustion mode. They have found that TPM emissions in the form of HCl and SO_x were the highest in agricultural residues (Figure 1.2) (Zeng et al. 2016). In addition, they found that the majority of K was in the slag, while a minority was emitted in the form of KCl and K-sulphates (Zeng et al. 2016). Yao et al. reported the combustion ash behavior of corncob in a 35 kW laboratory scale fixed bed downdraft gasifier (Yao, Zhou, et al. 2020) and in a 175 kW pilot scale fixed-bed downdraft gasifier (Yao, Zhao, et al. 2020). They found that the fly ash in the cyclone was rich in K-based compounds while the gasifier ash was more dense and rich in silicate, specifically alkali-silicates (Yao, Zhou, et al. 2020; Yao, Zhao, et al. 2020). However, agglomeration propensity was lower in the cyclone than in the gasification chamber, especially in the pilot-scale reactor (Yao, Zhao, et al. 2020). Most Cl was evacuated with the syngas, while most K and Ca were retained in the cyclone and gasification chamber, respectively (Yao, Zhao, et al. 2020).

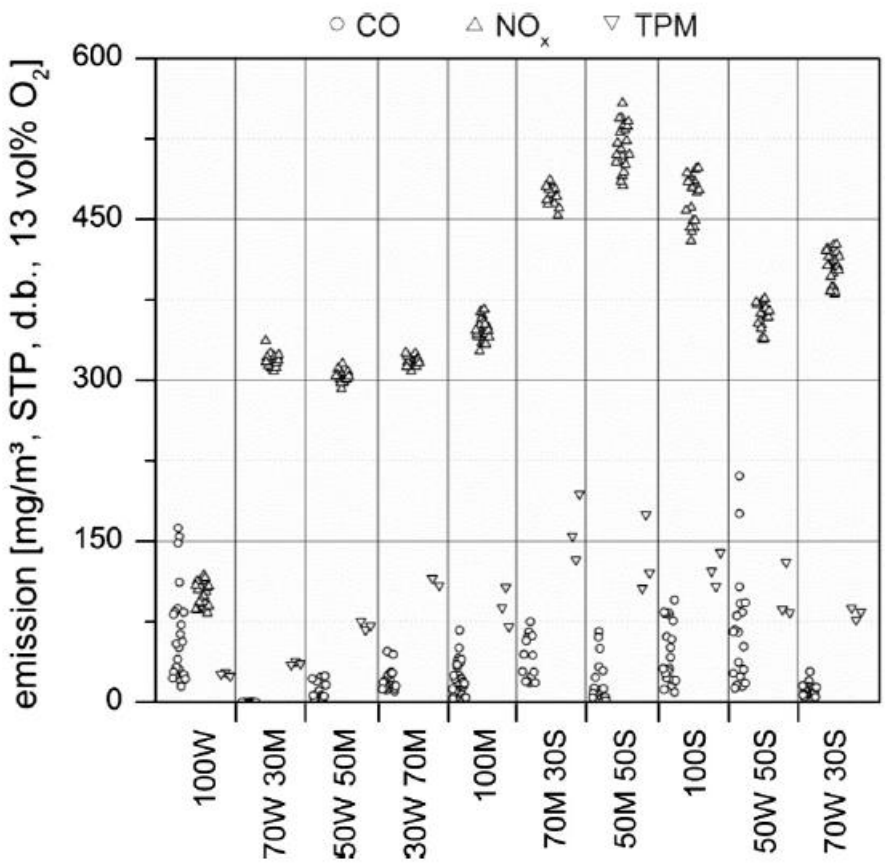

Figure 1.2: CO, NOx, and TPM distributions in miscanthus (M), straw (S), wood (S), and their blends combustion in a commercial boiler of 30KW (Zeng et al. 2016).

5.2.4. Controlling the ash-related operational problems of agricultural residues

Different authors proposed several solutions to control slagging tendency and emissions of agricultural feedstock. Leaching the agricultural residues prior to the thermochemical treatment can elevate their melting temperature to more than 1100°C (Arvelakis et al. 1999). The post-leaching ash will be depleted from alkali metals, S, and Cl (90-95 wt.% removal), and it will contain a higher amount of silicon than the untreated ash (Arvelakis et al. 1999; Schmidt, Clausen, and Luxhøi 1998). Another solution is to adapt the operating conditions accordingly. For instance, Yao et al. (Yao, Zhou, et al. 2020) showed that the increase in excess air ratio, gasification temperature, and retention time enhanced slagging, and hence alkali retention, in both the gasification chamber and the cyclone. In a short review, Xiaoping et al. (Xiaoping et al. 2020) presented the limiting slagging factors of agricultural residues (specifically for wheat straw): 700 °C reactor temperature, 600 mm fuel layer thickness, 60 min maximum residence time, and 1.86 excess air ratio. Slagging drastically increased with the increase of any of these parameters (Xiaoping et al. 2020).

Using an agricultural residue rich in P can also help to control the slagging tendency. P is more stable and has less slagging tendency than Si (Díaz-Ramírez et al. 2012). Hence, agricultural residues rich in phosphates will form ash with low slagging and high volatilization tendencies, contrary to those rich in Si (Boström et al. 2012; Díaz-Ramírez et al. 2012). Though, if the concentration of Si in a fuel is significantly high, K and P will volatilize into the fly ash (Boström et al. 2012). In comparison, if the concentration of P in the fuel is significantly high, a sticky coating of K and Ca forms and leads to agglomeration (Boström et al. 2012). Miles et al. (Miles and Miles 1996) proposed the application of a dual fluidized bed, where the alkali, S, and Cl contents are reduced in the first gasification chamber by their reaction with the bed. Then, the output gas of this chamber is to be circulated towards a second combustion chamber where it will burn with woody biomasses (Miles and Miles 1996). However, this solution did not account for the severe agglomeration that can occur in the first chamber. Feeding wet biomasses can also keep the temperature and hence the sintering level inside the reactor low (Miles and Miles 1996). Nonetheless, this solution can cause incomplete combustion and increase toxic emissions.

In conclusion, agricultural residues, specifically wheat straw in this work, present high sintering and slagging tendencies. Their emissions are also rich in HCl and SOx. The current slagging and emissions controlling techniques are limited, and more efficient solutions need to be proposed.

5.3. Additives

Additives are widely used to decrease agglomeration and sintering levels, but each has its problems (Mack et al. 2019; Holubcik et al. 2016; C. Wang et al. 2019; Yao et al. 2019; Höfer and Kaltschmitt 2017). Their cost is usually high, and their application depends on the feedstock (L. Wang et al. 2012; Mack et al. 2019). Aluminosilicate based additives, such as Kaolin ($Al_2Si_2O_5(OH)_4$) can effectively reduce the fine particulate matter emissions from biomass combustion, but they increase the gaseous emissions of HCl and SO_x (Höfer and Kaltschmitt 2017; Míguez et al. 2021). Kaolin also proved to be a good additive, especially in decreasing the slag formation (Luo and Zhou 2012; Zeng et al. 2016). The aluminosilicates additives (Kaolin) tend to adsorb the alkali metal from the ash, decreasing their contribution to particle formation and gaseous alkali emissions(Mack et al. 2019; Nguyen et al. 2021). As a result, high melting point alkali alumina-silicate compounds will form at the expense of increasing the HCl and SOx emissions (Míguez et al. 2021). In addition, Kaolin cost is usually high (Bhaskar and Pandey 2015), and its application is still under research (Becidan et

al. 2012). This was similar to dolomite Ca-based additives (Zhou, Rosén, and Engvall 2016). P-based additives, such as $NH_4H_2PO_4$ in the work of Wang et al. (Q. Wang et al. 2020), successfully decreased slag formation, but at the same time, decreased the integrated combustion characteristic index (an index relating the maximum combustion rate with the average burn rate and the ignition temperature; lower it is poorer the combustion is). The efficiency of this type of additives also depended on the inorganic composition of the fuel that they were added to (Q. Wang et al. 2020).

In conclusion, additives application to control the ash behavior is still limited, affected by high cost, side toxic emissions, and dependence on the feedstock ash. A Summary of the advantages and disadvantages of each additives family is presented in Table 1.4.

Table 1.4: Summary of the advantages and disadvantages of each additives family.

	Advantages	**Disadvantages**
Al-Si-based & Ca-based additives	reduced TPM emissions decrease slag	increase HCl and SOx emissions
		high cost
		application still under research
P-based additives	decrease slag	decrease the ignition temperature
		poor combustion

5.4. Biomass blending

Biomass combustion started to be applied at the end of the 1970s, using woody biomasses mixed with minor fractions of straws and grass residues (<10 wt.%) (Miles and Miles 1996). Biomass blending proved to be a more suitable solution than additives to fight slagging and agglomeration in terms of cost and effectiveness (Fournel et al. 2015). This technique triggered the interest of many researchers in the last years (Boström et al. 2012; P. Thy et al. 2010; Zeng et al. 2018; 2016; Peter Thy et al. 2006; Rodríguez et al. 2020). In section 5.4.1, the combustion ash interactions when oak bark is mixed with wheat straw will be discussed. Then, key literature points on biomass blending (with a focus on bark-straw blends) in combustion laboratory appliances will be provided in section 5.4.2 and reactors in section 5.4.3. The key factors that affect the ash behavior in the biomass blends will be discussed in section 5.4.3. For extra information, environmentally friendly disposal solutions of the ash from the blends were proposed in appendix A.

5.4.1. Ash interactions/reactions within the blend

In the beginning, the authors talked about synergy (non-linear or random interactions) effects when they studied the ash behavior of biomass mixtures (Becidan et al. 2012; Royo, Canalís, and Quintana 2020). Then, they started investigating more thoroughly the ash behavior by

referring to the presence of chemical reactions within the ash. Bostrom et al. (Boström et al. 2012) and Rebbling et al. (Rebbling et al. 2020) were among the few authors that tried to thoroughly study and relate the behavior of the ash to chemical reactions and interactions taking place among inorganic elements in the ash of biomass and their Blends. Mixing biomasses with different ash contents and compositions modifies the chemical composition and physical properties of the feedstock. Then upon heating, chemical reactions within the ash can form new solid phases in the mixture and reduce the percentage of the problematic phase (i.e. the liquid phase in this work) (Defoort et al. 2019). However, mixing without interaction can also occur, hindering the chemical reactions and enhancing the presence of the problematic phase. The occurrence of chemical reactions within the ash of biomass mixtures can be validated by:

1. New phases absent in the ash of the single feedstock appear in the ash of the blend.
2. The concentration of certain phases changes between the ash of the single feedstock and the mixture without following the mixing rule.

The chemical reactions within the ash of the biomass mixtures recently gained the interest of several researchers in the field (Boström et al. 2012; Zeng et al. 2018; Royo et al. 2019; Skrifvars et al. 1999; Defoort et al. 2019). Some of them suggested various reaction pathways that might take place between the inorganic elements of the ash of biomass (Boström et al. 2012; Rebbling et al. 2020; Santoso et al. 2020b). As discussed in sections 4.1 and 4.2, silica's tensile strength and adhesion force gradually increase between 400 °C and 700 °C. Then, SiO_2 starts reacting/capturing K-oxides on its matrix to form alkali-silicate compounds. These compounds are characterized by a low eutectic temperature, as low as 600 °C. When alkaline earth metal rich biomass, such as oak bark, is mixed with an alkali-metal rich residue, such as wheat straw, the K-silicate compounds encounter the alkaline earth metal oxides. Competition between the two types of metal oxides (Ca and Mg vs. K and Na) on the active sites of the silicate matrix occurs. Two scenarios can happen at this point: the first leads to a substitution of K in the Si-O matrix by Ca and Mg to produce binary alkaline earth-silicate compounds, and the second goes through reactions between the alkaline earth metal and the alkali-silicate on the silicate matrix to form solid ternary compounds (Boström et al. 2012; Rebbling et al. 2020). In both scenarios, alkaline earth metals will be incorporated into the matrix, especially due to their high affinity for silicate melts [33]. Consequently, once a wooden biomass (oak bark) is added to an agricultural residue (wheat straw), the ash melting point will increase, decreasing in the slagging tendency and the agglomeration propagation.

5.4.2. Biomass blending on a laboratory scale

Most literature in this domain avoided talking about chemical reactions or inorganic interactions within the ash of biomass blends. They rather tended to link the effect of blending to several factors related to the ash and its behavior. In this section, recent literature work around the effect of biomass blending on the combustion ash behavior in laboratory appliances will be elaborated in detail.

5.4.2.1. Bottom ash in furnaces

The main factors that the authors used to assess the effects of biomass blending on the ash behavior were the physical properties of the bottom ashes, their total volume, and their composition change.

First, biomass blending affected the physical properties of the bottom ash, especially the melting point. For instance, Link et al. (Siim Link, Yrjas, and Hupa 2018) determined the bottom ash physical properties of straw, wood, reed, and their blends using a Misura 3 laboratory furnace and a TGA-DTA until 1300 °C. They found that mixing wood with wheat straw and then with reed introduced new eutectic temperatures, increasing the blended feedstock's melting point compared to the agricultural one (Siim Link, Yrjas, and Hupa 2018). Thy et al. (Peter Thy et al. 2006) studied the ash behavior and slag formation of wood, rice straw, and their blends at various temperatures (982 ℃ to 1541 ℃) and blend fractions (10% to 50% straw) in a high temperature rapidly quenched laboratory furnace. They found that blending straw with wood decreased the liquidus (the lowest temperature at which the ash is completely liquid) and solidus (the highest temperature at which the ash is completely solid) temperatures from 2000 ℃ (wood) to 1260 ℃ (blend) and from 1350℃ (wood) to 800 ℃ (blend), respectively (Peter Thy et al. 2006). Similarly, Royo et al. (Royo et al. 2019) found that the melting temperature decreased from 1400 °C in the wooden pellets to 1100 ℃ in the blend (70%wood-30% straw).

Second, biomass blending affected the total volume of bottom ash and slag. The total ash volume always increases as the slagging propensity enhances. The increased slag propensity entrapped more particles from the fly ash, increasing the bottom ash volume even more. Hence, blending bark (wood) with straw decreased the bottom ash proportion and sintering degree compared to single straw. For instance, Royo et al. (Royo et al. 2019; Royo, Canalís, and Quintana 2022) found that the bottom ash proportion in the wood-straw mixture was larger than in the wood-corn blend (Royo et al. 2019). The higher the (Na+K)/(Si+P) ratio was, the higher the tendency of sintering stood, and a higher volume of bottom ash was reached (Royo, Canalís,

and Quintana 2022). Zapata et al. (Zapata et al. 2022) assessed the bottom ash sintering degree and proportion in straw, wood, and their blends (72%, 60%, and 35% straw) in a laboratory combustion furnace. They have found (Figure 1.3) that the sintering level and proportions decreased from 85% (for both) in the case of single straw to 70% sintering proportion and 52% sintering degree in the case of the blend with 35% straw (Zapata et al. 2022).

	WP100	WSP100	WSP72	WSP60	WSP35
Bottom ash proportion (%)	44.21	86.21	83.18	72.65	69.59
Sintering degree (%)	19.96	84.15	74.86	63.09	51.88
Total bottom ash collected (kg/MJ) [a]	0.23	3.12	1.82	1.24	1.56

[a] Calculated on LHV (d.b.).

Figure 1.3: Bottom ash proportion and sintering degree in straw (WSP), wood (WP), and their blends (Zapata et al. 2022).

Third, biomass blending affected the bottom ash composition, hence sintering and slagging. Blending bark (wood) with straw increased the concentration of alkaline earth and alkali metals in the combustion bottom ash. For instance, the bottom ash of biomass blends become rich in Si, K, Al, Ca, Fe, and Mg, while the fly ash are rich in Na, K, S, and Cl (Miles and Miles 1996; Royo, Canalís, and Quintana 2020; Boström et al. 2012; Royo, Canalís, and Quintana 2022; Becidan et al. 2012; X. Wang et al. 2020; Kortelainen et al. 2015). Ca, Si, and Al that might be found in the fly ash are primarily entrained from the bottom ash (Royo, Canalís, and Quintana 2020; Becidan et al. 2012). The interactions between Ca, Si, and K governed the behavior of the bottom ash. For instance, Rebbling et al. (Rebbling et al. 2020) found that the proportion of Ca in the slag increased when the Si proportion of the blend increased. Royo et al. (Royo et al. 2019) specified that the surplus of Si in herbaceous biomass mixture was reacting with the alkaline earth metals to hinder the sintering effect. In addition, Thy et al. (Peter Thy et al. 2006) reported having lost K completely from the bottom ash in the blends with less than 30 wt.% straw fraction. Hence, this fraction was the lower limit above which K retention in the slag increased. They also reported that the silica contents of the slag increased markedly from 14 to 82 wt.%, while Ca decreased from 49 to 2 wt.% as the straw fraction increased to 50 wt.% in the blend (Peter Thy et al. 2006).

5.4.2.2. Agglomeration in a fluidized combustion bed

Bark (wood)-straw blending proved to affect the bed agglomeration in a laboratory combustion fluidized bed. Thy et al. (P. Thy et al. 2010) studied the bed agglomeration behavior of wood-straw blends in a laboratory fluidized bed (alumino-silicate mullite sand as bed material) with different straw fractions (2.4%, 9.6%, 25%, 10.7% leached, and 25% leached) between 840°C and 1030°C and variable run duration between 0.9h and 5.5h. Authors related the increase in bed pressure and temperature with agglomeration (P. Thy et al. 2010). 2.4% straw blend was found to be the only one without agglomeration, while 9.6% straw completely defluidized the bed (P. Thy et al. 2010). The agglomerates were highly rich in Si and K and somehow poor in Ca, and the inner zone was composed mainly of Si and K, while the outer zone with less K and appreciable amounts of all other elements (Si, Ti, Al, Fe, Mg, Ca, and P) (P. Thy et al. 2010). Thy et al. (P. Thy et al. 2010) proposed an agglomeration mechanism in four steps for these types of mixtures. It starts with silicate fusion at a temperature above 500 °C. Then, molten silicates begin capturing the other inorganic elements on their matrix. Afterward, Si-derived compounds adhere to the bed by diffusion or reaction. In the end, the inorganic mixture (ash and bed) crystallizes upon cooling.

5.4.2.3. Fly ash and TPM emissions

Biomass blending affected emissions as it affected sintering. Becidan et al. (Becidan et al. 2012) reported that blending wood with demolition wood and then with coffee waste decreased S emissions. It also led to a decrease in HCl emissions due to the reaction of Cl with alkali metals to form KCl in the particulate matter or K-phosphates and K-sulfates in the bottom ash (Becidan et al. 2012). They referred to a speciation effect in the ash, where ash with new structures and properties that are difficult to predict and correlate was promoted by using pelletized blends of biomass (Becidan et al. 2012). Royo et al. (Royo et al. 2019) have found that 775°C was the temperature at which the ash fractioning initiates. Hence, bottom ash starts to fraction on the grate and volatilize into fly ash and TPM at this temperature.

In terms of particulate emissions (PM or TPM), Zeng et al. (Zeng et al. 2016) also presented a significant decrease due to blending. In Figure 1.2, they ranked the TPM emissions as follows: 100S>S-M blends>100M>W-S blends>W-M blends>100W (Zeng et al. 2016). This behavior was due to the significantly high content of K and Na in the straw, then miscanthus, then wood (Zeng et al. 2016). For instance, this reduction reached 60% when miscanthus was blended with wood compared to 70% in the straw-wood mixture (Zeng et al. 2016). Zeng et al. (Zeng et al. 2016) also found that blends with at least 50 wt.% wood decreased NO_x, SO_x,

HCl, fly ash, and TPM emissions. Below this percentage, the amounts of emissions increased again with the significant increase of the straw fraction. In addition, Thy et al. (Peter Thy et al. 2006) reported that reducing the melting temperature would also reduce K release into the gaseous phase.

In conclusion to section 5.4.2, increasing the agricultural residue fraction in the straw-bark (wood) blend increases the slagging tendency and lowers the emissions (K, Cl, and S retained in the slag). However, depending on the composition of the agricultural residue, a threshold blend fraction exists, upon which both emissions and slagging increase at the same time. This effect is related to the significant enrichment of K, S, and Cl in the blend as the agricultural residue fraction increases. Most importantly, the authors never mentioned chemical reactions/interactions within the ash of the biomass blends, rather focusing on relating the blending to physical properties and inorganic ratios affecting the ash behavior.

5.4.3. Biomass blending on an industrial/pilot scale

Chemical reactions/interactions within the combusted ash of bark (wood)-straw mixtures were rarely referred to in literature. The majority of the authors tried to link biomass blending fractions to sintering and emissions. In addition, the literature work conducted in this specific domain (bark-straw industrial scales combustion) was rare. Hence, in this section, recent literature work around the effect of biomass blending on the combustion ash behavior in pilot scale appliances will be elaborated in detail.

5.4.3.1. Bottom ash in furnaces

Bark-straw blending directly affected the bottom ash behavior in industrial boilers. In their study, Zeng et al. (Zeng et al. 2018) used various binary mixtures of wood, wheat straw, and miscanthus in a small pilot-scale combustion boiler with a nominal heat capacity of 30 kW. They found that adding wood to straw significantly increased the bottom ash proportion and sintering temperatures, especially in the mixtures with less than 70 wt.% wood (Zeng et al. 2018). Zeng et al. (Zeng et al. 2018) also reported that straw slag decreased from 60 wt.% to 30 wt.% when blended with wood. When mixed with wood, miscanthus slag also decreased from 50 wt.% to 10 wt.% (Zeng et al. 2018) (Figure 1.4).

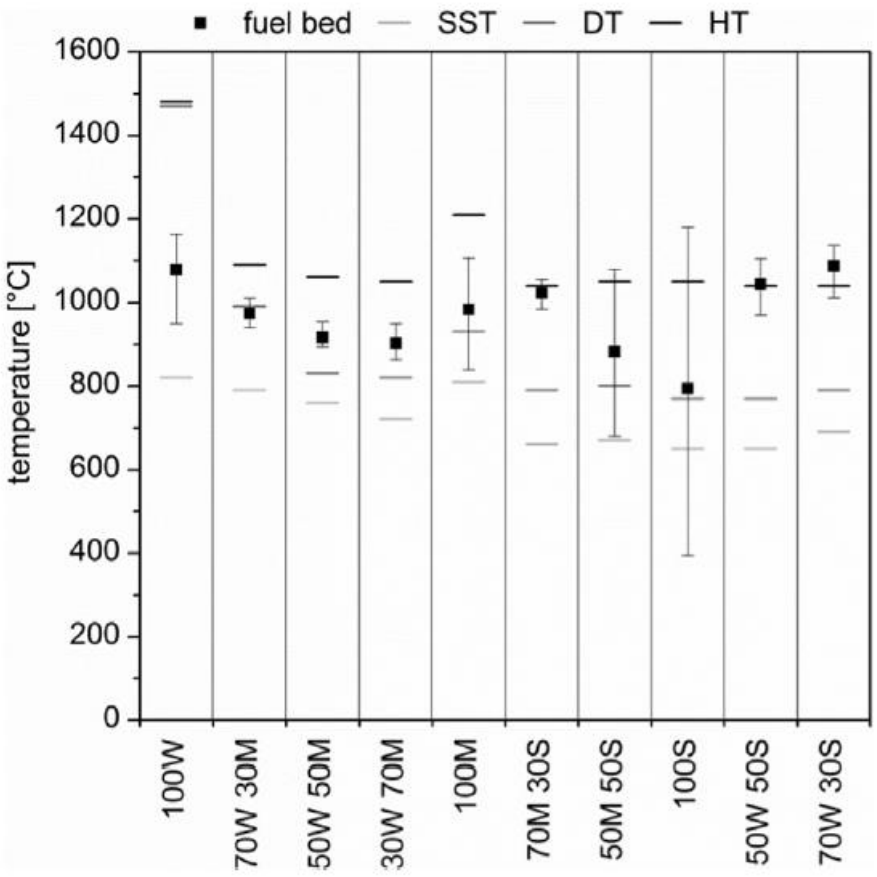

Figure 1.4: Comparison of fuel bed temperatures with the sintering temperature (SST), deformation temperature (DT) and hemispherical temperature (HT) of the various biomass and blends combustion in 30 kW boiler (Zeng et al. 2018).

In addition, Wang et al. (X. Wang et al. 2020) combusted an 80-20 bark-straw mixture in a 30 MW power plant. They reported that 60-70 wt.% of the total ash was slag while the rest was fly ash (X. Wang et al. 2020). Furthermore, Rebbling et al. (Rebbling et al. 2020) reported that increasing the reactor scale from 0.2 MWh to 2 MWh increased the slagging propensity.

5.4.3.2. Agglomeration in a fluidized combustion bed

In one of the earliest researches around biomass blending on an industrial level, Salour et al. (Salour et al. 1993) cofired wood and straw in more than 50 wt.% variable wood fraction mixture in a pilot fluidized bed combustor (alumina-silicate sand as bed material) at 800 °C. They had found that bed agglomeration was intensified when straw reached 50 wt.% in the wood-straw mixture (Salour et al. 1993). This was due to the increasing interactions within the ash of the two biomasses as straw fraction increased in the blend (Salour et al. 1993). Below this level, sintering was still within the acceptable operating range (Salour et al. 1993). Though, Salour et al. (Salour et al. 1993) mentioned the possible presence of chemical interactions without further explaining or studying them.

Furthermore, Schmidt et al. (Schmidt, Clausen, and Luxhøi 1998) gasified straw, wood, and their 50-50 blend in a 50 kt/y industrial boiler. The authors reported the intensification of corrosion and sintering at 540 °C in the case of straw compared to around 700 °C in the case of blend and around 1000 °C in the case of wood (Schmidt, Clausen, and Luxhøi 1998).

5.4.3.3. Fly ash and TPM emissions in combustion boilers

Adding woody biomass to straw decreases the TPM emissions on the industrial scale. This biomass rich in K and S to wood enhances KCl and S-compounds emissions. Hu et al. (Hu et al. 2020) studied the TPM emissions in a 30 MW grate boiler using bark, straw, and capsicum mixtures. They found that smaller particles with different shapes were emitted when blends were used (Hu et al. 2020). However, uniform bigger particles were seen when single biomasses were applied (Hu et al. 2020; Li et al. 2020; Naydenova et al. 2020). Hence, the yield of TPM increased in the case of blends compared to single wood, consisting mainly of K, Cl, and S (Hu et al. 2020).

Kortelaimen et al. (Kortelainen et al. 2015) combusted wood, straw, reed canary grass, and their mixtures in a 40 kW grate-fired installation. They found that mixing the reed canary grass with wood reduced the particulate matter emission by two folds compared to individual grass combustion (Kortelainen et al. 2015). In addition, the TPM particle size in the blend was larger than in wood combustion (Kortelainen et al. 2015). They were rich in KCl, especially in the case of straw-wood blends (Kortelainen et al. 2015). Kortelaimen et al. (Kortelainen et al. 2015) also reported that S and P were less retained in the bottom ash when wood was blended with the agricultural residues. The addition of K-rich biomasses also enhances their volatilization in the form of K-sulfates (Kortelainen et al. 2015).

Zeng et al. (Zeng et al. 2016) ranked SO_x emissions as a function of S contents in the feedstock as 100S>100M>blends>100W (Zeng et al. 2016). It also led to a decrease in HCl emissions due to the reaction of Cl with alkali metals to form KCl in the particulate matter or K-phosphates and K-sulfates in the bottom ash (Zeng et al. 2016). From Figures 1.5 and 1.6, they have found that TPM emissions along with the S and K releases decreased as wood was added to straw while the change in K release was insignificant (Zeng et al. 2016).

Fuel	$K_{release}$ wt%	$S_{release}$ wt%	$Cl_{release}$ wt%
100W	57.4	77.8	99.6
70W30M	36.5	82.6	99.5
50W50M	27.2	85.0	99.4
30W70M	5.3	76.4	99.3
100M	27.2	71.6	98.7
70M30S	25.8	73.0	97.3
50M50S	25.6	59.6	88.1
100S	30.8	82.3	99.0
50W50S	29.3	83.8	99.0
70W30S	22.3	79.0	99.1

Figure 1.5: Measured K, S, and Cl release in biomass (straw (S), miscanthus (M), and wood (W)) and their blends in 30 kW combustion boiler (Zeng et al. 2016).

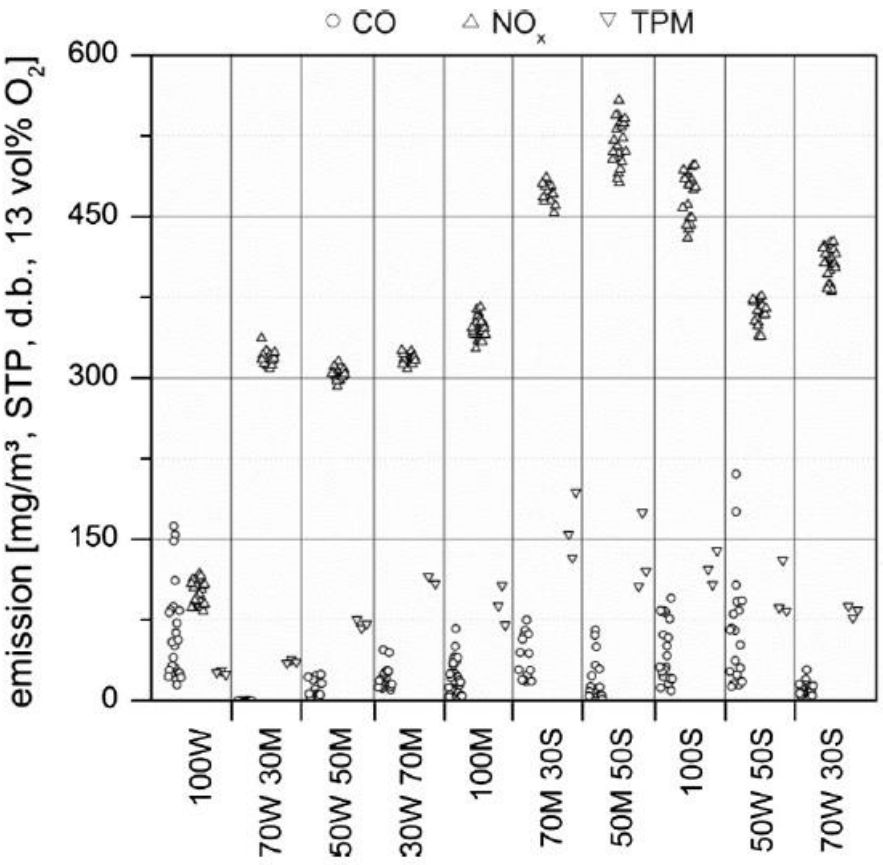

Figure 1.6: Measured CO, NOx, and TPM emissions from biomass (straw (S), miscanthus (M), and wood (W)) and their blends combustion in 30 kW boiler (Zeng et al. 2016).

In conclusion to section 5.4.3, biomass mixing had similar effects on the ash behavior in pilot reactors as in laboratory appliances. Adding bark to straw decreased the sintering level in boilers and agglomeration propensity in fluidized beds, increased the melting temperature, and reduced the toxic emissions. However, similar to the laboratory scale, the authors did not discuss any chemical reactions/interactions.

5.4.4. Operating factors affecting the ash behavior in the blends

Several factors can affect the ash behavior of biomass mixtures. They will be discussed in this section, as presented in the literature.

5.4.4.1. Type of biomass

However, the type of biomass, i.e. ash composition and elemental concentration, affect the ash behavior more than the applied temperature and reactor type (Siim Link, Yrjas, and Hupa 2018). In contrast with the case of single biomass, where inorganic elemental interactions are low, blending enhances the interaction effects between the inorganic elements and renders the effect of ash contents (blend composition and fraction) more important on the ash behavior (Miles and Miles 1996). This finding was highlighted in the work of Cruz et al. (N. C. Cruz et al. 2019). In their work, the authors conducted a thorough review of the parameters affecting the ash behavior in industrial combustion thermal power plants using 77 different biomasses (N. C. Cruz et al. 2019). Based on statistical approaches, they have found that the chemical composition of these biomasses, rather than the technology (fixed or fluidized bed) and the combustion temperature, affected the pH, ignition temperature, bottom ash composition and sintering, and fly ash composition and deposition (N. C. Cruz et al. 2019).

Furthermore, Kalis et al. (Kalis et al. 2018) studied the flame temperature, axial flow velocity, and H_2O and CO_2 concentrations in the gas as a function of straw fraction in wood-straw pellet mixtures in fixed bed burner in both combustion and gasification modes. Kalis et al. (Kalis et al. 2018) reported that the thermal interaction was enhanced when the straw fraction in the blend reached 20 wt.%. A similar percentage was also reported in the short technical review of Miles et al. (Miles and Miles 1996). Zeng et al. (Zeng et al. 2016; 2018) also reported a close straw percentage, i.e. 30 wt.%, in both wood-straw and wood-miscanthus mixtures as the threshold for slag intensification. Other authors reported other threshold values, as previously discussed (P. Thy et al. 2010; Peter Thy et al. 2006; Salour et al. 1993; Mediavilla, Fernández, and Esteban 2009).

5.4.4.2. Operating temperature

Though blend composition and fraction have the most important effect on the ash behavior, the operating parameters can still affect the ash behavior in the biomass blends, such as flame temperature and oxidizer velocity. Kalis et al. (Kalis et al. 2018) reported that the higher the flame temperature and the axial flow velocity are, the lower the sintering tendency is. Similarly, Thy et al. (Peter Thy et al. 2006) observed that the retention of K in the slag is negatively correlated with the operating temperature.

5.4.4.3. Air staging (adding a secondary air feed)

Staging can also affect the ash behavior in the blends. Becidan et al. (Becidan et al. 2012) found that staging decreased Cl emissions, displacing Cl from the gas phase towards the solid phase. However, the authors did not find any effect for staging on S emissions (Becidan et al. 2012). They also found that staging led to displacements towards larger particles from less than 0.1µm to over 0.1µm, decreasing TPM emissions (Becidan et al. 2012). Staging led to higher retention of K in the bottom ash in pure biomass, while it had no effect in the mixtures due to the interaction between the elements in the blends (Becidan et al. 2012). In parallel, Kortelaimen et al. (Kortelainen et al. 2015) also reported that air staging increased the bed temperature leading to an increase in the sintering effect, especially when agricultural residues were mixed with wood. Hence, emissions decreased since the metal retention in the bottom ash increased.

5.4.4.4. Air ratio

Air ratio (λ) variation (equation 1) is another factor to account for when studying the ash behavior in biomass mixtures. This parameter is always correlated to bed temperature. When λ increases, air flow rate increases which also increases ash entrainment and deposition rate (Royo, Canalís, and Quintana 2020). However, this same increase in airflow decreases the bed temperature and limits the volatility of the ash leading to a decrease in the deposition rate. Consequently, Royo et al. (Royo, Canalís, and Quintana 2020) have found that the volatility effect is more prominent than the entrainment effect, and hence deposition rate decreased with the increase in λ for all fuels. On the contrary, the bottom ash's sintering effect slightly varied with λ in the wood-herbaceous mixtures since the volatility effect counteracted the entrainment effect with λ increase (Royo, Canalís, and Quintana 2022).

5.4.4.5. Air preheating

Air preheating is another factor that can increase entrainment due to increased air velocity with temperature, leading to an increase in deposition rate and decrease in bottom ash proportion (Royo, Canalís, and Quintana 2020). In addition, according to Thy et al. (P. Thy et al. 2010),

leaching the straw in the blends significantly decreased bed agglomeration (low agglomeration even at 25% leached straw) on an industrial scale.

5.4.4.6. Using biomass blends vs ash (of biomass) blends

Several researchers investigated the use of biomass mixtures compared to biomass ash blends. A direct mixing of biomasses is used in the first approach, while ash mixtures are formed in the second after individually ashing the biomasses at 550 °C and mixing the ash after. Link et al. (S. Link, Yrjas, and Hupa 2017) concluded that the blend preparation method (biomass VS biomass ash) did not affect the ash fusion characteristics (deformation temperature, shrinkage temperature, flow temperature, and hemispherical temperature) in the blends of straw-wood and reed-straw.

Though the physical properties might not differ, newer researches proved that using ash mixture instead of biomass mixtures enhanced the interactions/reactions within the inorganic elements in the blend (Defoort et al. 2019). Defoort et al. (Defoort et al. 2019) showed that the amounts of several new compounds that appeared in the ash blend and did not exist in the single biomass, increased when mixtures of ash (ash test) were applied compared to when mixtures of biomass (pellet test) were used. This finding was directly related to an increased reactivity in the ash mixtures rather than in the biomass blends (Defoort et al. 2019). Nevertheless, the new compounds found by both the ash and pellet tests were the same (Defoort et al. 2019). Consequently, it can be concluded that the ash mixtures application increased the reactivity (i.e. the amount of the produced compounds) but did not change the reaction mechanism (i.e. similar qualitative compounds). In addition, Thy et al. (P. Thy et al. 2010; Peter Thy et al. 2006) also reported that the application of ash pellets rather than biomass pellets enabled them to study the chemical reaction between ash particles more accurately.

6. Prediction tools of ash behavior for biomass and their mixtures

A prediction tool can help adapting the applied biomass to the specific process to decrease the ash related problems. In addition, the prediction tool can help choosing the adequate biomass blend fraction and types to provide minimal ash related operational problematics in a certain type of reactor or process. This tool can replace the trial-and-error or systematic proportional mixing from 0 to 100, hence inducing significant time and economic savings. As a result, in this section, the three main prediction methods used in the literature will be presented and discussed. The experimental prediction tests will be elaborated in section 6.1. Then, prediction by indices will be elaborated in section 6.2. Finally, in section 6.3, the thermodynamic prediction tool will be discussed in detail.

6.1. Laboratory prediction tests

Various laboratory prediction tests were used to investigate the ash behavior of biomass mixtures on the industrial and pilot scales. Rodriguez et al. (Rodríguez et al. 2020) applied the Bioslag test to 24 different biomass blends of wood, straw almond shells, olive stones, etc. This test was based on particle size distribution (i.e. sieving) of the produced ash from the blends (Rodríguez et al. 2020). Rizvi et al. (Rizvi et al. 2015) used a thermogravimetric analysis-differential thermal analysis (TGA-DTA) to predict the slag viscosity and fouling of pine wood, peanut shells, sunflower stalk, and miscanthus. Similarly, Link et al. (Siim Link, Yrjas, and Hupa 2018) used the same tests to predict the physical properties of the ash from various straw-wood blends. Link et al. (Siim Link, Yrjas, and Hupa 2018) also tried another standard ashing test in which they ashed the blends at 550 °C then annealed the ash blends at various temperatures in a small laboratory furnace to assess their melting points (Siim Link, Yrjas, and Hupa 2018).Vega-Nieva et al. (Vega-Nieva, Alvarez, and Ortiz 2014) tried a rapid qualitative test based on direct human observation by the naked eye along with the Bioslag test to predict the ash behavior (presence of solidified liquid ash phase) of various biomasses (straw, poplar chip, almond shell, pinecone seed shell, etc.). Furthermore, Defoort et al. applied two combustion laboratory tests, using compressed biomass ash chips (called ash test) and compressed biomass pellets (called pellet test), to assess the different ash behavior and compositions of various mixtures of oak barks and wheat straws (Defoort et al. 2019).

The typical limitations of these tests are that they are usually time-consuming, are rarely compared to results obtained on a pilot scale (scale-up limitations), and depend on the feedstock, reactor type, and operating conditions (Rodríguez et al. 2020; Siim Link, Yrjas, and Hupa 2018; Rizvi et al. 2015). The authors reported that their results of the TGA-DTA were not reproducible (Rizvi et al. 2015; Siim Link, Yrjas, and Hupa 2018). Any small impurity in the biomass highly diverged the predicted values (Siim Link, Yrjas, and Hupa 2018). In addition, the results of certain tests were debatable and subjective (Vega-Nieva, Alvarez, and Ortiz 2014).

In addition, Gilbe et al. (Gilbe et al. 2008) compared the slagging tendencies predicted by the ash fusion test (SS ISO-540), TGA/DTA, thermodynamic phase diagrams, and a laboratory scale-sintering test with those in a 20 kW pilot reactor. They used 12 different single biomasses, including wheat straw and various barks (Gilbe et al. 2008). Gilbe et al. (Gilbe et al. 2008) found that the four tests reported the presence of slag in the pilot reactor. However, the same authors reported that the four laboratory tests failed to quantitatively predict the slagging

behavior in the pilot, leading to different experimental results compared with the predicted pilot values (Gilbe et al. 2008). The authors mentioned that further improvements need to be made on these tests, especially the TGA/DTA and the SS ISO 540 tests (Gilbe et al. 2008).

In conclusion, the laboratory prediction tests application remains highly limited.

6.2. Indices prediction tool

Empirically derived indices are widely used to predict the ash behavior of coal but showed significant limitations in the case of biomass (Rodríguez et al. 2020; L. Wang, Skreiberg, and Becidan 2014; Regueiro et al. 2017; Royo, Canalís, and Quintana 2020). This might be due to the abundant iron and alumina-silicate ash contents in coal compared to the high Ca and alkali-silicates amounts in biomass (Rodríguez et al. 2020; L. Wang, Skreiberg, and Becidan 2014).

For instance, Rodriguez et al. (Rodríguez et al. 2020) applied the hardness index, the modified alkali index ($[Na_2O+K_2O]/[CaO+MgO+Na_2O+K_2O]$), and the percentage of bases in ashes index ($[CaO+MgO+Na_2O+K_2O+Fe_2O_3]/[CaO+MgO+Na_2O+K_2O+Fe_2O_3+SiO_2+Al_2O_3+TiO_2]$) on 24 blended biomass samples. Teixeira et al. (Teixeira et al. 2012) used these same indices in addition to the fouling index to predict the ash behavior of wood, straw, and olive cake in a pilot combustion fluidized bed. Similarly, Rizvi et al. (Rizvi et al. 2015) used the same indices to predict the slag viscosity and fouling of pine wood, peanut shells, sunflower stalk, and miscanthus. Zeng et al. (Zeng et al. 2016) used (K+Na)/(2S+Cl) as an index to predict HCl and SOx emissions while they applied (K+Na+S+Cl+Pb+Zn) to foretell the particulate matter emission. For slagging prediction, they used (Si+P+K)/(Ca+Mg) index (Zeng et al. 2016). Regueiro et al. (Regueiro et al. 2017) used deposition indices to predict the deposition of wood fly ash and TPM in 12 kW fixed bed combustor. Wang et al. (L. Wang, Skreiberg, and Becidan 2014) used Si/K and (Si+K+P)/(Ca+Mg) indices to predict the sintering of barley straw in a TGA. Most importantly, in a thorough review using more than 77 biomasses, Vassilev et al. (Vassilev, Baxter, and Vassileva 2014) assessed the prediction capabilities of 11 indices, including fouling, agglomeration, sintering, etc.

All the studies above revealed that these chemical indices could be only preliminary and considered proximate indicators for predicting ash behavior. The approach based on the chemical composition alone cannot adequately predict or explain the real behavior of biomass fuels and their conversion products. Elemental interactions/reactions can take place to form new compounds. The latter will behave depending not only on ash composition but also on operating conditions and several other factors mentioned in section 5.4. Unfortunately, calculations using

the indices is based only on the bulk chemical composition of the biomass. Hence, they cannot represent, for example, the fluxing or refractory, active or inert, volatile or non-volatile, and soluble or insoluble proportions of each element in the biomass. Blending biomasses will further increase the heterogeneity of these interactions.

As a result, despite their preliminary success, authors reported that the use of these indices should be approached with caution and should always be validated by experimental tests prior to industrial applications (Zeng et al. 2018; Rodríguez et al. 2020; Vassilev, Baxter, and Vassileva 2014; Rizvi et al. 2015; Regueiro et al. 2017; Teixeira et al. 2012).

6.3. Thermodynamic prediction tool

Thermodynamic equilibrium calculation provides a competing prediction approach for the ash behavior of biomass and their mixtures. In section 6.3.1, the most recent literature work that used the process simulation prediction based on thermodynamic equilibrium calculations of the phase relationships between all the elements in the biomass and their blends in combustion will be presented. In parallel, the reported limitation of this prediction approach will be highlighted at the end of this section. Afterward, in section 6.3.2, a more simplified thermodynamic prediction approach based on the phase equilibrium relationships in the calculated ternary phase diagram CaO-K2O-SiO2 will be thoroughly assessed based on recent literature. Then, in sections 6.3.3 and 6.3.4, the binaries CaO-K_2O, CaO-SiO_2, and K_2O-SiO_2 will also be elaborated, highlighting the improvements that are still needed.

6.3.1. Process simulation thermodynamic equilibrium calculations

Advanced multicomponent/multiphase thermodynamic modeling can be an important tool in predicting ash-related processes in biomass combustion. Thermodynamic modeling can be used to predict the ash deposition, corrosion, bed agglomeration of fluidized beds, and ash interaction and compositions. However, consistent and accurate thermodynamic data are needed for all the ash phases that may form in furnace and boiler conditions (Lindberg et al. 2013).

This prediction tool can be more efficient than the costly and time-consuming experimental tests (section 6.1). The thermodynamic prediction tool also proved to perform better than indices (section 6.2). For instance, Rizvi et al. (Rizvi et al. 2015) compared the predicted slagging results by indices and ash fusion tests on soft wood, peanut shell, sunflower husk, and miscanthus with those simulated by FactSage 6.3 equipped with FToxid and FactPS databases using all the elements and at varying temperatures between 700 °C and 1500 °C. The authors found that the thermodynamic approach could qualitatively predict the crystalline compounds and slags (Rizvi et al. 2015). However, Rizvi et al. (Rizvi et al. 2015) reported that this approach

presented biased concentration variation with respect to the temperature change for all the compounds, especially for the slag. Nevertheless, the same authors found that this thermodynamic approach better predicted the ash behavior than indices (Rizvi et al. 2015). This is because thermodynamic equilibrium accounts for the physicochemical relations between the elements, while the indices fail to do so.

Furthermore, Porbatzki et al. (Porbatzki, Stemmler, and Müller 2011) used indices and compared their experimental results with those calculated by FactSage 5.5 (Porbatzki, Stemmler, and Müller 2011). They found coherent results between the simulation and the fluidized bed but less coherent with the furnace. In contrast, they reported limited prediction capabilities for the indices since they do not account for the physicochemical interactions between the elements (Porbatzki, Stemmler, and Müller 2011).

More recent work investigated the capabilities of such an approach to predict the combustion ash behavior of biomass and their blend (with a focus on wood (bark), straw, and their blends). Reinmoller et al. (Reinmöller et al. 2015) used FactSage 6.3 equipped with FToxid, FatcPS, FTsalt, and FTmisc databases in air on 23 different biomasses (including wood, bark, and straw) to investigate the slag and the mineral phase composition compared to experimental data (ash fusion test). More recently, Magdziarz et al. (Magdziarz et al. 2018) used the same approach on three woods and one straw. Dizaji et al. (Beidaghy Dizaji et al. 2022) tried to study the combustion ash transformation reactions of wheat straw using experimental ash test (ash annealing) compared with calculated results from simulations done with FactSage 8.0 equipped with FToxid, FTsalt, and FactPS databases at various temperatures. Link et al. (Siim Link et al. 2022) also used the same simulation approach (but with FactSage 7.3) compared with the standard ash melting test to assess the melting behavior and ash phase transformation in wood, reed, and their blends. In addition, Fakourian et al. (Fakourian et al. 2021) tried to model the ash deposit growth rates along with the melting fraction and temperature for a wide range of solid fuels (including woody biomass) in a 100 kW combustor using a simulation approach using FactSage 7.3. Wiinikka et al. (Wiinikka et al. 2007) also investigated the influence of fuel ash composition on high temperature aerosol formation during fixed bed combustion of woody biomass (two wood pellets and one bark pellet) were in a laboratory reactor compared to theoretically chemical equilibrium model calculations (FactSage 5.2 with FACT and SGTE databases). In parallel, Elled et al. (Elled, Åmand, and Steenari 2013) investigated the composition of agglomerated material. Also, they tried to highlight the reasons for sintering and agglomeration during thermochemical conversion of bark and its blend with straw in

fluidized bed reactors (using quartz sand as bed material) using experimental results in a 12 MW circulating fluidized bed compared to a thermodynamic equilibrium modeling using FactSage 6.2 equipped with FTsalt, FToxid, and Fact53 databases.

All these authors reported the limited success of this tool in predicting the real ash behavior of biomass and their mixtures compared with their experimental findings. For instance, the predicted amounts of the crystalline compounds was always different for the measured ones (Reinmöller et al. 2015; Magdziarz et al. 2018). The predicted melting temperature was also different from the measured ones (Reinmöller et al. 2015; Magdziarz et al. 2018; Siim Link et al. 2022). The measured slagging proportion was also different from the calculated one (Beidaghy Dizaji et al. 2022). Though the aerosol predicted values showed a preliminary match against the measured P-XRD results, some of the experimental values were not initially at equilibrium due to temperature or residence time limitations, which further biased the prediction (Wiinikka et al. 2007). In his thorough recent review, Lindberg et al. (Lindberg et al. 2013) summarized the main cause of all these limitations as the lack of comprehensive databases that contain the thermodynamic data of ash compounds and phases formed during combustion. Elled et al. (Elled, Åmand, and Steenari 2013) reported that this same problem led to biased predicted value for the agglomeration temperature (deviated liquidus temperature compared to experimental results). Elled et al. (Elled, Åmand, and Steenari 2013) further elaborated that the thermodynamic equilibrium assumes a reaction of the ash with all the silicate sand bed particles, while in real life, the reactions only happen on the surface of the bed.

In conclusion, the literature highlighted the need for further improvements in the process simulation prediction approach based on thermodynamic equilibrium.

6.3.2. Phase diagram CaO-K_2O-SiO_2 calculations

The phase relationships in the ternary phase diagram CaO-K_2O-SiO_2 consist of a more simplified prediction approach than the previous one in section 6.3.1. A century ago, Morey et al. (Morey, Kracek, and Bowen 1930) were the first to investigate the phase relations in the ternary CaO-K_2O-SiO_2 system. Compositions in this system are used in the glass production industry, such as bottles, containers, etc. (Mysen and Richet 2019). This system is also relevant for advanced ceramic applications, such as in biocompatible ceramic material production for biomedical applications (Tripathi et al. 2015). Most importantly, since around 90 wt.% of biomass ash is formed of Si, K, and Ca (Vassilev et al. 2010), a thorough knowledge of the phase equilibria in the CaO-K_2O-SiO_2 ternary system can help better understand and predict the

complicated chemical interaction of the inorganic elements in the biomass ash in real-life processes during combustion and gasification.

In general, the authors in the literature normalize the CaO, K_2O, and SiO_2 mole or weight percentage from the measured elemental composition on each biomass or blend. Then, they position the feedstock on the calculated ternary phase diagram CaO-K_2O-SiO_2 to get some qualitative information on its ash behavior. For instance, Ohman et al. (Öhman et al. 2000) used this diagram to qualitatively predict the presence of slag in wheat straw, wood, peat, cane trash, wood residues, reed canary grass, bark, and RDF in a fluidized combustion bed. Similarly, Rebbling et al. (Rebbling et al. 2020) used phase equilibria information of this ternary diagram to predict the slag formation of wood, peat, and their mixtures in three separate grate-fired combustion boilers of different sizes, 0.2 MWth, 2 MWth, and 4 MWth, respectively (Figure 1.7). In addition, Defoort et al. (Defoort et al. 2019) used this phase diagram information to predict the ash state (solid, liquid, or solid-liquid) of oak bark, wheat straw, and their mixtures in two different laboratory-scale combustion tests using biomass pellets and ash chips (Figure 1.8). Zhu et al. (Zhu et al. 2019) also tried to verify the deformation temperatures of more than 15 biomasses (including wood and straw) using the thermodynamic equilibrium information of this ternary phase diagram (using their normalized oxides percentages), after adding Al_2O_3 as a fourth oxide to the system (Figure 1.9), compared to experimental results on a laboratory scale.

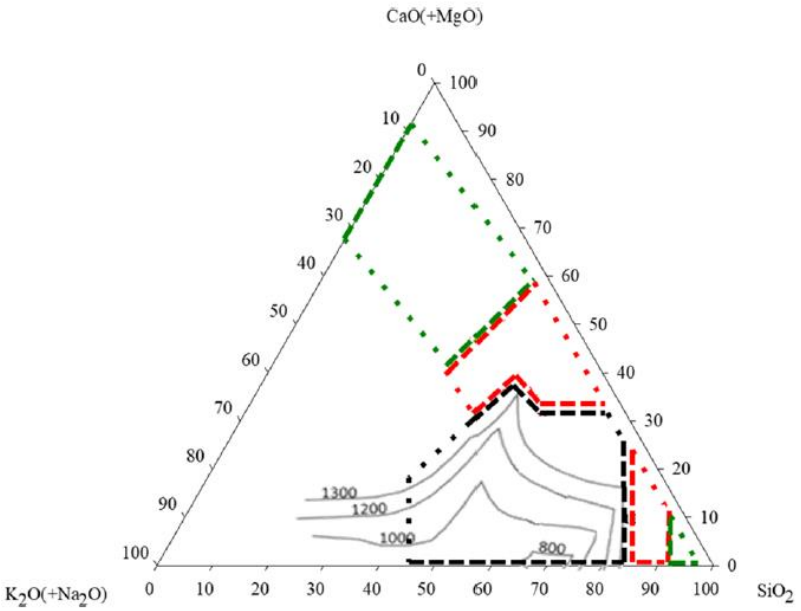

Figure 1.7: The liquid isotherms in the K_2O-CaO-SiO_2 system at various temperature used in Rebbling et al. (Rebbling et al. 2020).

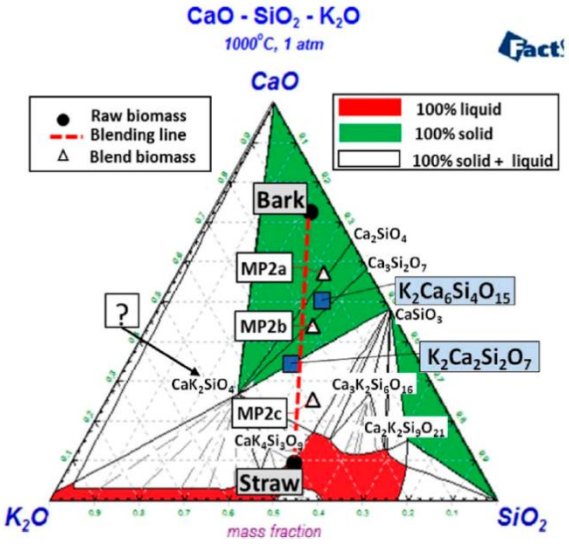

Figure 1.8: Isothermal section of the K_2O-CaO-SiO_2 system at 1000 °C used in Defoort et al.(Defoort et al. 2019).

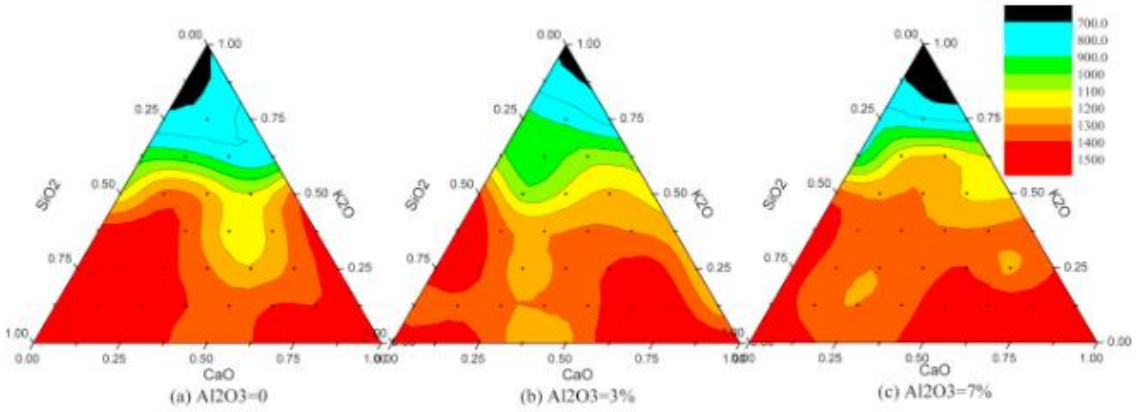

Figure 1.9: The deformation temperature distributions of simulated ashes from (Zhu et al. 2019).

All these authors reported the success of this tool to predict the state of the total ash after combustion. However, some crystalline phases appeared experimentally but were absent in the thermodynamic database, such as $K_2Ca_6Si_4O_{15}$ and $K_2Ca_2Si_2O_7$ (Defoort et al. 2019). Others were predicted but were never found experimentally, such as K_2CaSiO_4 (Defoort et al. 2019). In addition, the calculated liquidus line was shifted compared with the experimental results (Rebbling et al. 2020; Öhman et al. 2000; Zhu et al. 2019). Consequently, they all concluded that the thermodynamic database needs to be revised to calculate the equilibria in the entire composition and temperature space. It should be noted that an important drawback of the thermodynamic prediction tool is that it provides results at equilibrium, which might or might not be the case in real processes, especially on an industrial scale. Hence, laboratory tests remain a joint step to evaluate the ash behavior in a pilot plant.

To further highlight the limitations of the CaO-K_2O-SiO_2 system, a thorough investigation of the ternary components of this system was conducted. For instance, most of the current thermodynamic databases are still based on the work of Morey et al. (Morey, Kracek, and Bowen 1930). However, this work is outdated, and recent researches showed clear limitations that are still present in this system. In their work, Morey et al. (Morey, Kracek, and Bowen 1930) reported the presence of 7 ternary phases: K_2CaSiO_4 (1:1:1), $K_2Ca_3Si_6O_{16}$ (1:3:6), $K_2Ca_2Si_6O_{15}$ (1:2:6), $K_2Ca_2Si_9O_{21}$ (1:2:9), $K_4CaSi_6O_{15}$ (2:1:6), $K_4CaSi_3O_9$ (2:1:3), $K_8CaSi_{10}O_{25}$ (4:1:10) (Morey, Kracek, and Bowen 1930). Crystalline structures for two of the seven ternary compounds reported by Morey et al. (Morey, Kracek, and Bowen 1930), $K_4CaSi_3O_9$ and $K_8CaSi_{10}O_{25}$, were reported in the literature (Erik Arroyabe, Kaindl, and Kahlenberg 2009; Kahlenberg, Kaindl, and Többens 2006). However, crystalline structures for another four of the seven compounds shown by Morey el al. (Morey, Kracek, and Bowen 1930), $K_2Ca_2Si_6O_{15}$ (1:2:6), $K_2Ca_3Si_6O_{16}$ (1:3:6), $K_2Ca_2Si_9O_{21}$ (1:2:9), $K_4CaSi_6O_{15}$ (2:1:6) are still absent in the literature. Morey et al. (Morey, Kracek, and Bowen 1931) corrected in a later study $K_2Ca_2Si_6O_{15}$ for $K_2Ca_3Si_6O_{16}$. However, Arroyabe et al. (E. Arroyabe et al. 2009b) showed the misinterpretation of $K_2Ca_3Si_6O_{16}$ for $K_2Ca_4Si_8O_{21}$. Similarly, Schmidmair el al. (Schmidmair et al. 2017) reported the absence of $K_2Ca_3Si_6O_{16}$, which is misinterpreted for $K_2Ca_4Si_8O_{21}$. They have also found that $K_2Ca_2Si_9O_{21}$ does not exist and is misinterpreted for $K_2Ca_2Si_8O_{19}$ (Schmidmair et al. 2017). In a recent work done by Arroyabe et al. (Erik Arroyabe, Tessadri, et al. 2011), they reported the absence of K_2CaSiO_4 (1:1:1), and showed that it was misinterpreted for $K_2Ca_2Si_2O_7$ (1:2:2). Hence, $K_4CaSi_6O_{15}$ is the only ternary compound left for re-investigation from the initial work of Morey. In addition, Six new ternary crystalline compounds with identified structures have been acknowledged in literature but were absent in the work of Morey et al., and they are $K_2Ca_6Si_4O_{15}$ (1:6:4), $K_2Ca_4Si_8O_{21}$ (1:4:8), $K_2Ca_2Si_2O_7$ (1:2:2), $K_8CaSi_{10}O_{25}$ (4:1:10), $K_2Ca_3Si_3O_{10}$ (1:3:3), $K_2CaSi_4O_{10}$ and $K_2Ca_2Si_8O_{19}$ (Kahlenberg, Kaindl, and Többens 2006; E. Arroyabe et al. 2009b; Schmidmair et al. 2017; E. Arroyabe et al. 2009a; Erik Arroyabe and Kahlenberg 2011; Schmidmair, Kahlenberg, and Grießer 2018; Erik Arroyabe, Prechtel, et al. 2011).

In addition, the Si and Ca rich regions are abundant with experimentally measured thermodynamic properties, while data for the K-rich region are absent in the literature (D.-G. Kim et al. 2017; M. Chen et al. 2016a; Santoso et al. 2020a; M. Chen and Zhao 2016). The challenge of the experimental investigation of CaO-K_2O-SiO_2 phase equilibria is K evaporation from the samples during equilibration, which will bias the measurements (Santoso et al. 2020b).

Other problems are the omissions of some liquidus data in several primary fields, and even clear disagreement among the authors (Santoso et al. 2020b). For instance, recent calculations for this phase diagram by Chen et al. (M. Chen et al. 2016b) supported the appearance of $K_2Ca_2Si_2O_7$ at 1000 °C and $K_2Ca_6Si_4O_{15}$ at 1050 °C, and the absence of K_2CaSiO_4 as a primary phase. Chen et al. (M. Chen et al. 2016b) also reported a shift of the liquidus line to between 1000 °C and 1200 °C. Further calculations of this system by Santoso et al. (Santoso et al. 2020b) also predicted the appearance of $K_2Ca_2Si_2O_7$ between 1000 °C and 1100 °C and $K_2Ca_6Si_4O_{15}$ between 1100 °C and 1200 °C, while $K_2Ca_2Si_9O_{21}$ and $K_2Ca_3Si_6O_{16}$ were both absent. Santoso et al. (Santoso et al. 2020b) went further and presented new reaction mechanism pathways for the formation of these two new ternary compounds, in the following order (between 1000 °C and 1100 °C):

$$K_2Ca_2Si_2O_7 + CaSiO_3 \leftrightarrow Liquid + K_2Ca_6Si_4O_{15} \quad (S)$$

$$K_2Ca_6Si_4O_{15} + CaSiO_3 \leftrightarrow Liquid + Ca_3Si_2O_5 \quad (T)$$

$$Ca_3Si_2O_5 + K_2Ca_6Si_4O_{15} \leftrightarrow Liquid + Ca_2SiO_4 \quad (U)$$

Nevertheless, some of the calculations of Chen et al. (M. Chen et al. 2016b) and Santoso et al. (Santoso et al. 2020b) were based on estimations, especially those of the two new ternary compounds $K_2Ca_6Si_4O_{15}$ and $K_2Ca_2Si_2O_7$ (D. Kim 2017). These two compounds are located in the middle section of the diagram and hold several important tie lines. Hence, measuring their estimated properties and removing the K_2CaSiO_4 phase from this system can significantly enhance the prediction capabilities.

In conclusion, the thermodynamic database around the CaO, K_2O, and SiO_2 system still needs further investigations and thermodynamic properties measurements.

6.3.3. CaO-K_2O and CaO-SiO_2 binary diagrams investigation

The high volatilization and hygroscopic properties of K and its high corrosion deposition tendency inside the reactors and the instruments make the experimental measurement in the CaO-K_2O binary diagram very challenging and problematic. After a thorough literature review, one research presented experimental work in this binary was found. Cassou et al. (Cassou and Mocellin 1977) synthesized K_2O by slow oxidation of K-metal in an anhydrous N_2/O_2 atmosphere. K_2O purity reached 90%, with 3 to 4% KO_2, 5 to 6% K_2O_2, and 0.2 to 0.5% K_2CO_3 (Cassou and Mocellin 1977). Then, it was mixed with CaO and introduced using a hot-pressed CaO crucible into a vertical Vycor reactor operating under an N_2 atmosphere (Cassou and Mocellin 1977). Cassou et al. (Cassou and Mocellin 1977) reported that no intermediate crystalline phases could be detected up until 800 °C (Cassou and Mocellin 1977). Instead, they

found that K_2O was melting at 674 ± 20 °C, and CaO solid was readily dissolving into the melt by diffusion (Cassou and Mocellin 1977). The dissolution melt layer increased with the increase in CaO concentration in the blend, the temperature, and the residence time (Cassou and Mocellin 1977). Consequently, Cassou et al. (Cassou and Mocellin 1977) reported a single eutectic point in this system at 674 °C.

To verify this eutectic point, the work of Natola et al. (Natola and Touzain 1970) validated the melting point of K_2O at 685 ± 5 °C. Natola et al. (Natola and Touzain 1970) prepared K_2O using the same method reported in Cassou et al. (Cassou and Mocellin 1977). However, Natola et al. (Natola and Touzain 1970) mixed K_2O with K-metal and introduced the mixtures using a platinum crucible into a TGA-DTA, operating under a vacuum. The authors reported five peaks for the K_2O sample compared to one peak for the K-metal sample (Natola and Touzain 1970). From the TGA-DTA results, K_2O was found to exist in four crystalline phases (0 °C<ɤ<317 °C, 317 °C<β<372 °C, 372 °C<α'<446 °C, 446 °C<α<646 °C) (Natola and Touzain 1970). A liquid phase started to form at 64 °C on the pure metal side and coexisted with a liquid solution with all the different crystalline forms of K_2O (Natola and Touzain 1970). A common event was seen in both the K-metal and K_2O DTA diagrams at around 700 °C, which is referred to as K evaporation (Natola and Touzain 1970). Natola et al. corrected the measured melting point of K_2O from 646 °C to 685 °C, after considering the 7% K_2O_2 formed at the fusion point, (Natola and Touzain 1970). In conclusion, the CaO-K_2O diagram contains no intermediate compounds or solutions and has one eutectic at around 680 °C.

The CaO-SiO_2 binary phase diagram is well defined in the literature (White et al. 2016; Taylor and Dinsdale 1990). However, it is currently under investigation in another ongoing thesis by W. Abdul, university of Aberdeen (UK), 2023 (new measurements for certain thermodynamic properties), and will be out of the scope of this work.

6.3.4. K_2O-SiO_2 binary diagrams investigation

The K_2O-SiO_2 binary phase diagram is widely used in glass (Mysen and Richet 2019), glass-ceramic (Gonzaga et al. 2008; Song et al. 2015), and biofuel industries (Näzelius et al. 2015; Zevenhoven-Onderwater et al. 2001). The chemical reaction between SiO_2 refractories and K_2O vapor can be understood from the data in this diagram. This can help mitigate the operational problems resulting from their applications in certain reactors (Allendorf and Spear 2001). The K_2O-SiO_2 binary system can also be used in geological mineralogy studies since the minerals in the rocks on earth are abundant with K_2O-aluminosilicates (Deer, Howie, and Zussman 1992). Most importantly, the phase relation equilibria of this system can provide necessary information

on the ash behavior of biomass, especially agricultural residues rich in K and Si (Siim Link, Yrjas, and Hupa 2018; D.-G. Kim et al. 2017).

Similar to the case of CaO-K_2O binary, due to potassium's hygroscopic and volatile properties, experimental investigation of the K_2O-SiO_2 binary is limited to the high silica region. The thermodynamic properties of K_2SiO_3, $K_2Si_2O_5$, and $K_2Si_4O_9$ are well identified in the literature (Kracek, Bowen, and Morey 1937; Brown and Bennington 1987; Takahashi and Yoshio 1973; 1970b; 1970a; Stull et al. 1970; Richet 1980; Geisinger et al. 1987), along with their crystalline structures (Ďurovič 1974; Schweinsberg and Liebau 1974; 1972; Geisinger et al. 1987; Jong et al. 1998; Hoppe and Werthmann 1981). Low-temperature Cp (<600K) is usually measured by adiabatic calorimetry, while high-temperature Cp by drop calorimetry (K_2SiO_3 (Stull et al. 1970; Beyer 1980), $K_2Si_2O_5$ (Beyer 1980), and $K_2Si_4O_9$ (Richet 1980; Fasshauer et al. 1998)). Several liquid models were used to describe the liquid phase, such as the regular, quasi-regular, and sub-regular models (S. S. Kim and Sanders Jr. 1991), the modified quasichemical model (Wu, Eriksson, and Pelton 1993; Saulov 2007), the modified associate model (Allendorf and Spear 2001; Yazhenskikh, Hack, and Müller 2006), the random mixing model (Forsberg 2002), structural liquid model (Romero-Serrano et al. 2005), and the ionic sublattice model (L. Zhang, Schmetterer, and Masset 2013). However, the authors reported phase diagram reproduction limitations (Allendorf and Spear 2001; S. S. Kim and Sanders Jr. 1991; Romero-Serrano et al. 2005; Yazhenskikh, Hack, and Müller 2006; L. Zhang, Schmetterer, and Masset 2013), and the optimized liquid phase results were valid in the region between K_2SiO_3 and SiO_2 (Wu, Eriksson, and Pelton 1993; Forsberg 2002; Romero-Serrano et al. 2005; L. Zhang, Schmetterer, and Masset 2013).

In 1990, Bernet et al. (Bernet and Hoppe 1990) reported the presence of a fourth crystalline solid compound, K_4SiO_4, in the K-rich region. Though the authors identified its crystalline structure, the phase was never reproduced and the thermodynamic measurements of its properties were never done. In 2017, Kim et al. (D.-G. Kim et al. 2017) tried to investigate the K-rich region beyond K_2SiO_3 in this phase diagram. Consequently, they annealed two sealed mixtures in a platinum crucible, 40 mol% K_2O and 67 mol% K_2O each, in a TGA-DTA and a TGA-DSC until 1100 °C (D.-G. Kim et al. 2017). Kim et al. (D.-G. Kim et al. 2017) reported, for the first time in literature, a reproducible eutectic point between K_4SiO_4 and K_2SiO_3 at 714 ± 6 °C and 59 mol% K_2O (after taking K volatilization into consideration). The authors did not find any transition in the 67 mol% K_2O mixture up to 1200 °C (D.-G. Kim et al. 2017). Kim et al. (D.-G. Kim et al. 2017) are the latest researchers in literature to remodel the binary phase diagram K_2O-SiO_2. Though they were the first to add K_4SiO_4 with the new eutectic point to the

data, they estimated its enthalpy of formation at 298.15 K based on similar Na and Li oxide systems, and its entropy of formation at 298.15 K and Cp using the NKR data of K_2O and SiO_2 (D.-G. Kim et al. 2017). On the other hand, Jansen et al. (Jansen 1982) reported the presence of a fifth highly stable crystalline structure, $K_6Si_2O_7$, in the high K-rich region. However, until today, this compound was never added to any binary diagram of this system.

In conclusion, thermodynamic modeling of the K_2O-SiO_2 system in the entire composition range is still lacking, especially in the K-rich region and in terms of the thermodynamic properties of K_4SiO_4 and $K_6Si_2O_7$. In the absence of measured thermodynamic properties, density functional theory (DFT) could use the well-defined crystalline structure of the compounds to calculate their electronic structure and derive missing thermodynamic properties, (Kurth, Marques, and Gross 2005). This technique can help overcome all the current experimental limitations in this system.

In conclusion, the K_2O-SiO_2 binary system needs revision.

7. Conclusion

After this literature review of the main topics in the current work related to the effect of biomass blending on the combustion ash behavior supported by its thermodynamic prediction, several conclusions can be drawn out:

1. The ash of woody biomasses (such as oak bark) presents a high melting point and a low sintering tendency due to their high alkaline earth oxides composition.
2. The ash of agricultural residues (specifically wheat straw) presents high sintering and slagging tendencies. Their emissions are also rich in HCl and SOx. The current slagging and emissions controlling techniques are limited, and more efficient solutions need to be proposed.
3. Additives' application to control the ash behavior is still limited, affected by high cost, side toxic emissions, and dependence on the feedstock ash composition.
4. Biomass blending (bark [ash in the solid phase] with straw [ash in the liquid phase]) proved to be a more suitable solution than additives to fight slagging and agglomeration in combustion reactors in terms of cost and effectiveness.
5. Most literature in this domain avoided talking about chemical reactions or inorganic interactions within the ash of biomass blends. They rather tended to link the effect of blending to several factors related to the ash properties and its behavior.
6. Increasing the agricultural residue fraction in the straw-bark (wood) blend increases the slagging tendency and lowers the emissions (K, Cl, and S retained in the slag) in both

laboratory and pilot appliances. However, depending on the composition of the agricultural residue, a threshold blend fraction exists, upon which both emissions and slagging start to increase simultaneously.

7. The application of various laboratory prediction tests (Bioslag test, rapid qualitative test, TGA-DTA, ash test, and pellet test) remains highly limited, similar to empirical indices.
8. The literature highlighted the need for further improvements in the process simulation prediction approach based on the thermodynamic equilibrium.
    a. The liquidus need to be checked/remodeled.
    b. The thermodynamic database around the CaO, K_2O, and SiO_2 system still needs further investigations and thermodynamic properties measurements.
    c. The K_2O-SiO_2 binary system needs revision.

References

Alam, Md Tanvir, Baiqian Dai, Xiaojiang Wu, Andrew Hoadley, and Lian Zhang. 2021. "A Critical Review of Ash Slagging Mechanisms and Viscosity Measurement for Low-Rank Coal and Bio-Slags." *Frontiers in Energy* 15 (1): 46–67. https://doi.org/10.1007/s11708-020-0807-8.

Allendorf, Mark D., and Karl E. Spear. 2001. "Thermodynamic Analysis of Silica Refractory Corrosion in Glass-Melting Furnaces." *Journal of The Electrochemical Society* 148 (2): B59. https://doi.org/10.1149/1.1337603.

Arroyabe, E., R. Kaindl, D.M. Többens, and V. Kahlenberg. 2009a. "K2Ca6Si4O15—Structural and Spectroscopical Studies on a Mixed Tetrahedral–Octahedral Framework." *Journal of Solid State Chemistry* 182 (12): 3254–61. https://doi.org/10.1016/j.jssc.2009.09.013.

———. 2009b. "Synthesis, Crystal Structure, and Vibrational Spectroscopy of K2Ca4Si8O21—An Unusual Single-Layer Silicate Containing Q2 and Q3 Units." *Inorganic Chemistry* 48 (24): 11929–34. https://doi.org/10.1021/ic901762u.

Arroyabe, Erik, and Volker Kahlenberg. 2011. "Structural Investigations on the Fertilizer Component K2Ca2Si2O7." *European Journal of Mineralogy* 23 (1): 101–10. https://doi.org/10.1127/0935-1221/2011/0023-2080.

Arroyabe, Erik, Reinhard Kaindl, and Volker Kahlenberg. 2009. "Structural and Raman Spectroscopic Investigations of K4BaSi3O9 and K4CaSi3O9." *Zeitschrift Für Anorganische Und Allgemeine Chemie* 635 (2): 337–45. https://doi.org/10.1002/zaac.200800398.

Arroyabe, Erik, Felix Prechtel, Daniel M. Többens, Reinhard Kaindl, and Volker Kahlenberg. 2011. "K2Ca3Si3O10, a Novel Trisilicate: High-Pressure Synthesis, Structural, Spectroscopic and Computational Studies." *European Journal of Mineralogy* 23 (3): 425–35. https://doi.org/10.1127/0935-1221/2011/0023-2096.

Arroyabe, Erik, Richard Tessadri, Daniel M. Többens, and Volker Kahlenberg. 2011. "Does K2CaSiO4 Exist? A Phase-Analytical Study in the System K2O-CaO-SiO2 with Implications for the Characterization of Residual Materials: Does K2CaSiO4 Exist?" *Journal of the American Ceramic Society* 94 (8): 2652–55. https://doi.org/10.1111/j.1551-2916.2011.04397.x.

Arvelakis, S., C. Sotiriou, A. Moutsatsou, and E. G. Koukios. 1999. "Prediction of the Behaviour of Biomass Ash in Fluidized Bed Combustors and Gasifiers." *Journal of Thermal Analysis and Calorimetry* 56 (3): 1271–78. https://doi.org/10.1023/A:1010189919655.

Balland, M., K. Froment, G. Ratel, S. Valin, J. Roussely, R. Michel, J. Poirier, Y. Kara, and A. Galnares. 2017. "Biomass Ash Fluidised-Bed Agglomeration: Hydrodynamic Investigations." *Waste and Biomass Valorization* 8 (8): 2823–41. https://doi.org/10.1007/s12649-017-9853-9.

Becidan, Michaël, Dusan Todorovic, Øyvind Skreiberg, Roger A. Khalil, Rainer Backman, Franziska Goile, Alexandra Skreiberg, Aleksandar Jovovic, and Lars Sørum. 2012. "Ash Related Behaviour in Staged and Non-Staged Combustion of Biomass Fuels and Fuel Mixtures." *Biomass and Bioenergy* 41 (June): 86–93. https://doi.org/10.1016/j.biombioe.2012.02.005.

Beidaghy Dizaji, Hossein, Thomas Zeng, Hieronymus Hölzig, Jens Bauer, Gert Klöß, and Dirk Enke. 2022. "Ash Transformation Mechanism during Combustion of Rice Husk and Rice Straw." *Fuel* 307 (January): 121768. https://doi.org/10.1016/j.fuel.2021.121768.

Bernet, K., and R. Hoppe. 1990. “Zur Kristallstruktur von K4[SiO4].” *Zeitschrift für anorganische und allgemeine Chemie* 589 (1): 129–38. https://doi.org/10.1002/zaac.19905890115.

Beyer, R. P. 1980. *Thermodynamic Properties of Potassium Metasilicate and Disilicate / by R.P. Beyer [and Others]*. Report of Investigations - Bureau of Mines ; No. 8410. Washington: Dept. of the Interior, Bureau of Mines.

Bhaskar, Thallada, and Ashok Pandey. 2015. “Advances in Thermochemical Conversion of Biomass—Introduction.” In *Recent Advances in Thermo-Chemical Conversion of Biomass*, 3–30. Elsevier. https://doi.org/10.1016/B978-0-444-63289-0.00001-6.

Boström, Dan, Nils Skoglund, Alejandro Grimm, Christoffer Boman, Marcus Öhman, Markus Broström, and Rainer Backman. 2012. “Ash Transformation Chemistry during Combustion of Biomass.” *Energy & Fuels* 26 (1): 85–93. https://doi.org/10.1021/ef201205b.

Brown, R. R., and K. O. Bennington. 1987. “Thermodynamic Properties of Potassium Metasilicate (K2SiO3).” *Thermochimica Acta* 122 (2): 289–94. https://doi.org/10.1016/0040-6031(87)87048-X.

Cao, Wenhan, Jun Li, Leteng Lin, and Xiaolei Zhang. 2021. “Release of Potassium in Association with Structural Evolution during Biomass Combustion.” *Fuel* 287 (March): 119524. https://doi.org/10.1016/j.fuel.2020.119524.

Cassou, M., and A. Mocellin. 1977. “Observation of CaO Corrosion by K2O Melts.” *Journal of Materials Science* 12 (5): 909–14. https://doi.org/10.1007/BF00540972.

Chen, Mao, Xinmei Hou, Junhong Chen, and Baojun Zhao. 2016a. “Phase Equilibria Studies in the SiO2-K2O-CaO System.” *Metallurgical and Materials Transactions B* 47 (3): 1690–96. https://doi.org/10.1007/s11663-016-0623-z.

———. 2016b. “Phase Equilibria Studies in the SiO2-K2O-CaO System.” *Metallurgical and Materials Transactions B* 47 (3): 1690–96. https://doi.org/10.1007/s11663-016-0623-z.

Chen, Mao, and Baojun Zhao. 2016. “Viscosity Measurements of the SiO2–K2O–CaO System Relevant to Biomass Slags.” *Fuel* 180 (September): 638–44. https://doi.org/10.1016/j.fuel.2016.04.099.

Chen, Wei-Yin, Toshio Suzuki, and Maximilian Lackner, eds. 2017. *Handbook of Climate Change Mitigation and Adaptation*. 2nd ed. Springer International Publishing. https://www.springer.com/gp/book/9783319144085.

Cruz, Glauber, Alyson Rodrigues, Maria Souza, and Wolia Gomes. 2018. “Application of Cassava Harvest Residues (Manihot Esculenta Crantz) in Biochemical and Thermochemical Conversion Processes for Bioenergy Purposes: A Literature Review.” *AFRICAN JOURNAL OF BIOTECHNOLOGY* 17 (January): 37–50. https://doi.org/10.5897/AJB2017.16322.

Cruz, Nuno C., Flávio C. Silva, Luís A. C. Tarelho, and Sónia M. Rodrigues. 2019. “Critical Review of Key Variables Affecting Potential Recycling Applications of Ash Produced at Large-Scale Biomass Combustion Plants.” *Resources, Conservation and Recycling* 150 (November): 104427. https://doi.org/10.1016/j.resconrec.2019.104427.

Deer, W. A., R. A. Howie, and J. Zussman. 1992. “An Introduction to the Rock-Forming Minerals: Essex.” *England: Longman Scientific and Technology*.

Defoort, Françoise, Matthieu Campargue, Gilles Ratel, Hélène Miller, and Capucine Dupont. 2019. “Physicochemical Approach To Blend Biomass.” *Energy & Fuels* 33 (7): 5820–28. https://doi.org/10.1021/acs.energyfuels.8b04169.

Díaz-Ramírez, Maryori, Christoffer Boman, Fernando Sebastián, Javier Royo, Shaojun Xiong, and Dan Boström. 2012. “Ash Characterization and Transformation Behavior

of the Fixed-Bed Combustion of Novel Crops: Poplar, Brassica, and Cassava Fuels." *Energy & Fuels* 26 (6): 3218–29. https://doi.org/10.1021/ef2018622.

Ďurovič, S. 1974. "Die Kristallstruktur des K4[Si8O18]: Eine desymmetrisierte OD Struktur." *Acta Crystallographica Section B: Structural Crystallography and Crystal Chemistry* 30 (9): 2214–17. https://doi.org/10.1107/S0567740874006765.

Elled, A. -L., L. -E. Åmand, and B. -M. Steenari. 2013. "Composition of Agglomerates in Fluidized Bed Reactors for Thermochemical Conversion of Biomass and Waste Fuels: Experimental Data in Comparison with Predictions by a Thermodynamic Equilibrium Model." *Fuel* 111 (September): 696–708. https://doi.org/10.1016/j.fuel.2013.03.018.

Engineering Toolbox. 2019. "Fuels - Higher and Lower Calorific Values." https://www.engineeringtoolbox.com/fuels-higher-calorific-values-d_169.html.

European Environmental Agency. 2022. "Biomass." https://www.eea.europa.eu/help/glossary/eea-glossary/biomass#:~:text=The%20biodegradable%20fraction%20of%20products,of%20industrial%20and%20municipal%20waste.

Fakourian, Seyedhassan, Zachary McAllister, Andrew Fry, Yueming Wang, Xiaolong Li, Jost O. L. Wendt, and Jinze Dai. 2021. "Modeling Ash Deposit Growth Rates for a Wide Range of Solid Fuels in a 100 KW Combustor." *Fuel Processing Technology* 217 (June): 106777. https://doi.org/10.1016/j.fuproc.2021.106777.

Fasshauer, Detlef, Bernd Wunder, Niranjan Chatterjee, and Günther Höhne. 1998. "Heat Capacity of Wadeite-Type K2Si4O9 and the Pressure-Induced Stable Decomposition of K-Feldspar." *Contributions to Mineralogy and Petrology* 131 (April): 210–18. https://doi.org/10.1007/s004100050389.

Forsberg, S. 2002. "Optimization of Thermodynamic Properties of the K2O-SiO2 System at High Temperatures." *Journal of Phase Equilibria* 23 (3): 211–17. https://doi.org/10.1361/105497102770331695.

Fournel, Sébastien, Joahnn H. Palacios, Stéphane Godbout, and Michèle Heitz. 2015. "Effect of Additives and Fuel Blending on Emissions and Ash-Related Problems from Small-Scale Combustion of Reed Canary Grass." *Agriculture* 5 (3): 561–76. https://doi.org/10.3390/agriculture5030561.

Gebgeegziabher, Tesfaldet, Adetoyese Olajire Oyedun, Yu Zhang, and Chi Wai Hui. 2013. "Effective Optimization Model for Biomass Drying." In *Computer Aided Chemical Engineering*, edited by Andrzej Kraslawski and Ilkka Turunen, 32:97–102. 23 European Symposium on Computer Aided Process Engineering. Elsevier. https://doi.org/10.1016/B978-0-444-63234-0.50017-8.

Geisinger, Karen L., Nancy L. Ross, Paul F. McMillan, and Alexandra Navrotsky. 1987. "K2Si4O9: Energetics and Vibrational Spectra of Glass, Sheet Silicate, and Wadeite-Type Phases." *American Mineralogist* 72 (9–10): 984–94.

Gilbe, Carl, Erica Lindström, Rainer Backman, Robert Samuelsson, Jan Burvall, and Marcus Öhman. 2008. "Predicting Slagging Tendencies for Biomass Pellets Fired in Residential Appliances: A Comparison of Different Prediction Methods." *Energy & Fuels* 22 (6): 3680–86. https://doi.org/10.1021/ef800321h.

Gonzaga, Carla Castiglia, Paulo Francisco Cesar, Cristina Yuri Okada, Catia Fredericci, Flávio Beneduce Neto, and Humberto Naoyuki Yoshimura. 2008. "Mechanical Properties and Porosity of Dental Glass-Ceramics Hot-Pressed at Different Temperatures." *Materials Research* 11 (September): 301–6. https://doi.org/10.1590/S1516-14392008000300012.

Höfer, Isabel, and Martin Kaltschmitt. 2017. "Effect of Additives on Particulate Matter Formation of Solid Biofuel Blends from Wood and Straw." *Biomass Conversion and Biorefinery* 7 (1): 101–16. https://doi.org/10.1007/s13399-016-0217-7.

Holubcik, Michal, Jozef Jandacka, Matej Palacka, and Peter Vician. 2016. “Additives Application to Wheat Straw to Increasing the Ash Fusion Temperature.” *AIP Conference Proceedings* 1768 (1): 020014. https://doi.org/10.1063/1.4963036.

Hoppe, R., and R. Werthmann. 1981. “Ueber K2 Si O3 - Das Erste Cyclotrisilicat Eines Alkalimetalls - Sowie Rb2 Si O3, Cs2 Si O3, Rb2 Ge O3 Und Cs2 Ge O3.” *Revue de Chimie Minerale*, 1981, 18.

Hu, Zhongfa, Xuebin Wang, Lan Zhang, Shunzhi Yang, Renhui Ruan, Shengjie Bai, Yiming Zhu, Liang Wang, Hrvoje Mikulčić, and Houzhang Tan. 2020. “Emission Characteristics of Particulate Matters from a 30 MW Biomass-Fired Power Plant in China.” *Renewable Energy* 155 (August): 225–36. https://doi.org/10.1016/j.renene.2020.03.094.

Jamian, N R, M Rashid, S M M Muzi, N Hussein, D Munisamy, K M Pa’ad, A H M Ali, and S Y Yusuf. 2020. “Estimation of Particulate Emission Generation in Palm Oil Mill Boiler.” *IOP Conference Series: Materials Science and Engineering* 808 (1): 012039. https://doi.org/10.1088/1757-899X/808/1/012039.

Jansen, M. 1982. “Zur Struktur von Kaliumdisilicat.” *Journal Door Crystallography*, 1982, 160.

Jong, B. H. W. S. de, H. T. J. Supèr, A. L. Spek, N. Veldman, G. Nachtegaal, and J. C. Fischer. 1998. “Mixed Alkali Systems: Structure and ^{29} Si MASNMR of $Li_2Si_2O_5$ and $K_2Si_2O_5$.” *Acta Crystallographica Section B Structural Science* 54 (5): 568–77. https://doi.org/10.1107/S0108768198001062.

Kahlenberg, V., R. Kaindl, and D.M. Többens. 2006. “The Crystal Structure of the Interrupted Framework Silicate K9.6Ca1.2Si12O30 Determined from Laboratory X-Ray Diffraction Data.” *Journal of Solid State Chemistry* 179 (7): 1948–56. https://doi.org/10.1016/j.jssc.2006.03.044.

Kalis, Harijs, Antons Kolmickovs, Maksims Marinaki, and Liva Ozola. 2018. “Development of Combustion Dynamics at Co-Combustion of Straw with Wood.” In . https://doi.org/10.22616/ERDev2018.17.N114.

Kim, Donggeum. 2017. “Coupled Experimental Study and Thermodynamic Optimization of the K2O-Na2O-CaO-MgO-Al2O3-SiO2 System.” Canada: McGill University, Montreal, Quebec, Canada.

Kim, Dong-Geun, Marie-Aline Van Ende, Pierre Hudon, and In-Ho Jung. 2017. “Coupled Experimental Study and Thermodynamic Optimization of the K2O-SiO2 System.” *Journal of Non-Crystalline Solids* 471 (September): 51–64. https://doi.org/10.1016/j.jnoncrysol.2017.04.029.

Kim, Sung S., and Thomas H. Sanders Jr. 1991. “Thermodynamic Modeling of Phase Diagrams in Binary Alkali Silicate Systems.” *Journal of the American Ceramic Society* 74 (8): 1833–40. https://doi.org/10.1111/j.1151-2916.1991.tb07796.x.

Knudsen, Jacob N., Peter A. Jensen, and Kim Dam-Johansen. 2004. “Transformation and Release to the Gas Phase of Cl, K, and S during Combustion of Annual Biomass.” *Energy & Fuels* 18 (5): 1385–99. https://doi.org/10.1021/ef049944q.

Kortelainen, Miika, Jorma Jokiniemi, Ilpo Nuutinen, Tiina Torvela, Heikki Lamberg, Tommi Karhunen, Jarkko Tissari, and Olli Sippula. 2015. “Ash Behaviour and Emission Formation in a Small-Scale Reciprocating-Grate Combustion Reactor Operated with Wood Chips, Reed Canary Grass and Barley Straw.” *Fuel* 143 (March): 80–88. https://doi.org/10.1016/j.fuel.2014.11.006.

Kracek, F. C., N. L. Bowen, and G. W. Morey. 1937. “EQUILIBRIUM RELATIONS AND FACTORS INFLUENCING THEIR DETERMINATION IN THE SYSTEM IK2SiO3-SiO2.” *Journal of Physical Chemistry*, 1937, 41, 1183–1193.

Kurth, S., M. A. L. Marques, and E. K. U. Gross. 2005. “Density-Functional Theory.” In *Encyclopedia of Condensed Matter Physics*, edited by Franco Bassani, Gerald L. Liedl, and Peter Wyder, 395–402. Oxford: Elsevier. https://doi.org/10.1016/B0-12-369401-9/00445-9.

Lamberg, Heikki, Jarkko Tissari, Jorma Jokiniemi, and Olli Sippula. 2013. “Fine Particle and Gaseous Emissions from a Small-Scale Boiler Fueled by Pellets of Various Raw Materials.” *Energy & Fuels* 27 (11): 7044–53. https://doi.org/10.1021/ef401267t.

Li, Xiaomin, Xun Gong, Chuxuan Zhang, Tingfeng Liu, Wenyu Wang, and Yang Zhang. 2020. “Occurrence Characteristics of Ash-Forming Elements in Sea Rice Waste and Their Effects on Particulate Matter Emission during Combustion.” *Fuel* 273 (August): 117769. https://doi.org/10.1016/j.fuel.2020.117769.

Libra, Judy A., Kyoung S. Ro, Claudia Kammann, Axel Funke, Nicole D. Berge, York Neubauer, Maria-Magdalena Titirici, Christoph Fühner, Oliver Bens, and Jürgen Kern. 2011. “Hydrothermal Carbonization of Biomass Residuals: A Comparative Review of the Chemistry, Processes and Applications of Wet and Dry Pyrolysis.” *Biofuels* 2 (1): 71–106. https://doi.org/10.4155/bfs.10.81.

Lind, Terttaliisa, Esko I. Kauppinen, Jouni Hokkinen, Jorma K. Jokiniemi, Markku Orjala, Minna Aurela, and Risto Hillamo. 2006. “Effect of Chlorine and Sulfur on Fine Particle Formation in Pilot-Scale CFBC of Biomass.” *Energy & Fuels* 20 (1): 61–68. https://doi.org/10.1021/ef050122i.

Lindberg, Daniel, Rainer Backman, Patrice Chartrand, and Mikko Hupa. 2013. “Towards a Comprehensive Thermodynamic Database for Ash-Forming Elements in Biomass and Waste Combustion — Current Situation and Future Developments.” *Fuel Processing Technology* 105 (January): 129–41. https://doi.org/10.1016/j.fuproc.2011.08.008.

Link, S., P. Yrjas, and L. Hupa. 2017. “Impact of the Blending Method on the Melting Characteristics of Ashes of Biomass Blends.” *Proceedings of the 25th European Biomass Conference and Exhibition* 12-15 June 2017: 5 Pages. https://doi.org/10.5071/25THEUBCE2017-2BV.1.13.

Link, Siim, Patrik Yrjas, and Leena Hupa. 2018. “Ash Melting Behaviour of Wheat Straw Blends with Wood and Reed.” *Renewable Energy*, SI: Waste Biomass to Biofuel, 124 (August): 11–20. https://doi.org/10.1016/j.renene.2017.09.050.

Link, Siim, Patrik Yrjas, Daniel Lindberg, Andres Trikkel, and Valdek Mikli. 2022. “Ash Melting Behaviour of Reed and Woody Fuels Blends.” *Fuel* 314 (April): 123051. https://doi.org/10.1016/j.fuel.2021.123051.

Luan, Chao, Changfu You, and Dongke Zhang. 2014. “Composition and Sintering Characteristics of Ashes from Co-Firing of Coal and Biomass in a Laboratory-Scale Drop Tube Furnace.” *Energy* 69 (May): 562–70. https://doi.org/10.1016/j.energy.2014.03.050.

Luo, Zhongyang, and Jingsong Zhou. 2012. “Thermal Conversion of Biomass.” In *Handbook of Climate Change Mitigation*, edited by Wei-Yin Chen, John Seiner, Toshio Suzuki, and Maximilian Lackner, 1001–42. New York, NY: Springer US. https://doi.org/10.1007/978-1-4419-7991-9_27.

Luque, R., J. M. Campelo, and J. H. Clark. 2011. “1 - Introduction: An Overview of Biofuels and Production Technologies.” In *Handbook of Biofuels Production*, edited by Rafael Luque, Juan Campelo, and James Clark, 3–12. Woodhead Publishing Series in Energy. Woodhead Publishing. https://doi.org/10.1533/9780857090492.1.3.

Mack, Robert, Daniel Kuptz, Claudia Schön, and Hans Hartmann. 2019. “Combustion Behavior and Slagging Tendencies of Kaolin Additivated Agricultural Pellets and of Wood-Straw Pellet Blends in a Small-Scale Boiler.” *Biomass and Bioenergy* 125 (June): 50–62. https://doi.org/10.1016/j.biombioe.2019.04.003.

Magdziarz, Aneta, Marcin Gajek, Dorota Nowak-Woźny, and Małgorzata Wilk. 2018. "Mineral Phase Transformation of Biomass Ashes – Experimental and Thermochemical Calculations." *Renewable Energy*, Exergy analysis of renewable energy systems, 128 (December): 446–59. https://doi.org/10.1016/j.renene.2017.05.057.

Mediavilla, I., M.J. Fernández, and L.S. Esteban. 2009. "Optimization of Pelletisation and Combustion in a Boiler of 17.5 KWth for Vine Shoots and Industrial Cork Residue." *Fuel Processing Technology* 90 (4): 621–28. https://doi.org/10.1016/j.fuproc.2008.12.009.

Míguez, José Luis, Jacobo Porteiro, Frank Behrendt, Diana Blanco, David Patiño, and Alba Dieguez-Alonso. 2021. "Review of the Use of Additives to Mitigate Operational Problems Associated with the Combustion of Biomass with High Content in Ash-Forming Species." *Renewable and Sustainable Energy Reviews* 141 (May): 110502. https://doi.org/10.1016/j.rser.2020.110502.

Miles, T. R., and Jr Miles. 1996. "Experience with Biomass Fuel Blends in Combustion Systems," 1996 international joint power generation conference, Houston, TX (United States). https://www.osti.gov/biblio/427867.

Morey, G.W., F.C. Kracek, and N.L. Bowen. 1930. "The Ternary System K2O-CaO-SiO2." *Journal of the Society of Glass Technology* 14: 149–87.

———. 1931. "The Ternary System K2O-CaO-SiO2: A Correction." *J Soc Glass Technol* 14: 57–58.

Mysen, Bjorn, and Pascal Richet. 2019. *Silicate Glasses and Melts*. Elsevier. https://doi.org/10.1016/C2018-0-00864-6.

Nasir Ani, Farid. 2016. "8 - Utilization of Bioresources as Fuels and Energy Generation." In *Electric Renewable Energy Systems*, edited by Muhammad H. Rashid, 140–55. Boston: Academic Press. https://doi.org/10.1016/B978-0-12-804448-3.00008-6.

Natola, F., and PH. Touzain. 1970. "Diagramme de Phases Du Systhme K-K2O et Le Monooxyde de Potassium K2O." *Canadian Journal of Chemistry*, January 8, 1970, 48.

Naydenova, Iliyana, Ognyan Sandov, Florian Wesenauer, Thomas Laminger, and Franz Winter. 2020. "Pollutants Formation during Single Particle Combustion of Biomass under Fluidized Bed Conditions: An Experimental Study." *Fuel* 278 (October): 117958. https://doi.org/10.1016/j.fuel.2020.117958.

Näzelius, Ida-Linn, Jonathan Fagerström, Christoffer Boman, Dan Boström, and Marcus Öhman. 2015. "Slagging in Fixed-Bed Combustion of Phosphorus-Poor Biomass: Critical Ash-Forming Processes and Compositions." *Energy & Fuels* 29 (2): 894–908. https://doi.org/10.1021/ef502531m.

Nguyen, Hoang Khoi, Ji Hong Moon, Sung Ho Jo, Sung Jin Park, Dal Hee Bae, Myung Won Seo, Ho Won Ra, et al. 2021. "Ash Characteristics of Oxy-Biomass Combustion in a Circulating Fluidized Bed with Kaolin Addition." *Energy* 230 (September): 120871. https://doi.org/10.1016/j.energy.2021.120871.

Nirmala, Narasiman, Munusamy Subathra, Sivaprasad Shyam, Shanmuganantham S. Dawn, Kannappan P. Gopinath, and Jayaseelan Arun. 2022. "11 - Hydrothermal Gasification of Biomass for Hydrogen Production: Advances, Challenges, and Prospects." In *Innovations in Thermochemical Technologies for Biofuel Processing*, edited by Sonil Nanda and Dai-Viet Vo, 259–73. Elsevier. https://doi.org/10.1016/B978-0-323-85586-0.00011-1.

Öhman, Marcus, Anders Nordin, Bengt-Johan Skrifvars, Rainer Backman, and Mikko Hupa. 2000. "Bed Agglomeration Characteristics during Fluidized Bed Combustion of Biomass Fuels." *Energy & Fuels* 14 (1): 169–78. https://doi.org/10.1021/ef990107b.

Orang, Naz, and Honghi Tran. 2015. “Effect of Feedstock Moisture Content on Biomass Boiler Operation.” *Tappi Journal* 14 (October): 629–37. https://doi.org/10.32964/TJ14.10.629.

Porbatzki, Dirk, Michael Stemmler, and Michael Müller. 2011. “Release of Inorganic Trace Elements during Gasification of Wood, Straw, and Miscanthus.” *Biomass and Bioenergy* 35 (October): S79–86. https://doi.org/10.1016/j.biombioe.2011.04.001.

Rebbling, Anders, Peter Sundberg, Jonathan Fagerström, Markus Carlborg, Claes Tullin, Dan Boström, Marcus Öhman, Christoffer Boman, and Nils Skoglund. 2020. “Demonstrating Fuel Design To Reduce Particulate Emissions and Control Slagging in Industrial-Scale Grate Combustion of Woody Biomass.” *Energy & Fuels* 34 (2): 2574–83. https://doi.org/10.1021/acs.energyfuels.9b03935.

Regueiro, Araceli, David Patiño, Enrique Granada, and Jacobo Porteiro. 2017. “Experimental Study on the Fouling Behaviour of an Underfeed Fixed-Bed Biomass Combustor.” *Applied Thermal Engineering* 112 (February): 523–33. https://doi.org/10.1016/j.applthermaleng.2016.10.105.

Reinmöller, Markus, Mathias Klinger, Marcus Schreiner, and Heiner Gutte. 2015. “Relationship between Ash Fusion Temperatures of Ashes from Hard Coal, Brown Coal, and Biomass and Mineral Phases under Different Atmospheres: A Combined FactSage™ Computational and Network Theoretical Approach.” *Fuel*, The 10th European Conference on Coal Research and its Applications, 151 (July): 118–23. https://doi.org/10.1016/j.fuel.2015.01.036.

Rentizelas, A. A. 2016. “6 - Biomass Storage.” In *Biomass Supply Chains for Bioenergy and Biorefining*, edited by Jens Bo Holm-Nielsen and Ehiaze Augustine Ehimen, 127–46. Woodhead Publishing. https://doi.org/10.1016/B978-1-78242-366-9.00006-X.

Richardson, Yohan, Martin Drobek, Anne Julbe, Joël Blin, and François Pinta. 2015. “Biomass Gasification to Produce Syngas.” In *Recent Advances in Thermo-Chemical Conversion of Biomass*, 213–50. Elsevier. https://doi.org/10.1016/B978-0-444-63289-0.00008-9.

Richet, Pascal. 1980. “Heat Capacity of Liquid Silicates: New Measurements on NaAlSiO8 and K2SiO9.” *Geochimica et Cosmochimica Acta* 44 (10): 1535–41. https://doi.org/10.1016/0016-7037(80)90117-9.

Rizvi, T., P. Xing, M. Pourkashanian, L.I. Darvell, J.M. Jones, and W. Nimmo. 2015. “Prediction of Biomass Ash Fusion Behaviour by the Use of Detailed Characterisation Methods Coupled with Thermodynamic Analysis.” *Fuel* 141 (February): 275–84. https://doi.org/10.1016/j.fuel.2014.10.021.

Rodríguez, Juan Luis, Xana Álvarez, Enrique Valero, Luis Ortiz, Natalia de la Torre-Rodríguez, and Carolina Acuña-Alonso. 2020. “Design of Solid Biofuels Blends to Minimize the Risk of Sintering in Biomass Boilers.” *Journal of the Energy Institute* 93 (6): 2409–14. https://doi.org/10.1016/j.joei.2020.07.015.

Romero-Serrano, A., C. Gomez-Yañez, M. Hallen-Lopez, and J. Araujo-Osorio. 2005. “Thermodynamic Modeling of Alkali Metal Oxide-Silica Binary Melts.” *Journal of the American Ceramic Society* 88 (1): 141–45. https://doi.org/10.1111/j.1551-2916.2004.00022.x.

Royo, Javier, Paula Canalís, and David Quintana. 2020. “Chemical Study of Fly Ash Deposition in Combustion of Pelletized Residual Agricultural Biomass.” *Fuel* 268 (May): 117228. https://doi.org/10.1016/j.fuel.2020.117228.

———. 2022. “Chemical Study of Bottom Ash Sintering in Combustion of Pelletized Residual Agricultural Biomass.” *Fuel* 310 (February): 122145. https://doi.org/10.1016/j.fuel.2021.122145.

Royo, Javier, Paula Canalís, David Quintana, Maryori Díaz-Ramírez, Ana Sin, and Adeline Rezeau. 2019. "Experimental Study on the Ash Behaviour in Combustion of Pelletized Residual Agricultural Biomass." *Fuel* 239 (March): 991–1000. https://doi.org/10.1016/j.fuel.2018.11.054.

Salour, D., B.M. Jenkins, M. Vafaei, and M. Kayhanian. 1993. "Control of In-Bed Agglomeration by Fuel Blending in a Pilot Scale Straw and Wood Fueled AFBC." *Biomass and Bioenergy* 4 (2): 117–33. https://doi.org/10.1016/0961-9534(93)90033-Z.

Santoso, Imam, Pekka Taskinen, Ari Jokilaakso, Min-Kyu Paek, and Daniel Lindberg. 2020a. "Phase Equilibria and Liquid Phase Behavior of the K2O-CaO-SiO2 System for Entrained Flow Biomass Gasification." *Fuel* 265 (April): 116894. https://doi.org/10.1016/j.fuel.2019.116894.

———. 2020b. "Phase Equilibria and Liquid Phase Behavior of the K2O-CaO-SiO2 System for Entrained Flow Biomass Gasification." *Fuel* 265 (April): 116894. https://doi.org/10.1016/j.fuel.2019.116894.

Saulov, D. 2007. "Application of the Modified Quasichemical Model to Solutions with Strong Short-Range Ordering." *Journal of Non-Crystalline Solids* 353 (30–31): 2845–51. https://doi.org/10.1016/j.jnoncrysol.2007.06.010.

Schmidmair, Daniela, Volker Kahlenberg, and Anja Grießer. 2018. "K2CaSi4O10: A Novel Phase in the Ternary System K2O–CaO–SiO2 and Member of the Litidionite Group of Crystal Structures." *Journal of the American Ceramic Society* 101 (2): 919–27. https://doi.org/10.1111/jace.15230.

Schmidmair, Daniela, Volker Kahlenberg, Alessandra Praxmarer, Lukas Perfler, and Philipp Mair. 2017. "Investigations on the Crystal-Structure and Non-Ambient Behaviour of K2Ca2Si8O19 - a New Potassium Calcium Silicate." *Journal of Solid State Chemistry* 253 (September): 336–46. https://doi.org/10.1016/j.jssc.2017.06.011.

Schmidt, Erik Ravn, Jens Christian Clausen, and Fritz Luxhøi. 1998. "Large-Scale Handling and Use of Solid Biofuels." In *Volume 3: Coal, Biomass and Alternative Fuels; Combustion and Fuels; Oil and Gas Applications; Cycle Innovations*, V003T05A021. Stockholm, Sweden: American Society of Mechanical Engineers. https://doi.org/10.1115/98-GT-327.

Schweinsberg, H., and F. Liebau. 1972. "Darstellung und kristallographische Daten von K2Si2O5, KHSi2O5I und K2Si4O9." *Zeitschrift für anorganische und allgemeine Chemie* 387 (2): 241–51. https://doi.org/10.1002/zaac.19723870211.

———. 1974. "Die Kristallstruktur des K4[Si8O19]: ein neuer Silikat-Schichttyp." *Acta Crystallographica Section B: Structural Crystallography and Crystal Chemistry* 30 (9): 2206–13. https://doi.org/10.1107/S0567740874006753.

Shi, Wenju, Jin Bai, Lingxue Kong, Xiaoming Li, Jingpei Cao, Zongqing Bai, and Wen Li. 2022. "The Investigation and Regulation of Fusion Characteristics of Coal Ash with High Sulfur and Basic Oxides Level for the Slagging Gasifier." *Fuel* 311 (March): 122574. https://doi.org/10.1016/j.fuel.2021.122574.

Sippula, Olli, Kati Hytönen, Jarkko Tissari, Taisto Raunemaa, and Jorma Jokiniemi. 2007. "Effect of Wood Fuel on the Emissions from a Top-Feed Pellet Stove." *Energy & Fuels* 21 (2): 1151–60. https://doi.org/10.1021/ef060286e.

Skrifvars, B.-J., M. Öhman, A. Nordin, and M. Hupa. 1999. "Predicting Bed Agglomeration Tendencies for Biomass Fuels Fired in FBC Boilers: A Comparison of Three Different Prediction Methods." *Energy and Fuels* 13 (2): 359–63. https://doi.org/10.1021/ef980045+.

Song, Li, Jianfang Wu, Zhen Li, Xiaofei Hao, and Yongsheng Yu. 2015. "Crystallization Mechanisms and Properties of α-Cordierite Glass–Ceramics from K2O–MgO–Al2O3–

SiO2 Glasses." *Journal of Non-Crystalline Solids* 419 (July): 16–26. https://doi.org/10.1016/j.jnoncrysol.2015.03.023.

Speight, James G. 2011. *An Introduction to Petroleum Technology, Economics, and Politics: Speight/An Introduction*. Hoboken, NJ, USA: John Wiley & Sons, Inc. https://doi.org/10.1002/9781118192528.

Strzalka, Rafal, Tobias Gabriel Erhart, and Ursula Eicker. 2013. "Analysis and Optimization of a Cogeneration System Based on Biomass Combustion." *Applied Thermal Engineering* 50 (2): 1418–26. https://doi.org/10.1016/j.applthermaleng.2011.12.039.

Stull, D. R., D. L. Hildenbrand, F. L. Oetting, and G. C. Sinke. 1970. "Low-Temperature Heat Capacities of 15 Inorganic Compounds." *Journal of Chemical & Engineering Data* 15 (1): 52–56. https://doi.org/10.1021/je60044a035.

Takahashi, Katsuaki, and T. Yoshio. 1970a. "Energy Relations in Alkali Silicates by Solution Calorimetry." https://doi.org/10.2109/JCERSJ1950.78.35.

———. 1973. "Thermodynamic Quantities of Alkali Silicates in the Temperature Range from 25°C to Melting Point." https://doi.org/10.2109/JCERSJ1950.81.940_524.

Takahashi, Katsuaki, and Tetsuo Yoshio. 1970b. "O-R Bond Energy in Alkali Silicates (R2O-SiO2)." *Ceramic Society Magazine*, 1970, 78.

Taylor, J. R., and A. T. Dinsdale. 1990. "Thermodynamic and Phase Diagram Data for the CaO-SiO2 System." *Calphad* 14 (1): 71–88. https://doi.org/10.1016/0364-5916(90)90041-W.

Teixeira, Paula, Helena Lopes, Ibrahim Gulyurtlu, Nuno Lapa, and Pedro Abelha. 2012. "Evaluation of Slagging and Fouling Tendency during Biomass Co-Firing with Coal in a Fluidized Bed." *Biomass and Bioenergy*, Biorefinery, 39 (April): 192–203. https://doi.org/10.1016/j.biombioe.2012.01.010.

The Bioenergy Association in New Zealand and Australia. 2019. "Woody Biomass - Fuel Drying, BANZ Information Sheet 12."

Thy, P., B.M. Jenkins, R.B. Williams, C.E. Lesher, and R.R. Bakker. 2010. "Bed Agglomeration in Fluidized Combustor Fueled by Wood and Rice Straw Blends." *Fuel Processing Technology* 91 (11): 1464–85. https://doi.org/10.1016/j.fuproc.2010.05.024.

Thy, Peter, Bryan M. Jenkins, Charles E. Lesher, and Sidsel Grundvig. 2006. "Compositional Constraints on Slag Formation and Potassium Volatilization from Rice Straw Blended Wood Fuel." *Fuel Processing Technology* 87 (5): 383–408. https://doi.org/10.1016/j.fuproc.2005.08.015.

Tripathi, Himanshu, Sumit Kumar Hira, Arepalli Sampath Kumar, Uttam Gupta, Partha Pratim Manna, and S.P. Singh. 2015. "Structural Characterization and in Vitro Bioactivity Assessment of SiO2–CaO–P2O5–K2O–Al2O3 Glass as Bioactive Ceramic Material." *Ceramics International* 41 (9): 11756–69. https://doi.org/10.1016/j.ceramint.2015.05.143.

Tsukada, Mayumi, Hajime Yamada, and Hidehiro Kamiya. 2003. "Analysis of Biomass Combustion Ash Behavior at Elevated Temperatures." *Advanced Powder Technology* 14 (6): 707–17. https://doi.org/10.1163/15685520360731990.

Ubando, Aristotle T., Charles B. Felix, and Wei-Hsin Chen. 2020. "Biorefineries in Circular Bioeconomy: A Comprehensive Review." *Bioresource Technology* 299 (March): 122585. https://doi.org/10.1016/j.biortech.2019.122585.

United States Environmental Protection Agency. 2014. "Particulate Matter Emission." file:///C:/Users/ea260260/Downloads/PM-emissions.pdf.

Vakkilainen, Esa K. 2021. "Industrial Applications of Steam Generated from Biomass." In *Reference Module in Earth Systems and Environmental Sciences*. Elsevier. https://doi.org/10.1016/B978-0-12-819727-1.00050-9.

Vassilev, Stanislav V., David Baxter, Lars K. Andersen, and Christina G. Vassileva. 2010. "An Overview of the Chemical Composition of Biomass." *Fuel* 89 (5): 913–33. https://doi.org/10.1016/j.fuel.2009.10.022.

Vassilev, Stanislav V., David Baxter, and Christina G. Vassileva. 2013. "An Overview of the Behaviour of Biomass during Combustion: Part I. Phase-Mineral Transformations of Organic and Inorganic Matter." *Fuel* 112 (October): 391–449. https://doi.org/10.1016/j.fuel.2013.05.043.

———. 2014. "An Overview of the Behaviour of Biomass during Combustion: Part II. Ash Fusion and Ash Formation Mechanisms of Biomass Types." *Fuel* 117 (January): 152–83. https://doi.org/10.1016/j.fuel.2013.09.024.

Vega-Nieva, D., C. Alvarez, and L. Ortiz. 2014. "Results of New Laboratory Methods and Slagging Classification Systems for the Prediction and Quantification of Ash Slagging in Woody and Herbaceous Biomass Fuels." In *Central European Biomass Conference*.

Visser, H. J. M., S. C. van Lith, and J. H. A. Kiel. 2008. "Biomass Ash-Bed Material Interactions Leading to Agglomeration in FBC." *Journal of Energy Resources Technology* 130 (1). https://doi.org/10.1115/1.2824247.

Wang, Chang'an, Lei Zhao, Ruijin Sun, Yueyi Hu, Guantao Tang, Wufeng Chen, Yongbo Du, and Defu Che. 2019. "Effects of Silicon-Aluminum Additives on Ash Mineralogy, Morphology, and Transformation of Sodium, Calcium, and Iron during Oxy-Fuel Combustion of Zhundong High-Alkali Coal." *International Journal of Greenhouse Gas Control* 91 (December): 102832. https://doi.org/10.1016/j.ijggc.2019.102832.

Wang, Liang, Johan E. Hustad, Øyvind Skreiberg, Geir Skjevrak, and Morten Grønli. 2012. "A Critical Review on Additives to Reduce Ash Related Operation Problems in Biomass Combustion Applications." *Energy Procedia* 20: 20–29. https://doi.org/10.1016/j.egypro.2012.03.004.

Wang, Liang, Øyvind Skreiberg, and Michael Becidan. 2014. "Investigation of Additives for Preventing Ash Fouling and Sintering during Barley Straw Combustion." *Applied Thermal Engineering*, PRES'13 Process Integration, 70 (2): 1262–69. https://doi.org/10.1016/j.applthermaleng.2014.05.075.

Wang, Qian, Kuihua Han, Peifu Wang, Shijie Li, and Mingyang Zhang. 2020. "Influence of Additive on Ash and Combustion Characteristics during Biomass Combustion under O2/CO2 Atmosphere." *Energy* 195 (March): 116987. https://doi.org/10.1016/j.energy.2020.116987.

Wang, Xuebin, Yiming Zhu, Zhongfa Hu, Lan Zhang, Shunzhi Yang, Renhui Ruan, Shengjie Bai, and Houzhang Tan. 2020. "Characteristics of Ash and Slag from Four Biomass-Fired Power Plants: Ash/Slag Ratio, Unburned Carbon, Leaching of Major and Trace Elements." *Energy Conversion and Management* 214 (June): 112897. https://doi.org/10.1016/j.enconman.2020.112897.

White, Jesse, Jaewoo Lee, Oscar Hessling, and Björn Glaser. 2016. "Reactions Between Liquid CaO-SiO2 Slags and Graphite Substrates." *Metallurgical and Materials Transactions B*, September. https://doi.org/10.1007/s11663-016-0788-5.

Wiinikka, Henrik, Rikard Gebart, Christoffer Boman, Dan Boström, and Marcus Öhman. 2007. "Influence of Fuel Ash Composition on High Temperature Aerosol Formation in Fixed Bed Combustion of Woody Biomass Pellets." *Fuel* 86 (1): 181–93. https://doi.org/10.1016/j.fuel.2006.07.001.

Wu, Ping, Gunnar Eriksson, and Arthur D. Pelton. 1993. "Optimization of the Thermodynamic Properties and Phase Diagrams of the Na2O–SiO2 and K2O–SiO2 Systems." *Journal of the American Ceramic Society* 76 (8): 2059–64. https://doi.org/10.1111/j.1151-2916.1993.tb08333.x.

Xiaoping, Ren, Liu Fang, Tang Xintong, Sun Xiaoting, Yang jing, and Yang song. 2020. "Study on the Slagging of Biomass Briquette Combustion." Edited by W. Qin, L. Wang, and V. Yepes. *E3S Web of Conferences* 165: 03035. https://doi.org/10.1051/e3sconf/202016503035.

Yao, Xiwen, Zhicheng Zhao, Shoukun Chen, Haodong Zhou, and Kaili Xu. 2020. "Migration and Transformation Behaviours of Ash Residues from a Typical Fixed-Bed Gasification Station for Biomass Syngas Production in China." *Energy* 201 (June): 117646. https://doi.org/10.1016/j.energy.2020.117646.

Yao, Xiwen, Haodong Zhou, Kaili Xu, Qingwei Xu, and Li Li. 2019. "Evaluation of the Fusion and Agglomeration Properties of Ashes from Combustion of Biomass, Coal and Their Mixtures and the Effects of K2CO3 Additives." *Fuel* 255 (November): 115829. https://doi.org/10.1016/j.fuel.2019.115829.

———. 2020. "Investigation on the Fusion Characterization and Melting Kinetics of Ashes from Co-Firing of Anthracite and Pine Sawdust." *Renewable Energy* 145 (January): 835–46. https://doi.org/10.1016/j.renene.2019.06.087.

Yatkin, Sinan, and Abdurrahman Bayram. 2007. "Elemental Composition and Sources of Particulate Matter in the Ambient Air of a Metropolitan City." *Atmospheric Research* 85 (1): 126–39. https://doi.org/10.1016/j.atmosres.2006.12.002.

Yazhenskikh, Elena, Klaus Hack, and Michael Müller. 2006. "Critical Thermodynamic Evaluation of Oxide Systems Relevant to Fuel Ashes and Slags. Part 1: Alkali Oxide–Silica Systems." *Calphad* 30 (3): 270–76. https://doi.org/10.1016/j.calphad.2006.03.003.

Zapata, S., M. Gómez, C. Bartolomé, P. Canalís, and J. Royo. 2022. "Ash Behaviour during Combustion of Agropellets Produced by an Agro-Industry—Part 1: Blends Design and Experimental Tests Results." *Energies* 15 (4). https://doi.org/10.3390/en15041479.

Zeng, T., A. Pollex, N. Weller, V. Lenz, and M. Nelles. 2018. "Blended Biomass Pellets as Fuel for Small Scale Combustion Appliances: Effect of Blending on Slag Formation in the Bottom Ash and Pre-Evaluation Options." *Fuel* 212 (January): 108–16. https://doi.org/10.1016/j.fuel.2017.10.036.

Zeng, T., N. Weller, A. Pollex, and V. Lenz. 2016. "Blended Biomass Pellets as Fuel for Small Scale Combustion Appliances: Influence on Gaseous and Total Particulate Matter Emissions and Applicability of Fuel Indices." *Fuel* 184 (November): 689–700. https://doi.org/10.1016/j.fuel.2016.07.047.

Zevenhoven-Onderwater, Maria, Rainer Backman, Bengt-Johan Skrifvars, and Mikko Hupa. 2001. "The Ash Chemistry in Fluidised Bed Gasification of Biomass Fuels. Part I: Predicting the Chemistry of Melting Ashes and Ash–Bed Material Interaction." *Fuel* 80 (10): 1489–1502. https://doi.org/10.1016/S0016-2361(01)00026-6.

Zhai, Ming, Xuesong Li, Di Yang, Zhaoyang Ma, and Peng Dong. 2022. "Ash Fusion Characteristics of Biomass Pellets during Combustion." *Journal of Cleaner Production* 336 (February): 130361. https://doi.org/10.1016/j.jclepro.2022.130361.

Zhang, Jiajun, and Xiaolei Zhang. 2019. "15 - The Thermochemical Conversion of Biomass into Biofuels." In *Biomass, Biopolymer-Based Materials, and Bioenergy*, edited by Deepak Verma, Elena Fortunati, Siddharth Jain, and Xiaolei Zhang, 327–68. Woodhead Publishing Series in Composites Science and Engineering. Woodhead Publishing. https://doi.org/10.1016/B978-0-08-102426-3.00015-1.

Zhang, Ligang, Clemens Schmetterer, and Patrick J. Masset. 2013. "Thermodynamic Description of the M2O–SiO2 (M=K, Na) Systems." *Computational Materials Science*, Multiscale simulation of heterogeneous materials and coupling of thermodynamic models, 66 (January): 20–27. https://doi.org/10.1016/j.commatsci.2012.04.040.

Zhao, Peitao, Yafei Shen, Shifu Ge, Zhenqian Chen, and Kunio Yoshikawa. 2014. "Clean Solid Biofuel Production from High Moisture Content Waste Biomass Employing Hydrothermal Treatment." *Applied Energy* 131 (October): 345–67. https://doi.org/10.1016/j.apenergy.2014.06.038.

Zhou, Chunguang, Christer Rosén, and Klas Engvall. 2016. "Biomass Oxygen/Steam Gasification in a Pressurized Bubbling Fluidized Bed: Agglomeration Behavior." *Applied Energy* 172 (June): 230–50. https://doi.org/10.1016/j.apenergy.2016.03.106.

Zhu, Yiming, Houzhang Tan, Yanqing Niu, and Xuebin Wang. 2019. "Experimental Study on Ash Fusion Characteristics and Slagging Potential Using Simulated Biomass Ashes." *Journal of the Energy Institute* 92 (6): 1889–96. https://doi.org/10.1016/j.joei.2018.11.005.

2. Chapter 2. Materials and methods

This chapter presents the various raw materials used in this work, such as biomass feedstock, biomass ash, and pure compounds. In addition, it shows the experimental procedures and setups used to conduct the necessary experiments on the biomass and their ash at various scales and those applied to synthesize the pure ternary compounds of interest. The analysis instruments and methods were also discussed in detail. Furthermore, this chapter discusses the thermodynamic calculation and simulation approaches and presents the tools (software, databases, inputs, etc.) used.

1. Biomass Feedstock

1.1.Biomass origin

Oak bark, wheat straw, and two mixtures were received in the form of compressed pellets (1.5cm (L) x 0.5cm (D) on average) (Figure 2.1). Three different barks and three different wheat straw sources were used:

- Two oak barks (BC and BF) sawmill residues from the Southwest of France and a hardwood bark (BI) residue from northern Italian logs preparation in the wood industry.
- Two wheat straws (WC and WF) from the Southwest of France and a wheat straw (WI) from northern Italy.

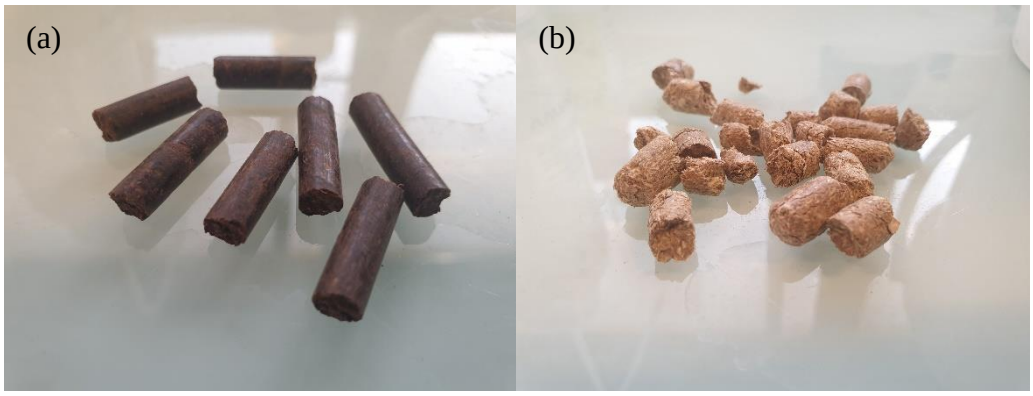

Figure 2.1: Oak barks (BC, BF, and BI) (a) and wheat straws (WC, WF, and WI) (b) as received as biomass pellets.

1.2.Blend preparation

BXWY referred to blends formed by the oak bark X and the wheat straw Y, shown in section 1.1. The blends were formed with various bark weight fractions in the biomass blend, denoted by α, as shown in Table 2.2.

RAGT Energie company, Alby, France supplied, milled, and prepared the biomasses used to prepare the pelletized blends BCWC. The detailed method was explained in Defoort et al. (Defoort et al. 2019). For instance, a Toy hammer mill with two grids of 1 mm and 4 mm was used to mill the biomasses. After blending the two biomasses with the specific bark weight fraction in the biomass blend (α), a Kahl pelletizing press was used to form the pellets. The pellets' density and durability were regulated according to the NF 17 225-6 standard. A compression ratio (ratio of the length of the compression channel of the die to the diameter of the die hole) of 4.5 was also applied. BFWF was prepared in the work of Valin et al. (Valin et al. 2020) with the same procedure in Defoort et al. (Defoort et al. 2019).

The other mixtures were formed according to the procedure below. Single biomass pellets were ground in a Fisher Bioblock Scientific Retsch steel grinder below 1 mm. After drying the

biomass powder at 105 °C for 24h, bark-straw mixtures of 10 g each were put in a plastic bottle and mixed in a "turbula" mixer (Willy A. Bschofen AG Maschinenfabrik CH-4005 Basel/Schweiz mixer) at around 20 rpm, with various bark weight fractions (α) (Table 2.2). The bark weight fraction (α) of each biomass mixture (Table 2.2) was varied in a way to cover a large part of the CaO-K_2O-SiO_2 phase diagram.

Afterward, each biomass pellet and their ground mixtures were ashed at 550°C for 2h in natural air. This step at 550 °C removed all the organic oxygen and hydrogen (along with organic nitrogen and part of chlorine), while preserving the majority of the other elements. Then 0.5 g of ash of each mixture and single biomasses were compressed as ash chips (1.3 cm diameter) under a pressure of 10 bar to favor the contact between the inorganic ash particles.

Note that the bark biomass weight fraction (α) in the biomass bark-straw mixture is linked to the bark ash weight fraction (β) in the ash bark-straw mixture, taking into account the ash yield of every single biomass (noted A_1 for bark and A_2 for straw) and is:

$$\beta = \alpha A_1/(\alpha A_1 + (1-\alpha)A_2) \quad (1)$$

For instance, a BCWC biomass mixture of 50% biomass bark weight percentage corresponds to an ash mixture of 59% ash bark weight percentage in the mixture.

1.3.Elemental composition

The elemental composition of every single biomass ash (Table 2.1) and ash mixture (Table 2.2) was measured by SOCOR laboratory. An Elementar Vario EL cube CHN analyzer measured the C, H, and N contents. C (std ±1%), H (std ±2%), and N (std ±15%) contents were measured according to the NF EN 15104 norm. In addition, an inductively coupled plasma atomic emission spectroscopy (ICP−AES) was used to measure the inorganic contents. Si contents were measured by the ICP using a corresponding internal method (std = ±5%). Ca, K, P, Al, Mg, Fe, Na, and Mn amounts were measured according to the NF EN ISO 16967 norm (std = ±5%). Furthermore, the amounts of S and Cl were evaluated in an ion chromatography after combusting the samples in a bomb calorimeter, according to the EN 15289 norm (std = ±15%).

Afterward, the measured results on biomass were converted to weight percentages in ash by taking the ash contents of each biomass in consideration.

Then, the weight percentage of each oxide in each biomass or mixture was calculated as follows:

$$O_i = \frac{E_i \times \frac{TO_i}{EO_i}}{Ash} \times 100 \quad (2)$$

Where O_i is the percentage oxides of element i in the specific feedstock.

E_i is the weight percentage (wt.%) of the inorganic element measured by the ICP-AES.

TO_i is the molecular weight (g/mol) of the oxide i.

EO_i is the molecular weight (g/mol) of element i.

Ash is the ash contents (wt.%) of the feedstock (for the case of the mixtures of ash, Ash is 1).

The measured elemental composition is shown in Table 2.1 (for single biomass) and Table 2.2 (for biomass ash mixtures) along with their calculated results in oxides. The normalized wt.% of SiO_2, CaO, and K_2O were also reported in Tables 2.1 and 2.2 for each single biomass and each biomass ash mixture, respectively. It should be noted that in the case of biomass, the total carbon and sulfur (organic + inorganic) was reported first, followed by the inorganic carbon and inorganic sulfur (C (ash550 °C) & S (ash550 °C)) in the ash, in Table 2.1.

Table 2.1: Biomass measured and calculated oxide composition on a dry ash basis along with their SiO_2, CaO, and K_2O weight percentages.

		WC	WF	WI	BC	BF	BI
C (total)	*wt.%*	43.6	46.67	48.42	48.6	49.23	46.1
H	*wt.%*	5.5	5.31	5.72	5.8	4.45	6
O (calc.)	*wt.%*	44.3	38.4	41.2	36.6	34.2	38.8
N	*wt.%*	0.54	0.72	0.49	0.6	0.48	0.75
S (total)	*wt.%*	0.094	0.1	0.07	0.0378	0.003	0.059
Cl	*wt.%*	0.141	0.329	0.113	0.007	0.005	0.008
Ash 550 °C	*wt.%*	5.8	8.47	3.98	8.4	11.68	8.3
Si	*mg/kg db*	9915	21472	7371	4787	12090	7215
Ca	*mg/kg db*	2926	3418	2756	25588	29517	20834
K	*mg/kg db*	14307	17103	9976	2611	2806	6505
P	*mg/kg db*	673	1029	666	319	267	715
Al	*mg/kg db*	44	91	244	734	1651	913
Mg	*mg/kg db*	461	930	543	722	624	1566
Fe	*mg/kg db*	82	108	224	346	1208	753
Na	*mg/kg db*	206	140	183	116	277	462
Mn	*mg/kg db*	49	60	47	689	399	33
S (ash550 °C)	*g/100g ash*	0.94	1.404	1.76	0.378	0.088	0.38
C (ash550 °C)	*g/100g ash*	4.36	1.2	0.9	4.86	6.1	6.4
CO_2	*wt.%*	15.987	4.400	3.300	17.820	22.367	23.467
SO_3	*wt.%*	2.346	3.503	4.380	0.943	0.220	0.941
SiO_2	*wt.%*	36.632	54.324	39.685	12.212	22.181	18.627
CaO	*wt.%*	7.058	5.646	9.686	42.616	35.355	35.116
K_2O	*wt.%*	29.714	24.324	30.195	3.744	2.894	9.440
P_2O_5	*wt.%*	2.658	2.782	3.831	0.870	0.524	1.974
Al_2O_3	*wt.%*	0.143	0.202	1.157	1.651	2.670	2.077
MgO	*wt.%*	1.318	1.821	2.262	1.425	0.886	3.130
Fe_2O_3	*wt.%*	0.202	0.182	0.805	0.589	1.479	1.297
Na_2O	*wt.%*	0.479	0.223	0.620	0.186	0.320	0.750
MnO_2	*wt.%*	0.134	0.111	0.186	1.298	0.541	0.063
Oxides wt.% on the basis of SiO_2, CaO, and K_2O							
SiO_2		49.9%	64.4%	49.9%	20.8%	36.7%	29.5%
CaO		9.6%	6.7%	12.2%	72.8%	58.5%	55.6%
K_2O		40.5%	28.9%	37.9%	6.4%	4.8%	14.9%

Table 2.2 : Ash mixtures measured and calculated oxide composition on a dry ash basis along with their SiO_2, CaO, and K_2O weight percentages.

α = Bark weight fraction in the biomass mixture and β = Bark weight fraction in the ash mixture

	BCWC	BCWI	BCWF	BIWC	BIWI	BFWC	BFWI	BFWF
(α)	0.50	0.31	0.56	0.62	0.55	0.35	0.24	0.50
(β)	0.59	0.49	0.56	0.69	0.72	0.52	0.48	0.58
				All elements in wt.%				
C	6.30	5.20	5.50	5.00	4.60	4.40	4.00	4.90
O	45.75	46.24	48.75	47.95	46.79	48.62	50.34	47.19
S	0.79	0.76	0.64	0.56	0.65	0.80	Not measured	0.56
Cl	0.56	0.36	0.45	0.34	0.26	0.61	Not measured	0.29
Si	11.62	11.10	13.40	14.30	13.40	13.50	14.00	16.00
Ca	20.95	20.49	18.83	13.47	15.90	14.69	15.37	17.37
K	11.00	12.27	9.38	13.15	12.44	14.21	12.34	10.18
P	0.55	0.73	0.46	0.83	1.04	0.66	0.75	0.52
Al	0.82	0.75	0.80	1.59	1.69	0.85	1.05	1.16
Mg	0.71	1.04	0.72	1.44	1.66	0.68	0.95	0.76
Fe	0.45	0.59	0.67	0.78	0.89	0.53	0.73	0.70
Na	0.26	0.22	0.16	0.54	0.61	0.27	0.25	0.16
Mn	0.26	0.25	0.23	0.06	0.07	0.19	0.22	0.21
Ash 550 °C	7.10	5.37	8.43	7.34	6.36	7.87	5.84	10.08
				Oxides wt.%				
CO2	23.1%	19.1%	20.2%	18.3%	16.9%	16.1%	14.7%	18.0%
SO3	2.0%	1.9%	1.6%	1.4%	1.6%	2.0%	0.0%	1.4%
SiO2	24.9%	23.8%	28.7%	30.6%	28.7%	28.9%	30.0%	34.3%
CaO	29.3%	28.7%	26.3%	18.8%	22.2%	20.5%	21.5%	24.3%
K2O	13.2%	14.8%	11.3%	15.8%	15.0%	17.1%	14.9%	12.3%
P2O5	1.3%	1.7%	1.1%	1.9%	2.4%	1.5%	1.7%	1.2%
Al2O3	1.5%	1.4%	1.5%	3.0%	3.2%	1.6%	2.0%	2.2%
MgO	1.2%	1.7%	1.2%	2.4%	2.8%	1.1%	1.6%	1.3%
Fe2O3	0.6%	0.9%	1.0%	1.1%	1.3%	0.8%	1.1%	1.0%
Na2O	0.3%	0.3%	0.2%	0.7%	0.8%	0.4%	0.3%	0.2%
MnO2	0.4%	0.4%	0.4%	0.1%	0.1%	0.3%	0.4%	0.3%
				Oxides wt.% on the basis of SiO2, CaO, and K2O				
SiO2	36.9%	35.4%	43.3%	46.9%	43.5%	43.4%	45.2%	48.4%
CaO	43.4%	42.6%	39.7%	28.8%	33.7%	30.9%	32.4%	34.3%
K2O	19.6%	22.0%	17.0%	24.2%	22.7%	25.7%	22.4%	17.3%

2. Ternary oxides synthesis materials and reaction pathways

$CaCO_3$ (Alfa Aesar, 99.95%), K_2CO_3 (Alfa Aesar, 99%), and SiO_2 (C600 Sibelco, 99.7%) were used in the synthesis. Before formulating the mixture, several steps were done to prepare the reactants. $CaCO_3$ was calcined at 1000 °C for 1h in the air to produce CaO (to get rid of all the possible weight loss prior to equilibration that can come from the CO_2 loss in $CaCO_3$). K_2CO_3 was dried at 350 °C for 1h under a primary vacuum. SiO_2 was dried at 500 °C for 1h in air. The main objective was to remove any water traces since the products are highly hygroscopic. For instance, they contained K that reacts fast with water to produce the stable KOH(g) (Arroyabe et al. 2011).

Three hypothetical reaction pathways were applied as follows, one for each crystalline phase:

$$\mathbf{K_2CO_3 + 2SiO_2 + 2CaO \rightarrow \boldsymbol{K_2Ca_2Si_2O_7} + CO_2} \quad \textbf{(A)}$$

$$\mathbf{2K_2CO_3 + 3SiO_2 + CaO \rightarrow \boldsymbol{K_4CaSi_3O_9} + 2CO_2} \quad \textbf{(B)}$$

$$\mathbf{K_2CO_3 + 4SiO_2 + 6CaO \rightarrow \boldsymbol{K_2Ca_6Si_4O_{15}} + CO_2} \quad \textbf{(C)}$$

The mass of the reactants in the CaO, K_2CO_3, and SiO_2 mixtures, which were to be annealed, were manually mixed in an agate mortar, initially following the stoichiometric ratios listed above in a way to obtain pure ternary phases. The preparation of all the samples for annealing was conducted in a glove box. Then, 0.5 g of the mixed reactants were manually compressed as chips (~ 1 cm diameter) to favor the contact between the inorganic particles.

The total weight loss was measured by the simple mass balance on the samples between the beginning and the end of the annealing experiment. Since CaO was used instead of $CaCO_3$ (CaO calcined from $CaCO_3$), the measured total weight loss contained only the CO_2 and K volatilization from just K_2CO_3. After calculating the theoretical CO_2 loss from reactions A, B, and C using stoichiometric ratios, the rest of the measured total weight loss is K loss. Consequently, once the optimum synthesis conditions (temperature and time) for each compound were found, the last synthesis was repeated after adding the necessary amounts of K_2CO_3 to compensate for the measured/calculated K loss.

3. Experimental setups

In this section, all the experimental setups used in this work will be described in detail. First, section 3.1 will present the one used for biomass samples and their ash. Then, section 3.2 will describe the one used to synthesize the ternary oxide phases of interest.

3.1.Setups for Biomass and their ash

Several experimental tests were applied on various biomass and biomass ash samples at different temperatures and reaction times. The first two tests (ash test (A) and pellet test (P)) were on a laboratory scale and were adapted from the work of Defoort et al. (Defoort et al. 2019) (sections 3.1.1 and 3.1.2). They were conducted in laboratory scale furnaces in the CEA laboratory. The various sets of temperatures and residence times applied in these two laboratory setups were presented in section 3.1.3. In addition, two combustion pilot reactors, a fixed bed, and a moving bed, were used (section 3.1.4). The experiments were done at RAGT Company in Albi, France. Furthermore, experiments were conducted in a pilot fluidized bed reactor in combustion and gasification modes on the platform of CEA Grenoble (section 3.1.5). It should be noted that no duplicates were conducted for any of the pilot experiments.

3.1.1. Laboratory ash test setup

The laboratory conditions of the ash test (A) favor the chemical equilibrium (strong proximity of ash grains). In this test, the biomass pellets (1.5cm x 0.5cm) of the various single biomasses and their mixtures (Tables 2.1 and 2.2) were heated at 550℃ for 2h in static atmospheric conditions (in air) in a Nabertherm LT 15/11/330 furnace (26 cm width, 16 cm height, and 40 cm depth) (Figure 2.2) then cooled down to room temperature. This step at 550 °C helped eliminate all organic carbon and hydrogen (along with organic nitrogen and part of chlorine) while preserving the majority of the other elements. Afterwards, 0.5 g of ash were compressed as ash chips (1.3 cm diameter) under a pressure of 10 bar to favor the contact between the inorganic particles. The compressed ash chip was put in a 95-5 wt.% Pt-Au crucible – this material was selected to avoid any interaction between the sample and the crucible - and was heated in a vertical Nabertherm RT 50-250/13 furnace (Figure 2.3) in static atmospheric conditions at a heating rate of 10 °C/min until the setpoint temperature was reached. Residence time in Table 2.3 started to be counted when the final temperature was reached. At the end of each experiment, samples were quenched in air [i.e. ~5 °C /s] until room temperature.

Figure 2.2: Nabertherm LT 15/11/330 furnace.

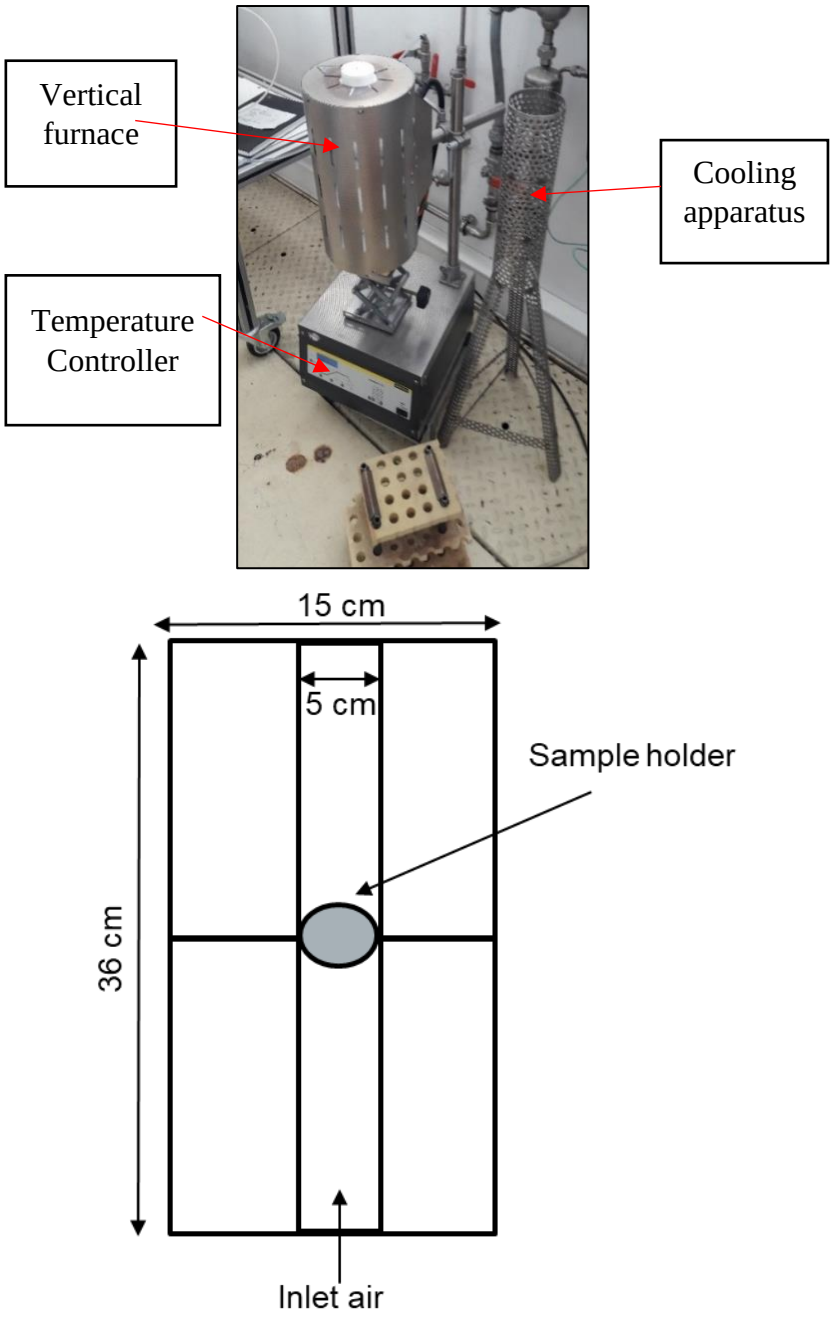

Figure 2.3 : Nabertherm RT 50-250/13 furnace and ash test annealing apparatus.

3.1.2. Laboratory pellet test setup

Biomass pellets are usually used in the pilot and industrial-scale reactors. Hence, the laboratory pellet test conditions simulate the conditions in a pilot reactor (low proximity of ash grains dispersed in the biomass matrix).In the Pellet test (P), biomass pellets (1.5cm x 0.5cm) of BC, WC, and their mixture BCWC were heated directly in a Nabertherm LT 15/11/330 furnace (Figure 2.2) in static atmospheric conditions at a heating rate of 10°C/min until the setpoint temperature was reached. Alumina crucibles were used in this test (10 cm in length, 2 cm in width, and 2 cm in height) (Figure 2.4). Residence time started to be counted when the setpoint

temperature was reached. At the end of each experiment, samples were quenched in air [i.e. ~5 °C /s] until room temperature. The furnace for the pellet test could not reach 1200 °C (maximum operating temperature of 1000 °C).

Figure 2.4: Alumina crucible (10 cm length, 2 cum width, and 2 cm height) used in the pellet test.

3.1.3. Laboratory tests operating conditions variation

Temperature and residence time was varied in each laboratory test, as indicated in Table 2.3. In addition, the cooling rate (slow cooling [i.e. ~0.05 °C/s] versus quenched cooling [i.e. ~5 °C/s]) was varied for just the ash test at 1000 °C and 6h, while quenching was applied in all the other experiments. Each test was performed in duplicate.

Table 2.3: Temperature and residence time at final temperature in the ash (A) and pellet (P) tests.

	20 min	1 h	2 h	3 h	4 h	5 h	6 h	24 h	40 h	64 h
850 °C	P	P					A	A		A
1000 °C	A & P	A & P		A	A	A	A & P		A	
1200 °C	A	A	A	A			A			

3.1.4. Pilot combustion burners setups

In the Pilot test (Pilot), 5 kg/h of biomass pellets (1.5cm x 0.5cm) were combusted in a 25 kW Multiheat 2.5 fixed bed furnace for 2h (Figure 2.5). Three thermocouples were inserted in the furnace of the fixed bed reactor to measure the temperature during the test (Figure 2.6). In addition, 10 kg/h of the biomass pellets were combusted in a 30 kW Guntamatic Powercom moving bed boiler for 5h (Figure 2.7). The two pilot reactors applied the same compressed biomass pellets of the BCWC mixture used in the pellet test. However, individual straw (WC) and bark (BC) biomass pellets were only used in the fixed bed boiler.

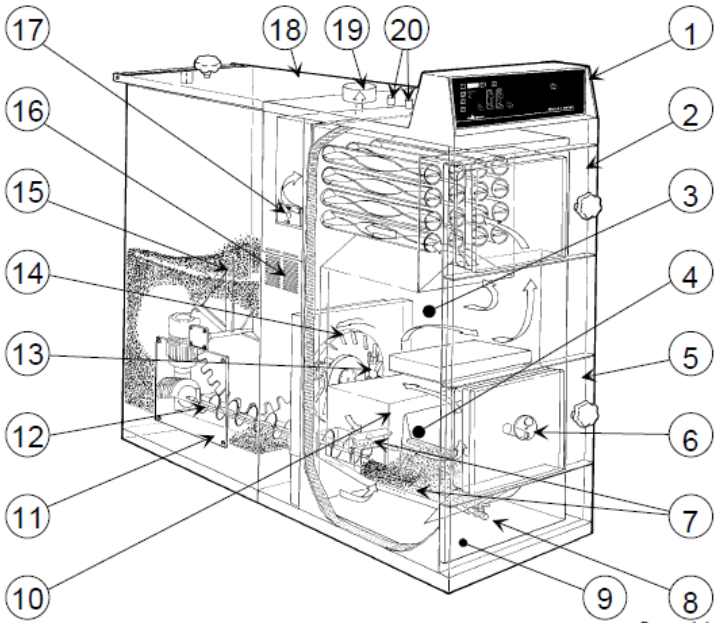

1. Boiler panel 2. Upper ash door
3. Combustion chamber, upper part
4. Combustion tunnel 5. Lower ash door
6. Combustion control peephole
7. Combustion air openings
8. Boiler drain valve 9. Bleeding the air channels
10. Refractory tunnel (heart of combustion)
11. Magazine inspection hatch (right and left side)
12. Fuel screw 13. Hydraulic flame arrester
14. Fan 15. Mixing arms
16. Combustion air inlets (right and left side)
17. Ash trap (right and left side)
18. Magazine filler door 19. Smoke nozzle
20. Boiler flow and return

Figure 2.5: Fixed bed combustion reactor (25 kW Multiheat 2.5) (HS TARM 2005).

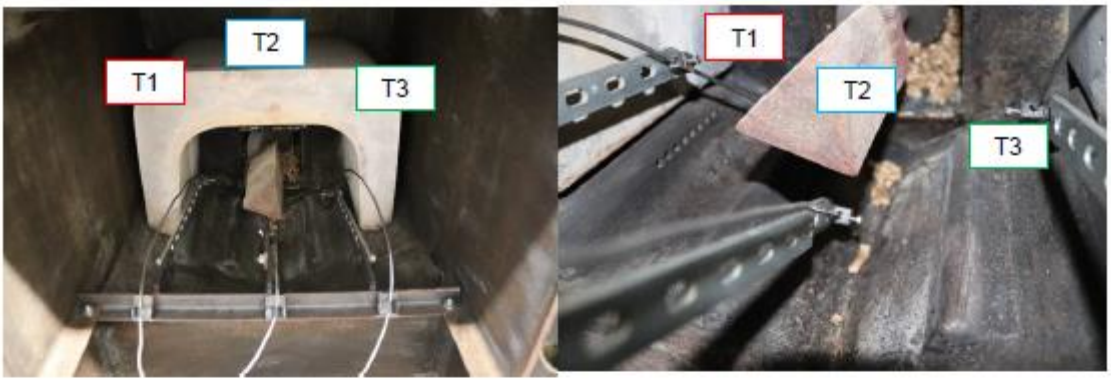

Reactor Chamber width is 23 cm and depth is 40 cm.

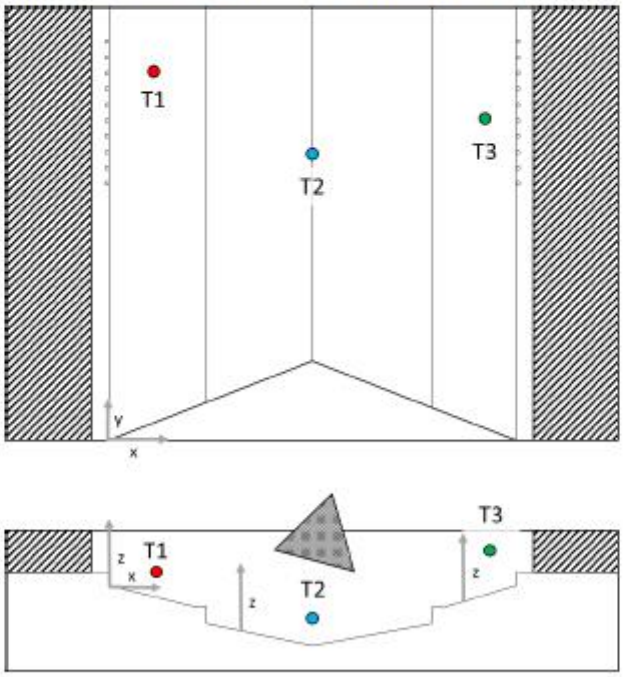

Thermocouples coordinates inside the reactor chamber:

T1 : x = 4cm	**; y = 35cm**	**; z = 2,5cm**
T2 : x = 11,5cm	**; y = 28cm**	**; z = 1cm**
T3 : x = 17cm	**; y = 37cm**	**; z = 1,5cm**

Figure 2.6: Thermocouple position inside the reactor chamber of the fixed bed reactor.

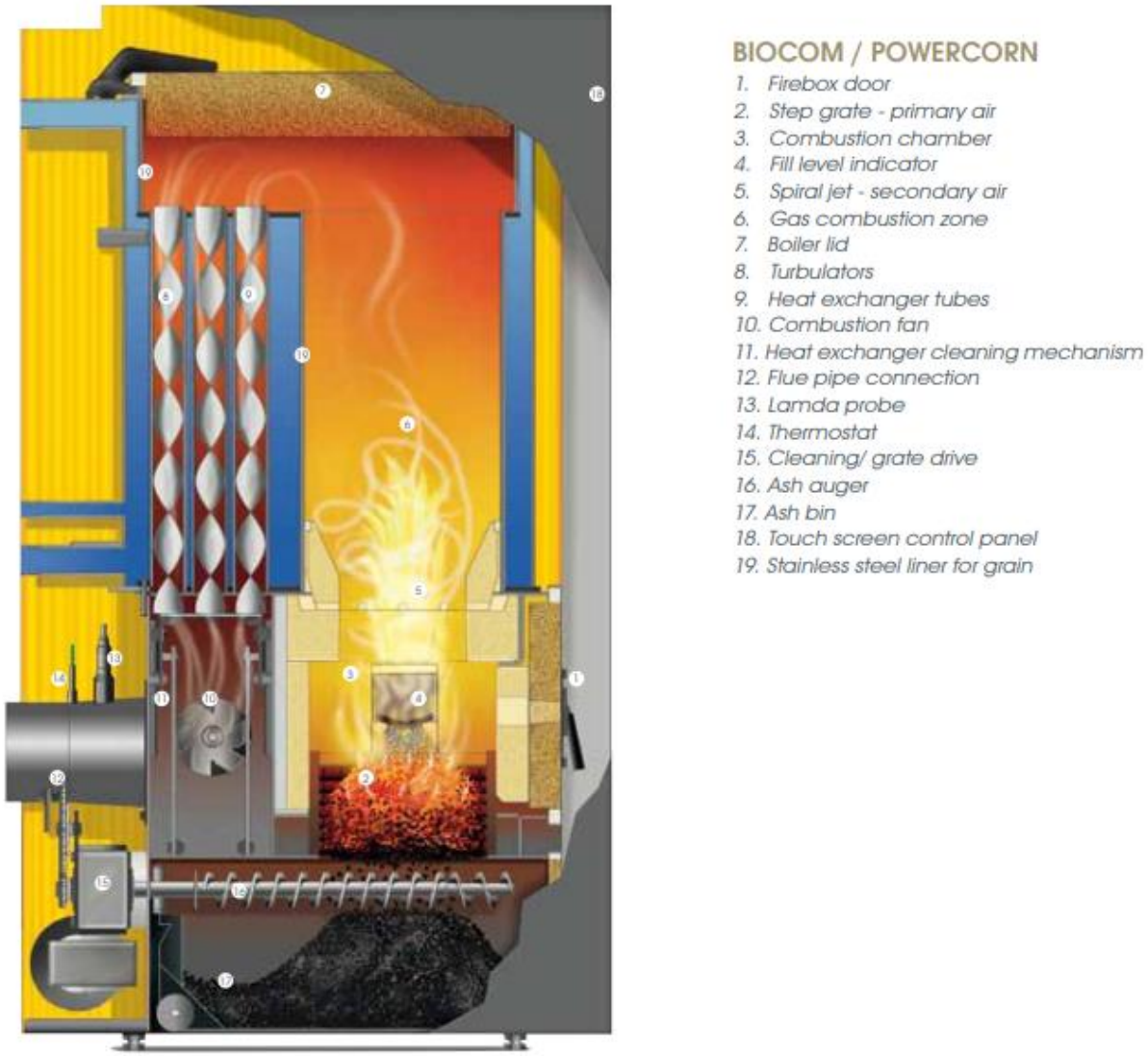

Figure 2.7: Moving bed pilot reactor (30 kW Guntamatic Powercom) (Guntamatic, n.d.).

3.1.5. Pilot fluidized bed setup

The fluidized bed setup is explained in detail in the work of Valin et al. (Valin et al. 2020; 2010).

According to Figure 2.8, the vertical fluidized bed was formed of an external vessel (57 cm internal diameter and 435 cm height), an internal reactor in the lower part (12.4 cm internal diameter and 95 cm height), and an internal disengagement zone (20 cm internal diameter and 154 cm height). Three thermocouples were introduced in the lower reactor part at 5 cm, 10 cm, and 15 cm altitude, respectively (Figure 2.8.b), from the gas distributor. The reactor could withstand a maximum pressure of 40 bar due to the external stainless steel vessel surrounding the reactor chamber and the screw.

The reactor and the feeding screw were heated by 9 and 2 electric resistance heaters, respectively. Its maximum temperature was 1000 °C. It was cooled by hot and pressurized water, flowing in a coiled tube welded to its outer surface. A plate with 12 nozzles and 4 holes (1 mm diameter each) was used as a gas distributor. A nickel-based alloy Hastelloy® X (Haynes International) high-temperature filters were used to remove 99.9% of the particulate matter below 0.5 µm in the output gas. A cyclone was added to help remove the remaining particulates from the output gas. Three heat exchangers (15 °C, 0 °C, and -20 °C) were used to cool down the exit gas from around 600 °C to the exit temperature. The cooled gas was directed to a micro gas chromatograph (µGC) coupled with a thermal conductivity detector (TCD) for analysis.

6 kg of BCWC biomass mixture was introduced into a bunker and fed to the reactor chamber through a horizontal feeding screw at a rotation velocity of 70 rpm and a feeding rate of 4 kg/h. Before each test, 5 kg of fresh olivine, coming from Austria, were poured into the reactor as bed materials. Its particle size was between 200 and 500 µm. Argon was injected in the bunker and along the conveying screw to avoid syngas flow back. A mixture of steam and N_2 was used in the biomass gasification mode. Then, the remaining char from the gasification run were recovered, sieved, weighted, and a minor quantity was kept for analysis. Then, the majority of the char was refed to the same reactor but in a combustion mode, under a flow of a mixture of air and N_2. The coupled two runs (gasification then combustion) could depict a dual fluidized bed operation.

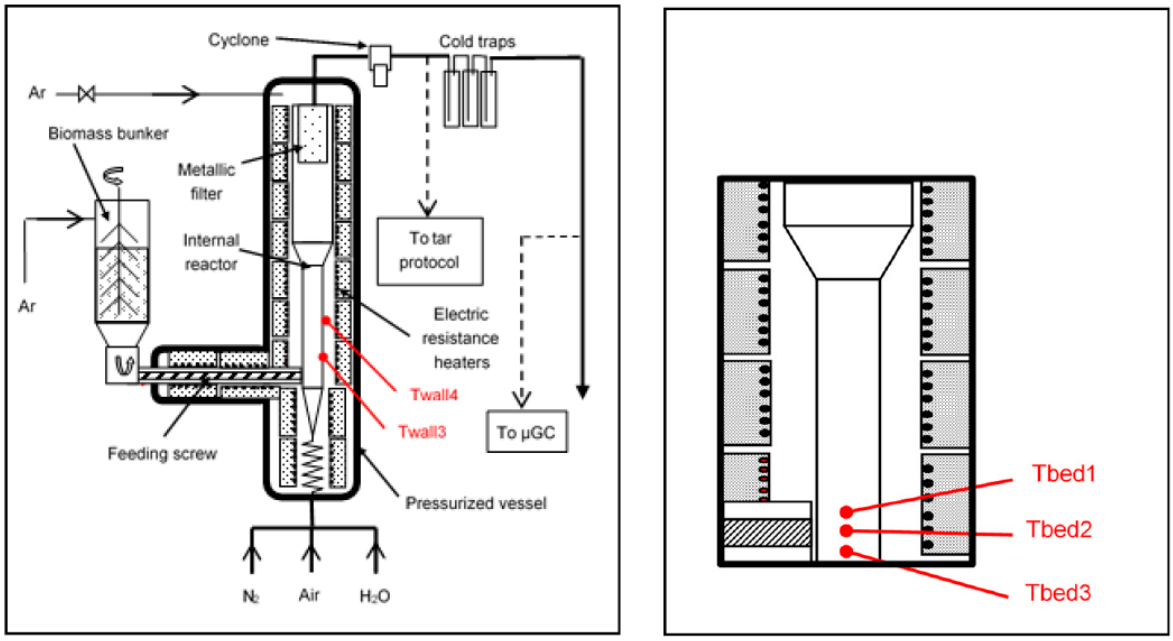

Figure 2.8: Fluidized bed setup (a) along with a representation of its reaction chamber (b) (Valin et al. 2020; 2010).

3.2.Set up for the ternary phases synthesis

All the syntheses were done at SIMaP laboratory in a Nabertherm GmbH R 50/250/12 furnace with a quartz tube inserted inside (Figure 2.9). Samples were first manually compressed, put in Pt or Au-Pd (20-80) crucible, covered with a lid, and then inserted into the quartz tube. Samples were slid in the tube until reaching the middle of the reactor chamber using a metallic graduated stick. Afterward, the quartz tube was closed and well-sealed on both ends using a metallic joint constantly flushed inside with cold water. The tube was flushed with Argon as carrier gas with a flow rate of 25 mL/h. Various set-point temperatures and residence times were applied depending on the aimed product. However, a temperature ramp of 10 °C/min for heating up was always used. At the end of the annealing experiments, samples were left inside the quartz tube under a constant flow of argon to cool down to room temperature.

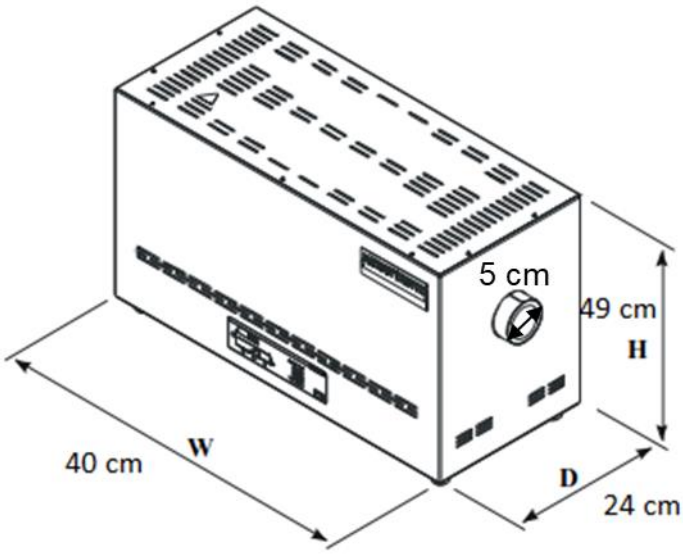

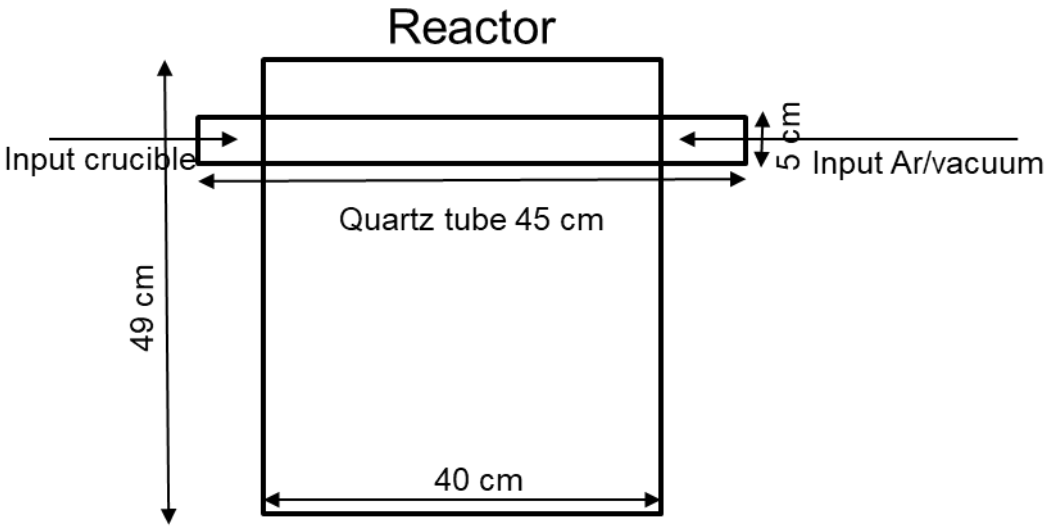

Figure 2.9 : Nabertherm GmbH R 50/250/12 synthesis setup at SIMaP laboratory [the Alumina crucible is 10 cm length, 2 cum width, and 2 cm height)].

4. Analyses instruments and methods

4.1.P-XRD analysis

Bruker D8 Advance Powder X-Ray diffraction (P-XRD) with Cu Kα (40 kV and 30 mA) was used in CEA Grenoble to qualitatively and quantitatively analyze the various solid phases present in the samples along with the amorphous content. Samples were manually ground in an agate mortar. They were placed in an amorphous silica sample holder and then flattened with glass to obtain a well-defined surface. Diffractograms were obtained over a 2θ interval between 15° and 70°.

The identification and semi-quantification of the crystalline phases were first performed using Bruker EVA software and its I/Icor module, as used in Defoort et al. (Defoort et al. 2019). Another robust software, Highscore Plus, was used to search and match the crystal compounds in the sample and sort them out according to their higher occurrence percentage. Moreover, this software is more vigorous than EVA since once a compound is added to the fixed list, the probable compounds left are re-ranked in the order of higher probability of occurrence. In addition, full XRD quantification was conducted in this work by applying the Rietveld refinement method, using Highscore Plus. Furthermore, the quantification of the amorphous phase present in the sample was also performed by using an internal standard.

Rietveld theory

The Rietveld refinement method is a full-pattern analysis that minimizes the difference (M) between experimental (y(obs)) and calculated (y(calc)) XRD diagrams by a least-squares procedure (Rietveld 1969; Paufler 1995):

$$M = \sum_{i=1}^{n} w_i \left[y_i\ (obs) - y_i\ (calc) \right]^2 = minimum \qquad (3)$$

With w_i the weight of each observation point and the sum i is over all data points.

Refinement is done on a point-by-point basis. The calculated intensity at a given step (y(calc)) is determined by summing the contributions from the background and all neighboring Bragg reflections (k) for all phases (p) as given by:

$$y_i(calc) = \sum_f S_f \sum_k p_k L_k (F_k)^2 G(\Delta\theta_{ik}) P_k + y_i(bkg) \qquad (4)$$

Where S is the scale factor

L_k is the Lorentz-polarization factor for the kth Bragg reflection

F_k is the structure factor.

p_k is the multiplicity factor.

P_k is the preferred orientation function.

θ_{ik} is the Bragg angle for the kth reflection.

$G(\Delta\theta_{ik})$ is the reflection profile function.

$y_i(bkg)$ is the refined background.

The parameters that can be adjusted in the least-squares refinement, in principle simultaneously, include: lattice parameters (a, b, c, α, β, γ), atomic positions (x, y, z), atomic site occupancies, atomic thermal vibrational parameters, isotropic or anisotropic, profile and asymmetry, preferred orientation, background function, 2h-zero correction, and overall scale factor. The number of parameters to refine is proportional to the number of Bragg peaks in a diffractogram. Practically, these parameters can be entered individually in the refinement program, but text files now exist (CIF files) that group together all these data for each mineral. These files can be found on different internet databases, such as the American mineralogist crystal structure database (Downs and Hall-Wallace 2003).

Rietveld refinement converges when the following R equations become constants:

Profile R: $R_{profile} = |yi - yci| / \sum_i yi$ (5)

$$R_{weighted\ profile} = [\sum_i wi\ (yi - yci)^2 / \sum_i wi.yi^2]^{1/2} \quad (6)$$

Structure R: $R_{Bragg} = \left|I_k - I_k^{calc}\right| / \sum_i I_k$ (7)

$$R_F = \sum_k \left|(I_k)^{1/2} - \left(I_k^{calc}\right)^{1/2}\right| / \sum_k (I_k)^{1/2} \quad (8)$$

Highscore Plus software used for Rietveld analysis

Several efficient Rietveld programs are available nowadays for structure refinement and quantitative analysis. Fullprof is considered to be the essential software among all the others (Casas-Cabanas et al. 2007; Frontera and Rodríguez-Carvajal 2003). However, it is highly sophisticated, and writing the Rietveld code, a text file containing the original crystallographic information in the cif files, is never straightforward. In addition, from experience in this work, this software crashed when refining a mixture of phases (typically more than three phases). Other software than Fullprof exist and deliver the same type of results but in a more user-friendly way. The TOPAS software that is linked to the Bruker XRD diffractometer was not

available in this work. On the contrary, the Highscore Plus software from Panalytical Instruments was available and was used in this work for Rietveld refinement and full quantification, instead of Fullprof.

In terms of refinement steps in Highscore Plus, the set of patterns that explained the diffractogram peaks were first added to the refinement control list. Then, the background of the measured diffractogram was defined. It would be the initial pillar in building the model. After a thorough study of several samples, it was found that the parameters to be refined should be in the following order:

1. the peaks positions of the model (i.e. zero shift),
2. the lattice parameters (i.e. cells),
3. the peak height (i.e. scale),
4. and the peak shape (i.e. v).

Until here, each of the parameters listed above was refined separately, one after the other. The last step was to refine the parameters mentioned above (i.e. zero shift, scale, cells, and v) one last time, altogether.

Amorphous quantification with internal standard addition

To achieve the full quantification of the crystalline structures including the amorphous contents, a known weight percentage of internal standard was added to each sample. The internal standard should not have any peak of its P-XRD diffractogram overlapping with a major peak of the P-XRD diffractogram of the sample. Hence, Anatase TiO_2 (99.2 wt.% Anatase and 0.8 wt.% Rutile, Sigma-Aldrich) was found to be a suitable standard, as shown in Figure 2.10.

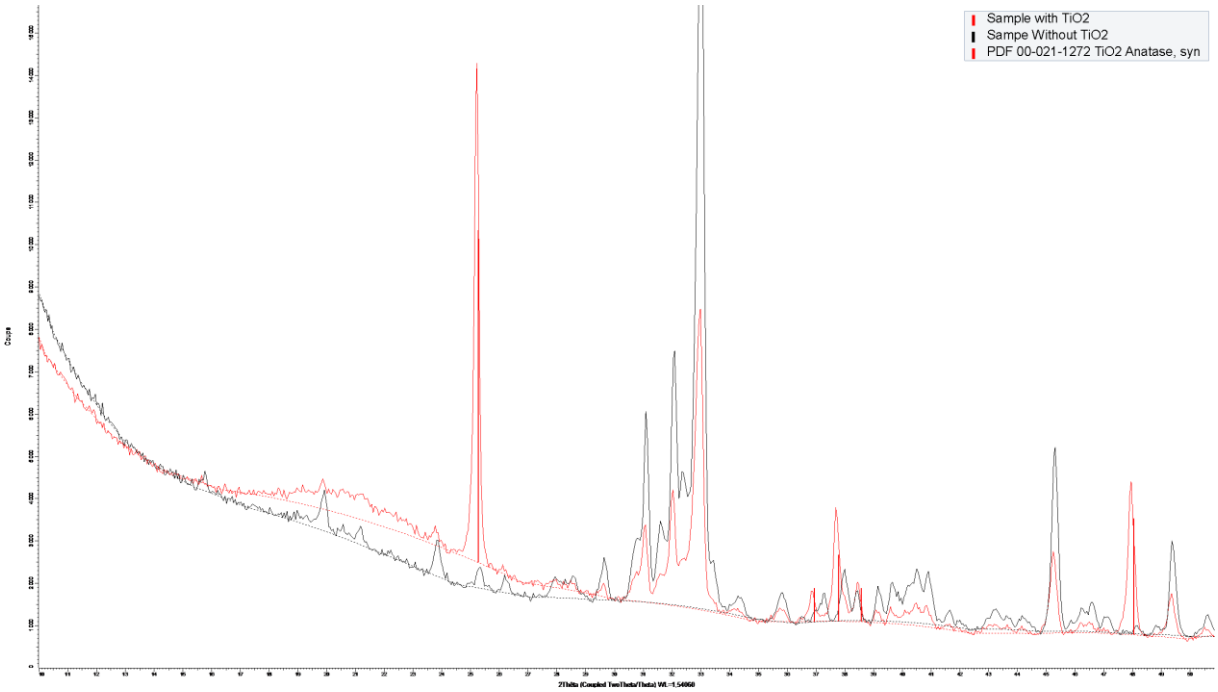

Figure 2.10: P-XRD analysis of the internal standard TiO2 Anatase.

In terms of picking the initial weight percent of the standard, it is necessary that the most important peaks of the standard and the sample to be analyzed have the same order of magnitude of height. In addition, the standard should be added to the sample in a percentage that maintains the small peaks of the sample (i.e. they will not disappear due to the dilution by the standard). Consequently, by trial and error, it was found that 10 wt.% of TiO_2 Anatase powder was suitable.

Then, the 10 wt.% of TiO_2 Anatase powder was crushed, manually ground, and mixed with the sample in a way to fill the sample holder (~0.25g total mass of sample and TiO_2 standard in each analysis). The Rietveld refinement analysis of the P-XRD diffractogram (90 wt.% sample + 10 wt.% TiO_2) gave the percentage of all the crystalline phases in the presence of TiO_2 Anatase (standard).

Afterward, the actual total % of the pure sample that refers (or is proportional) to the 90 wt.% sample (i.e. without TiO_2 Anatase) (T) needs to be calculated from the P-XRD measurements by the proportionality rule as follows:

$$T = P_{XRD,Anatase}\ x\ \frac{100 - P_{m,Anatase}}{P_{m,Anatase}} \qquad (9)$$

With

$P_{XRD,\ Anatase}$ is the percentage of TiO_2 Anatase measured by the P-XRD in the total sample.

$P_{m,\ Anatase}$ is the measured weight percentage of TiO_2 Anatase (standard) used in the total sample, which was 10 wt.%.

Then, the actual weight percentage of each phase i in the pure sample (i.e. without TiO_2 Anatase) (p_i) was calculated as follow:

$$p_i = \frac{P_{XRD,i}}{T}\ x\ 100 \quad (10)$$

With $P_{XRD,\ i}$ is the percentage of phase i measured by XRD in the total sample (i.e. sample + TiO_2 Anatase).

Then, the amorphous weight percentage (Amorphous) was calculated by simple difference:

$$Amorphous = 100 - \sum p_i \quad (11)$$

Each quantification was performed twice. The average relative error (when two refinements were done on the same sample with different TiO_2 weight percentages) corresponding to the Rietveld analysis was around 5%. Since the P-XRD analysis was conducted on ash samples, the results calculated by the mixing rule in the following sections/chapters of the BCWC biomass mixture (50-50 bark-straw biomass mixture) will always correspond to 61-39 wt.% bark-straw ash mixture.

It should be noted that the amorphous phase consists of a solidified molten ash that may entrap micrometered crystals. ICDD 2020 crystallography database was used in the two software mentioned above.

4.2. SEM/EDX analysis

The tendency to form an amorphous phase and analyze the inorganic semi-quantitative composition of specific samples was evaluated using a Philips XL30 scanning electron microscopy (SEM) equipped with an energy dispersive X-ray fluorescence Oxford Instruments EDX system (INCA software) at CEA Grenoble. The analyses were conducted at 20 kV and with a working distance (WD) of 11. For the latter, both surface mapping and point analyses were used. Ash test samples of BCWC at 1200 °C for 20 min and 6 h were embedded under vacuum in an epoxy resin. They were then polished with water-free lubricants. Before the analysis, a graphite coating was applied to each sample to increase its conductivity.

4.3.Sieving measurements

Particles sieving was performed in the ashes collected after the pellet and pilot tests. For the pellet test, the particle size was measured after putting the ashes in a box, which was manually

shaken for about 1 min to break the loose bridges between particles characterizing their tendency to agglomerate as they could have been done in a pilot test, a method inspired by Steenari et al. (Steenari et al. 2009). Sieves were chosen in the following decreasing order: 4500 µm, 2500 µm, 900 µm, and 630 µm. Particles whose size was bigger than 2500 µm were considered as significant agglomerates. Particles whose size is bigger than 900 µm are referred to as total agglomerates. The ones that were smaller than 630 µm were considered solid powder (i.e. in the solid state). The mass fraction between 900 µm and 630 µm was considered to be partially sintered.

4.4.TGA/DTA

A SETARAM Setsys 16/18 EO simultaneous thermogravimetric analysis-differential thermal analysis (TGA-DTA-MS) was used at CEA Grenoble to evaluate the weight loss and differential heat flow over time as a function of temperature (Figure 2.11). A piece of ash chip of BCWC mixture obtained at 550 °C and compressed at 10 bar was used as the sample. It was put in a Pt crucible (3 mm diameter and 7 mm height) under air flow rate (50 mL/min). The TGA program was composed of a 10 °C/min ramp until 1350 °C then a 20 min isothermal plateau followed by slow cooling (10 K/min).

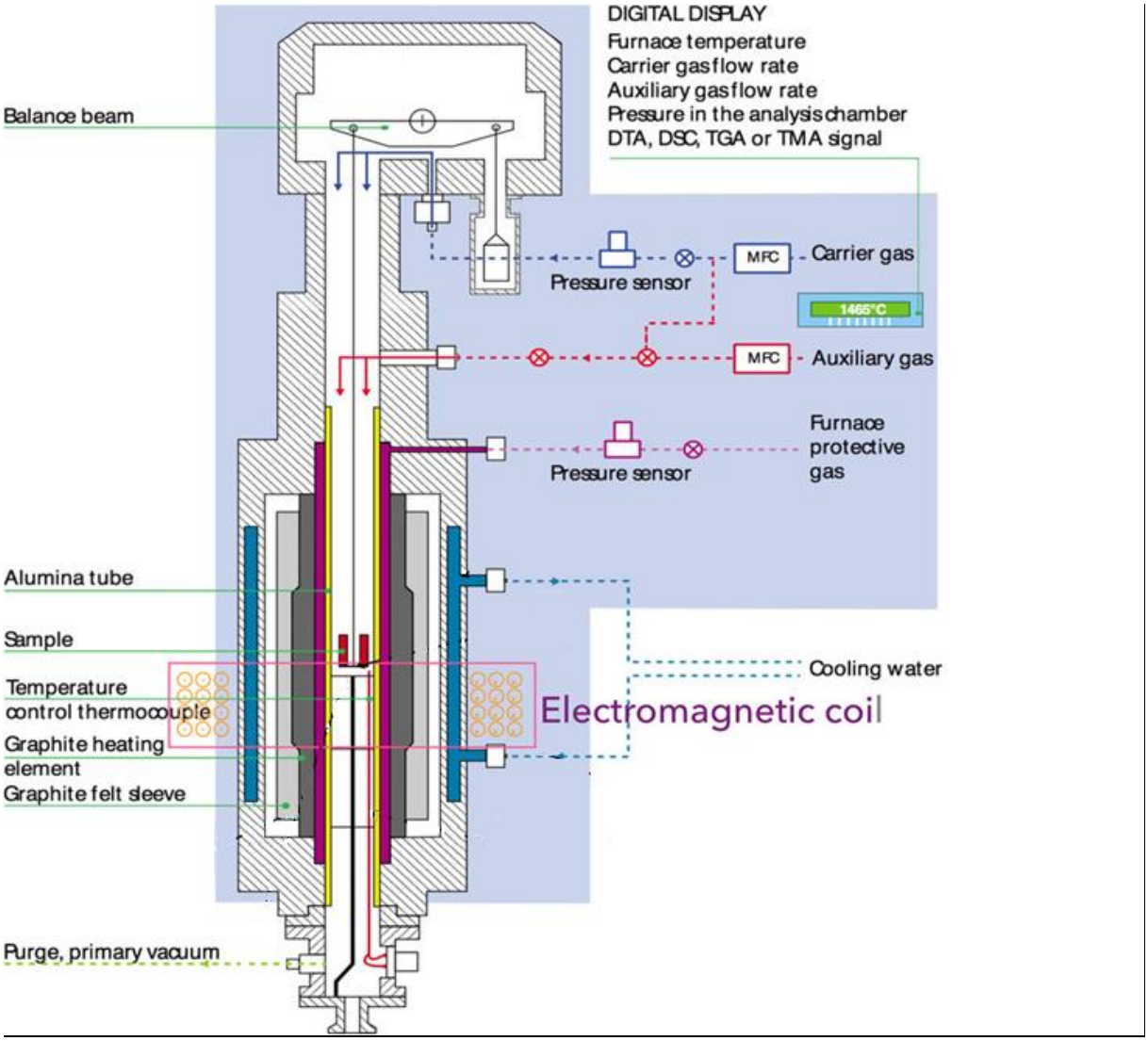

Figure 2.11: TGA – DTA (SETARAM Setsys 16/18 EO (Hasier, Riolo, and Nash 2017)).

According to Figure 2.12, the mass loss was measured by the level difference of the horizontal tangent line to the peaks on the mass loss curve. An event was said to happen when the heating curve changed its trajectory. Then, the temperature at which the event happened was determined by the intersection between the tangent line to 2/3 of the propagation before trajectory change and the tangent line to 2/3 of the propagation after trajectory change. The baseline of the new event was taken as the horizontal tangent to the point at which the previous event changed trajectory. SETARAM conducted the temperature calibration on a regular basis. After a thorough discussion with the technician responsible for the equipment, the temperature uncertainty is in the range of 5 °C.

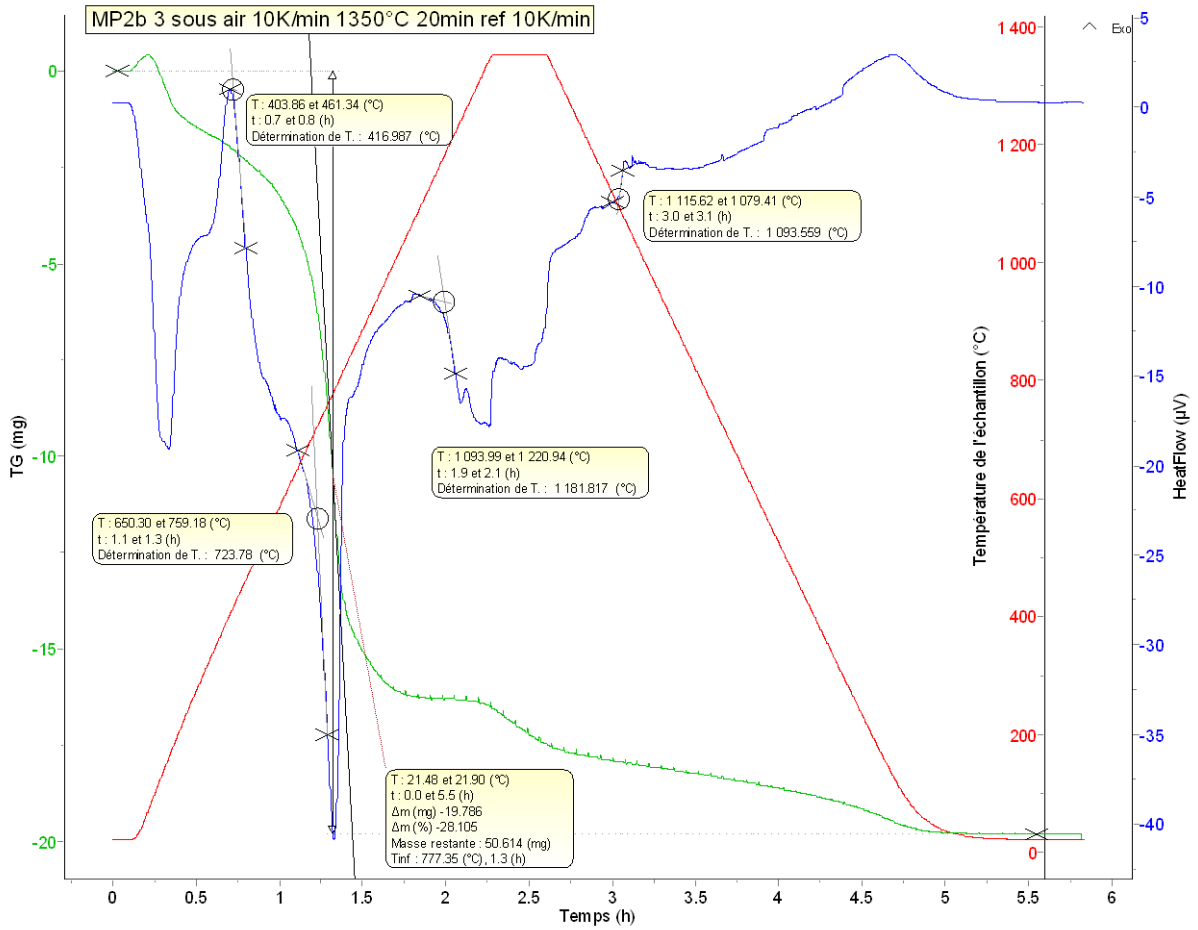

Figure 2.12: the standard method used to identify the temperature at which an event occurs in the TGA-DTA analysis.

4.5.Total and elemental weight loss analysis (between 550 °C and T)

4.5.1. Total weight loss analysis

The total static weight loss was measured from the ash test experiments described in section 3.1.1.1 using a simple mass balance between the beginning of each experiment and its end. Dynamic total weight loss was evaluated using the TGA-DTA analysis described in section 4.4.

4.5.2. Elemental weight loss (or elemental volatilization)

Using the proportionality rule, the elemental weight loss (L_i) was calculated from the ICP-AES results in Table 2.2 as follows:

$$L_i = \left(1 - \frac{(1-m_t) \times m_{fin,i}}{m_{in,i}}\right) \times 100 \qquad (12)$$

Where $m_{in,i}$ denotes the weight percentage of each element (i) measured by the ICP-AES in the BCWC mixture at 550 °C and $m_{fin,i}$ denotes the one measured at either 1000 °C or 1200 °C.

4.6.TGA/DSC

A SETARAM Labsys apparatus with a DSC measuring top was used at Simap laboratory to measure the fusion temperature of the synthesized ternary compounds (Figure 2.13). A 20 mg of compressed sample (compressed at a pressure of 10 bar) was introduced inside the furnace in a Pt crucible (3mm diameter and 7 mm height) under a flow of argon of 40 mL/h (gauge pressure of 1 bar). The heating rate was set to 10K/min ramp until 1400 °C with no plateau, followed by slow cooling (10K/min).

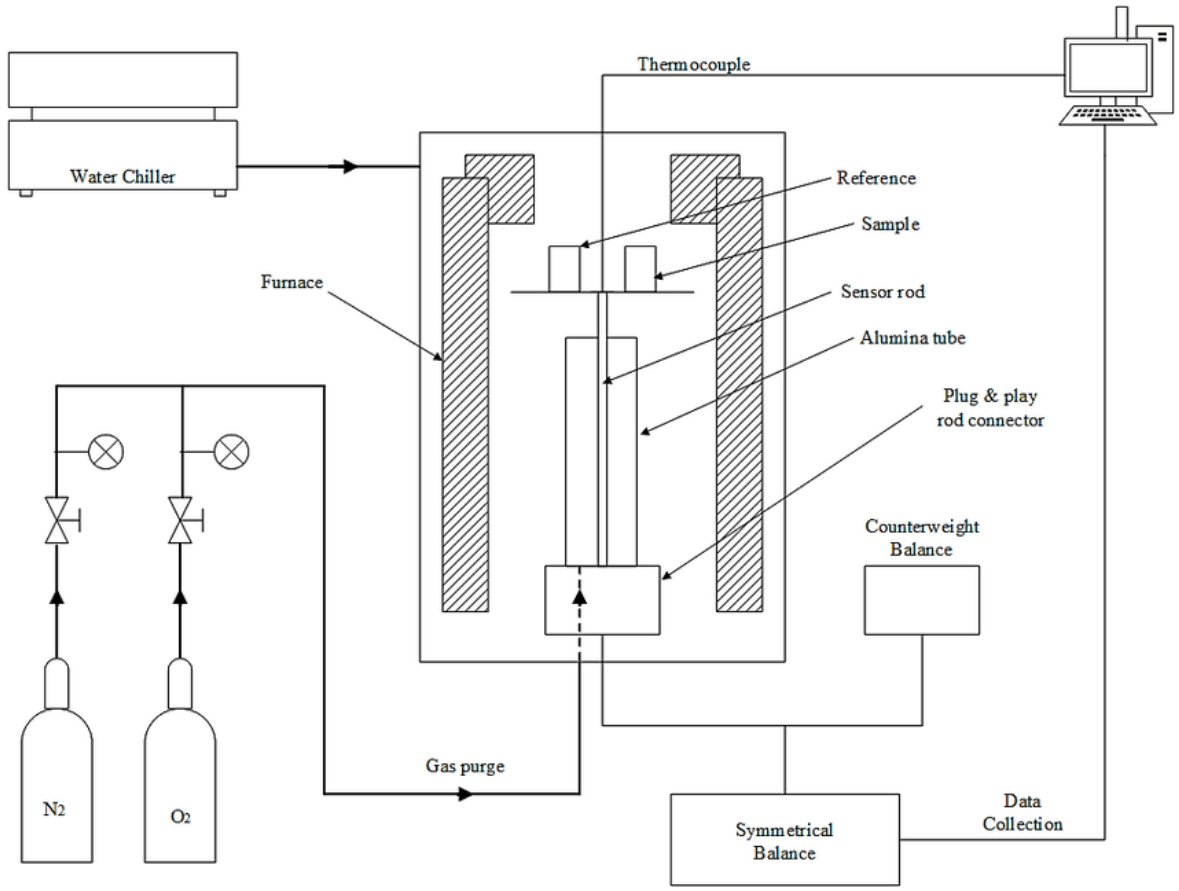

Figure 2.13:SETARAM Labsys apparatus (Department of Mechanical Engineering, Universiti Teknologi Petronas, 32610 Bandar Seri Iskandar, Perak Darul Ridzuan, Malaysia et al. 2016)

The calorimeter was calibrated on temperature using the melting points of NaCl, K_2SO_4, and CaF_2.

4.7.Solution calorimetry

The standard heat of formation of the ternary samples were determined using solution calorimetry in a C80 type calorimeter (Figure 2.14) at NUST-MISiS Moscow. The solvent used was molten 2PbO·B2O3 at 800 °C/ 1073.15 K in an atmosphere of dry air. The dry air was

bubbled through the solvent with a rate of 5 mL/min. This air bubbling provided constant agitation and helped the dissolution of the samples in the solvent. It also ensured a high oxygen fugacity in the melt to maintain a consistent oxidation state of the dissolved oxides.

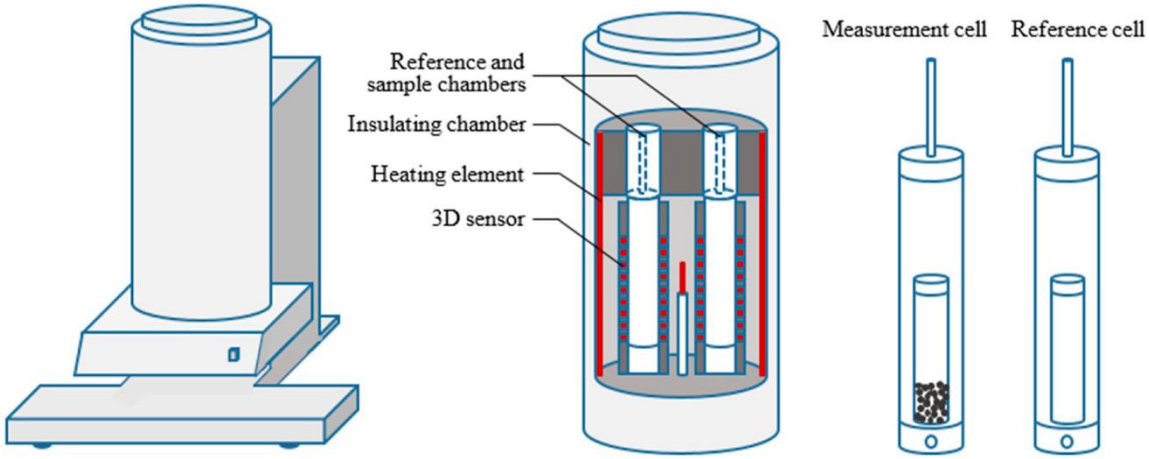

Figure 2.14: C80 type solution calorimeter (Lu et al.).

Two paths were used to measure the enthalpy of formation: the first was the drop solution calorimetry in lead borate solvent and the second was transposed temperature drop into an empty Pt crucible. The heat of the drop solution was a sum of the heat of the solution in the melt plus the heat content. Water was removed from the atmosphere of the calorimeter even at 800 °C / 1073.15 K and does not interact with the solvent. Thus the heat effect contained two contributions: the enthalpy of dehydration at 800 °C / 1073.15 K and the heat content of the sample (hydrated Mordenite).

In all calorimetric experiments, samples were compressed pellets of 7–15 mg (5mm diameter and 1–2mm height). The dissolution of each sample in the solvent bath was complete within about 1 h. The lead borate bath was changed between each experiment. The software Calisto from Setaram was used to record the output signals from the calorimeter and process them. All experiments were performed under a flow of air (30-40 mL/min).

5. Thermodynamic calculations and simulations

Thermodynamic simulation is a commonly used tool that can predict complex systems' chemical behavior and elemental interactions assuming they are at equilibrium. It is based on the minimization of the Gibbs energy of the system, which can be calculated using the thermodynamic data of all the phases that might be present. The thermodynamic databases are developed based on the so-called CALculation of PHAse Diagram (CALPHAD) methodology. This methodology was introduced in the 1960s by Larry Kaufman (Jung and Van Ende 2020).

It is based on the optimization of the Gibbs energy functions to reproduce the known phase diagrams and use them to predict unknown phase equilibria (Saunders and Miodownik 1998; Spencer 2008).

Using the CALPHAD method, one self-consistent set of model equations for the Gibbs energies is obtained by critically and simultaneously evaluating all the available thermodynamic and phase equilibrium data for the system at hand. The optimized model should reproduce the data for all the phases as functions of temperature and composition in the best way possible. Low-order (binary and ternary) subsystems can sometimes be used to provide good estimates for unexplored phase diagrams and thermodynamic properties in high-order systems (Jung and Van Ende 2020). Since industrial material processes often involve complex unstudied chemical reactions, thermodynamic software, such as FactSage, can be used in this case to predict the phase equilibria in these complex multicomponent systems, assuming that all the elements and phases are homogeneously distributed and available for reaction.

This section will start by introducing FactSage software and the applied databases. Then, it will present the phase diagram and the global simulation approaches.

5.1. FactSage software

This software was introduced in 2001 as a commercially available software resulting from the fusion of the F*A*C*T/ FACT-Win (Thermfact, Canada) with ChemSage (GTT-Technology, Germany) thermochemical packages (Jung and Van Ende 2020). F*A*C*T system originated back to 1976 (Bale et al. 2016). Until the 1990s, FactSage was mainly used for high-temperature pyro-metallurgical processes (Jung and Van Ende 2020). However, since 2000s, many new thermodynamic databases for steel, light alloys, copper, silicon, nuclear materials, aqueous solution, etc., have been developed to cover a wide range of material science and engineering applications (Jung and Van Ende 2020).

To accurately conduct the thermodynamic calculations, the set of constraints (temperature, pressure, initial elements, and their composition, etc.) of the algorithm that minimizes the total Gibbs energy of a system should be defined. In addition, a correct thermodynamic database covering the given system of interest should be applied.

FactSage uses the ChemSage FORTRAN routine to handle complex thermodynamic calculations involving up to 40 elements and a maximum of 200 solutions and 1500 stoichiometric phases per equilibrium calculation (Jung and Van Ende 2020; Bale et al. 2016).

Therefore, FactSage is considered a powerful tool to perform equilibrium calculations for a complex system, such as the $CaO-K_2O-SiO_2$ system.

5.2.Thermodynamic databases

In this work, four different thermodynamic databases were equipped with FactSage to conduct the thermodynamic calculations and simulations: FactPS, FToxid, FTsalt, and GTOx. The contents of each database are extracted from the FactSage documentation module and the work of Jung et al. (Jung and Van Ende 2020), Bale et al. (Bale et al. 2016), and Lindberg et al. (Lindberg et al. 2013) for the FACT databases, and from the work of Hack et al. (Hack et al. 2012) for GTT database. More details on the contents of each used database are provided in Appendix B.

5.2.1. FactPS

FactPS database was used in this work to provide thermodynamic data for all stoichiometric compounds. It contains thermodynamic data of over 4900 stoichiometric phases in solid, liquid, gas, and ionic states (Jung and Van Ende 2020; Bale et al. 2016; Lindberg et al. 2013).

5.2.2. FToxid

FToxid database (also called FACT oxide database) contains thermodynamic data for pure oxides and oxide solid solutions formed by 23 elements (as well as for dilute solutions of S, SO_4, PO_4, H_2O/OH, CO_3, F, Cl, and I in the molten slag phase). In addition, the FToxid database contains the molten slag phase (Jung and Van Ende 2020; Bale et al. 2016; Lindberg et al. 2013).

5.2.3. FTsalt

The FTsalt databases was used to add data for pure salts and salt solutions of 27 main cations (Li^+, Na^+, K^+, Rb^+, Cs^+, Mg^{2+}, Ca^{2+}, Sr^{2+}, Ba^{2+}, Mn^{2+}, Al^{3+}, Fe^{2+}, Fe^{3+}, Co^{2+}, Ni^{2+}, Zn^{2+}, Pb^{2+}, La^{3+}, Ce^{3+}, Th^{4+}, U^{3+}, U^{4+}, Pu^{3+}, Pu^{4+}, Cr^{2+}, Cr^{3+}, Mo^{5+}) and 9 main anions (F^-, Cl^-, Br^{2-}, I^-, NO_3^-, NO_2^-, OH^-, CO_3^{2-}, SO_4^{2-}) (Jung and Van Ende 2020; Bale et al. 2016; Lindberg et al. 2013).

5.2.4. GTOX

GTOX database was used in this work as an alternative to the FToxid database. The first was developed by the GTT team in Jülich in Germany in 2012 (Hack et al. 2012), while the Canadian FACT team established the second based on the recent Ph.D. thesis of Kim in 2017 (D.-G. Kim et al. 2017; D. Kim 2017). According to Hack et al. (Hack et al. 2012), FToxid lacks the accessibility of the Gibbs energy parameters and shows remarkable deviation from experimental information, especially for systems with K_2O.

GTOX thermodynamic database contains calculated phase diagrams and thermodynamic properties for any composition and temperature for the system CaO-MgO-Al_2O_3-CrOx-FeO_x-K_2O-Na_2O-SiO_2 (Hack et al. 2012). More details for the solution (LIOS) and the compounds contained in this database are provided in Appendix B.

5.3.Phase diagram approach

Calculations of the ternary phase diagram K_2O-CaO-SiO_2 were conducted using the "phase diagram" module of FactSage (version 8.1, June 2021) at three different temperatures (850℃, 1000℃, 1200℃). GTOX and FToxid are among the widely used thermodynamic databases in the market that contain thermodynamic data for oxides and their solutions. Hence, GTOX (2018) and FToxid 8.1 (2021) databases were used to calculate the phase diagrams. The biomass and their mixtures were positioned in each phase diagram based on the calculate CaO, K_2O, and SiO_2 wt.% in Tables 2.1 and 2.2.

5.4.Global simulation approach

Global simulations of predicted amounts of crystalline phases, liquid slag, and volatilization behavior were conducted to assess the database quality further. The main difference between the global simulation and the phase diagram approach is that the latter uses only Ca, Si, and K oxides without gas, while the former considers the weight percentages of the other elements and the gaseous atmosphere (air). The FactSage software was also used to conduct the simulations using its "Equilib" module. Two sets of databases were applied for database comparison:

- Set 1: GTOX (version 2018) for oxides (compounds & solutions) combined with FactPS (June 2021) for the gas species and additional inorganic solid phases.
- Set 2: FToxid 8.1 (June 2021) for oxides (compounds & solutions) combined with FactPS (June 2021) for the gas species and additional inorganic solid phases and FTSalt (June 2021) for salt melts and solutions.

The SGTE pure substance database is usually recommended with GTOX (Hedayati et al. 2021), but authors did not have access to it; that is why it was replaced by FactPS in dataset 1. The thermodynamic data of FTSalt are compatible with FToxid but not with GTOX. Hence, FTSalt was used with the former rather than with the latter.

The predicted results using the global simulations on the pellet test using the two sets of databases were conducted using the full elemental analysis of only BC and WC biomass in Table 2.1 since the analyses were similar for the other biomass ashes. In the simulations, the

bark weight fraction in the biomass samples (α) was varied between 0 and 1 in air. A simulation temperature of 1000 °C was set. Then, α was fixed at 0.5, and the simulation was conducted at varying temperatures. Air was used as the atmosphere with a λ of 1.2.

On the other hand, the predicted results using the global simulations on the ash test between the two sets of databases were conducted using the elemental analysis of each ash sample from single biomasses and mixtures in Tables 2.4 and 2.5. 0.5 g of compressed ash chips were applied in this laboratory test. Hence, the simulation inputs from Tables 2.1 and 2.2 were converted to per 0.5 g ash (results shown in Tables 2.4 and 2.5). In this case, since the global simulation was conducted on ash samples, bark weight fraction in the ash bark-straw mixture (β) was used. Then, β was fixed at 0.67, and the simulation was conducted at varying temperatures. The partial pressure of oxygen was kept constant by setting its activity at 0.21 during the simulation since the experimental reactions were conducted in a 0.7 L vertical laboratory furnace opened to air. The weight of nitrogen inside the reactor was calculated using the ideal gas equation at 1 atm and 1000 °C. It was found to be 0.147 g/h. Since the experiments were conducted for 6h, the weight of nitrogen, added to the feedstock in the inputs of the simulations, was 0.882 g.

Table 2.4 : Calculated elemental composition of each biomass ash used in the ash test.

g/0.5g ash	**WC**	**WF**	**WI**	**BC**	**BF**	**BI**
C	0.02180	0.00600	0.00450	0.02430	0.03050	0.03200
O	0.22570	0.22352	0.20966	0.26002	0.25996	0.23116
S	0.00470	0.00702	0.00878	0.00189	0.00044	0.00189
Cl	0.00071	0.00165	0.00057	0.00003	0.00003	0.00004
Si	0.08547	0.12676	0.09260	0.02849	0.05176	0.04346
Ca	0.02522	0.02018	0.03462	0.15231	0.12636	0.12550
K	0.12334	0.10096	0.12533	0.01554	0.01201	0.03918
P	0.00580	0.00607	0.00836	0.00190	0.00114	0.00431
Al	0.00038	0.00054	0.00306	0.00437	0.00707	0.00550
Mg	0.00397	0.00549	0.00682	0.00430	0.00267	0.00944
Fe	0.00071	0.00064	0.00282	0.00206	0.00517	0.00454
Na	0.00178	0.00083	0.00230	0.00069	0.00119	0.00278
Mn	0.00042	0.00035	0.00059	0.00410	0.00171	0.00020

Table 2.5: Calculated elemental composition of each biomass ash blend used in the ash test

α = Bark weight fraction in the biomass mixture and β = Bark weight fraction in the ash mixture

g/0.5g ash	**BCWC**	**BCWI**	**BCWF**	**BIWC**	**BIWI**	**BFWC**	**BFWI**	**BFWF**
(α)	0.500	0.314	0.559	0.616	0.550	0.352	0.242	0.500
(β)	0.590	0.490	0.557	0.697	0.718	0.522	0.484	0.580
C	0.0315	0.0260	0.0275	0.0250	0.0230	0.0220	0.0200	0.0245
O	0.2288	0.2312	0.2437	0.2397	0.2340	0.2431	0.2517	0.2359
S	0.0039	0.0038	0.0032	0.0028	0.0032	0.0040	Not measured	0.0028
Cl	0.0028	0.0018	0.0023	0.0017	0.0013	0.0030	Not measured	0.0014
Si	0.0581	0.0555	0.0670	0.0715	0.0670	0.0675	0.0700	0.0800
Ca	0.1047	0.1025	0.0942	0.0674	0.0795	0.0734	0.0768	0.0868
K	0.0550	0.0614	0.0469	0.0658	0.0622	0.0711	0.0617	0.0509
P	0.0028	0.0036	0.0023	0.0041	0.0052	0.0033	0.0038	0.0026
Al	0.0041	0.0037	0.0040	0.0079	0.0085	0.0042	0.0052	0.0058
Mg	0.0035	0.0052	0.0036	0.0072	0.0083	0.0034	0.0048	0.0038
Fe	0.0022	0.0030	0.0034	0.0039	0.0044	0.0027	0.0037	0.0035
Na	0.0013	0.0011	0.0008	0.0027	0.0030	0.0013	0.0013	0.0008
Mn	0.0013	0.0013	0.0011	0.0003	0.0003	0.0009	0.0011	0.0011

References

Arroyabe, Erik, Richard Tessadri, Daniel M. Többens, and Volker Kahlenberg. 2011. "Does K2CaSiO4 Exist? A Phase-Analytical Study in the System K2O-CaO-SiO2 with Implications for the Characterization of Residual Materials: Does K2CaSiO4 Exist?" *Journal of the American Ceramic Society* 94 (8): 2652–55. https://doi.org/10.1111/j.1551-2916.2011.04397.x.

Bale, C.W., E. Bélisle, P. Chartrand, S.A. Decterov, G. Eriksson, A.E. Gheribi, K. Hack, et al. 2016. "FactSage Thermochemical Software and Databases, 2010–2016." *Calphad* 54 (September): 35–53. https://doi.org/10.1016/j.calphad.2016.05.002.

Barin, Ihsan., Platzki, Gregor.,. 1995. *Thermochemical Data of Pure Substances*. Weinheim; New York: VCH.

Casas-Cabanas, M., J. Rodríguez-Carvajal, J. Canales-Vázquez, Y. Laligant, P. Lacorre, and M. R. Palacín. 2007. "Microstructural Characterisation of Battery Materials Using Powder Diffraction Data: DIFFaX, FAULTS and SH-FullProf Approaches." *Journal of Power Sources*, 13th International Meeting on Lithium Batteries, 174 (2): 414–20. https://doi.org/10.1016/j.jpowsour.2007.06.216.

Defoort, Françoise, Matthieu Campargue, Gilles Ratel, Hélène Miller, and Capucine Dupont. 2019. "Physicochemical Approach To Blend Biomass." *Energy & Fuels* 33 (7): 5820–28. https://doi.org/10.1021/acs.energyfuels.8b04169.

Department of Mechanical Engineering, Universiti Teknologi Petronas, 32610 Bandar Seri Iskandar, Perak Darul Ridzuan, Malaysia, N. Aniza, S. Hassan, Department of Mechanical Engineering, Universiti Teknologi Petronas, 32610 Bandar Seri Iskandar, Perak Darul Ridzuan, Malaysia, M. Inayat, and Department of Mechanical Engineering, Universiti Teknologi Petronas, 32610 Bandar Seri Iskandar, Perak Darul Ridzuan, Malaysia. 2016. "Thermogravimetric Kinetic Analysis of Malaysian Poultry Processing Waste Material under Inert and Oxidative Atmospheres." *Journal of Mechanical Engineering and Sciences* 10 (2): 1943–55. https://doi.org/10.15282/jmes.10.2.2016.1.0185.

Downs, Robert T., and Michelle Hall-Wallace. 2003. "The American Mineralogist Crystal Structure Database." *American Mineralogist* 88 (1): 247–50.

Frontera, C., and J. Rodríguez-Carvajal. 2003. "FullProf as a New Tool for Flipping Ratio Analysis." *Physica B: Condensed Matter*, Proceedings of the Fourth International Workshop on Polarised Neutrons for Condensed Matter Investigations, 335 (1): 219–22. https://doi.org/10.1016/S0921-4526(03)00241-2.

Guntamatic. n.d. "Guntamatic Product Overview Manual."

Hack, Klaus, Tatjana Dr.Jantzen, Michael Müller, Elena Yazhenskikh, and Guixuan Wu. 2012. *A Novel Thermodynamic Database for Slag Systems and Refractory Materials*. Conference: 5th International Congress on the Science and Technology of Steelmaking (2012) At: Dresden, Germany.

Hasier, John, Maria Annichia Riolo, and Philip Nash. 2017. "Curie Temperature Determination via Thermogravimetric and Continuous Wavelet Transformation Analysis." *EPJ Techniques and Instrumentation* 4 (1): 5. https://doi.org/10.1140/epjti/s40485-017-0040-y.

Hedayati, Ali, Hamid Sefidari, Christoffer Boman, Nils Skoglund, Norbert Kienzl, and Marcus Öhman. 2021. "Ash Transformation during Single-Pellet Gasification of Agricultural Biomass with Focus on Potassium and Phosphorus." *Fuel Processing Technology* 217 (June): 106805. https://doi.org/10.1016/j.fuproc.2021.106805.

HS TARM. 2005. "NOTICE D'UTILISATION ET D'INSTALLATION - HS MULTI HEAT 2.5."

Jung, In-Ho, and Marie-Aline Van Ende. 2020. “Computational Thermodynamic Calculations: FactSage from CALPHAD Thermodynamic Database to Virtual Process Simulation.” *Metallurgical and Materials Transactions B* 51 (5): 1851–74. https://doi.org/10.1007/s11663-020-01908-7.

Kim, Donggeum. 2017. “Coupled Experimental Study and Thermodynamic Optimization of the K2O-Na2O-CaO-MgO-Al2O3-SiO2 System.” Canada: McGill University, Montreal, Quebec, Canada.

Kim, Dong-Geun, Marie-Aline Van Ende, Pierre Hudon, and In-Ho Jung. 2017. “Coupled Experimental Study and Thermodynamic Optimization of the K2O-SiO2 System.” *Journal of Non-Crystalline Solids* 471 (September): 51–64. https://doi.org/10.1016/j.jnoncrysol.2017.04.029.

Lindberg, Daniel, Rainer Backman, Patrice Chartrand, and Mikko Hupa. 2013. “Towards a Comprehensive Thermodynamic Database for Ash-Forming Elements in Biomass and Waste Combustion — Current Situation and Future Developments.” *Fuel Processing Technology* 105 (January): 129–41. https://doi.org/10.1016/j.fuproc.2011.08.008.

Lu, Xiaojia, Yanjun Wang, Lionel Estel, Narendra Kumar, Henrik Grénman, and Sébastien Leveneur. 2020. “Evolution of Specific Heat Capacity with Temperature for Typical Supports Used for Heterogeneous Catalysts.” *Processes* 8 (8): 911. https://doi.org/10.3390/pr8080911.

Navrotsky, Alexandra. 2014. “Progress and New Directions in Calorimetry: A 2014 Perspective.” Edited by D. J. Green. *Journal of the American Ceramic Society* 97 (11): 3349–59. https://doi.org/10.1111/jace.13278.

“NIST-JANAF Table.” n.d. https://janaf.nist.gov/.

Paufler, P. 1995. “R. A. Young (Ed.). The Rietveld Method. International Union of Crystallography. Oxford University Press 1993. 298 p. Price £ 45.00. ISBN 0–19–855577–6.” *Crystal Research and Technology* 30 (4): 494–494. https://doi.org/10.1002/crat.2170300412.

Rietveld, H. M. 1969. “A Profile Refinement Method for Nuclear and Magnetic Structures.” *Journal of Applied Crystallography* 2 (2): 65–71. https://doi.org/10.1107/S0021889869006558.

Saunders, N., and A. P. Miodownik. 1998. *CALPHAD (Calculation of Phase Diagrams): A Comprehensive Guide*. Pergamon Materials Series, v. 1. Oxford ; New York: Pergamon.

Spencer, P. J. 2008. “A Brief History of CALPHAD.” *Calphad* 32 (1): 1–8. https://doi.org/10.1016/j.calphad.2007.10.001.

Steenari, B.-M., A. Lundberg, H. Pettersson, M. Wilewska-Bien, and D. Andersson. 2009. “Investigation of Ash Sintering during Combustion of Agricultural Residues and the Effect of Additives.” *Energy and Fuels* 23 (11): 5655–62. https://doi.org/10.1021/ef900471u.

Valin, Sylvie, Serge Ravel, Jacques Guillaudeau, and Sébastien Thiery. 2010. “Comprehensive Study of the Influence of Total Pressure on Products Yields in Fluidized Bed Gasification of Wood Sawdust.” *Fuel Processing Technology* 91 (10): 1222–28. https://doi.org/10.1016/j.fuproc.2010.04.001.

Valin, Sylvie, Serge Ravel, Philippe Pons de Vincent, Sébastien Thiery, Hélène Miller, Françoise Defoort, and Maguelone Grateau. 2020. “Fluidised Bed Gasification of Diverse Biomass Feedstocks and Blends—An Overall Performance Study.” *Energies* 13 (14): 3706. https://doi.org/10.3390/en13143706.

3. Chapter 3. Thermodynamic prediction approaches

In this chapter, an evaluation of the thermodynamic predictive approaches of the ash behavior will be discussed. Hence, in section 1, the phase diagram prediction approach will be presented, emphasizing the different predicted results between the diagrams calculated using the GTOX database and those calculated using the FToxid database. In section 2, the global simulation approach, will be applied in two different "process" situations. The first one (in agreement with the ash test in section 3.1.1 in chapter 2) was performed in annealed ashes where a steady-state (assumed to be the equilibrium state) was checked. The second one performed on biomass pellet (in accord with the pellet test in section 3.1.2 in chapter 2) is close to a real biomass combustion process.

1. Phase diagram approach

The CaO-K_2O-SiO_2 ternary phase diagram may have the capability to predict the state of the biomass ash and their ash mixtures, i.e. if they are in the solid, the liquid, or the solid-liquid phases (De Fusco and Defoort 2016). In Figure 3.1, the calculated isothermal sections of the ternary phase diagrams CaO-K_2O-SiO_2 at 850 °C, 1000 °C, and 1200 °C using GTOX and FToxid were shown. 850 °C approaches the typical temperature reached in a fluidized bed processe, 1000 °C is closer to the combustion boiler one, and 1200 °C simulates more the entrained flow reactor temperature. The green sections referred to the pure solid region, while the red ones referred to the liquid region. The white sections denoted the solid-liquid mixed regions (De Fusco and Defoort 2016).

In terms of binary sub-systems, the two thermodynamic databases contained the same binary phases, besides K_4SiO_4, which was added in FToxid based on Kim et al. (D.-G. Kim et al. 2017). For the ternary system, FToxid included two ternary phases, $K_2Ca_6Si_4O_{15}$ and $K_2Ca_2Si_2O_7$ (called O15 and O7, respectively), which were absent in GTOX. However, the thermodynamic data of these two ternary phases were never measured and were only based on estimations (D. Kim 2017). Other ternary compounds, such as $K_4CaSi_3O_9$, $K_2Ca_3Si_6O_{16}$, and $K_2Ca_2Si_9O_{21}$, were calculated at equilibrium using the GTOX database at 850 °C and 1000 °C but were not at equilibrium at 1000 °C using FToxid. Most importantly, the various tie lines (equilibrium lines) and solidus and liquidus lines differed between the two databases.

In order to better understand the differences between the two databases, the standard enthalpy and entropy of formation of the ternary compounds with respect to the pure simple oxides CaO, K_2O, and SiO_2-low quartz in each database were calculated at 25 °C (298 K) and are shown in Table 3.1. This Table included values for only the phases found in the calculated ternary phase diagrams CaO-K_2O-SiO_2 at 850 °C, 1000 °C, and 1200 °C. The values in this Table highlight the first factor leading to the different ternary diagrams calculated using each database, as shown in Figure 3.1. From the data in Table 3.1, although the values of the common binary compounds were similar (less than 20 kJ/mol for $\Delta H_{f,\ 298K}$ and less than 10 J/(mol.K) for S°) , those of the ternary compounds were different (more than 20 kJ/mol for $\Delta H_{f,\ 298K}$ and more than 10 J/(mol.K) for S°). This was mainly related to different estimated or calculated values adapted in each database. In turn, this affected the tie lines and the equilibria between the compounds. Another factor was the addition of O15 and O7 that changed the whole equilibrium, especially in the central section of the diagram. One last factor may be the different models used to

describe the thermodynamic properties of the liquid phase (the associate model in GTOX vs. the quasichemical model in FToxid) applied in each database.

In conclusion, FToxid provided a phase diagram containing more ternary compounds than GTOX, especially the addition of $K_2Ca_6Si_4O_{15}$ and $K_2Ca_2Si_2O_7$ to its database, which was found to be stable in this system according to the literature in chapter 1.

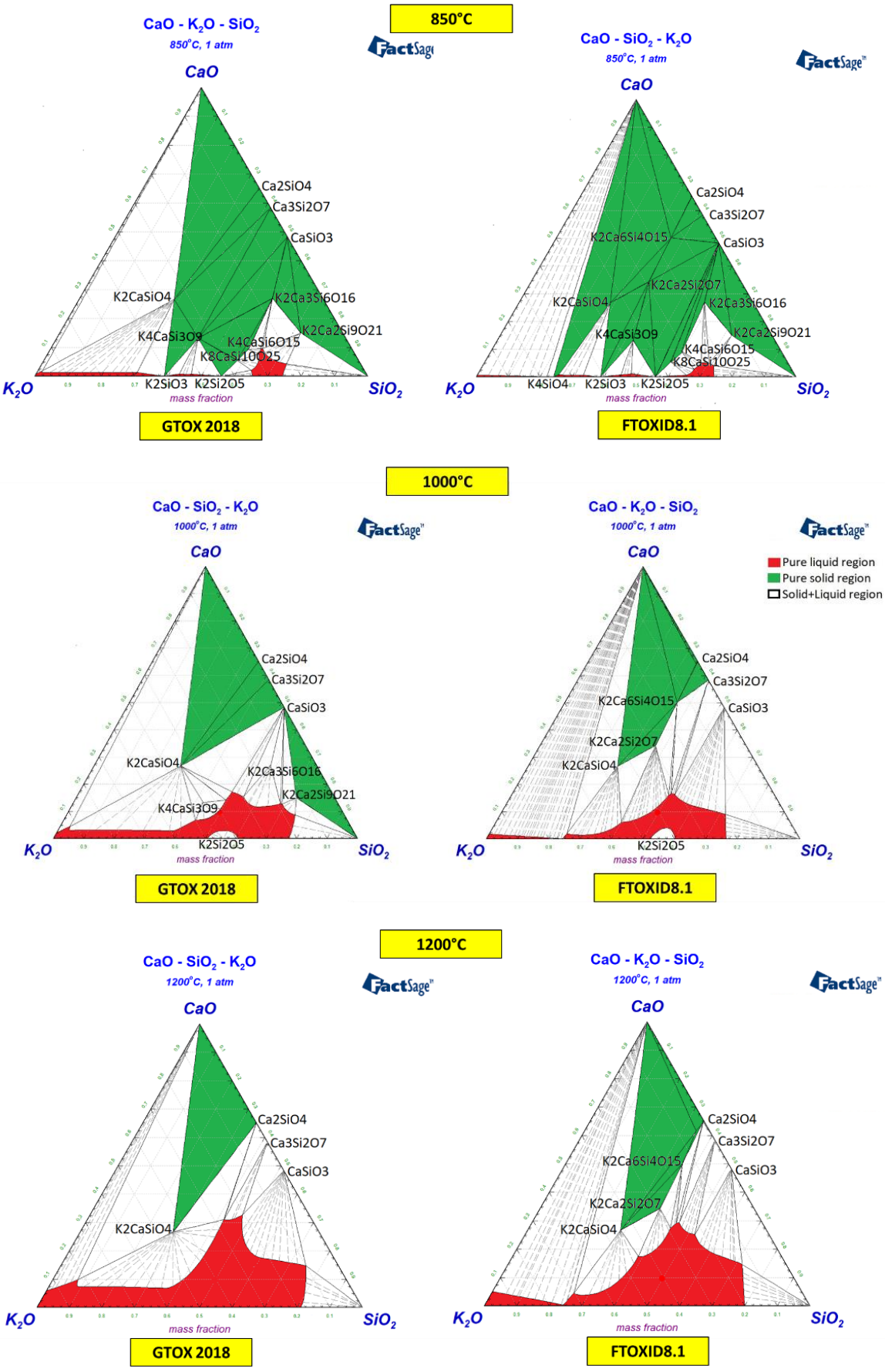

Figure 3.1: Calculated ternary phase diagrams CaO-K_2O-SiO_2 at 850 °C, 1000 °C, and 1200 °C using GTOX and FToxid.8.1.

.

Table 3.1: Comparison between GTOX and FTOXID in terms of the enthalpy and entropy of formations at 298K of binary and ternary compounds (ΔHf is referred to pure oxides K_2O, CaO, and SiO_2)

	FTOXID 8.1		GTOX 2018	
	ΔH_f (kJ/mol)	**S° (J/mol.K)**	**ΔH_f (kJ/mol)**	**S° (J/mol.K)**
K2CaSiO4	-297.71	196.49	-381.68	172.29
K2Ca2Si2O7	-430.92	268.55		
K2Ca6Si4O15	-740.16	490.49		
K4CaSi3O9	-654.81	380.00	-906.83	213.80
K4CaSi6O15	-686.71	564.00	-761.37	515.64
K8CaSi10O25	-1391.92	897.00	-1534.78	800.00
K2Ca2Si9O21	-537.02	558.30	-639.02	500.00
K2Ca3Si6O16	-569.03	512.50	-684.99	428.45
Ca2SiO4	-126.63	119.66	-140.28	120.57
Ca3Si2O7	-223.76	205.56	-225.60	210.89
CaSiO3	-88.89	79.81	-88.43	81.99
K4SiO4	-412.20	245.47		
K2SiO3	-271.60	146.15	-287.96	146.15
K2Si2O5	-320.80	190.58	-339.44	182.00

2. Global simulation approach

The previous phase diagram approach used Ca, K, and Si oxides in the prediction (atmosphere absent), while the global approach used all the elements in the calculations, considering the air atmosphere. Hence, the first section 2.1 will compare both approaches with the FToxid database using only the three main Ca, K, and Si oxides in the case of the ash test and then the pellet test. Then, a thorough comparison of the predicted results using each database set will be discussed in section 2.2 on the predicted volatilization and crystalline composition as a function of either temperature or bark weight fraction in the feedstock biomass mixture (α) or ash mixture (β). Until here, slag A and FTsalt were used in the simulations using the FToxid database set. Hence, in section 2.3, the effects of adding each inorganic element, using or not FTsalt, and choosing Slag A or Slag B in FToxid on the predicted results will also be highlighted. The elemental composition of the bark BC and straw WC presented in Tables 2.1 and 2.2 in chapter 2 were used. The simulations were done first at a constant temperature of 1000 °C and with varying bark weight fractions in the blends (0-1). Then, the simulations were repeated at varying temperatures and in just the 50-50 bark-straw blend. For the pellet test simulations, air was used as atmosphere with a λ equal to 1.2. On the other hand, in the ash test, the O_2 activity was fixed at 0.21 and N_2 weight at 1.125 g.

2.1. Comparison between the phase diagram and the global simulation approaches with the 3 main inorganic oxides (ash and pellet test)

In order to compare the prediction differences between the phase diagram and the global simulation approaches, calculations were conducted using the same inorganic elements Ca, K, and Si. Hence, the global simulation in this section was done using C, H, N, and O along with just Ca, K, and Si as inorganic elements for the ash test (Figure 3.2.a and 3.2.c) and the pellet test (Figure 3.2.b and 3.2.d). The FTOXID dataset 2 (with FactPS and FTSalt) was used at 1000 °C (Figure 3.4).

In the ash test simulation, no inorganic volatilization was calculated with the global simulation approach (Figure 3.2.c). The condensed predicted phases (Figure 3.2.a) agreed with the phase diagram calculation (Figure 3.3). To illustrate this, in Figure 3.2.a, the ash of pure bark (BC) started in a three-phase region (CaO-Ca_2SiO_4-$K_2Ca_6Si_4O_{15}$) and then moved into another three-phase region as the bark weight fraction decreased in the mixture until β=0.85 (CaO-$K_2Ca_6Si_4O_{15}$-K_2CaSiO_4). Beyond this composition, as the ash bark content β further decreased, reaching 0.65, $K_2Ca_2Si_2O_7$ appeared and replaced CaO in the three-phase region. Liquid appeared at β=0.6, where the mixture stayed in a $K_2Ca_2Si_2O_7$-$K_2Ca_6Si_4O_{15}$-liquid three-phase region until β=0.28. For $0.05<\beta<0.28$, the mixture was in the $K_2Ca_2Si_2O_7$-liquid two-phase region, after which it reached the pure liquid region for pure straw WC. The pathway mentioned above from the global simulation was precisely according to the proposed phase diagram pathway drawn as the yellow line in Figure 3.3.

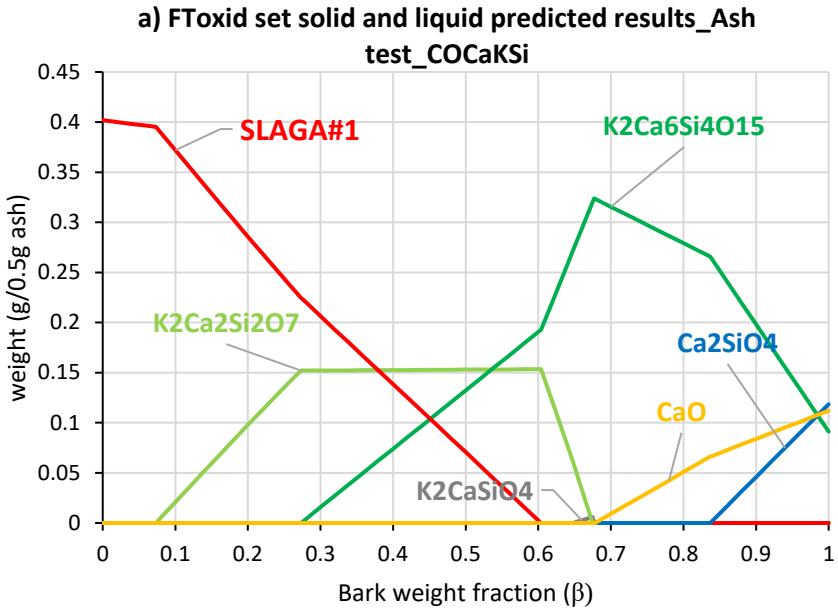
a) FToxid set solid and liquid predicted results_Ash test_COCaKSi
weight (g/0.5g ash)
Bark weight fraction (β)
SLAGA#1
K2Ca6Si4O15
K2Ca2Si2O7
Ca2SiO4
CaO
K2CaSiO4
0.45
0.4
0.35
0.3
0.25
0.2
0.15
0.1
0.05
0
0 0.1 0.2 0.3 0.4 0.5 0.6 0.7 0.8 0.9 1

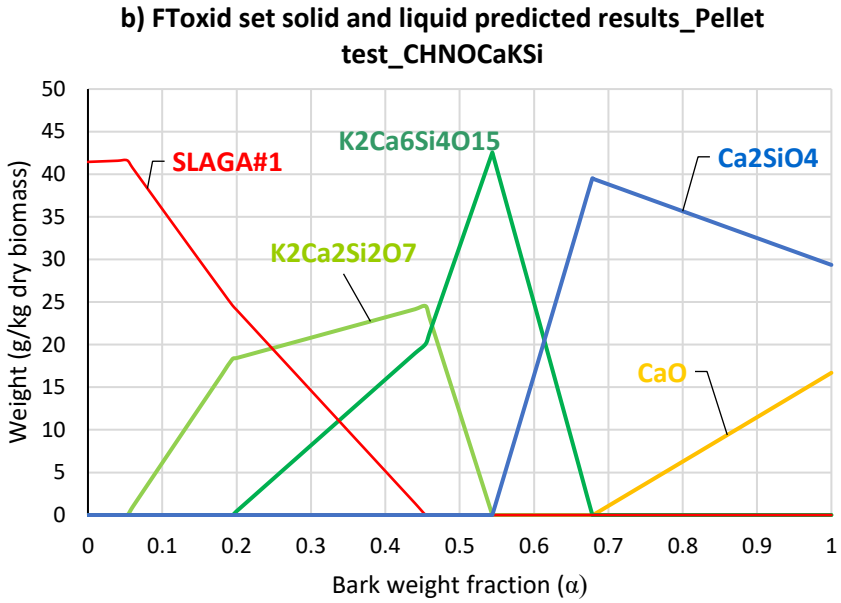
b) FToxid set solid and liquid predicted results_Pellet test_CHNOCaKSi
Weight (g/kg dry biomass)
Bark weight fraction (α)
SLAGA#1
K2Ca6Si4O15
K2Ca2Si2O7
Ca2SiO4
CaO
50
45
40
35
30
25
20
15
10
5
0
0 0.1 0.2 0.3 0.4 0.5 0.6 0.7 0.8 0.9 1

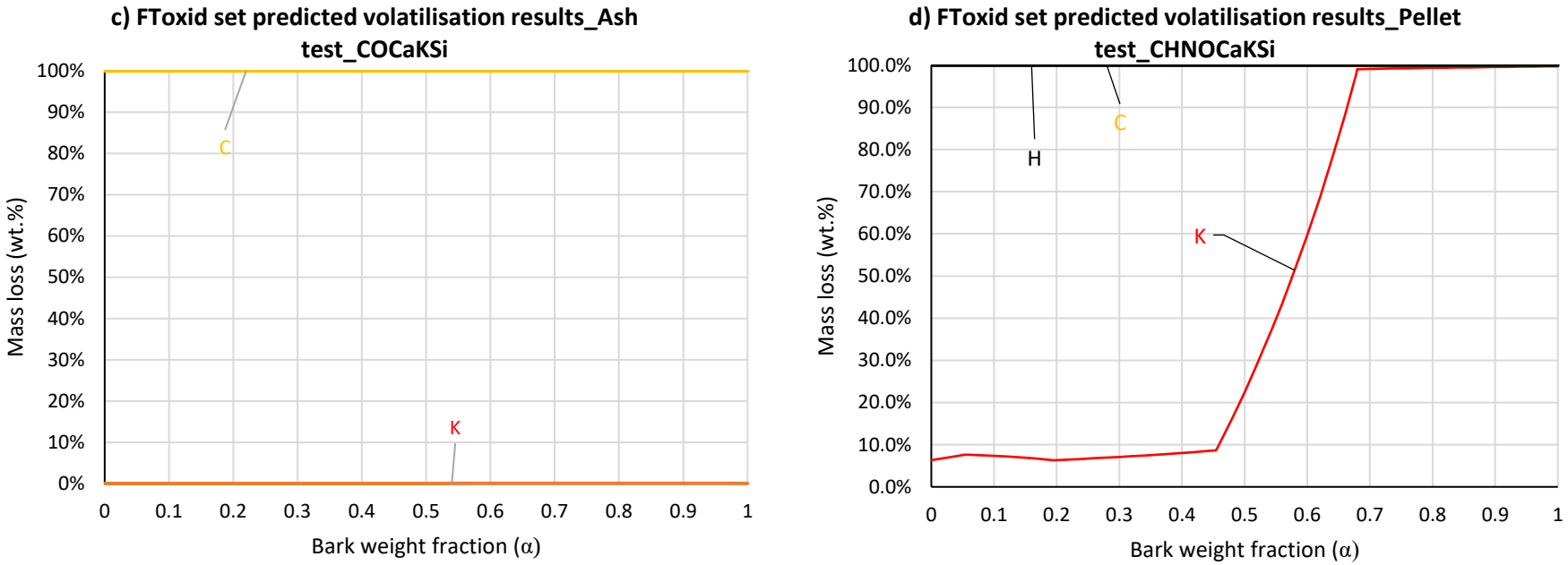

Figure 3.2: Global simulation at various BC weight fraction in WC-BC ash (a and c) and pellet (b and d) mixtures calculated at 1000 °C using the three oxides and FToxid dataset.

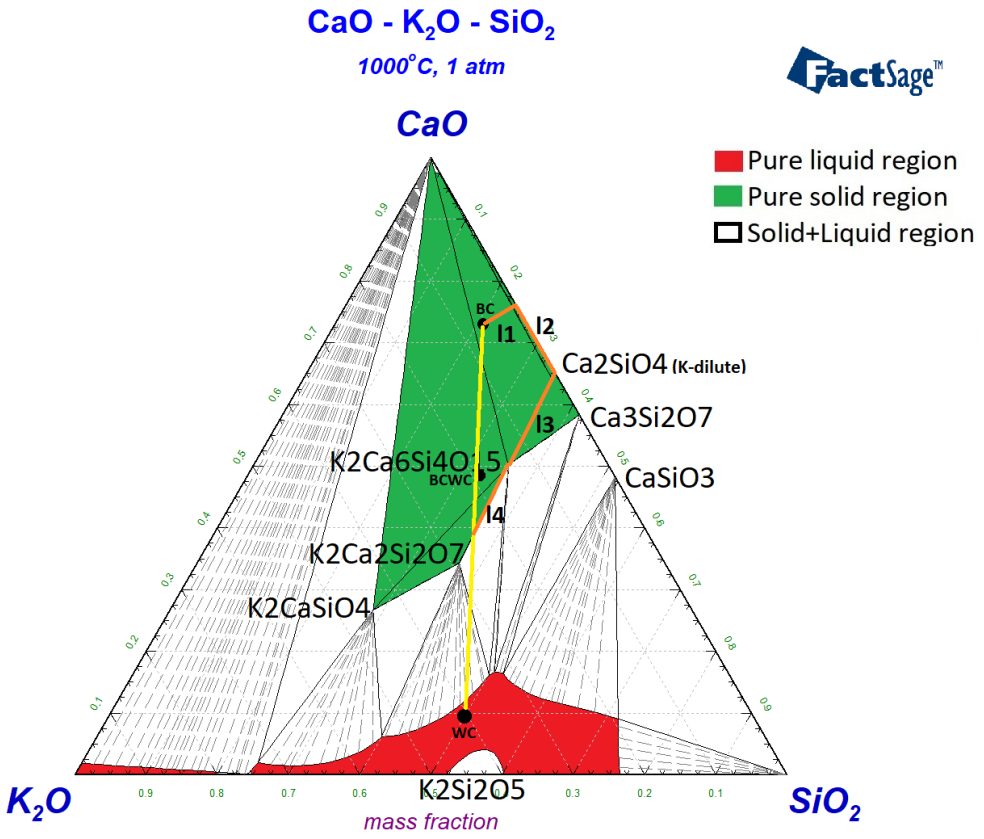

Figure 3.3: Ternary phase diagram CaO-K_2O-SiO_2 using FToxid 8.1 at 1000 °C.

On the contrary, **in the pellet test simulation**, the phases calculated in the biomass bark-rich mixtures (drawn as the orange line in Figure 3.3) differed between the phase diagram and global approaches. Contrary to the ash test simulations in Figure 3.2.a, Figure 3.2.b showed that for bark (α=1), there were no phases including potassium, but only CaO and Ca_2SiO_4. This could be explained by the loss of all potassium in the gas phase in the form of KOH(g), as shown in Figure 3.2.d (α>0.68). The presence of hydrogen in the biomass highly destabilized the potassium and increased its volatility, especially in the form of KOH(g). The same trend followed up to α=0.68, corresponding to l1 and l2 in Figure 3.3.

For α<0.68, there was a decrease in K volatilization (Figure 3.2.d). In this section (i.e. 0.55<α<0.68), some potassium was hindered in the condensed phases, and the blend moved in a two-phase region ($K_2Ca_6Si_4O_{15}$ with Ca_2SiO_4). This corresponded to l3 in Figure 3.3. K-loss further decreased for 0.45<α<0.55 (Figure 3.2.d), and the blend moved in another two-phase

region formed by $K_2Ca_6Si_4O_{15}$ and $K_2Ca_2Si_2O_7$ (Figure 3.2.b). This corresponded to l4 in Figure 3.3.

Potassium volatilization reached its lowest value of around 8 wt.% for $\alpha < 0.45$ (Figure 3.2.d). In this region, the liquid phase started to appear in the pellet test simulations and to coexist with the two ternary phases $K_2Ca_6Si_4O_{15}$ with $K_2Ca_2Si_2O_7$ (three-phase field in figure 3.3). Hence, at this point, the orange line pathway of the pellet test simulation was superposed with the yellow line pathway of the ash test simulation and the phase diagram approach. The pure liquid region was found for $\alpha < 0.05$ (i.e. for straw) in Figure 3.2.b, in which small potassium volatilization remained (Figure 3.2.d).

In conclusion, when the main inorganic oxides (CaO, K_2O, SiO_2) were used as inputs:

- In the case of the ash test, both approaches (phase diagram and global) exhibited the same behavior. This was mainly due to the absence of K-volatilization in the global simulation approach.
- In the case of the pellet test, differences between the two approaches (phase diagram and global) were present mainly in the bark-rich mixtures. In this section, large potassium volatilization occured, and no ternary compound was present in the condensed phases. Potassium reacted with the hydrogen and oxygen present in the biomass pellet and volatilized in the form of KOH(g)

2.2.Comparison between the database sets for ash and pellet tests

The conditions for the calculations in the global simulation are summarized in Table 3.2. **Figure 3.4** shows the variation of the predicted amounts of the crystalline solids and liquid in the pellet test (Figures 3.4.a and 3.4.c) and in the ash test (Figure 3.4.b and 3.4.d) as a function of the changes in the **bark weight fraction in the BC-WC biomass (α) and ash (β) mixtures at 1000 °C**. Figures 3.4.a and 3.4.b shows the predicted condensed phases using the GTOX dataset. Figures 3.4.c and 3.4.d presented those using the FToxid dataset. Predicted volatilizations are shown in Figures 3.4.e to 3.4.h.

To deepen the understanding of the differences between the predicted results using each database set, **Figure 3.5** shows the predicted results **for BCWC mixture at various temperatures** using GTOX in the pellet (Figure 3.5.a and 3.5.e) and ash tests (Figure 3.5.b and 3.5.f) and using FToxid in the pellet (3.5.c and 3.5.g) and ash tests (Figure 3.5.d and 3.5.h).

For simplification, this section will first focus on comparing the predicted results between the two datasets in the pellet test (section 2.2.1 for the solid/liquid compounds and section 2.2.2 for the volatilization). Then, in section 2.2.3, the prediction differences between the two test (pellet test vs ash test) types using the same database set. In sections 2.2.1, 2.2.2, and 2.2.3, the predicted results were calculated at a constant temperature of 1000 °C and with varying bark weight fractions in the blends (Figure 3.4). Hence, in section 2.2.4, the same analysis conducted in sections 2.2.1, 2.2.2, and 2.2.3 will be repeated, but at varying temperatures and constant bark weight fraction (Figure 3.5).

Table 3.2: Conditions for the calculations in the global simulation approach

Test type	Biomass/ash Composition	Atmosphere	Database set	Variable parameter	Fixed parameter
Pellet test	Table 2.1 & 2.2 chapter 2	Air with λ=1.2	GTOX set 1	Bark fraction α	1000 °C
Ash test	Table 2.4 & 2.5 chapter 2	Air with constant O2 activity at 0.21	FToxid set 2	Bark fraction β	1000 °C
Pellet test	Table 2.1 & 2.2 chapter 2	Air with λ=1.2	GTOX set 1	400 °C-1500 °C	α=0.5
Ash test	Table 2.4 & 2.5 chapter 2	Air with constant O2 activity at 0.21	FToxid set 2	400 °C-1500 °C	β= 0.68

2.2.1. Effect of using FToxid vs GTOX datasets in the pellet test on the predicted crystalline/liquid results at constant temperature of 1000 °C and varying bark fraction in the blend

To simplify the discussion, only the predicted results in the pellet test (Figures 3.4.a vs 3.4.c) will be discussed in this section. For instance, more liquid amounts and higher Ca_2SiO_4 and $Ca_3Si_2O_7$ contents were predicted using the GTOX dataset than the FToxid dataset in both ash and pellet tests. In addition, the stability range of Ca_2SiO_4 was wider in the calculated results using the GTOX dataset than the ones using the FToxid dataset. Most importantly, K_2CaSiO_4 was not at equilibrium in the simulation using the FToxid dataset, while $K_2Ca_6Si_4O_{15}$ was absent from the GTOX database.

From the results in Figures 3.4.a vs 3.4.c, it can be seen that the range of stability of $K_2Ca_6Si_4O_{15}$ (FToxid) was proportional to the one of K_2CaSiO_4 (GTOX) with a quantitative difference in both pellet and ash tests, as if these two phases were replacing each other. Since the thermodynamic properties of Ca_2SiO_4 and $Ca_3Si_2O_7$ (Table 3.1) were similar, the aforementioned difference in their prediction between the two database sets must be directly linked to the addition of $K_2Ca_6Si_4O_{15}$ in the FToxid database. This might led to their decreasing stability in FToxid, as they were a direct reactant in the formation reaction of $K_2Ca_6Si_4O_{15}$.

From Figures 3.4.a and 3.4.c, calculations using the FToxid dataset predicted some minor phases with Mg and Al, while those using the GTOX dataset failed to do that. $CaSiO_3$ and the K-based phases such as K_2SO_4, K_3PO_4, $KAlSiO_4$, and $KAlO_2$ found with FToxid calculations were absent from the ones using GTOX. In GTOX, a slag solution phase called LIOS is modeled. This solution dissolves oxides, metals, sulfides, sulfates, and fluorides. Consequently, the K-bearing compounds must have dissolved within this slag phase. On the contrary, FToxid slag solution showed a lower solubility for these crystalline compounds. Nevertheless, from the results in Figures 3.4.a and 3.4.c, some of these minor compounds were predicted using GTOX but at a lower temperature than FToxid (<700 °C).

To highlight the prediction difference between the databases in a simple way, the 50-50 bark-straw biomass mixture (α) case (pellet test BCWC) in Figure 3.4 (3.4.a vs 3.4.c) will be taken as an example. Using the GTOX dataset (Figure 3.4.a), liquid, $Ca_3Si_2O_7$, Ca_2SiO_4, and K_2CaSiO_4 were present in the mixture at equilibrium. On the contrary, using the FToxid dataset (Figure 3.4.c), less liquid and minor amounts of $Ca_3Si_2O_7$ were present. In addition, the major crystalline solid was $K_2Ca_6Si_4O_{15}$ in the simulations using the FToxid dataset (Figure 3.4.c) instead of the $Ca_3Si_2O_7$ and K_2CaSiO_4 in the ones using GTOX (Figure 3.4.a). K_2SO_4, $KAlSiO_4$, and an Mg-based compound were present in this blend in Figure 3.4.c while absent in the results in Figure 3.4.a. All these differences may be related to the different liquid phase models (the associate model in GTOX vs. the quasichemical model in FToxid) as well as the different compounds and their thermodynamic data (Table 3.1) used in each database.

In the straw-rich region (α & $\beta \sim 0$), in the case of the pellet test (Figures 3.4.a vs 3.4.c), calculations using GTOX set predicted 100% liquid, while the ones using FToxid predicted major liquid contents with minor amounts of K_2SO_4. On the other hand, in the bark-rich domain (α & $\beta \sim 1$), simulations using the two datasets predicted significant amounts of CaO and Ca_2SiO_4. However, less liquid contents, K_2SO_4, and Mg-based compounds were predicted using the FToxid dataset than the GTOX dataset.

2.2.2. Effect of using FToxid vs GTOX datasets in the pellet test on the predicted volatilization results at constant temperature of 1000 °C and varying bark fraction in the blend

In terms of elemental volatilization, according to Figures 3.4.e and 3.4.g, simulation using both datasets predicted full C and Cl volatilization in the form of CO_2(g), KCl(g), and K_2Cl_2(g). Both databases showed minor differences in K predicted volatilization. Na volatilization was higher using the GTOX dataset while S ones were lower. This was directly related to using LIOS solution in GTOX that dissolves the entire S, which was not the case in FToxid solution. The predicted volatilizations for the rest of the inorganic elements were negligible at 1000 °C and were omitted from Figure 3.4.

2.2.3. Effect of using ash test vs pellet test using same datasets on the predicted results at constant temperature of 1000 °C and varying bark fraction in the blend

Similar conclusions can be drawn in the two tests on the different predicted results using each database set aside. The behavior of the liquid phase, K_2CaSiO_4, $K_2Ca_6Si_4O_{15}$, Ca_2SiO_4, $Ca_3Si_2O_7$, and the minor phases were all the same in the ash as in the pellet tests when the same database set was used.

However, small differences were found by comparing the predicted solid and liquid contents between the ash and pellet tests using the same database sets. Using the GTOX set (Figures 3.4.a vs 3.4.b), the predicted range of stability of Ca_2SiO_4 was wider in the pellet test than the ash test, while the ranges of $Ca_3Si_2O_7$ and K_2CaSiO_4 were wider in ash than in pellet tests. Similarly, using the FToxid set (Figures 3.4.c vs 3.4.d), the range of stability of $K_2Ca_6Si_4O_{15}$ was wider in the ash than in pellet tests at the expanse of a tighter Ca_2SiO_4 range.

The answer for this behavior could be found in the predicted volatilizations in Figures 3.4.e to 3.4.h. From these Figures, pellet test simulations presented higher K-volatilization than the ash test using both datasets. This was directly related to the presence of H in the pellet test (biomass pellet) and its absence in the ash test (ash chips prepared at 550 °C). Consequently, more K was released into the gaseous phase in the form of KOH in the pellet tests than in the ash test simulations. As a result, in the pellet test simulation using both datasets, less K were remained in the solid phase to produce $K_2Ca_6Si_4O_{15}$ (FToxid) or K_2CaSiO_4 (GTOX). In addition, due to the higher O_2 contents in the pellet test than in the ash test, higher S volatilization was predicted in the form of SOx (SO_2 and SO_3) in the pellet test while it was negligible in the ash test.

Furthermore, in Figure 3.4, the total ash solid and liquid were predicted to increase in the pellet test but to decrease in the ash test with the increase in the bark weight fraction in the blends. In the ash test, the total ash contents were normalized at 0.5g. However, in the pellet test, the

measured ash contents were used. Consequently, the total ash solid and liquid were more dependent on the liquid contents in the case of the ash test. The latter decreased with the increase in the bark weight percentage in the ash blend at the expense of increased total volatilization (bark rich region). In contrary, the total ash solid and liquid was independent of these factors in the case of the pellet test.

2.2.4. Effect of using FToxid vs GTOX datasets in the ash test vs pellet test on the predicted results at varying temperatures in the 50-50 bark-straw blend

For the case of varying temperatures (Figures 3.5.a vs 3.5.b, 3.5.c vs 3.5.d, 3.5.e vs 3.5.f, and 3.5.g vs 3.5.h), the same conclusions that were drawn in sections 2.2.1, 2.2.2, and 2.2.3 in the case of varying bark fraction (at constant temperatures of 1000 °C) were applied. The small differences in each case (FToxid vs GTOX datasets and ash test vs pellet test) will be discussed.

In the case of varying temperatures, the conclusions of section 2.2.1 exactly apply here. However, small differences in the predicted volatilization using each dataset (Figure 3.5.e vs 3.5.g) were present compared to section 2.2.2. For instance, S, K, and Na showed a higher volatilization temperature range using GTOX than FToxid. C and H were also predicted to fully volatilize at a very low temperature (<400 °C) in the results using the two datasets, similarly to Cl (400 °C<T<700 °C).

In conclusion, in section 2.2, significant differences were evident in the predicted condensed phases and volatilizations between the two database sets at varying temperatures and bark weight fractions in the blends, especially regarding the ternary phases (K_2CaSiO_4, $K_2Ca_6Si_4O_{15}$, and $K_2Ca_2Si_2O_7$), the slag behavior, and the minor K, Mg, and Al-based compounds.

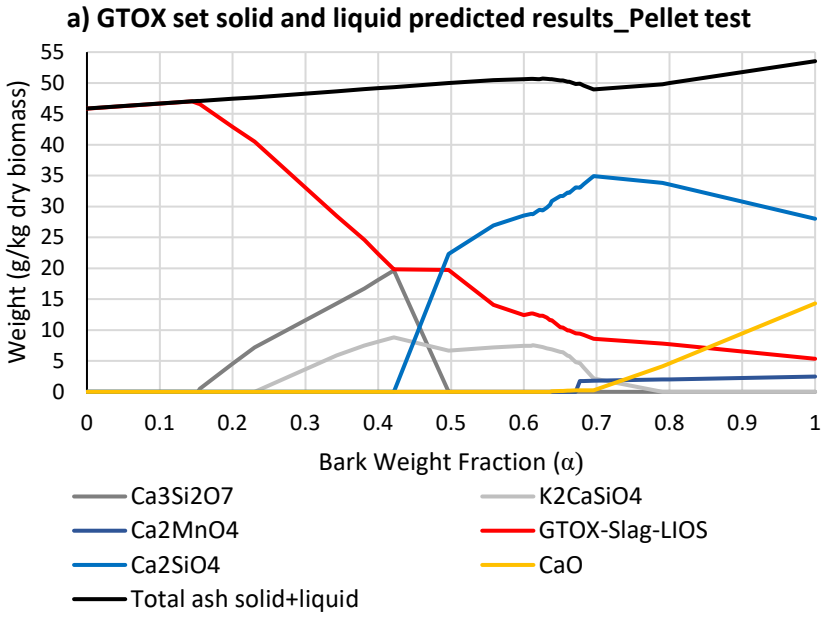
a) GTOX set solid and liquid predicted results_Pellet test
Weight (g/kg dry biomass)
55
50
45
40
35
30
25
20
15
10
5
0
0 0.1 0.2 0.3 0.4 0.5 0.6 0.7 0.8 0.9 1
Bark Weight Fraction (α)
Ca3Si2O7
K2CaSiO4
Ca2MnO4
GTOX-Slag-LIOS
Ca2SiO4
CaO
Total ash solid+liquid

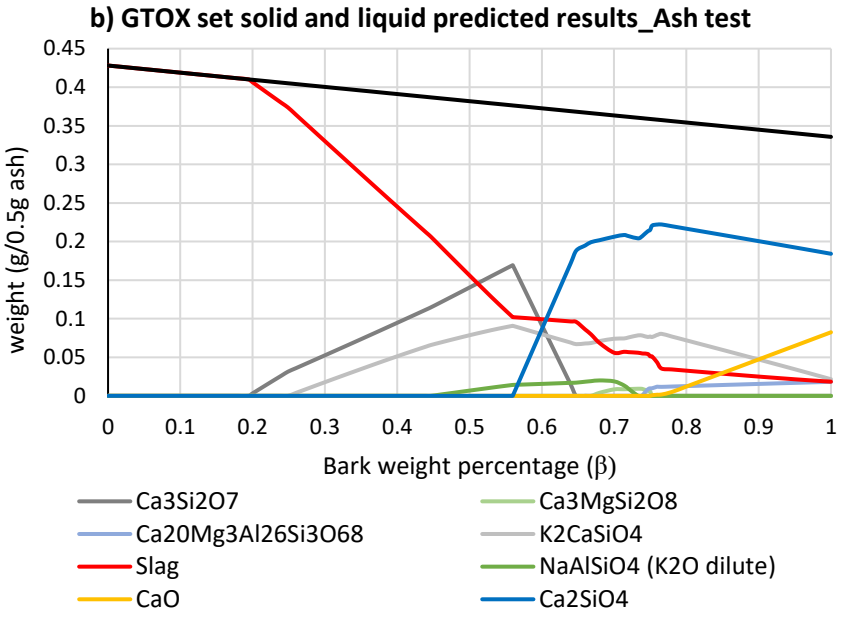
b) GTOX set solid and liquid predicted results_Ash test
weight (g/0.5g ash)
0.45
0.4
0.35
0.3
0.25
0.2
0.15
0.1
0.05
0
0 0.1 0.2 0.3 0.4 0.5 0.6 0.7 0.8 0.9 1
Bark weight percentage (β)
Ca3Si2O7
Ca3MgSi2O8
Ca20Mg3Al26Si3O68
K2CaSiO4
Slag
NaAlSiO4 (K2O dilute)
CaO
Ca2SiO4

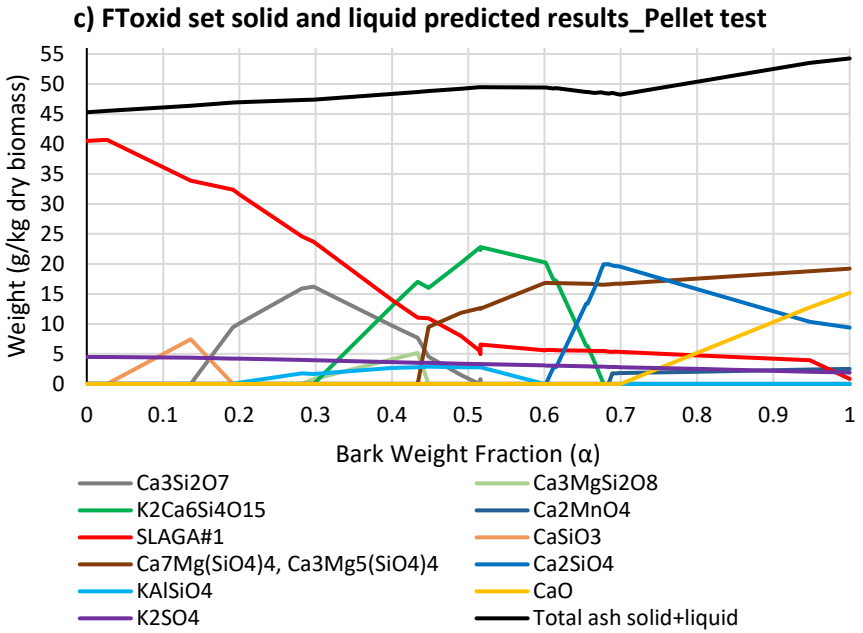
c) FToxid set solid and liquid predicted results_Pellet test
Weight (g/kg dry biomass)
Bark Weight Fraction (α)
Ca3Si2O7
Ca3MgSi2O8
K2Ca6Si4O15
Ca2MnO4
SLAGA#1
CaSiO3
Ca7Mg(SiO4)4, Ca3Mg5(SiO4)4
Ca2SiO4
KAlSiO4
CaO
K2SO4
Total ash solid+liquid

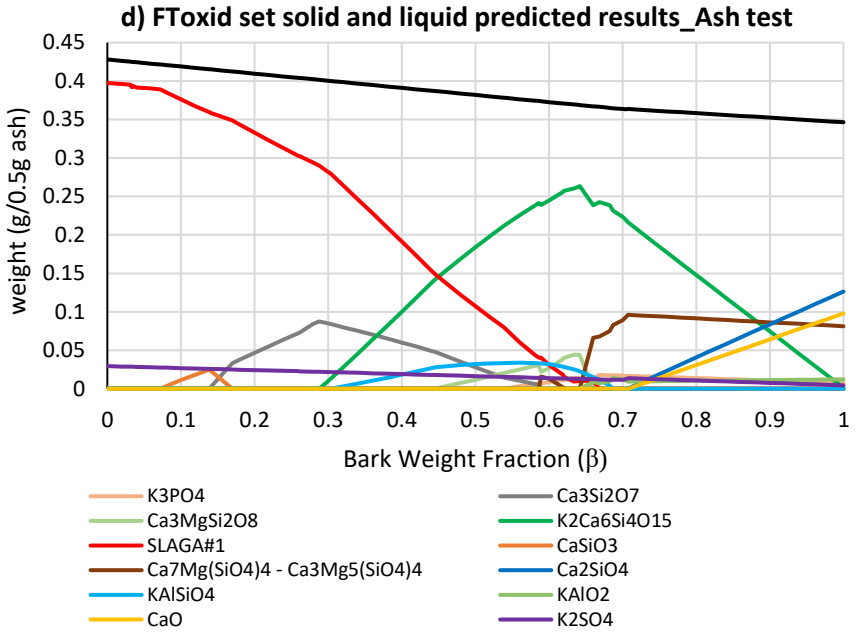
d) FToxid set solid and liquid predicted results_Ash test
weight (g/0.5g ash)
Bark Weight Fraction (β)
K3PO4
Ca3Si2O7
Ca3MgSi2O8
K2Ca6Si4O15
SLAGA#1
CaSiO3
Ca7Mg(SiO4)4 - Ca3Mg5(SiO4)4
Ca2SiO4
KAlSiO4
KAlO2
CaO
K2SO4

e) GTOX set predicted volatilization results_Pellet test

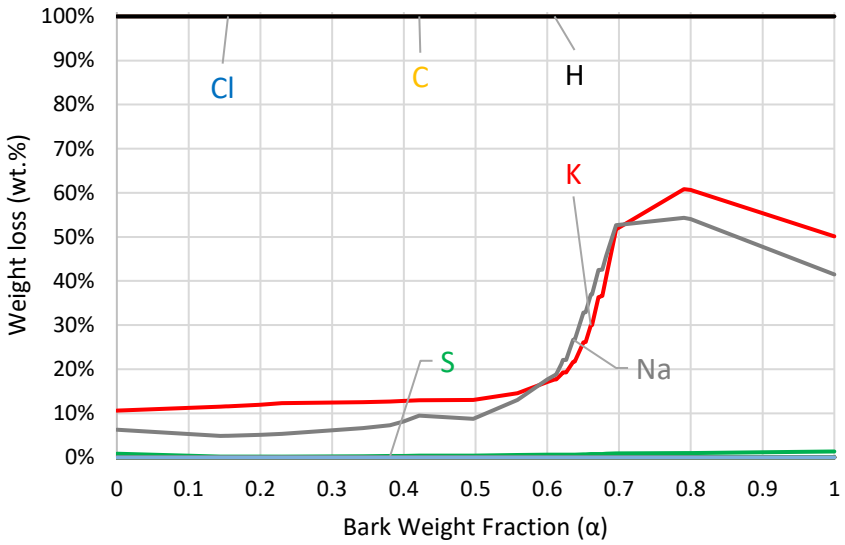

f) GTOX set predicted volatilization results_Ash test

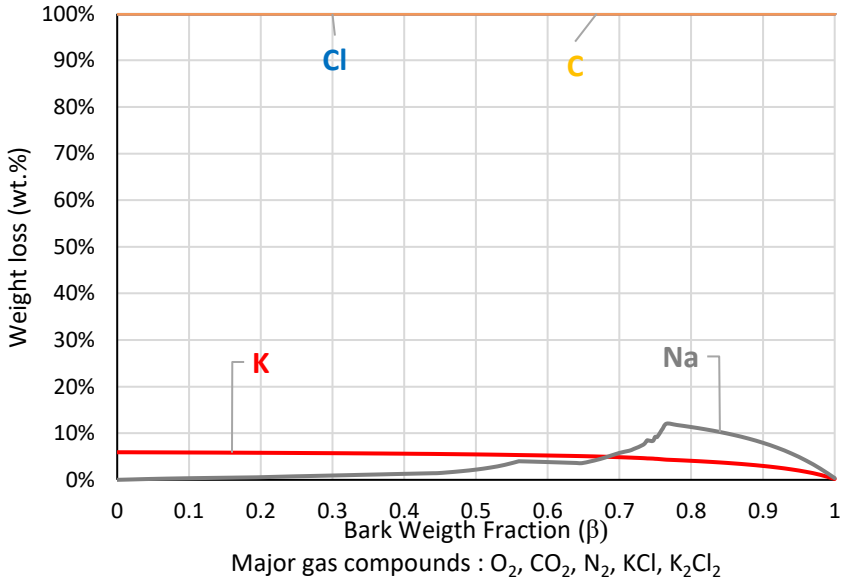

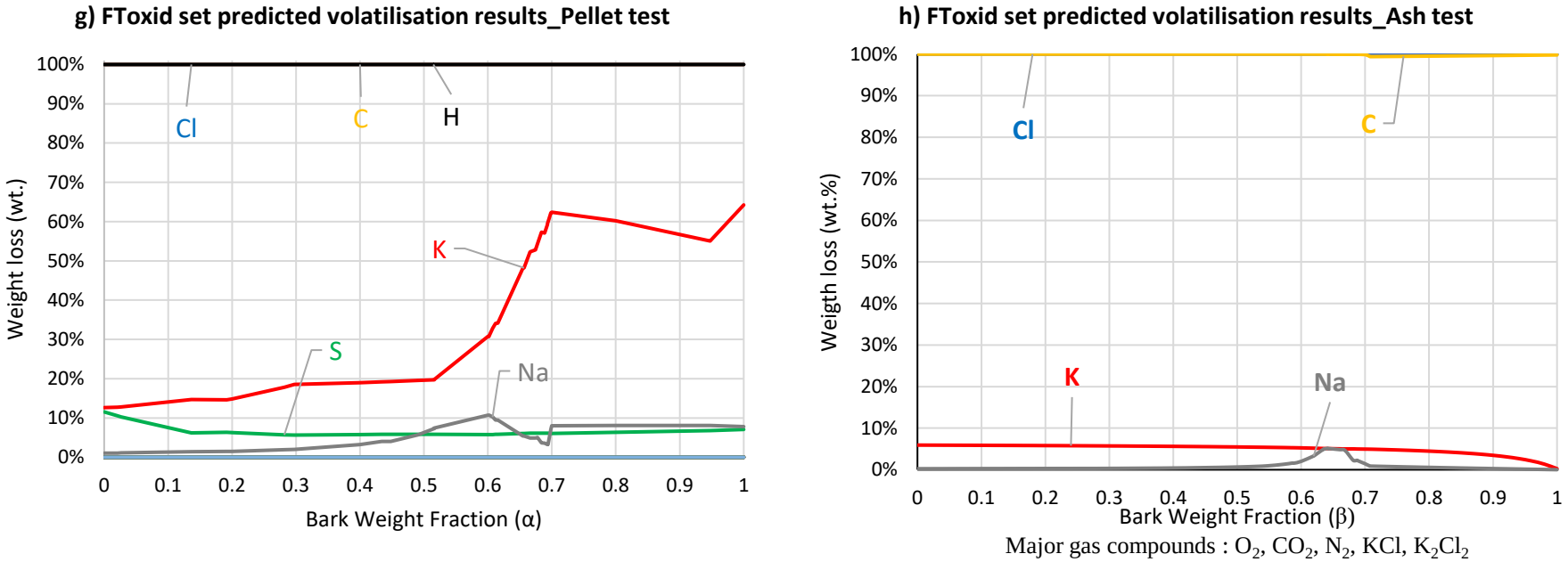

Figure 3.4: Global simulation at various BC weight fraction in WC-BC pellet and ash mixtures calculated at 1000 °C using GTOX (a,b,e,f) and FToxid (c,d, g,h) database sets

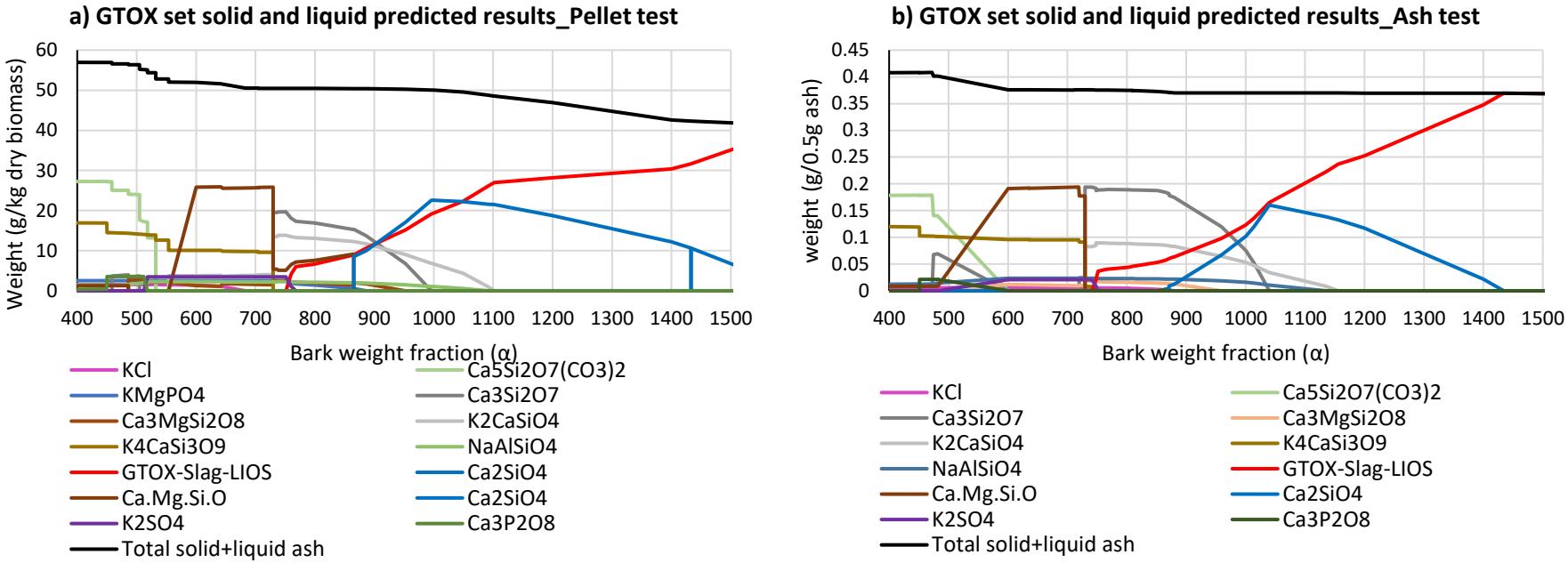
a) GTOX set solid and liquid predicted results_Pellet test
Weight (g/kg dry biomass)
Bark weight fraction (α)
KCl
KMgPO4
Ca3MgSi2O8
K4CaSi3O9
GTOX-Slag-LIOS
Ca.Mg.Si.O
K2SO4
Total solid+liquid ash
Ca5Si2O7(CO3)2
Ca3Si2O7
K2CaSiO4
NaAlSiO4
Ca2SiO4
Ca2SiO4
Ca3P2O8
b) GTOX set solid and liquid predicted results_Ash test
weight (g/0.5g ash)
Bark weight fraction (α)
KCl
Ca3Si2O7
K2CaSiO4
NaAlSiO4
Ca.Mg.Si.O
K2SO4
Total solid+liquid ash
Ca5Si2O7(CO3)2
Ca3MgSi2O8
K4CaSi3O9
GTOX-Slag-LIOS
Ca2SiO4
Ca3P2O8

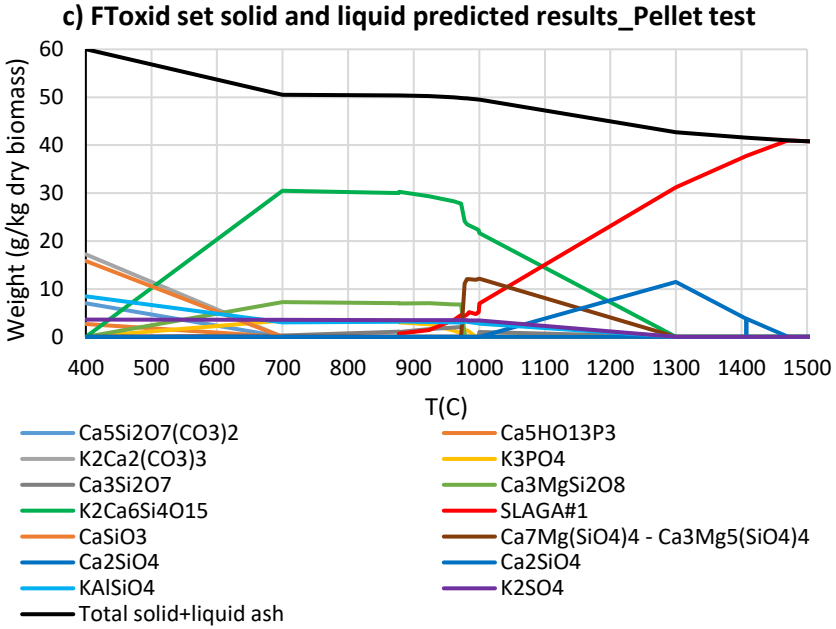
c) FToxid set solid and liquid predicted results_Pellet test
Weight (g/kg dry biomass)
60
50
40
30
20
10
0
400 500 600 700 800 900 1000 1100 1200 1300 1400 1500
T(C)
Ca5Si2O7(CO3)2
Ca5HO13P3
K2Ca2(CO3)3
K3PO4
Ca3Si2O7
Ca3MgSi2O8
K2Ca6Si4O15
SLAGA#1
CaSiO3
Ca7Mg(SiO4)4 - Ca3Mg5(SiO4)4
Ca2SiO4
Ca2SiO4
KAlSiO4
K2SO4
Total solid+liquid ash

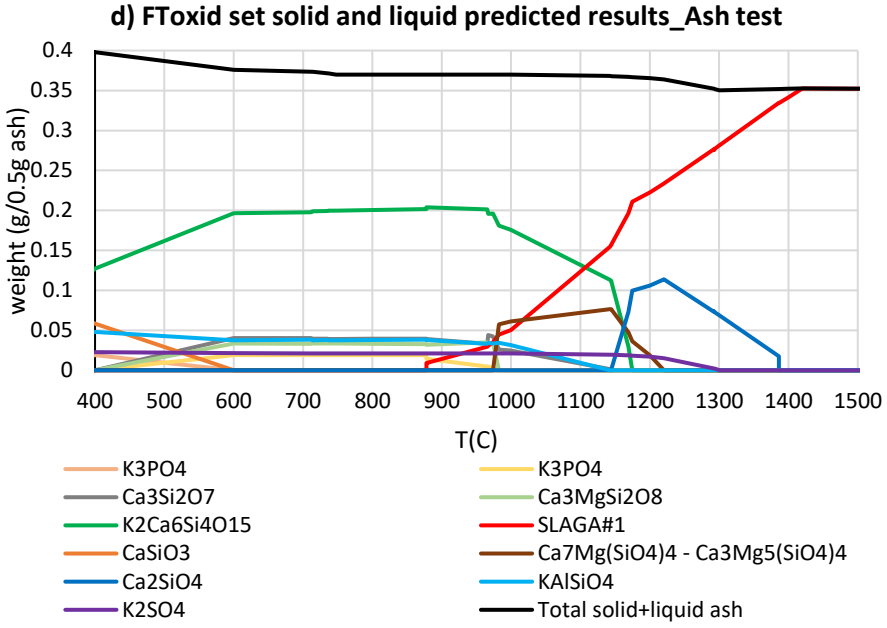
d) FToxid set solid and liquid predicted results_Ash test
weight (g/0.5g ash)
0.4
0.35
0.3
0.25
0.2
0.15
0.1
0.05
0
400 500 600 700 800 900 1000 1100 1200 1300 1400 1500
T(C)
K3PO4
K3PO4
Ca3Si2O7
Ca3MgSi2O8
K2Ca6Si4O15
SLAGA#1
CaSiO3
Ca7Mg(SiO4)4 - Ca3Mg5(SiO4)4
Ca2SiO4
KAlSiO4
K2SO4
Total solid+liquid ash

e) GTOX set predicted volatilization results_Pellet test

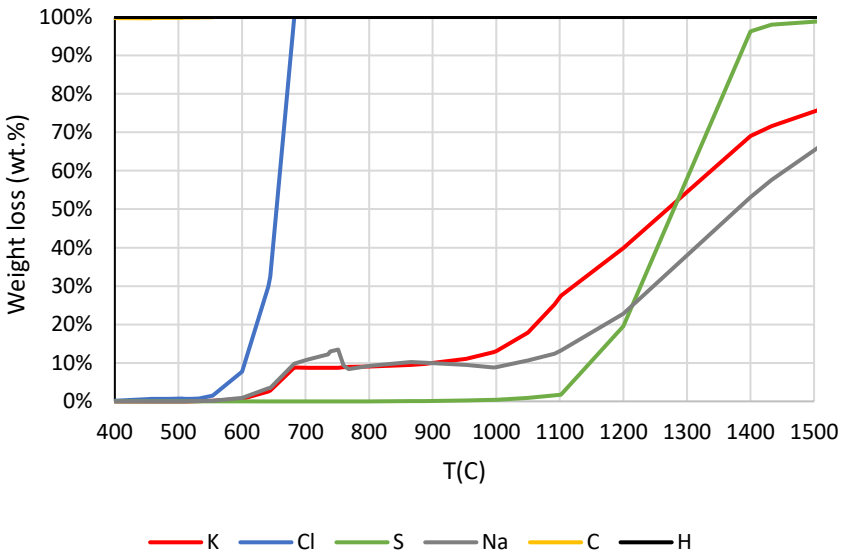

f) GTOX set predicted volatilization results_Ash test

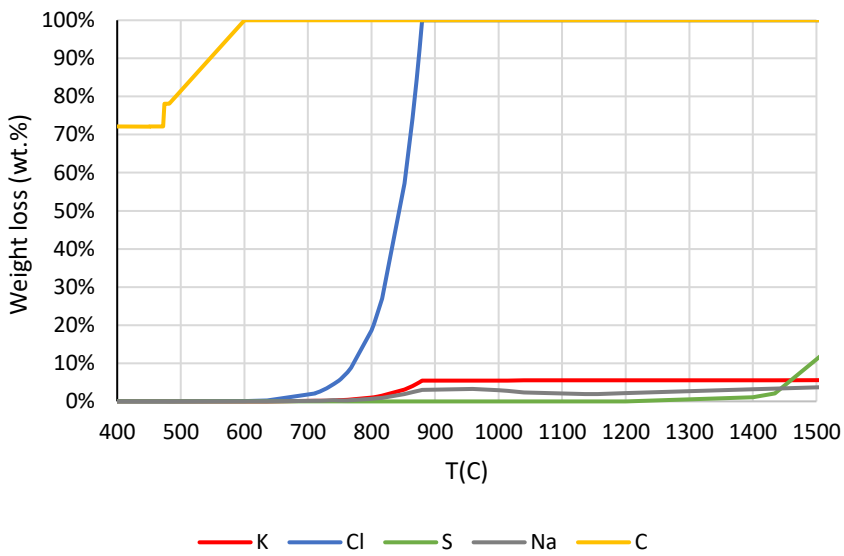

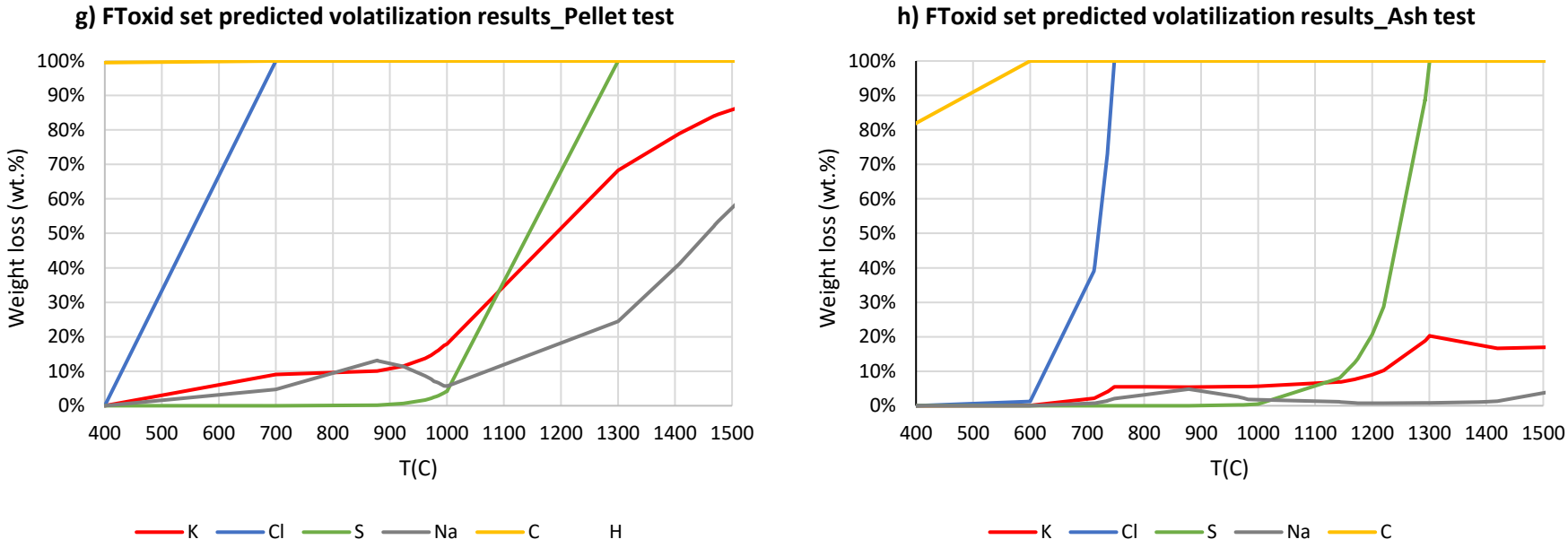

Figure 3.5: Global simulation of BCWC mixture at various temperatures in ash and pellet tests using GTOX (a,b,e,f) and FToxid (c,d, g,h) database sets.

2.3.Parameters affecting the global simulations using FToxid database set

Some differences were observed when comparing the global simulation results in Figures 3.2.b and 3.2.d (using three oxides) against those in Figures 3.4.c and 3.4.g (using all elements) in the pellet test. $K_2Ca_2Si_2O_7$ was present among the phases predicted by the simulations in Figure 3.2.b (using only 3 oxides), while it was absent from the predicted results using all elements (Figure 3.4.c) at the expense of more liquid and Ca_2SiO_4 contents. This was similar in the ash test simulations (Figures 3.2.a vs 3.4.d). In parallel, the overall K volatilization was higher in the pellet test simulations using full elements simulations (Figure 3.4.g) than using the three oxides case (Figure 3.2.d). However, K volatilization in the three elements simulation in the ash test was negligible (Figure 3.2.c) compared to a minor one in the case of the full elements simulations (Figure 3.4.h). As a result, it was clear that another inorganic element (i.e. S, Cl, Na, Mg, P, Fe, or Mn) was affecting K volatility and destabilizing $K_2Ca_2Si_2O_7$, and will be investigated in section 2.3.1. It is also worth investigating the effect of adding FTsalt to the database set and changing the slag on the predicted results using the FToxid database set (section 2.3.2).

2.3.1. Elemental addition effect on the predicted results using FToxid database set

To further investigate this effect, simulations were repeated, adding one element X (X denoted Mn, Na, Fe, Al, S, Mg, Cl, and P) to the combination C, H, O, N, Ca, K, and Si. FToxid oxide solution Slag A was always used. From the results in Appendix C.1, the addition of each new element X led to the addition of crystalline solids and solutions linked to it, like $KAlSiO_4$ and $KAlO_2$ in the case of Al (i.e. for the CHNOCaKSiAl system), $Ca_3Fe_2Si_3O_{12}$ in the case of Fe (CHNOCaKSiFe), etc. (Figure C1). Nevertheless, this single addition kept $K_2Ca_2Si_2O_7$ stable and K volatility immovable. Hence, additional elements were added simultaneously, and the results are shown in Figures C2 to C5. To simplify the comparison of these results, Table C1 was set in place. This Table shows the comparison between the individual addition of Na, P, Cl, and Mg to the set of elements (called best_O7) that consisted of Ca, K, Si, S, Fe, Al, and Mn. In this set (i.e. best_O7), the main phases (i.e. Ca_2SiO_4, Slag, $K_2Ca_2Si_2O_7$, and $K_2Ca_6Si_4O_{15}$) were all present and stable in the experimental simulations at 1000 °C.

In conclusion, $K_2Ca_2Si_2O_7$ was found to be stable in the various combinations of CHNOCaKSi with Al, S, Fe, Mn, and Na (Figure C2). However, the elements that were found to destabilize $K_2Ca_2Si_2O_7$ were P, Cl, and Mg: Mg (Figure C3) by its replacement reaction with Ca, P (Figure C4) due to its competition with K and Ca on the silicate matrix, and Cl (Figure C5) due to its reaction with K to produce KCl(g) in the gaseous phase. As a result, the simulations validated that some minor inorganic elements could affect the predicted ash behavior.

2.3.2. Effect of slag A vs slag B and adding FTsalt on the predicted results using FToxid database set

In GTOX, a slag solution phase, called LIOS, is modeled. This solution dissolves oxides, metals, sulfides, sulfates, and fluorides. Consequently, the K-bearing compounds must have dissolved within this slag phase. On the other hand, several potential liquid solution descriptions are available in the FToxid 8.1 database called Slag A or Slag B.

According to the documentation file of the FToxid database, slag A is a liquid solution of various oxides that can dissolve sulfur as sulfides. It is wider used in literature than slag B (Xiao et al. 2021; Gao et al. 2020; Liao and Zhao 2021). In contrast, the FactSage description of Slag B says that it is a liquid solution of various oxides that can dissolve sulfur as sulfates as a dilute solution with a maximum concentration of 10 wt.%. Sulfates, especially in the form of K_2SO_4, rather than sulfides, are generally found in the biomass ash. Hence, Slag B is usually chosen for feedstock rich in sulfur due to its ability to handle both silicates and sulphates interactions with various positively charged ions (Skoglund et al. 2016) and to accommodate for SO_3 dissolution (Hsieh 2019). However, according to the documentation file of the FToxid database, slag B was never optimized for the system CaO-K_2O-SiO_2. Consequently, Slag A was chosen in FToxid in all experimental simulations in this work rather than Slag B.

A detailed analysis of the effect of using Slag A vs. Slag B and adding FTSalt to the experimental simulations is presented in Appendices C.2 and C.3.

In conclusion, there is no important effect for adding the FTsalt database to FToxid database set 2. This is normal because most FTsalt phases are stable at lower temperatures (carbonates, chlorides, and sulfates). Therefore, it is advisable to use FTsalt for calculations at lower temperatures or for calculations versus temperature.

In addition, using slag B in the simulations rather than slag A destabilized several major K-rich phases found experimentally, such as $KAlSiO_4$, $K_2Ca_6Si_4O_{15}$, and $K_2Ca_2Si_2O_7$. Instead of reacting with alkaline earth-silicate compounds, K was dissolved in slag B. Hence, simulations using this slag increased the liquid contents and the amounts of some alkaline earth-silicate binary phases, such as $Ca_3Si_2O_7$ and Ca_2SiO_4. As a result, Slag A will be adopted in the rest of this work.

3. Conclusion

In this chapter, the differences between the predicted results using each database set (FToxid, GTOX), test type (ash, pellet), and prediction approach (phase diagram, global) were discussed in detail. As a result, several conclusions can be drawn as follow:

- FToxid provided a phase diagram containing more ternary compounds than GTOX, especially the addition of $K_2Ca_6Si_4O_{15}$ and $K_2Ca_2Si_2O_7$ to its database.
- For the ash test, global simulation and phase diagram approaches were similar, contrary to the pellet test.
- In the global simulation approach in pellet and ash tests, the differences in the predicted results using FToxid vs GTOX database sets can be summarized as follows:

	FToxid	**GTOX**
Liquid	less	more
Ca_2SiO_4	less	more
$Ca_3Si_2O_7$	less	more
K_2CaSiO_4	absent	present
$K_2Ca_6Si_4O_{15}$	present	absent
Mg and Al minor phases	present	absent
$CaSiO_3$	present	absent
K-based compounds	present	absent
C and Cl volatilization	total	total
K and Na volatilization	less	more
S volatilization	more	less

- Several factors affect the predicted results using the FToxid database set:

- P, Cl, and Mg destabilized $K_2Ca_2Si_2O_7$.
- Slag B destabilized several major K-rich phases.
- FTsalt addition had no effects on the predicted results

After comparing the prediction results between the two databases sets, it will be interesting to compare their findings against experimental ones. This will help refine the database choice in real-life processes predictions.

References

De Fusco, Lucio, and Francoise Defoort. 2016. “A Thermochemical Approach Based on Phase Diagrams to Characterize Biomass Ash and Select the Optimal Thermal Conversion Technology.” *Proceedings Venice2016, Sixth International Symposium on Energy from Biomass and Waste*, 2016.

Gao, Jing, Changqing Dong, Ying Zhao, Xiaoying Hu, Wu Qin, Xiaoqiang Wang, Junjiao Zhang, Junjie Xue, and Xuming Zhang. 2020. “Vitrification of Municipal Solid Waste Incineration Fly Ash with B2O3 as a Fluxing Agent.” *Waste Management* 102 (February): 932–38. https://doi.org/10.1016/j.wasman.2019.12.012.

Hsieh, Peter Y. 2019. “Sintering and Collapse of Synthetic Coal Ash and Slag Cones as Observed through Constant Heating Rate Optical Dilatometry.” *Fuel* 235 (January): 567–76. https://doi.org/10.1016/j.fuel.2018.08.055.

Kim, Donggeum. 2017. “Coupled Experimental Study and Thermodynamic Optimization of the K2O-Na2O-CaO-MgO-Al2O3-SiO2 System.” Canada: McGill University, Montreal, Quebec, Canada.

Kim, Dong-Geun, Marie-Aline Van Ende, Pierre Hudon, and In-Ho Jung. 2017. “Coupled Experimental Study and Thermodynamic Optimization of the K2O-SiO2 System.” *Journal of Non-Crystalline Solids* 471 (September): 51–64. https://doi.org/10.1016/j.jnoncrysol.2017.04.029.

Liao, Jinfa, and Baojun Zhao. 2021. “Phase Equilibria Study in the System ‘Fe2O3’-ZnO-Al2O3-(PbO+CaO+SiO2) in Air.” *Calphad* 74 (September): 102282. https://doi.org/10.1016/j.calphad.2021.102282.

Skoglund, Nils, Linda Bäfver, Johan Fahlström, Erik Holmén, and Caroline Renström. 2016. “Fuel Design in Co-Combustion of Demolition Wood Chips and Municipal Sewage Sludge.” *Fuel Processing Technology*, Fuel quality impacts on power production — The first 50 years, 141 (January): 196–201. https://doi.org/10.1016/j.fuproc.2015.08.037.

Xiao, Huixia, Yifei Wang, Jilin Li, Zebin Bao, Liying Mu, and Guangsuo Yu. 2021. “Prediction of Coal Ash Fusibility Based on Metal Ionic Potential Concentration.” *Journal of the Energy Institute* 98 (October): 29–34. https://doi.org/10.1016/j.joei.2021.04.018.

4. Chapter 4: Dilution VS reaction within the ash of biomass and their blends

As shown in chapter 1, mixing biomasses has a good potential to solve operational problems in thermochemical valorization processes related to ash behavior. However, for this mixing solution to be effective, a chemical reaction within the ash of the blends should happen. Consequently, in the present chapter, the presence of a chemical reaction compared to a simple mixing effect within the ash of the biomass mixtures was studied at the laboratory (section 1) then at pilot scales (section 2), mainly under combustion conditions. In addition, the operating conditions were varied at a laboratory scale directly on ash then on biomass (pellet) to study their effects on the reactivity of the ash within the mixtures. A prediction laboratory test for the ash behavior in the combustion pilot burners will also be proposed in this chapter.

1. Laboratory experiments

In this section, the ash behavior in the two laboratory apparatus, ash test and pellet test (shown in chapter 2 in sections 3.1.1 (ash test) and 3.1.2 (pellet test)), using BC, WC, and BCWC blend is thoroughly studied. The ash contents and compositions of these feedstock was already presented in chapter 2 in section 1.

In section 1.1, the presence of chemical reactions in comparison with simple mixing (i.e. mixing rule) within the ash of the biomass and their mixture will be assessed in detail. Then, the effects of operating conditions on the ash reactivity will be discussed (section 1.2).

1.1. Chemical reaction in comparison with simple mixing effects in the laboratory ash and pellet tests

The P-XRD results on mineralogical compositions after annealing in the ash test (i.e. using compressed ash chips) and after combustion in the pellet test (i.e. using biomass pellets) at 1000°C for 6h (after quench) are presented in Figure 4.1 for pure straw (WC), pure bark (BC), and their 50-50 wt.% biomass mixture (BCWC). In addition, the calculated results by simple mixing rule (50-50) of the mineralogical composition of the ash mixtures were also added to Figure 4.1. These calculations were based on the measured ash compositions of BC and WC in the pellet and the ash tests.

Contrary to the ash test performed in a platinum crucible, straw ash in the pellet test melted and interacted with the alumina crucible (Figure 4.2), so their P-XRD measurements were not possible. It should also be noted that access to a pt boats was impossible. Consequently, in the case of straw in the pellet test, the concentrations of the phases found when pure straw was used in the pellet test were estimated based on the results of pure straw in the pilot fixed bed reactor and in the ash test.

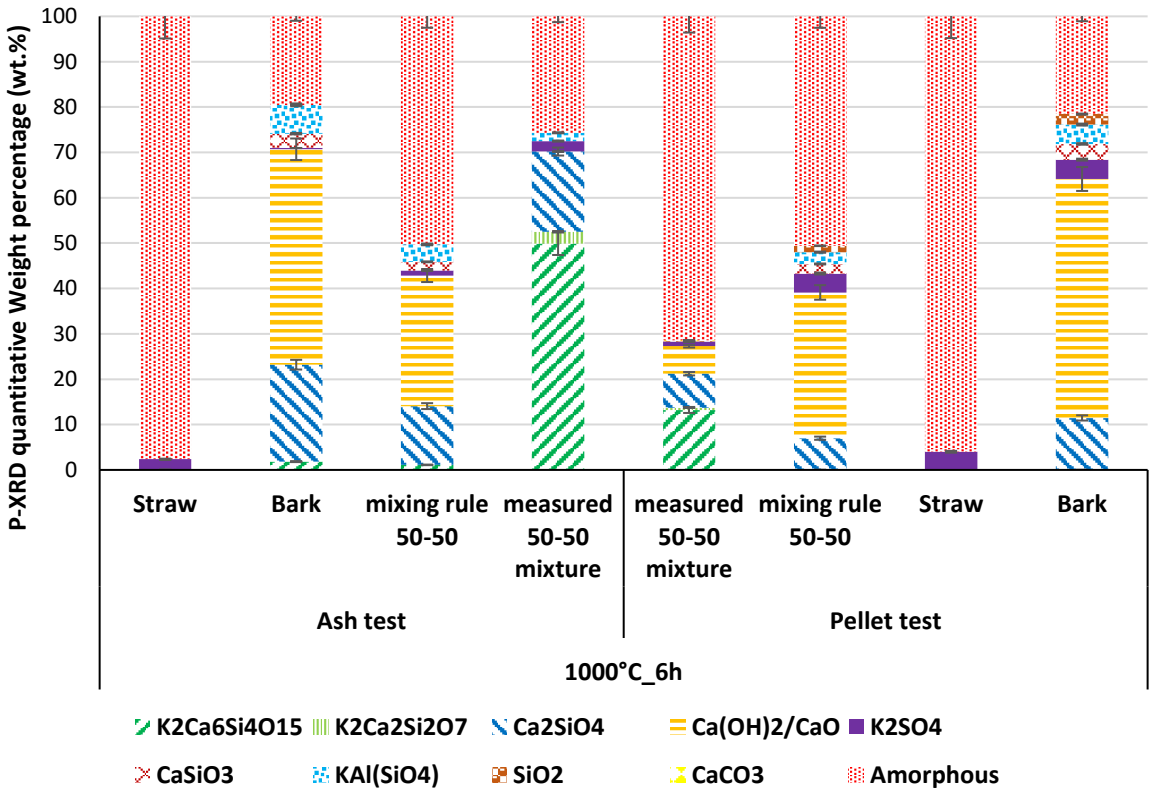

Figure 4.1: P-XRD analysis of single oak bark, single wheat straw, and their mixture at 1000 °C after 6h in the laboratory ash and pellet tests.

Figure 4.2: Straw melting and reacting with the Alumina crucible (10 cm length, 2 cum width, and 2 cm height) in the pellet test at 1000 °C and 1h.

1.1.1. In the case of single biomass

The ash reaction mechanism is complex and highly depends on the ash composition and operating conditions (Vassilev, Baxter, and Vassileva 2013; Boström et al. 2012; Rebbling et al. 2020). In the case of single biomass, a reaction within the ash can occur. From the results in Figure 4.1, in the ash test, bark produced ash-rich in solid CaO (47 wt.%) and Ca_2SiO_4 (21 wt.%) along with around just 20 wt.% of amorphous phase (the rest corresponded to minor phases). Slightly higher concentrations of CaO (53 wt.%) and amorphous phase (22 wt.%) and lower concentration of Ca_2SiO_4 (11 wt.%) were found in the pellet than in the ash test. Hence, negligible differences were noticed between the two tests in the case of single bark biomasses.

The bark ash behavior in both tests can be explained by the results in Table 2.1 in chapter 2. For instance, the bark ash contained 71 wt.% calcium in that table compared to 10 wt.% in the straw ash. On the other hand, the potassium contents in the bark ash were 7 wt.% compared to 50 wt.% in the straw ash. In parallel, Si contents reached 13 wt.% in the bark ash and 35 wt.% in the straw ash. Consequently, SiO_2 starts to gradually melt between 400 °C and 700 °C (Tsukada, Yamada, and Kamiya 2003). As a result of the abundant Ca contents in the bark, Ca easily reacted with Si to form calcium-silicate compounds. In addition, Ca is originally liberated as small micrometer-sized particles in the form of $Ca(OH)_2$, $CaCO_3$, and CaO in combustion reactors (Höfer and Kaltschmitt 2017). These particles will increase the CaO refractory character; hence, most of it will remain in the solid oxide form.

On the other hand, the amorphous phase was abundant in the straw ash samples (Figure 4.1). For instance, in Figure 4.1, the amorphous amount reached around 96 wt.% in both ash and pellet tests at 1000 °C, with minor K_2SO_4 contents (<4 wt.%). It should be noted that the majority of the amorphous phase (measured by the P-XRD in the Figures in this chapter) is ash in the liquid phase (assumed to be solidified silicate liquid), with a minority of micro-metered crystalline compounds dissolved within.

The ash behavior of straws can also be explained by their elemental inorganic composition, shown in Table 2.1 in chapter 2. From the results in this Table, around 80 wt.% of the ash of this fuel were composed of Si and K compared to 20 wt.% in bark ash (Table 2.1 chapter 2). Alkali metals (i.e. K and Na) are the less stable oxides and may be reduced by the carbon-hydrogen fuel matrix to vapor in the form of KOH(g) and NaOH(g) (Boström et al. 2012). Hence, they can react with the silicates in the matrix following an acid-base reaction to form alkali-silicate oxides (Boström et al. 2012). Then, as the fuel particles are burning out, it shrinks and the ash particles approach each other with an increasing opportunity for contact (Boström

et al. 2012; Rebbling et al. 2020). This will lead to an aggregation of the molten potassium-silicate particles, forming larger droplets and initiating slag formation.

In conclusion, in the case of single biomass, the combustion ash behavior was similar in both the ash and pellet test. Hence, the interactions between the inorganic elements, as received from nature and in ash, were the same. K-Si-rich straw ash was abundant with the amorphous phase, while Ca-rich bark ash was rich with CaO and Ca_2SiO_4 in the form of solid powder.

1.1.2. In the case of biomass blends

Chemical reactions within the ash increased when fuels were mixed. As discussed earlier in chapter 1, the occurrence of chemical reactions within the ash of biomass mixtures can be validated by:

1. New phases absent in the ash of the single feedstock appear in the ash of the blend.
2. The concentration of certain phases changes between the ash of the single feedstock and the mixture without following the mixing rule.

In this work, the chemical composition of the feedstock was significantly altered upon mixing, which was reflected for example in the change of the Ca/(K+Si) ratio from 0.1 in the straw and 3.5 in the bark to 0.9 in the fuel mixture (Table 2.1 chapter 2).

Consequently, when straw (rich in alkali-silicate oxides) was mixed with bark (rich in alkaline earth oxides), two ternary phases $K_2Ca_6Si_4O_{15}$ and $K_2Ca_2Si_2O_7$ appeared in the measured mixture in the ash test (Figure 4.1). They were not present in the single biomass trials. These results confirmed the presence of chemical reactions within the ash of the blend. In contrast with the mixing law results (i.e. mixing without chemical interaction), CaO and $CaSiO_3$ were absent in the measured XRD results of the mixture in the ash test (Figure 4.1). CaO and Ca-Si compounds in the bark ash might have reacted with the alkali-silicates in the straw ash to produce the new solid ternary crystalline compounds mentioned before.

Furthermore, in Figure 4.1, Ca_2SiO_4 (in bark) and K_2SO_4 (in straw) decreased in the mixture, in contrast to the mixing rule. Hence, another indication of the presence of chemical reactions within the blend ash was the proportion of the existing phases in the ash mixture that did not follow those calculated by the mixing rule. Most importantly, the proportion of the amorphous phase in the ash test, when following the mixing rule without chemical reaction, should be theoretically 50 wt.% in the mixture. However, its content was measured by the P-XRD to be

25 wt.% (Figure 4.1). Consequently, the chemical reactions within the ash of the biomass mixture in the ash test dominated the mixing rule effects.

Upon mixing, the low melting point alkali-silicate compounds in the straw ash can encounter the alkaline earth oxides in the bark ash. Two scenarios can happen at this point: the first leads to a substitution of K in the Si matrix by Ca to produce binary alkaline earth-silicate compounds, and the second goes through reactions between the alkaline earth metal and the alkali-silicate on the silicate matrix to form solid ternary compounds (Boström et al. 2012; Rebbling et al. 2020). In both scenarios, alkaline earth metals will be incorporated into the matrix, especially due to the high affinity of silicate melts to them. Consequently, the melting temperature of the ash would increase at the expense of decreasing the agglomeration propagation. Several authors showed several reaction pathways for this incorporation leading to more stable compounds that were seen in several studies concerning the combustion of biomass, such as $Ca_2K_2Si_9O_{21}$ in the work of Rebling et al. (Rebbling et al. 2020) and $K_2Ca_6Si_4O_{15}$ and $K_2Ca_2Si_2O_7$ in the work of Defoort et al. (Defoort et al. 2019)

Furthermore, in the results presented in Figure 4.1, lower proportions of $K_2Ca_2Si_2O_7$ and $K_2Ca_6Si_4O_{15}$ were found in the pellet test (0.5 wt.% and 13 wt.%, respectively) than in the ash test measurements (3 wt.% and 50 wt.%, respectively), similar to the results of Defoort et al. (Defoort et al. 2019). In addition, unreacted $CaO/Ca(OH)_2$ remained in the pellet test in the mixture, contrary to the ash test. This means that the bark ash did not fully react with the straw ash when the pellet test was used instead of the ash test. Measured Ca_2SiO_4 and $CaO/Ca(OH)_2$ in the pellet test were also successfully predicted by the mixing rule. Furthermore, the proportion of the amorphous phase in the pellet test mixture case was close to the one predicted by the mixing rule i.e. without reaction effect between the two biomasses (71 wt.% measured by P-XRD vs 50 wt.% calculated by the mixing rule). As a result, the ash reactivity was lower in the pellet test than in the ash test. Using compressed ash chips, the ash test provided higher physical proximity between inorganic constituents, which was thought to enhance the reactions. On the contrary, the reaction in the pellet test was less marked due to the presence of organic materials, which evaporated during combustion and left a higher porosity in the sample (i.e. lower grain proximity). Consequently, contrary to the ash test and despite the presence of chemical reactions, mixing rule effects were dominant in the pellet test.

In conclusion, in the case of blends, ash reactions were more abundant when compressed ash chips were used instead of biomass pellets. Despite their minor presence when biomass pellets were applied, mixing rule effects were more dominant. $K_2Ca_6Si_4O_{15}$ and $K_2Ca_2Si_2O_7$ were the direct crystalline products of these reactions. CaO was a major reactant in the reactions, which led to a significant decrease in the amorphous amounts.

1.2. Effect of operating conditions on ash reactivity

The variation of the crystalline and amorphous proportions in the bark-straw mixture BCWC as a function of residence time and temperature are studied for the ash and the pellet tests, respectively. For the ash test, long residence times were selected to check if the mineralogical composition stabilized, i.e. to check if equilibrium was reached (no mass transfer versus time). For the pellet test, temperature and short residence time close to the ones encountered in the pilot-scale reactors were studied in this section, and longer residence times were omitted.

It should be noted that an external k-type thermocouple was introduced in the Nabertherm LT 15/11/330 used in the pellet test and the Nabertherm RT 50-250/13 used in the ash test. It was found that the measured temperature in both furnaces in early residence times was different from the final set point temperature by ± 20 °C. Hence, laboratory experiments at 20 minutes of residence were slightly inaccurate regarding operating temperature. However, due to the high-applied temperature range and the slight temperature deviation, the results at the short residence time (i.e. 20 min) were still considered acceptable.

1.2.1. Ash test results

In Figures D.1 and D.2 (Appendix D), the measured diffractogram of each ash test that was performed for different residence times at 850 °C, 1000 °C, and 1200 °C with the bark-straw mixture (BCWC) are shown. The quantification of the crystalline and amorphous proportions in BCWC as a function of residence time and temperature are shown in Figure 4.3.

It is observed in Figure 4.3, the proportion of $K_2Ca_2Si_2O_7$ (light green) increased by 4 wt.% at 850 °C while it decreased from 13 wt.% to 1 wt.% at 1000 °C with the increase in residence time. By comparing the results between 24 h and 6 h at 850 °C, similar phase proportions were found. Hence, a steady state was reached at 850 °C after 24 h annealing, which was assumed to be the equilibrium condition in this case.

The amount of $K_2Ca_6Si_4O_{15}$ (dark green) peaked at around 50 wt.% (i.e. equilibrium is reached when mass transfer ceased) at 1000 °C and 5 h to 6 h, conditions that were considered as optimum for this type of mixture. Most importantly, the appearance of $K_2Ca_6Si_4O_{15}$ was always

conjugated with a decrease in the amorphous phase. For instance, in Figure 4.3, the increase of $K_2Ca_6Si_4O_{15}$ from 8 wt.% to 51 wt.% was conjugated with a decrease in the amorphous concentration from 43 wt.% to 26 wt.% as residence time increased from 20 min to 40 h at 1000 °C.

The increase in $K_2Ca_6Si_4O_{15}$ at the expense of $K_2Ca_2Si_2O_7$ proportions at 1000 °C in this work supports the reactant-product reversible reaction pathway between these two crystalline compounds, as presented in the work of Santoso et al. (Santoso et al. 2020). In their work, Santoso et al. suggested the reaction of $K_2Ca_2Si_2O_7$ with calcium-silicate compounds to produce $K_2Ca_6Si_4O_{15}$ (Santoso et al. 2020). In another formation mechanism, the calcium alkaline earth metals in the bark can react with potassium-silicates in the straw to produce this phase. Either way, the formation of $K_2Ca_6Si_4O_{15}$ decreased the available amounts of silicates that can react with potassium, limiting the amorphous phase formation. Consequently, when using bark-straw biomass mixture in a furnace or a FB, mixture formulation and reactor operation should be directed in a way to obtain the highest proportion possible of $K_2Ca_6Si_4O_{15}$.

Similar amounts of Ca_2SiO_4 were also present in all samples. Minor proportions of $CaO/Ca(OH)_2$ were observed at 850 °C and 1000 °C at short residence times, but this compound was absent at 1000 °C and long residence times (5 h) and at 1200 °C. This, in turn, supports the finding that the reaction was complete and steady-state (assumed to be equilibrium state) was reached for 1000 °C at 5 h and 1200 °C at around 3 h.

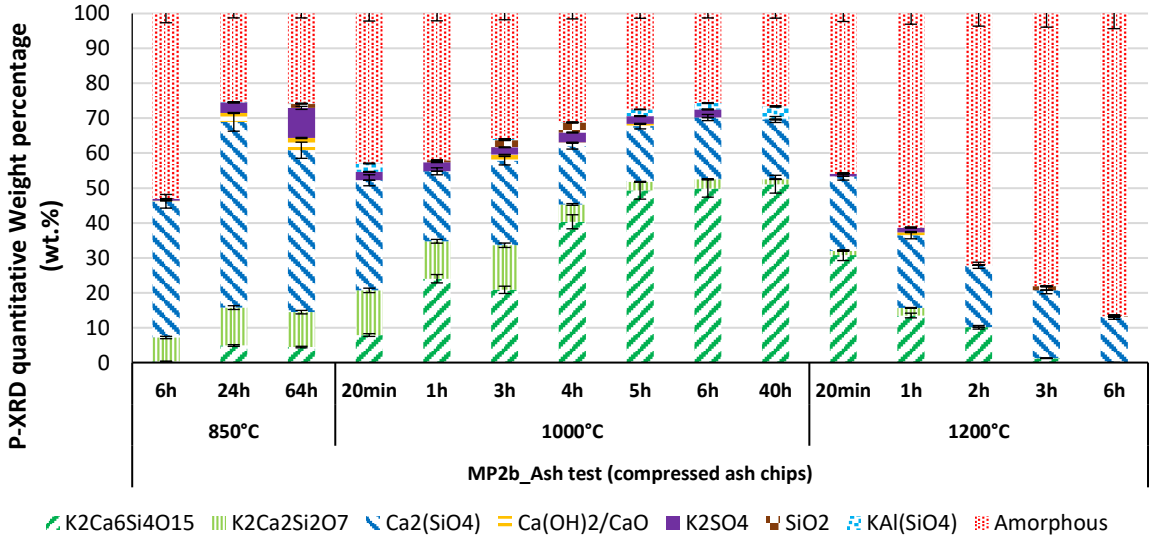

Figure 4.3: P-XRD results of the ash test for the bark-straw mixture (BCWC) at various temperatures and residence times.

As shown in Figure 4.3, with the increase in residence time at 1200 °C, a steady state was approached after around 3h, conditions at which $K_2Ca_6Si_4O_{15}$ and $K_2Ca_2Si_2O_7$ were decomposed. To validate this decomposition, SEM-EDX analysis, as presented in Figure 4.4, showed the variation of the phases at 1200 °C between 20 min (Figure 4.4.a) and 6h (Figure 4.4.b) in the BCWC biomass mixture for each different shape, and the results were also compared to the ones of Chen et al. (Chen et al. 2016). Electron probe X-ray microanalysis (EPMA) techniques were used in their work, starting from various mixtures of $CaCO_3$-K_2CO_3-SiO_2 (Chen et al. 2016). They provided EPMA pictures for the crystalline phases of interest (Chen et al. 2016).

Following the results in Figure 4.3, the ternary phases of interest, $K_2Ca_6Si_4O_{15}$ and $K_2Ca_2Si_2O_7$, were present at 20min in Figure 4.4.a but absent at 6 h in Figure 4.4.b at 1200 °C. According to the EDX analysis and similarly to the findings of Chen et al. (Chen et al. 2016), $K_2Ca_6Si_4O_{15}$ has a rectangular-oval shape while $K_2Ca_2Si_2O_7$ looks like long sticks and Ca_2SiO_4 was characterized by a circular shape.

For the case of 20 min residence time (Figure 4.4.a), the sample was highly heterogeneous, while the one at 6 h was characterized by its higher homogeneous propensity. The equilibrium, supported by the P-XRD results in Figure 4.3, might have affected this varying morphology transforming a heterogeneous structure into a more homogenous one as it was reached. $K_2Ca_6Si_4O_{15}$ in the 20 minutes sample (Figure 4.4.a) was highly surrounded by amorphous layers, which refers to its possible disappearance at 1200 °C with increasing time (i.e. as equilibrium was approached) by fusion and reaction with elements in the liquid phase.

Finally, the impact of the observed cooling rates on the final mineralogical compositions between slow (~0.05 °C/s) and fast (~5 °C/s) cooling in the ash test was negligible.

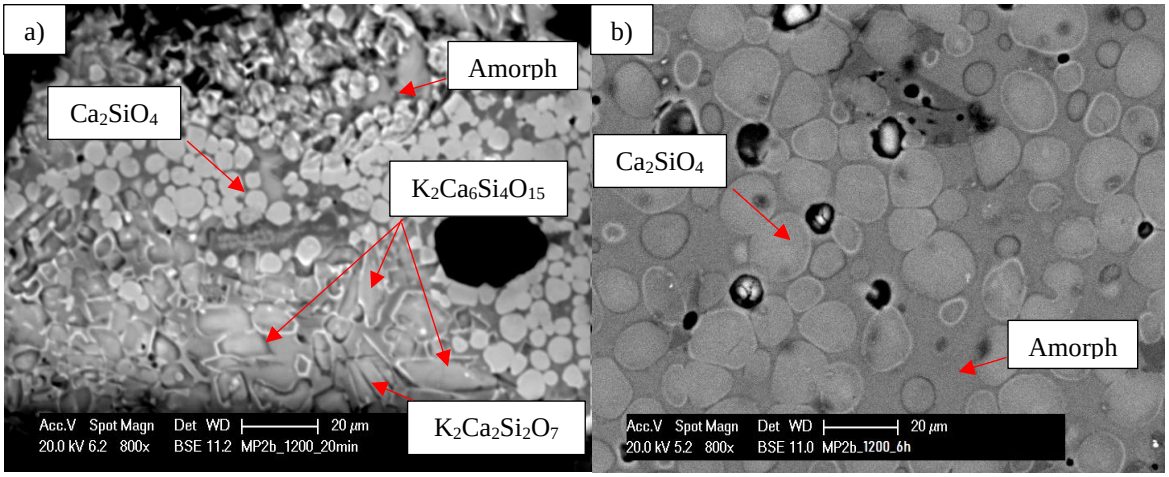

Figure 4.4: SEM-EDX analysis between 20min (a) and 6h (b) for the bark-straw mixture (BCWC) at 1200°C in ash test.

In conclusion, in the case of the blend, equilibrium was reached at 850 °C (24 h), 1000 °C (6 h), and 1200 °C (6 h) within the ash test. A reversible reactant-product reaction pathway existed between $K_2Ca_2Si_2O_7$ and $K_2Ca_6Si_4O_{15}$. $K_2Ca_6Si_4O_{15}$ relative proportion was inversely proportional to the amorphous phase. Its concentration peaked at 1000 °C, at which equilibrium (steady-state) was reached after 6 h. However, both ternary compounds existed at a lower proportion at 850 °C and disappeared at 1200 °C.

1.2.2. Pellet test P-XRD results

In Figure D.3 (Appendix D), the measured diffractogram of each of the pellet test for the bark-straw mixture (BCWC) is shown. The quantification of the crystalline and amorphous proportions in the BCWC blend as a function of residence time and temperature are shown in Figure 4.5.

The two ternary compounds $K_2Ca_6Si_4O_{15}$ and $K_2Ca_2Si_2O_7$ in the pellet test, as visible in Figure 4.5, showed similar behavior to those in the ash test in Figure 4.3 with respect to temperature (at 850 °C and 1000 °C) and residence times. However, their proportions were significantly lower than the ash test. This was due to the lower reactivity in the pellet test, as explained in section 1.1. This lower reactivity was also visible in the negligible change in the amorphous phase proportion and its constant high proportion, along with the constant presence of CaO under all operating conditions. Hence, due to this lower reactivity level and in contrast with the ash test, the effects of operating conditions on ash reactivity of biomass mixtures in the pellet test were less significant.

Though by comparing the composition of the samples between 850 °C and 1000 °C at the same residence time (20 min then 1 h), the mineralogical compositions changed, which can be

attributed to an increased reactivity with temperature since $CaCO_3$ present at 850 °C was calcined to CaO at 1000 °C and 20 min then reacted. Four-time less CaO was found at 1000 °C after 1 h, while four-time more $K_2Ca_6Si_4O_{15}$ was found due to chemical reaction, but both with low overall concentrations. The pellet test will probably never reach a complete equilibrium state since the distance between the inorganic particles will never be close enough to each other and due to the presence of the organic matrix in the samples, contrary to the case of the ash test.

Finally, Defoort et al. (Defoort et al. 2019) showed that the pelletizing parameters (pellet compression rate) did not affect the ash reactivity.

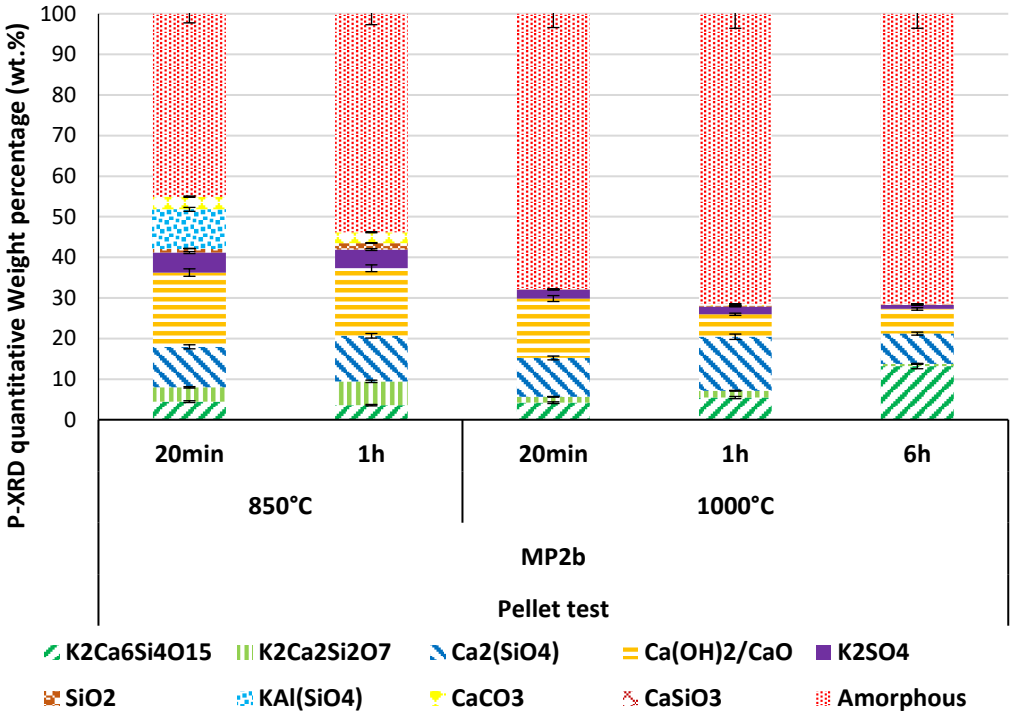

Figure 4.5: P-XRD results of the pellet test at various temperatures and residence times in the 50-50 blend BCWC.

In conclusion, in the case of the blend, the two ternary compounds, $K_2Ca_6Si_4O_{15}$ and $K_2Ca_2Si_2O_7$, were found in the pellet test, but at significantly lower proportions than in the ash test. Due to the lower reactivity in the pellet than in the ash test, CaO was always present, and the amorphous contents insignificantly changed with the change in the temperature and the residence time.

1.2.3. Pellet test sieving results

The particle size distribution was analyzed using the sieving method, as described in section 4.3 in chapter 2. The sieving fractions of the produced ash from the BCWC mixture under the various operating conditions are shown in Figure 4.6. Particles smaller than 630 µm refer to

solid powder, whereas those bigger than 900 µm are considered as being agglomerates, which contain solidified liquid ash. Similar approach was used in literature (Vega-Nieva, Alvarez, and Ortiz 2014; Rodríguez et al. 2020; Defoort et al. 2019; Steenari et al. 2009). Hence, the concentrations of the amorphous phase and the ones of agglomerates are directly correlated and proportional. As a result, sieving measurement is another method than P-XRD to quantify the total contents of the ash in the liquid and solid states.

It can be seen from the results in Figure 4.6 that in the pellet test for the case of the 50-50 bark-straw mixture, the fraction of the large particle size (agglomerates > 900 µm) increased with the increase in residence time. It can also be seen that temperature affected the formation of agglomerates by comparing the pellet test between 850 °C and 1000 °C under a fixed residence time of 1 h, where the large particle size fraction significantly increased from 38 wt.% to 57 wt.%.

In Figure 4.6, agglomerates' weight fractions above 900 µm at 1000 °C were 60 wt.% at 20 min, 55 wt.% at 1 h, and 83 wt.% at 6 h. In comparison, from Figure 4.5, the amorphous phase fraction quantified by P-XRD for the pellet test under the same operating conditions were 68 wt.%, 71 wt.%, and 71 wt.%, respectively. Hence, the differences between the two methods were 13%, 29%, and 14%, respectively, meaning a difference of around 20%. Considering the small sample weights used in the sieving of the pellet test that can induce several measurement errors and the fact that agglomerates entrap a certain amount of crystalline phases, it can be said that both methods can be, to a certain extent, used for amorphous quantification. However, the PXRD-internal standard-Rietveld refinement methodology performed better than the sieving one.

In conclusion, for a bark-straw blend tested in the pellet test, the amorphous fraction increased with the temperature and residence time increase. In addition, the sieving distribution method can be used in parallel with the P-XRD analysis for amorphous and total solid-phase ash quantification.

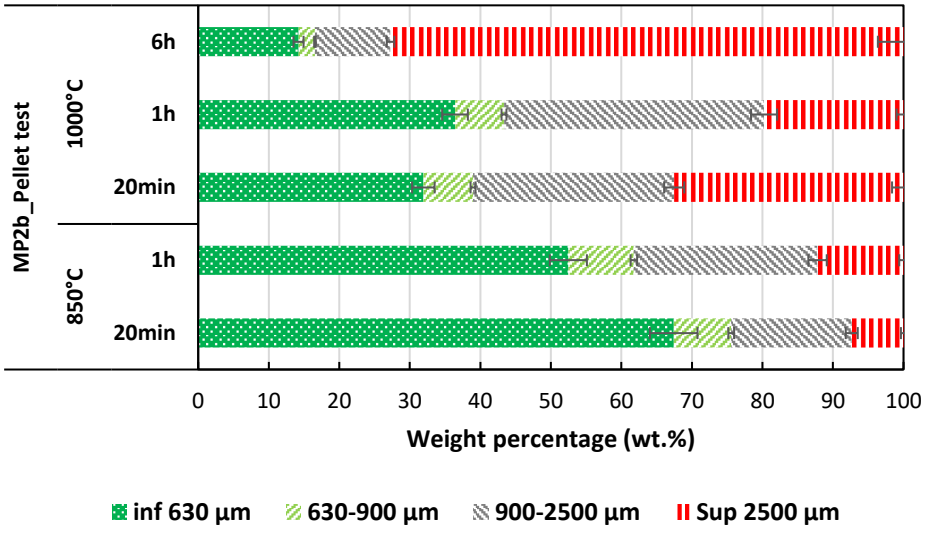

Figure 4.6: Particle size distribution of the pellet test for the bark-straw mixture MP2b (BCWC) under various operating conditions.

2. Pilot experiments

In this section, the ash behavior of biomass and their mixtures was investigated in pilot-scale reactors. In section 2.1, BC, WC, and BCWC blend were used in a fixed bed combustion burner while BCWC was applied in a moving bed combustion reactor. Their ash behavior is studied based on the P-XRD analysis in section 2.1.1 and the sieving results in section 2.1.2. A comparison with the pellet test results was also conducted to test the prediction capabilities of the latter. Then, in section 2.2, BCWC was used in a fluidized bed reactor in both gasification and combustion modes. Based on P-XRD (section 2.2.1) and sieving (section 2.2.2) analyses, a detailed ash analysis behavior was studied.

2.1.Combustion in pilot burners

The detailed experimental setups of the two combustion burners were presented in section 3.1.4 in chapter 2.

2.1.1. Operating conditions of the boilers

In the moving grid pilot reactor, the temperature was not measured. However, after thorough discussions with the engineer who conducted the experiments, the operating temperature was estimated to be in the range of 900 °C ± 20 °C and the residence time around 20 min ± 3 min. On the other hand, in the fixed bed reactor, residence time was around 1h40min (the time left and shown in Figure 4.7 corresponding to the cooling time). In addition, the temperature distribution measured by each thermocouple using each type of biomass inside the fixed bed reactor is depicted in Figure 4.7.

The average (between T1, T2, and T3) combustion temperature (0 min < t < 80 min) was measured and was found to be 700 °C when wheat straw was applied (Figure 4.7.a), 950 °C when the bark was used (Figure 4.7.b), and around 1000 °C in the case of the blend (Figure 4.7.c). It should be noted that no uncertainty was calculated due to the absence of duplicates. Nevertheless, thermocouple T1 was fixed closer to the primary air entrance than T2 and T3. Hence, it was able to reflect the real temperature of the combustion zone more accurately.

The temperature inside the combustion chamber was a function of the excess air ratio and the biomass feed. It was controlled by changing these two parameters in a way to keep the gaseous emissions within their tolerable range, i.e. keeping CO emissions below 150 mg/Nm^3 and NO_x below 250 mg/Nm^3. However, the slag formation inside the chamber can block the reactor and lead to poor combustion, increasing the gaseous emissions. Consequently, the temperature inside the combustion chamber will be decreased. The main gaseous emissions in both pilot reactors are presented in Figure 4.8.

For instance, 78 wt.% of the ash of wheat straw was composed of Si and K (Table 2.1 chapter 2). As explained in section 4.2 in chapter 1, the high alkali contents in the biomass ash will react with the silica matrix and significantly lower the ash melting point (Boström et al. 2012). In parallel, wheat straw is known to melt between 400 °C and 960 °C, reaching severe melting at temperatures between 680 °C and 780 °C (Link, Yrjas, and Hupa 2018). As a result, due to their high sintering level, straw melted at low temperature and caused poor combustion. Accordingly, from the results in Figure 4.8, the straw emissions reached as high as 600 mg/Nm^3 of CO (fourth the limitations) and as high as 480 mg/Nm^3 for NO_x (twice the limitation). Consequently, the combustion temperature inside the reactor chamber remained low (~ 700 °C on average) to account for the increased emissions.

On the other hand, 71 wt.% of bark ash was made of Ca (Table 2.1 in chapter 2). Hence, the high calcium contents will stabilize the melting behavior of the ash and increase its melting point (Boström et al. 2012). In parallel, the bark is known to have a high melting temperature above 1000 °C (melting 1060 °C-1500 °C) (Thy et al. 2006; Link, Yrjas, and Hupa 2018)). Accordingly, from Figure 4.8, CO emissions easily stayed within their acceptable range (30 mg/Nm^3). Consequently, the average temperature in the reactor chamber in the case of bark attained 1000 °C. Though, the NO_x emissions peaked at this very high operating temperature.

When the bark was mixed with the straw, Ca contents increased to 42 wt.% compared to the straw. Consequently, more Ca was added to the alkali-silica matrix, increasing the melting point

of the ash blend. In addition, the increased ash interactions in the blend also affected the slag formation. In sections 2.1.1 and 2.1.2, the ash behavior in the pilot reactor will be further elaborated based on P-XRD and sieving analysis. As bark, BCWC (called MP2b in Figure 4.8) emissions were low in terms of CO but high in terms of NO_x. In addition, the reactor chamber temperature was also high.

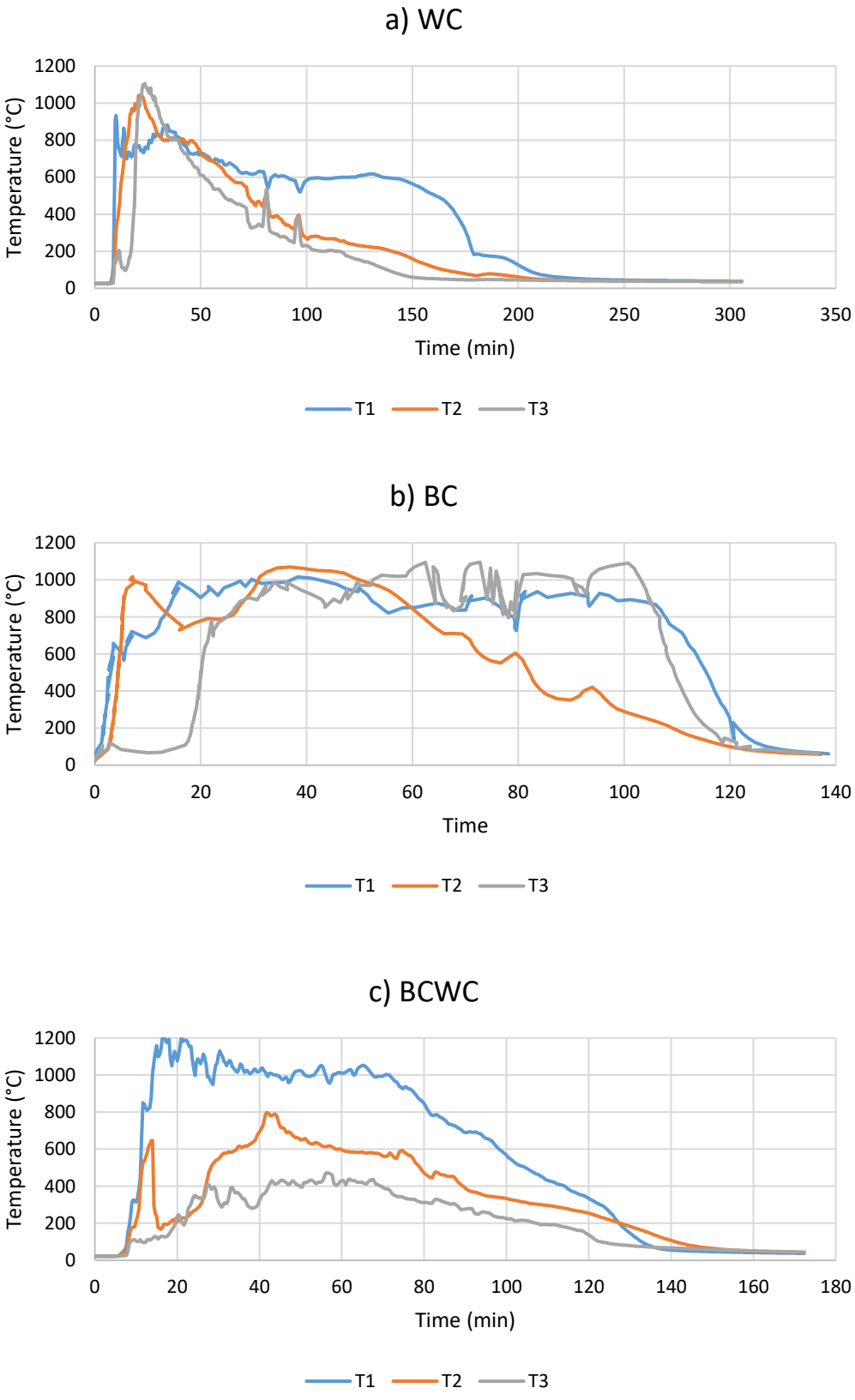

Figure 4.7: Instantaneous temperature measured by T1, T2, and T3 in the fixed bed pilot reactor trials using WC (a), BC (b), and BCWC (c).

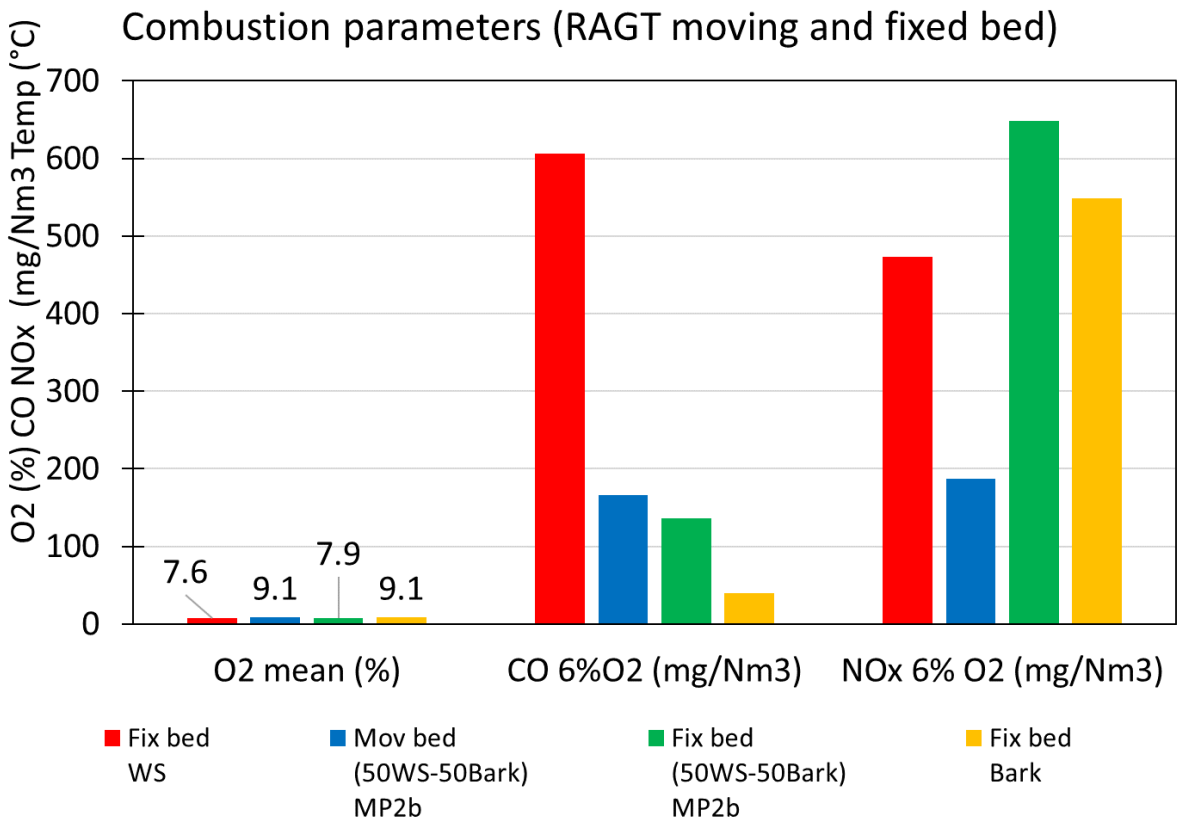

Figure 4.8: Gaseous emissions in the fixed and moving bed pilot reactors for straw (WC) bark (BC) and mixture MP2b (BCWC)

2.1.2. Combustion burner ash analysis by P-XRD

The P-XRD results of the ashes collected after the pellet combustion of single biomass (bark, straw) and 50-50 bark-straw mixture in the fixed and moving bed combustion pilots are shown in Figure 4.9. Moreover, this figure shows the results of the mixing rule calculated from the ashes collected from the fixed bed pilot test using every single feedstock.

It is observed that in the fixed bed pilot, straw was rich in amorphous contents (95 wt.%) while the bark was more abundant with CaO (31 wt.%) and Ca_2SiO_4 (21 wt.%). $K_2Ca_2SiO_7$ (first ternary phase) and $K_2Ca_6Si_4O_{15}$ (second ternary phase) were absent or negligible in the ash of the single straw and single bark. However, $K_2Ca_2SiO_7$ and $K_2Ca_6Si_4O_{15}$ were both identified in the samples of the biomass mixture after experiments in both pilot reactors. CaO calculated to be at 22 wt.% by the mixing rule in the blend was measured at around 5 wt.% in the fixed bed reactor and 7 wt.% in the moving grid reactor. Ca_2SiO_4 and amorphous contents were predicted to be 15 wt.% and 52 wt.% by the mixing rule calculation. In comparison, they were measured at 19 wt.% and 60 wt.% in the fixed bed reactor and 10 wt.% and 69 wt.% in the moving grid pilot reactor.

Hence, similarly to the laboratory pellet test experiments, despite the abundance of the mixing effect without interaction, some reaction within the ash took place in both pilot reactors.

Both pilots used the same biomass pellets of the laboratory pellet test. Hence, the pellet test, specifically at 1000 °C for 20 minutes and 1 h can be used to possibly simulate/predict the pilot-scale ash behavior. Pellet test P-XRD results of BCWC at 1000 °C and 1 h in Figure 4.5 were close to the ones measured on pilot scale (Figure 4.9), recording 71 wt.% amorphous phase, 5 wt.% $K_2Ca_6Si_4O_{15}$, 5 wt.% CaO and 13 wt.% Ca_2SiO_4. Similarly, close phase distributions were exhibited in the case of single biomasses by comparing the results in Figures 4.1 and 4.9.

In chapter 1 section 6.1, several laboratory prediction tests were discussed, such as the Bioslag test (Rodríguez et al. 2020), TGA-DTA (Rizvi et al. 2015), ash fusion test (SS ISO-540) (Gilbe et al. 2008), and more. However, The typical limitations of these tests are that they are usually time-consuming, were rarely compared to results obtained on a pilot scale, and depended on the feedstock, reactor type, and operating conditions (Rodríguez et al. 2020; Link, Yrjas, and Hupa 2018; Rizvi et al. 2015; Gilbe et al. 2008). Though the current pellet test suffers from the same limitations, its main advantage is that it was validated with pilot-scale results. Hence, its results are more reliable.

Consequently, despite the scale increase between the pellet test and the pilots, the pellet test showed great prediction capabilities for the pilots in terms of crystalline and amorphous phases' fractions for both single feedstock and their biomass mixture.

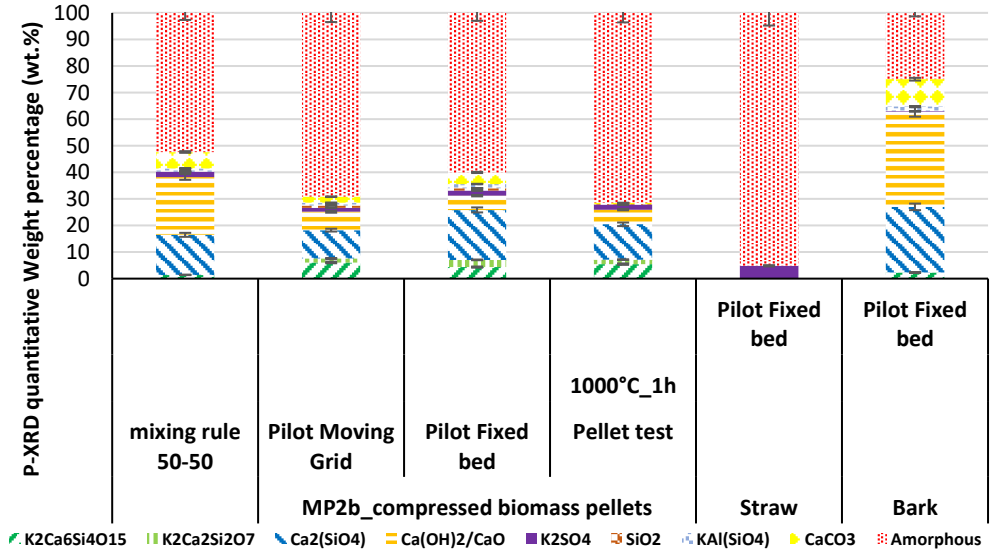

Figure 4.9: P-XRD average crystalline and amorphous distribution in pilot boiler reactors for straw (WC) bark (BC) and mixture MP2b (BCWC).

2.1.3. Combustion burner ash analysis by sieving

Similar to section 1.1.3, the sieving fractions of the produced ash from the fixed and moving bed reactors were plotted for the single bark, single straw, and BCWC mixture in Figure 4.10. Furthermore, the mixing rule was also calculated from the ashes of the single biomass of the fixed bed reactor and plotted in the same Figure.

Particles smaller than 630µm are considered solid powder, whereas those bigger than 900µm are considered agglomerates. Straw was problematic if applied in a furnace since more than 75 wt.% of it showed significant agglomeration (>2500µm) and around 84 wt.% total agglomeration (>900µm). Bark was ideal for furnace combustion application since more than 60 wt.% of it remained as a solid powder (<630µm). Without chemical reaction (i.e. mixing rule is valid), significant agglomeration should theoretically be in the range of 50 wt.% (>2500µm) and total agglomeration around 60 wt.% (>900µm). However, the presence of chemical reactions within the ash of the feedstock mixture further enhanced the decrease of the significant agglomeration to less than 25 wt.%, (>2500µm) and total agglomeration to around 50 wt.% (>900µm), on average. This made the application of straw in the pilot boiler less problematic when mixed with bark.

It should be noted that the mass of agglomerate fractions above 900µm of bark, straw, and the biomass mixture of both pilot reactors in Figure 4.10 were close and proportional to the amorphous phase fraction quantified by PXRD in Figure 4.9 (95 wt.% in Figure 4.9 VS 84 wt.% in Figure 4.10 for straw, 25 wt.% in Figure 4.9 VS 37 wt.% in Figure 4.10 for bark, 65 wt.% in Figure 4.9 VS 53 wt.% in Figure 4.10 for the mixtures on average). Hence, both methods can provide amorphous / agglomeration quantification. In parallel, from the sieving fractions of the pellet test at 1000 °C and 1 h for the mixture case in Figure 4.6, the total agglomeration was measured to be 57 wt.% while the one of pilots in Figure 4.10 was measured to be 53 wt.% on average. Hence, the pellet test was also able to predict the agglomerates' proportion of the pilot reactors.

In conclusion, similar to the pellet test case, sieving and P-XRD analysis methods provided similar amorphous / agglomeration quantification. In addition, from the sieving results, the pellet test could also predict the agglomerates' proportion of the pilot reactors.

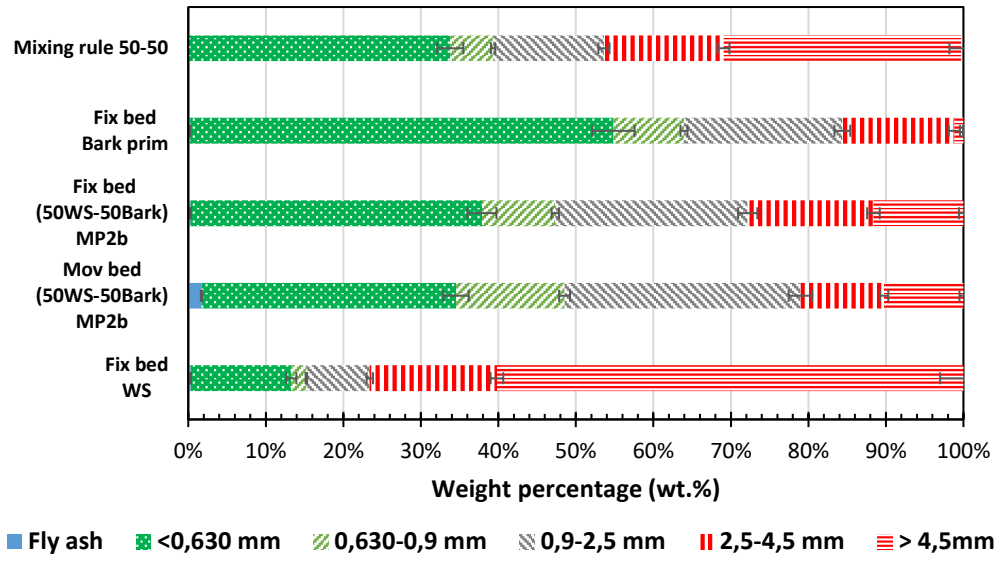

Figure 4.10: Particles size distribution of ash in the pilots' reactors using single bark (BC), single straw (WC), and MP2b (BCWC) mixture.

2.1.4. Particle size distribution in the pellet and pilot burner tests

The composition and the proportion of the phases present in each sieved section of the ash produced in the pilot-scale boilers (quantification) are reproduced in Figure 4.11.a, while the ones obtained in the laboratory pellet test (semi-quantification) are presented in Figure 4.11.b. For the pilot test, the collected ashes were sieved with the same mesh as for the pellet test. First, they were weighed to get the weight percentage. Then, P-XRD measurements were done for the phases present in each particulate size fraction. A simple mass balance (mixing rule) was conducted to obtain the average pilot-scale proportion of crystalline and amorphous phases using each fraction's weight percentage and crystalline composition.

From the sieving results in both cases (pilot and pellet tests), CaO was identified, which was a main component of BC. This compound is characterized by a very high melting point (Foex 1965). Accordingly, it was concentrated within the smallest particles less than 900µm, which were in the solid phase (more like powder). In contrast, silicate compounds were more concentrated in the bigger particles above 900µm, which contained more liquid as their size increased (more like big chunks of molten solids). Alkali-silicates are the main reason behind slag formation (Link, Yrjas, and Hupa 2018; Boström et al. 2012). This explains the proportion of silicate in the bigger size particles.

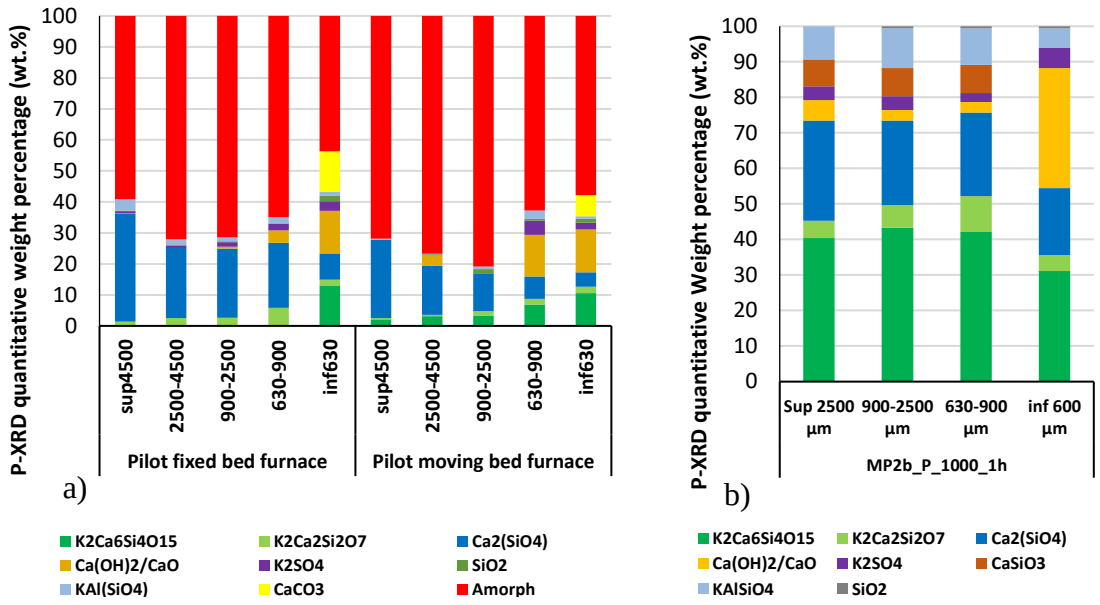

Figure 4.11: P-XRD analysis for each sieving fraction quantitatively in the pilot burners (a) and semi-quantitatively in the pellet test at 1000 °C and 1h for the combustion of MP2b (BCWC) mixture.

In conclusion, at both laboratory and pilot scales, small meshes (particles smaller than 900µm) were concentrated with Ca-compounds while big meshes (particles bigger than 900µm) with Si-compounds.

2.2.Ash behavior in the fluidized bed reactor

The detailed experimental setup of the fluidized bed was presented in section 3.1.5 in chapter 2. 4 kg/h of BCWC biomass mixture (6 kg in total) was first introduced in a gasification chamber under a flow of a mixture of steam (32.5 NL/min) and N_2 (8-12 NL/min). The fluidization ratio was 2.9, and the bed materials called Olivine consisted of $MgSiO_3$ (protoenstatite) 6.6%, Mg_2SiO_4 (Forsterite) 82.9%, $MgSiO_3$ (Clinoenstatite) 4.8%, and $MgFe_2O_4$ (Magnesioferrite) 5.7%.

Then, the remaining char from the gasification run were recovered and refed in the same reactor but in a combustion mode, under a flow of a mixture of air (40 NL/min) and N_2 (8-12 NL/min). The fluidization ratio was 3.8, and the bed materials were also Olivine. The coupled two runs (gasification then combustion) could depict a dual fluidized bed operation. In sections 2.2.1 and 2.2.2, the presence of agglomeration in each mode will be preliminary investigated based on the temperature distribution measured by each thermocouple and the sieving results, respectively. Then, in section 2.2.3, the ash behavior in the pilot fluidized bed reactor will be further elaborated based on P-XRD analysis results. Note that the composition of the gaseous

species (CO, H2, etc) was recorded, and it is out of the scope of this work to discuss these results.

2.1.1. Temperature distribution in the fluidized bed reactor

Figure 4.12 shows the temperature distribution that was measured using the three thermocouples in the reactor chamber and the two thermocouples on the reaction walls in the biomass gasification run (Figure 4.12.a) and in the char combustion run (Figure 4.12.b). From Figure 4.12.a, the five thermocouples reported a homogeneous temperature of 835 ± 1 °C in the whole gasification chamber. This is a sign of good fluidization, and no bed agglomeration occurred (Valin et al. 2020). However, in the combustion run (Figure 4.12.b), though the two wall thermocouples reported a similar temperature of around 800 °C, the three thermocouples in the reactor chamber showed different temperatures. For instance, their reported temperature increased to 1060 °C (Figure 4.12.b). To overcome the sudden temperature increase due to the exothermic combustion of the char, the air flow rate was manually decreased (half the normal flow rate value). Unfortunately, it was a bit late, and a small defluidization of the bed occurred, manifested in Figure 4.12.b by the small temperature difference measured by the three thermocouples embedded in the bed (± 50 °C). Hence, some bed agglomeration should have been formed and will be checked in the later section.

Consequently, by comparing Figures 4.12.a and 4.12.b, it was clear that probably no agglomeration was present in the gasification run, opposite to the combustion run due to a too high temperature reached during the combustion mode.

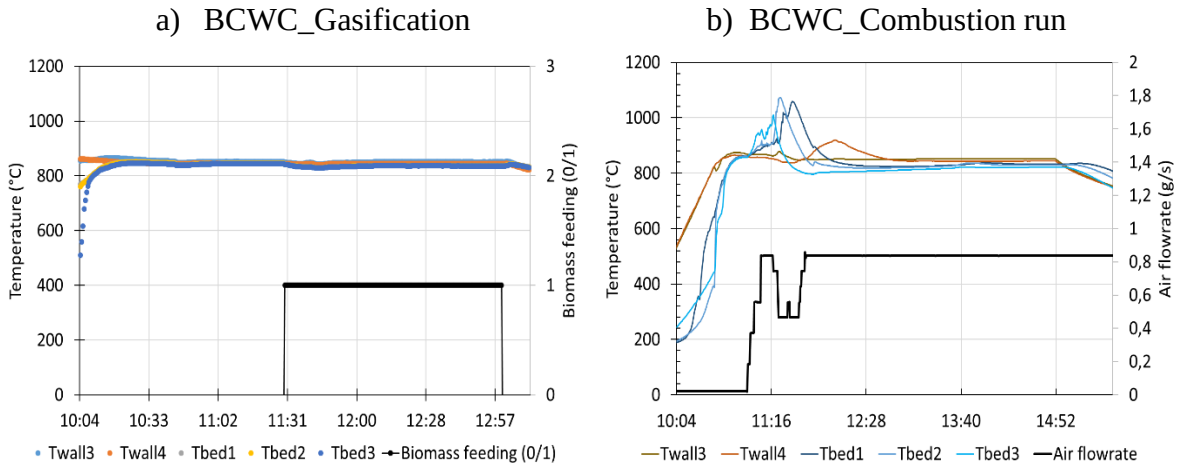

Figure 4.12: The temperature distribution measured using the three thermocouples in the reactor chamber and the two thermocouples on the reaction walls in the biomass gasification run (a) and in the char combustion run (b) for the BCWC mixture.

2.1.2. Sieving results in the fluidized bed reactor

The results in Figure 4.13 supported the conclusion of the section before. This figure reports the ash weight percentage of each sieved ash fraction (in each mesh) produced in each run with respect to the total amount of ash. The latter was calculated based on the measured ash contents at 815 °C and the total mass of dry feedstock introduced for the BCWC mixture (i.e. 448 g). The total sieved ash percentage exceeded 100% in the combustion run in contrast with the gasification run. This was due to the combustion ash that retained more bed materials than the gasification ash.

Consequently, contrary to the gasification run, some agglomeration was observed in the combustion run.

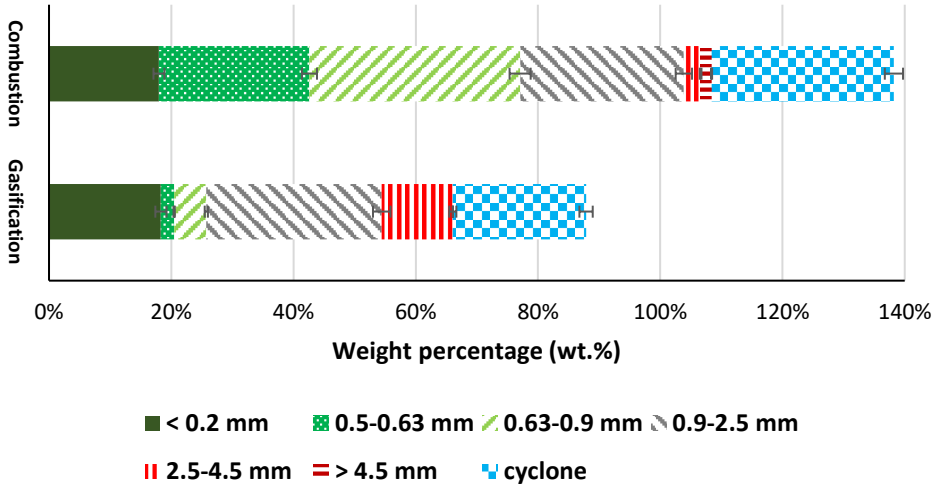

Figure 4.13: Particle size distribution of the ash in the pilots' fluidized bed reactor in combustion and gasification runs for the BCWC mixture.

2.1.3. P-XRD analysis results in the fluidized bed reactor

To further understand the different ash behavior between the two runs, the P-XRD results of the ash collected in the cyclone and from the reactor chamber in the combustion and gasification modes compared with the raw olivine bed materials are shown in Figure 4.14. In the case of a fluidized bed, the choice of meshes was directly based on the size of the bed material, which was between 0.2 mm and 0.5 mm. Hence, particles bigger than 0.5 mm were considered agglomerates (>2.5 mm referred to significant agglomerates). On the other hand, those smaller than 0 0.2 mm, were supposed to be in the solid powder phase, i.e. did not contain any agglomerates. Consequently, the results in Figure 4.14 showed those of just >2.5 mm (called big mesh) and <0.2 mmm (called small mesh) meshes and those of the cyclone.

According to the results in Figure 4.14, cyclone ash, in both gasification and combustion, was abundant with $CaCO_3$. CaO can easily react with CO_2 during the gasification/combustion process or in storage in air before their P-XRD analysis. In addition, according to the results in section 1.1.1, this compound was a primary one in the BC feedstock (along with CaO) (Defoort et al. 2019). Due to the fluidization effect, $CaO/CaCO_3$ seems to be easily evacuated from the reactor chamber into the cyclone instead of staying in the bottom ash and reacting with the straw ash. This was shown by its 64 wt.% in the gasification run and 69 wt.% in the combustion run in the cyclone. In contrast, $CaCO_3$ was approximately absent or negligible in the other samples. KCl, one of the major TPM compounds (Zeng et al. 2016; Hu et al. 2020), was also present in the cyclone of the two runs.

Mg_2SiO_4, the main compound of Olivine (i.e. the bed material), as shown in Figure 4.14, was entrained from the reactor chamber in the gasification cyclone but was absent from the combustion cyclone. The presence of agglomeration in the combustion reactor would have retained most of the bed materials within the reactor chamber, hindering its entrainment towards the cyclone. Similarly, the absence of bed agglomeration in the gasification run led to an entrainment of SiO_2 and Ca_2SiO_4 from the reactor chamber to the cyclone. These two compounds were absent from the combustion cyclone due to increased agglomeration, hence compound entrapment in the reactor chamber.

The increased agglomeration effect in the combustion run was also highlighted by its increased amorphous contents in both the big and small meshes (63 wt.% and 24 wt.% respectively) compared to the gasification run (45 wt.% and 16wt.% respectively). Along with the molten ash phase, the amorphous contents should also contain some bed materials and micrometer crystalline particles. Traces of MgO and $CaSiO_3$ were also found in the small meshes.

According to section 1.1.1, $K_2Ca_6Si_4O_{15}$ and $K_2Ca_2Si_2O_7$ were the two primary phases produced by a chemical reaction within the ash of this biomass mixture (BCWC) at a temperature of 1000 °C. However, the ternary compounds were never found in the fluidized bed ashes. In addition, the abundance of $CaCO_3$ (initially coming from BC) supported the small chemical reactions within the ash of the blend. This can be due to several factors. First, the temperature measured in the gasification mode was less than 850 °C. Second, as shown in section 1.1, ash reactivity decreased with the increasing scale due to the decreasing proximity of the ash particles. This proximity further decreased in the fluidized bed, in which the ash particles were spread all around the bed of the reactor chamber. Third, the presence of bed materials between the ash particles hindered or shifted their reactions. So instead of reacting with each other, they were

reacting with the bed materials. This reaction produced minor amounts of $CaMgSiO_4$ and $Ca_2MgSi_2O_7$ found in the meshes in the combustion run at a high temperature. These two compounds were never seen in any other used appliances in this work using the same blend. Fourth, the gasification instead of combustion may have an incidence that was not studied in this work.

The high temperature (1060 °C) reached in the combustion mode can explain the larger agglomeration compared to the one reached in the gasification mode.

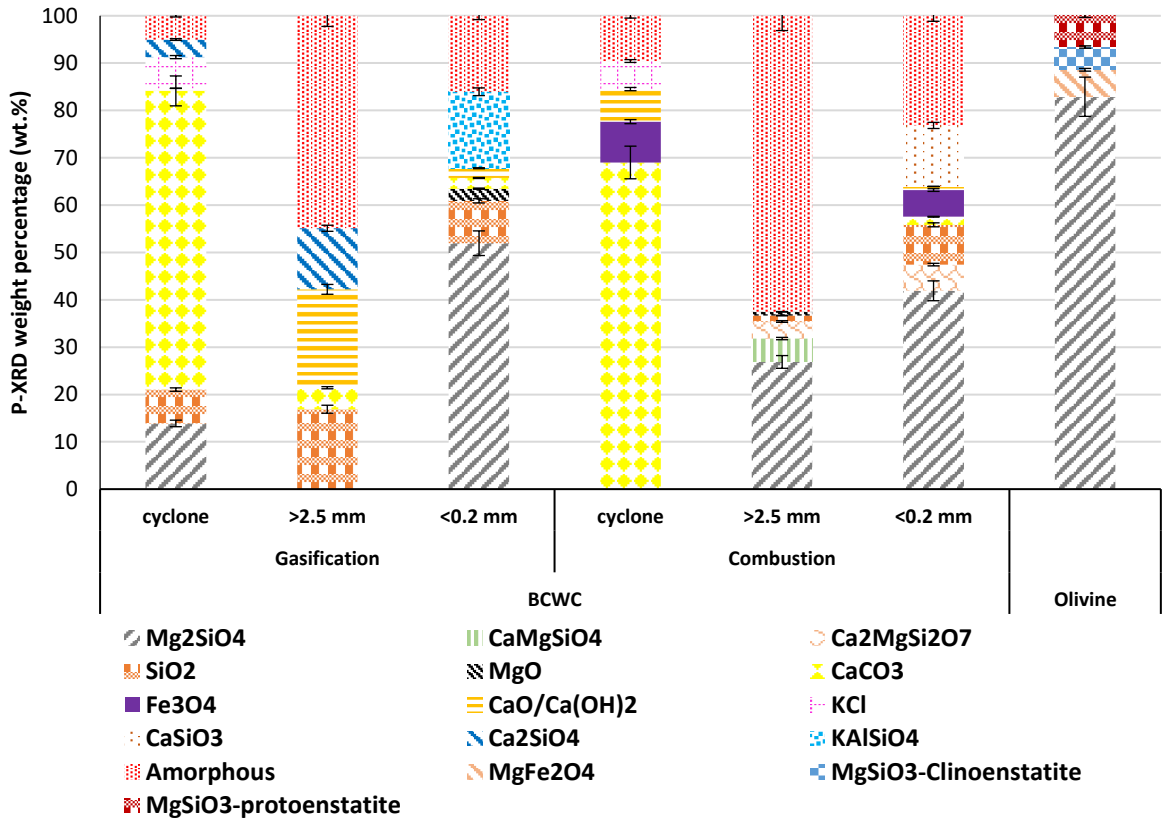

Figure 4.14: P-XRD average crystalline and amorphous distributions of the ash collected in the cyclone and from the reactor chamber in the combustion and gasification runs in the fluidized pilot bed reactor.

3. Conclusion

The chemical reactions effect was dominant when ash mixtures (i.e. ash test) were used, while mixing rule influence was the most important when biomass mixtures were applied on both laboratory (i.e. pellet test) and pilot scales, with only a small chemical reactivity found in the second case (i.e. pellet and pilot). Chemical reactions in gasification and combustion modes were more complex in the fluidized bed reactor. The inorganic elements were reacting with the bed materials instead of each other. Hence, in terms of tests, the ash reactivity of the BCWC

mixture can be ranked in the decreasing order: ash test > pellet test > pilot burner. This, in turn, affected the effects of operating conditions on ash behavior that were ranked in the same aforementioned order.

The temperature then residence time had higher effects on ash reactivity than cooling and pellet compression rates. $K_2Ca_6Si_4O_{15}$ and $K_2Ca_2Si_2O_7$ were the main products of the chemical reactions in 50-50 bark (BC)-straw (WC) biomass and ash mixtures. They were absent in the single feedstock but highly stable at 1000 °C and 6 h in the blend in the ash test, conditions at which equilibrium was experimentally reached. Their appearance and their increasing proportions led to a decrease in the amorphous proportion. Hence, optimizing the blend to increase their concentration has the potential to solve slagging problems.

The laboratory pellet test was able to predict the pilot burner behavior in terms of crystalline and amorphous proportions along with agglomeration distribution for both individual biomasses and biomass mixtures. Hence, using the pellet laboratory test before any pilot burner operation has the potential to make economic savings and reduce the operational problems related to ash behavior in industrial-scale reactors. These results on biomass mixtures should be checked for other types of biomass, other mixtures in combustion but also in gasification/combustion in the fluidized bed.

References

Boström, Dan, Nils Skoglund, Alejandro Grimm, Christoffer Boman, Marcus Öhman, Markus Broström, and Rainer Backman. 2012. "Ash Transformation Chemistry during Combustion of Biomass." *Energy & Fuels* 26 (1): 85–93. https://doi.org/10.1021/ef201205b.

Chen, Mao, Xinmei Hou, Junhong Chen, and Baojun Zhao. 2016. "Phase Equilibria Studies in the SiO2-K2O-CaO System." *Metallurgical and Materials Transactions B* 47 (3): 1690–96. https://doi.org/10.1007/s11663-016-0623-z.

Defoort, Françoise, Matthieu Campargue, Gilles Ratel, Hélène Miller, and Capucine Dupont. 2019. "Physicochemical Approach To Blend Biomass." *Energy & Fuels* 33 (7): 5820–28. https://doi.org/10.1021/acs.energyfuels.8b04169.

Foex, Marc. 1965. "Measurement of the Solidification Points of Several Refractory Oxides by Means of a Solar Furnace." *Solar Energy* 9 (1): 61–67. https://doi.org/10.1016/0038-092X(65)90162-3.

Gilbe, Carl, Erica Lindström, Rainer Backman, Robert Samuelsson, Jan Burvall, and Marcus Öhman. 2008. "Predicting Slagging Tendencies for Biomass Pellets Fired in Residential Appliances: A Comparison of Different Prediction Methods." *Energy & Fuels* 22 (6): 3680–86. https://doi.org/10.1021/ef800321h.

Höfer, Isabel, and Martin Kaltschmitt. 2017. "Effect of Additives on Particulate Matter Formation of Solid Biofuel Blends from Wood and Straw." *Biomass Conversion and Biorefinery* 7 (1): 101–16. https://doi.org/10.1007/s13399-016-0217-7.

Hu, Zhongfa, Xuebin Wang, Lan Zhang, Shunzhi Yang, Renhui Ruan, Shengjie Bai, Yiming Zhu, Liang Wang, Hrvoje Mikulčić, and Houzhang Tan. 2020. "Emission Characteristics of Particulate Matters from a 30 MW Biomass-Fired Power Plant in China." *Renewable Energy* 155 (August): 225–36. https://doi.org/10.1016/j.renene.2020.03.094.

Link, Siim, Patrik Yrjas, and Leena Hupa. 2018. "Ash Melting Behaviour of Wheat Straw Blends with Wood and Reed." *Renewable Energy*, SI: Waste Biomass to Biofuel, 124 (August): 11–20. https://doi.org/10.1016/j.renene.2017.09.050.

Rebbling, Anders, Peter Sundberg, Jonathan Fagerström, Markus Carlborg, Claes Tullin, Dan Boström, Marcus Öhman, Christoffer Boman, and Nils Skoglund. 2020. "Demonstrating Fuel Design To Reduce Particulate Emissions and Control Slagging in Industrial-Scale Grate Combustion of Woody Biomass." *Energy & Fuels* 34 (2): 2574–83. https://doi.org/10.1021/acs.energyfuels.9b03935.

Rizvi, T., P. Xing, M. Pourkashanian, L.I. Darvell, J.M. Jones, and W. Nimmo. 2015. "Prediction of Biomass Ash Fusion Behaviour by the Use of Detailed Characterisation Methods Coupled with Thermodynamic Analysis." *Fuel* 141 (February): 275–84. https://doi.org/10.1016/j.fuel.2014.10.021.

Rodríguez, Juan Luis, Xana Álvarez, Enrique Valero, Luis Ortiz, Natalia de la Torre-Rodríguez, and Carolina Acuña-Alonso. 2020. "Design of Solid Biofuels Blends to Minimize the Risk of Sintering in Biomass Boilers." *Journal of the Energy Institute* 93 (6): 2409–14. https://doi.org/10.1016/j.joei.2020.07.015.

Santoso, Imam, Pekka Taskinen, Ari Jokilaakso, Min-Kyu Paek, and Daniel Lindberg. 2020. "Phase Equilibria and Liquid Phase Behavior of the K2O-CaO-SiO2 System for Entrained Flow Biomass Gasification." *Fuel* 265 (April): 116894. https://doi.org/10.1016/j.fuel.2019.116894.

Steenari, B.-M., A. Lundberg, H. Pettersson, M. Wilewska-Bien, and D. Andersson. 2009. "Investigation of Ash Sintering during Combustion of Agricultural Residues and the

Effect of Additives." *Energy and Fuels* 23 (11): 5655–62. https://doi.org/10.1021/ef900471u.

Thy, Peter, Bryan M. Jenkins, Charles E. Lesher, and Sidsel Grundvig. 2006. "Compositional Constraints on Slag Formation and Potassium Volatilization from Rice Straw Blended Wood Fuel." *Fuel Processing Technology* 87 (5): 383–408. https://doi.org/10.1016/j.fuproc.2005.08.015.

Tsukada, Mayumi, Hajime Yamada, and Hidehiro Kamiya. 2003. "Analysis of Biomass Combustion Ash Behavior at Elevated Temperatures." *Advanced Powder Technology* 14 (6): 707–17. https://doi.org/10.1163/15685520360731990.

Valin, Sylvie, Serge Ravel, Philippe Pons de Vincent, Sébastien Thiery, Hélène Miller, Françoise Defoort, and Maguelone Grateau. 2020. "Fluidised Bed Gasification of Diverse Biomass Feedstocks and Blends—An Overall Performance Study." *Energies* 13 (14): 3706. https://doi.org/10.3390/en13143706.

Vassilev, Stanislav V., David Baxter, and Christina G. Vassileva. 2013. "An Overview of the Behaviour of Biomass during Combustion: Part I. Phase-Mineral Transformations of Organic and Inorganic Matter." *Fuel* 112 (October): 391–449. https://doi.org/10.1016/j.fuel.2013.05.043.

Vega-Nieva, D., C. Alvarez, and L. Ortiz. 2014. "Results of New Laboratory Methods and Slagging Classification Systems for the Prediction and Quantification of Ash Slagging in Woody and Herbaceous Biomass Fuels." In *Central European Biomass Conference*.

Zeng, T., N. Weller, A. Pollex, and V. Lenz. 2016. "Blended Biomass Pellets as Fuel for Small Scale Combustion Appliances: Influence on Gaseous and Total Particulate Matter Emissions and Applicability of Fuel Indices." *Fuel* 184 (November): 689–700. https://doi.org/10.1016/j.fuel.2016.07.047.

5. Chapter 5. Assessing the prediction capabilities of the thermodynamic equilibrium tools with respect to experimental data

In this chapter, the prediction capabilities of the thermodynamic equilibrium tools i.e. phase diagram and global simulations approaches, presented in chapter 3, will be thoroughly assessed with respect to the experimental results obtained on ash samples that were checked to be at equilibrium within the ash test (chapter 4). Furthermore, experimental results of the real situation of biomass combustion (pellet test) will also be discussed.

Indeed, in chapter 4, it was demonstrated that the chemical reactivity and the ash interactions were higher in the ash than the pellet test, and experimental equilibrium was reached at 1000 °C and 6 h in the ash test. Hence, the effect of the variation of ash composition on the predicted results using the thermodynamic equilibrium tools was studied on ash samples annealed in ash test at 1000 °C and 6 h for six biomass ashes (section 1) and eight ash mixtures (section 2). In addition, the effect of temperature was studied on the ashes of the BCWC mixture annealed at three temperatures (850 °C, 1000 °C, and 1200 °C) in the ash test (section 2). TGA-DTA analysis data up to 1350 °C were also used to support the thermodynamic prediction tool assessment.

In section 3, the prediction capabilities of the thermodynamic equilibrium tools will also be evaluated in the case of a real process such as the combustion of the BCWC biomass mixture in the pellet test at two temperatures (850 °C and 1000 °C).

1. Single biomass ash prediction

In this section, a full analysis of the capabilities of the thermodynamic approaches to predict the ash behavior of single barks and straws that were shown to be at equilibrium will be elaborated on in detail. Then, to further investigate this prediction capability, the calculated results will be compared against measured ones by TGA/DTA (may or may not be at equilibrium). This will help discuss the capabilities of the global simulations in predicting the total and elemental volatilization along with the characteristic temperatures. At the end of this section, an extra analysis for the condensed phases using SEM-EDX and P-XRD compared to prediction in bark BC and straw WC ash samples will be elaborated.

1.1. Thermodynamic prediction approach for the condensed phases

To assess the prediction capabilities of the phase diagram approach, the single biomasses ash were positioned in the CaO-K_2O-SiO_2 phase diagram calculated at 1000 °C in Figure 5.1, based on their normalized CaO, SiO_2, and K_2O weight percentages shown in Tables 2.1 and 2.2 in chapter 2.

Figure 5.2 shows the measured P-XRD results for each straw and bark ash sample compared to those predicted by the global simulation approach using each database set at 1000 °C.

In Figure 5.1, the three straws were located in the pure liquid region. Accordingly, the P-XRD results in Figure 5.2 showed that all measured wheat straw samples at 1000 °C were in the liquid phase with minor K_2SO_4 concentration (< 10 wt.%). The amorphous content is proportional to the alkali-silicate oxide contents and inversely proportional to the alkaline earth metal oxide amounts (Boström et al. 2012; Rebbling et al. 2020). Hence, the measured amorphous content in the straw ash samples in Figure 5.2 could be ranked similarly to their K_2O weight percentages (Table 2.1 in chapter 2), in the following increasing order: WF < WI < WC. In terms of predictions, simulations using the GTOX dataset failed to predict the presence of K_2SO_4 in the three straws, showing instead a total solubility of K and S in the liquid phase LIOS. In contrast, calculations using the FToxid dataset successfully predicted the straw behavior, with a minor quantitative difference with the P-XRD measured values (<5% uncertainty).

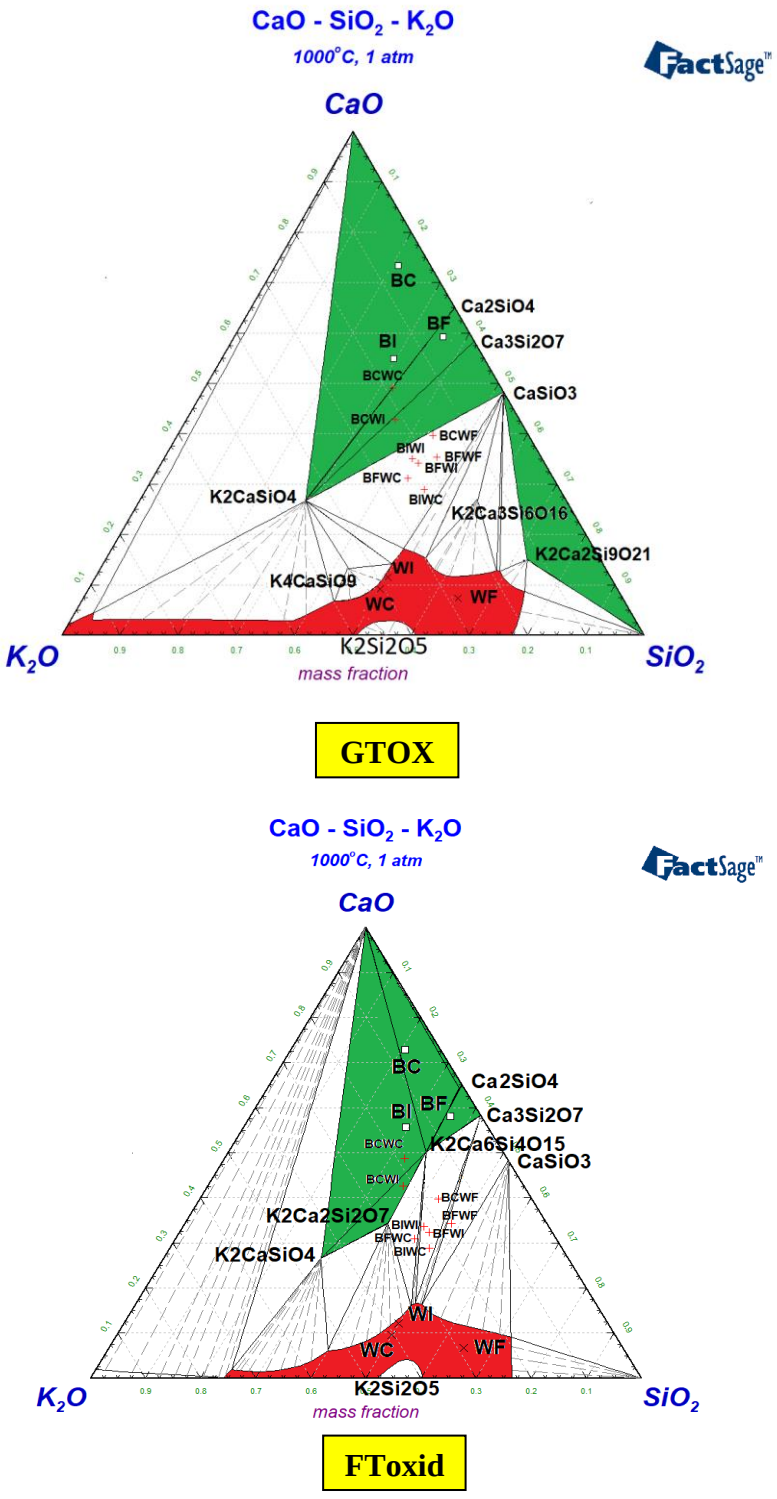

Figure 5.1: Position of the various single biomass ashes and their mixtures in the form of ash in the phase diagram calculated at 1000 °C using GTOX and FToxid (red section=pure liquid region, green section=pure solid region, and white section=solid-liquid region).

On the other hand, the three barks, using their normalized SiO_2, K_2O, and CaO weight percentages were located in the pure solid region in Figure 5.1. According to the results in Figure 5.2, all measured oak bark samples showed low amorphous contents (<30 wt.%). It should be noted that the measured amorphous contents contain molten/liquid ash mixed with

small crystals of µm size. Hence, most of the amorphous contents found by the P-XRD analysis should be ash in the liquid phase.

As a result, from a first impression, the global simulation findings contradicted the phase diagram results. One reason for this difference can be related to adding other elements (such as P, Mg, and Cl, as shown in section 2.3 in chapter 3) to CaO, SiO_2, and K_2O that destabilized certain solid phases and increased the liquid contents. Hence, the global simulation approach could better account for the liquid phase than the phase diagram approach. This was clear in Figure 5.2 from the predicted results using the GTOX dataset that reported the presence of amorphous content, contrary to those reported by the FToxid dataset. Another reason can be related to the estimated thermodynamic properties of the compounds in the middle section of the ternary diagram (i.e. $K_2Ca_2Si_2O_7$ and $K_2Ca_6Si_4O_{15}$) (Kim 2017) and the reported absence of K_2CaSiO_4 in literature (Arroyabe et al. 2011). Once the latter is taken out and the thermodynamic properties of the formers are measured, several tie lines might change, affecting the solid, liquid, and solid-liquid sections. As a result, the phase diagram approach provided a good but limited qualitative ash state prediction for single barks cases.

To further investigate the P-XRD findings in each bark in Figure 5.2, the elemental composition according to Table 2.1 in chapter 2 is discussed. BF was the most abundant in Si among the three bark samples. Hence, it presented the highest amorphous contents among the three barks. BC and BF presented close weight percentages of CaO, K_2O, and SiO_2. This explains the close concentration of each phase found in their ashes (Figure 5.2). BI was the richest in Si, K, Na, P, Fe, and Mg and the poorest in Ca. It contained three times the K contents in BC and BF at the expense of less Ca. Therefore, the measured $CaO/(CaOH)_2$ concentration in this sample was the lowest at the expense of the abundance of K_2SO_4 and $KAlSiO_4$ concentrations. Ca_2SiO_4 (olivine-γ) was present in all the measured samples, while the predicted K_2CaSiO_4 was experimentally absent. This was not surprising as Ca_2SiO_4 is the most stable compound in the $CaO\text{-}SiO_2$ binary system.

It should be noted that the measured amorphous / liquid concentration might be over-estimated in all the samples. In Figure 2.10, an amorphous peak coming from TiO_2 was seen between 18° and 23° in the sample with TiO_2. Hence, this might refer to micro-crystallized particles that exist in the TiO_2 anatase sample, which was used as the internal standard. Consequently, this type of particles can diffract more the angle, and lead to a higher measured amorphous concentration. In addition, from a previous work on the same samples (Defoort et al. 2019), the

SEM pictures showed a non-homogeneous liquid distribution on the ash matrix. Hence, instead of a global equilibrium (as in the equilibrium prediction case), local equilibrium was seen in the experimental samples. This can also increase the differences between the predicted and the measured results.

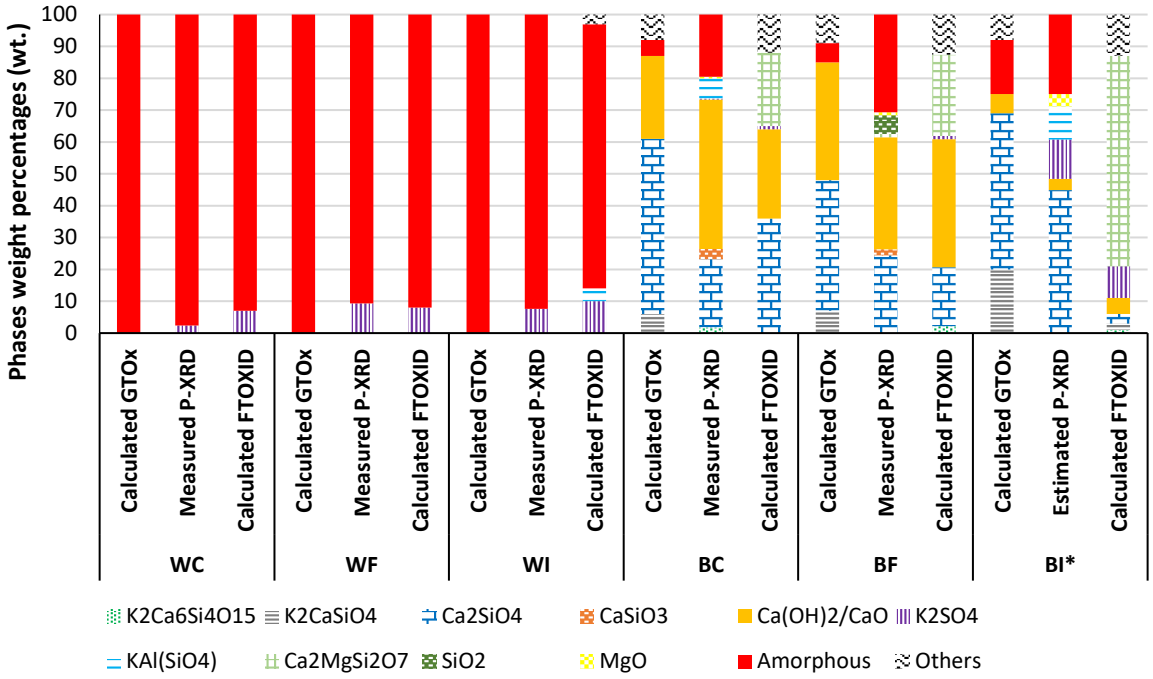

Figure 5.2: Measured (P-XRD) phases within the ash of the various biomasses versus predicted ones by the global simulation using GTOX and FToxid database sets after annealing for 6h at 1000 °C. The uncertainty for the measured P-XRD results was in the range of 2 wt.%.

**The crystalline/amorphous compositions of BI were estimated based on the amorphous percentage of BC and BF and BI measured XRD compositions without TiO2.*

In terms of predictions, calculations using both databases failed to predict the existence of the minor phases present in all bark samples, such as $CaSiO_3$ (wollastonite), K_2SO_4, $KAlSiO_4$, SiO_2 (Quartz), and MgO. $Ca_2MgSi_2O_7$, always predicted by the calculations using the FToxid dataset, was never found experimentally. In contrast, the simulations using the FToxid dataset failed to predict the amorphous contents that were found experimentally and in the prediction using the GTOX dataset. Nevertheless, despite the qualitative agreement, the measured and the predicted concentrations of the amorphous phase remained different. Both databases showed good prediction capabilities for Ca_2SiO_4 and $CaO/Ca(OH)_2$ crystalline phases. However, the relative quantitative prediction uncertainty for these two compounds always ranged between 5% and 50%. Here again, the presence of K_2CaSiO_4 in the prediction using GTOX at equilibrium always hindered good predictions. In conclusion, despite its success in the case of single straws, the global simulation approach showed some limitations in the case of barks. This

might be directly related to the higher amounts of CaO in the barks than in straws, which increased the ash elemental interactions.

In conclusion, in the case of annealed ash of single biomass, the phase diagram approach using both databases provided a good qualitative ash state prediction (solid, liquid, or solid-liquid). Limited predictions using this approach were found in the solid region (i.e. oak barks cases). The global simulation approach was effective in the case of straw (especially using FToxid), but showed limitations in the case of barks. The prediction limitation in the case of bark using both approaches was related to the presence of more Ca in its ash, which increased the interactions with K and Si that were happening within its ash. On the other hand, the inorganic interactions within the straw ash were simpler since they were governed by just two elements (K and Si).

1.2.Bark ash (BC) TGA-DTA analysis

Figure 5.3 depicts the ash behavior of bark BC up to 1350 °C using TGA-DTA analysis. The weight loss in green, the heat flow in blue, and the temperature in red were all measured with respect to time. Three trials using bark ash samples (bark BC) were tested: two replicate trials (straight and dotted lines) up to 1300 °C with a plateau of 1h, then fast cooling (25 °C/min), and the third one (dashed line) up to 1350 °C with a plateau of 20 min then slow cooling (10 °C/min). All samples gave reproducible results (error < 2%). The heat flow curve is shown in V rather than in W due to the absence of any calibration. Hence, relating the measured heat flow to the heat of reaction was impossible.

The TGA-DTA results in Figure 5.3, show that the bark had only one reaction at 720 °C with a weight loss of around 32 wt.% and a strong endothermic peak. The event can be attributed to decarbonation (i.e. decomposition of carbonates) with CO_2 release, an endothermic reaction. CO_2 was the only gaseous species measured by the MS coupled to the DTG-DTA. No thermal events and negligible mass loss (< 1 wt.%) were seen on the plateau at 1300 °C and 1350 °C.

The fast cooling method (in the 1300 °C maximum temperature case) showed a significant exothermic heat flow curve that did not exist in the slow cooling one (in the 1350 °C maximum temperature case).

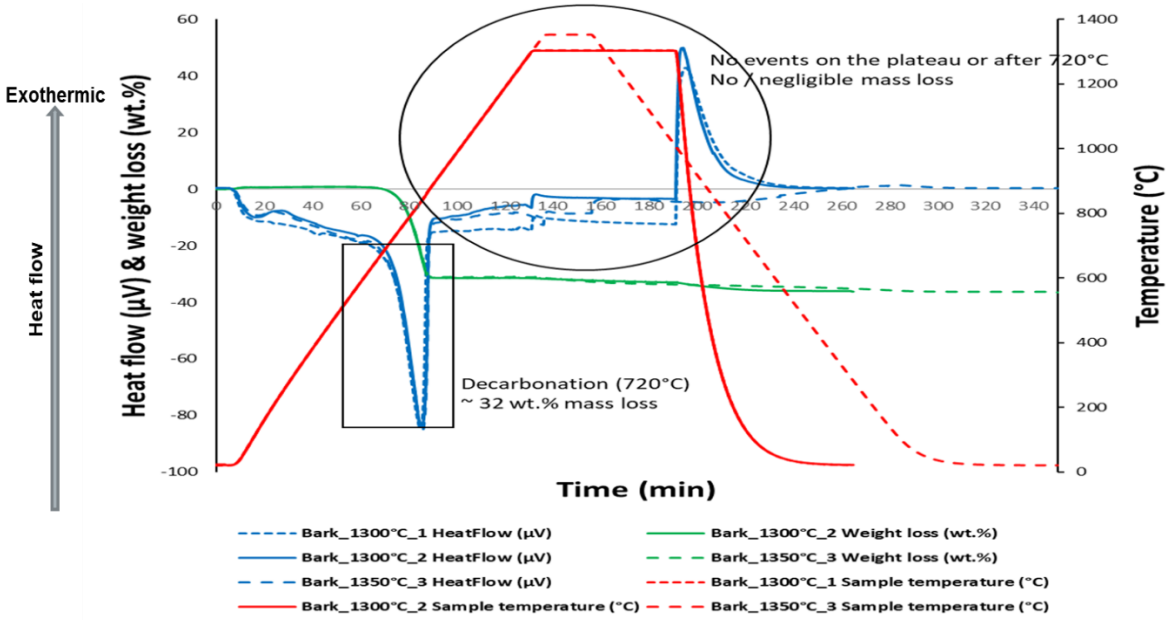

Figure 5.3: Bark ash TGA-DTA results.

To further understand the bark ash behavior, thermodynamic simulation of the TGA-DTA experiments was performed in air versus temperature (Figure 5.4). The solidus predicted at 992 °C was never seen in the TGA-DTA analysis. On one hand, more annealing time should have been given for the changes to happen using the TGA-DTA. On the other hand, the predicted solidus might be biased due to thermodynamic database limitations.

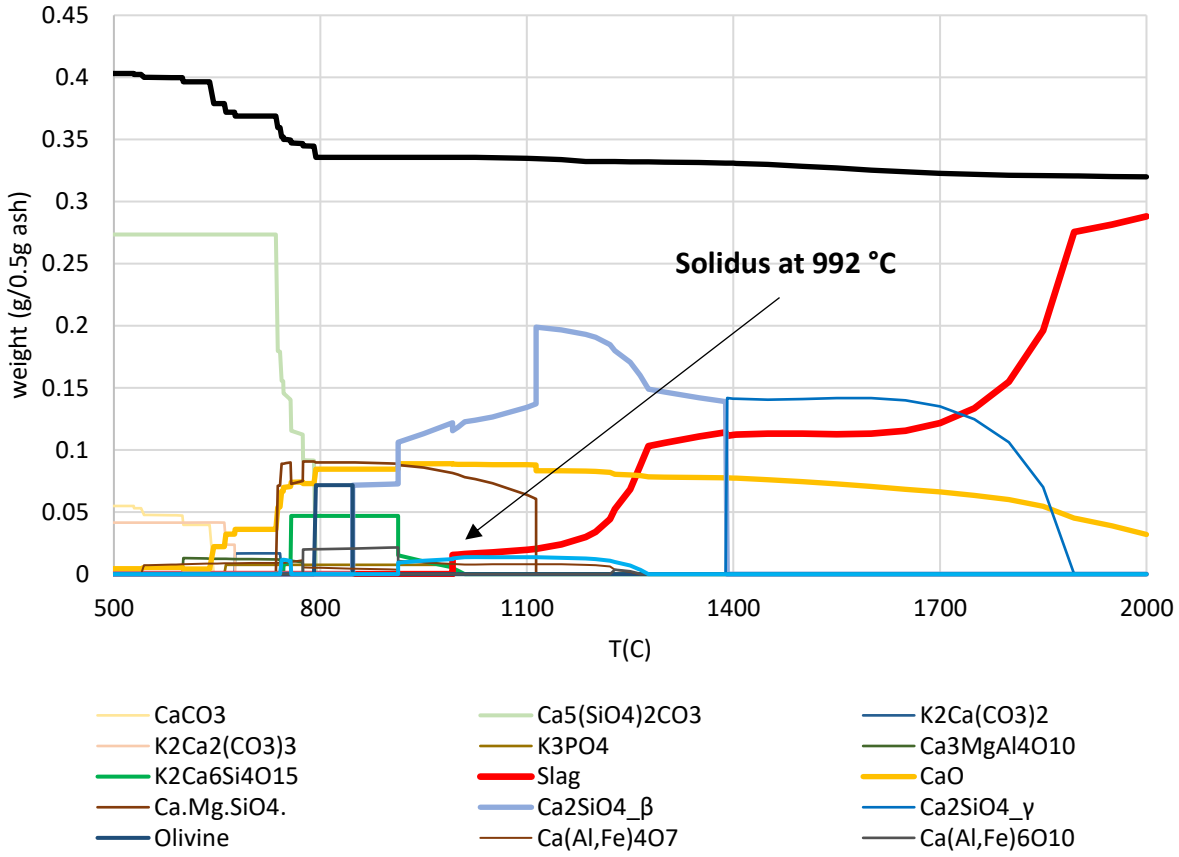

Figure 5.4: Predicted bark ash condensed composition with respect to temperature simulated using FToxid dataset.

The results in section 1.1 already proved the quantitative discrepancies between the measured condensed phases and those predicted using the FToxid dataset. From section 1.1, predictions using GTOX dataset also proved to be limited. Hence, it will be omitted from this comparison. Consequently, in Table 5.1, a qualitative comparison was developed between the predicted (using FToxid dataset) and the measured bark phases at various temperatures. In this table, the results of the ashes collected after the TGA-DTA tests at 1300 °C and 1350 °C are reported along with the results obtained in the ashes at 550 °C and in the ashes collected after the ash test at 1000 °C (6 h) and 1200 °C (6 h). This table will focus on the major condensed phases.

Table 5.1: Thermodynamic calculation using FToxid dataset VS measured P-XRD results (solid & liquid) on bark ash sample annealed at various temperatures.

	550 °C	1000 °C	1200 °C	1300 °C	1350 °C
K_2SO_4		T			
$K_2Ca_6Si_4O_{15}$		T			
Slag		T P	T P	T P	T P
CaO / $Ca(OH)^2$	T	T P	T P	T P	T P
Carbonates (K and Ca)	T P				
Ca_2SiO_4		T P	T P	T P	T P
$KAlSiO_4$		T	T		
$CaSiO_3$		P	P	P	P

T	Thermodynamically predicted
P	P-XRD detected

A reasonable agreement can be seen between the predicted and the measured values in Table 5.1, especially for the three main major phases (slag (liquid), CaO, and Ca_2SiO_4) at all temperatures. The other phases, K_2SO_4, $K_2Ca_6Si_4O_{15}$, and $KAlSiO_4$, were predicted in the ash test but absent experimentally. In opposite, $CaSiO_3$ was never predicted but always detected experimentally.

Figure 5.5 shows the SEM-EDX results on the Bark in ash test at 1200 °C. According to the P-XRD analysis at 1200 °C, Ca_2SiO_4, CaO, $CaSiO_3$, and slag were all detected by SEM in this sample. The EDX analysis showed a bark slag rich in Al, Si, and K. Hence, this supported the finding that most Ca was in the form of CaO in the bark samples.

In conclusion, in the case of bark BC, the P-XRD and SEM-EDX measurements agreed with each other and with the main major condensed phase predicted with global simulation.

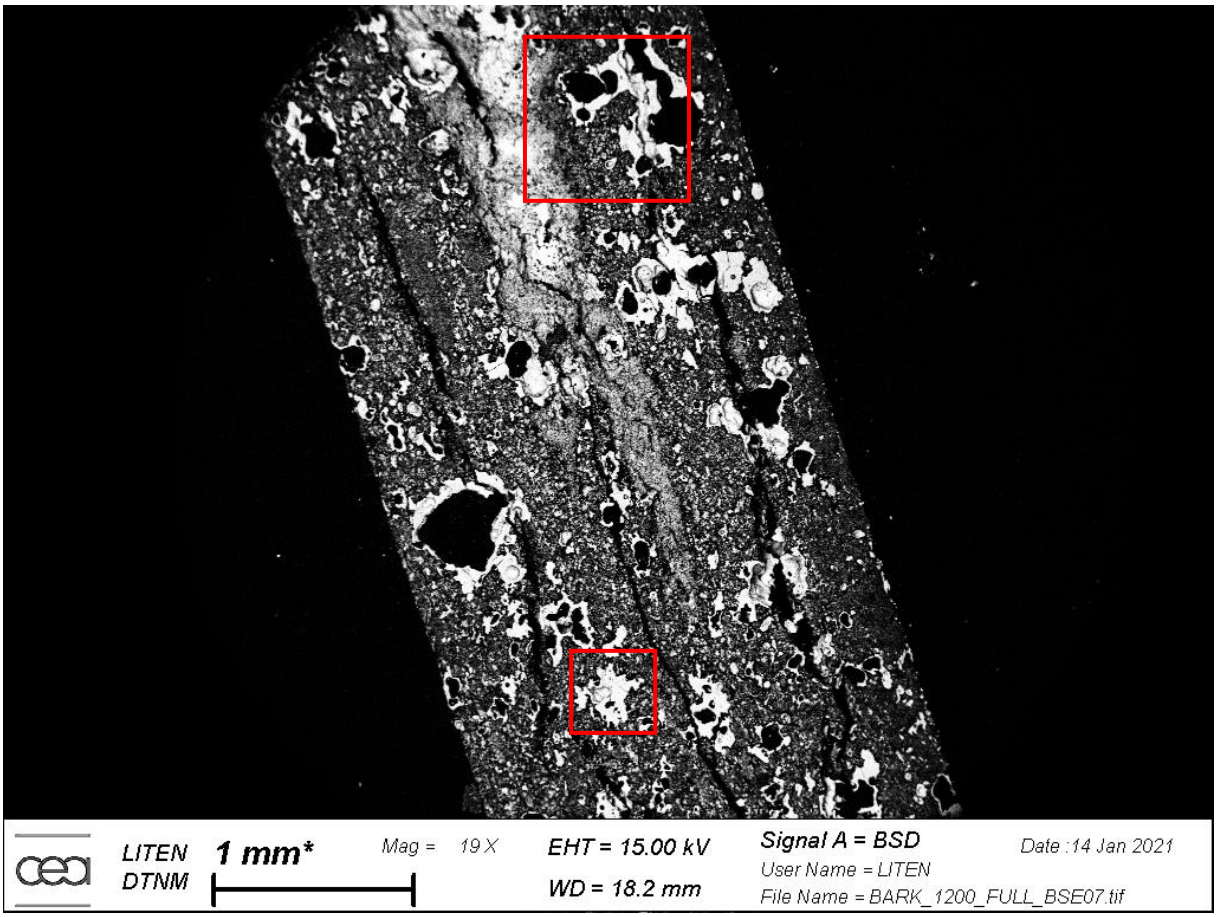
LITEN
DTNM
1 mm*
Mag = 19 X
EHT = 15.00 kV
WD = 18.2 mm
Signal A = BSD
User Name = LITEN
File Name = BARK_1200_FULL_BSE07.tif
Date :14 Jan 2021

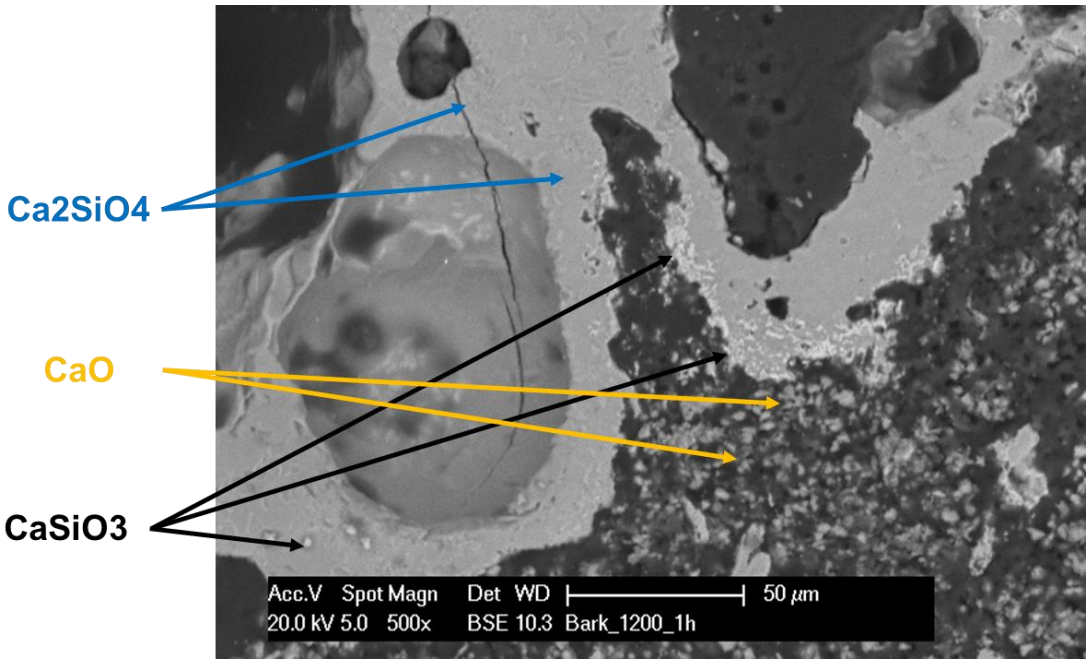
Ca2SiO4
CaO
CaSiO3
Acc.V Spot Magn Det WD 50 µm
20.0 kV 5.0 500x BSE 10.3 Bark_1200_1h

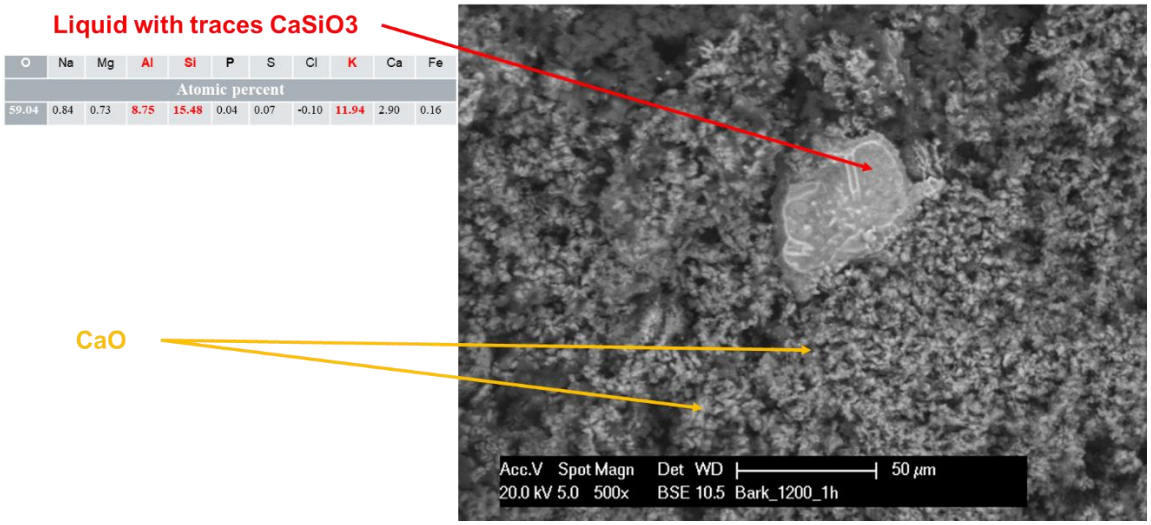

Figure 5.5: SEM-EDX analysis on Bark ash annealed at 1200 °C in ash test (zoomed sections in red on the first Figure).

1.3.Bark ash total and elemental weight loss (volatilization)

Figure 5.6 shows the total bark ash weight loss predicted by the thermodynamic calculations using the FToxid dataset (grey) and measured by the ash test (orange) and TGA-DTA (blue). From this Figure, the agreement between the measured total weight loss in the ash test and the predicted values was evident. In addition, the differences with the measured TGA-DTA weight loss were less than 2 wt.% (absolute). Calculation reported in Figure 5.4 showed that several carbonate phases were present below a temperature of around 800 °C ($CaCO_3$, $K_2Ca(CO_3)_2$, etc.). They decomposed at a temperature lower than 800 °C, decreasing the total solid and liquid

ash weight. This was close to the TGA-DTA results (Figure 5.6) that kept sharply decreasing until reaching 850 °C.

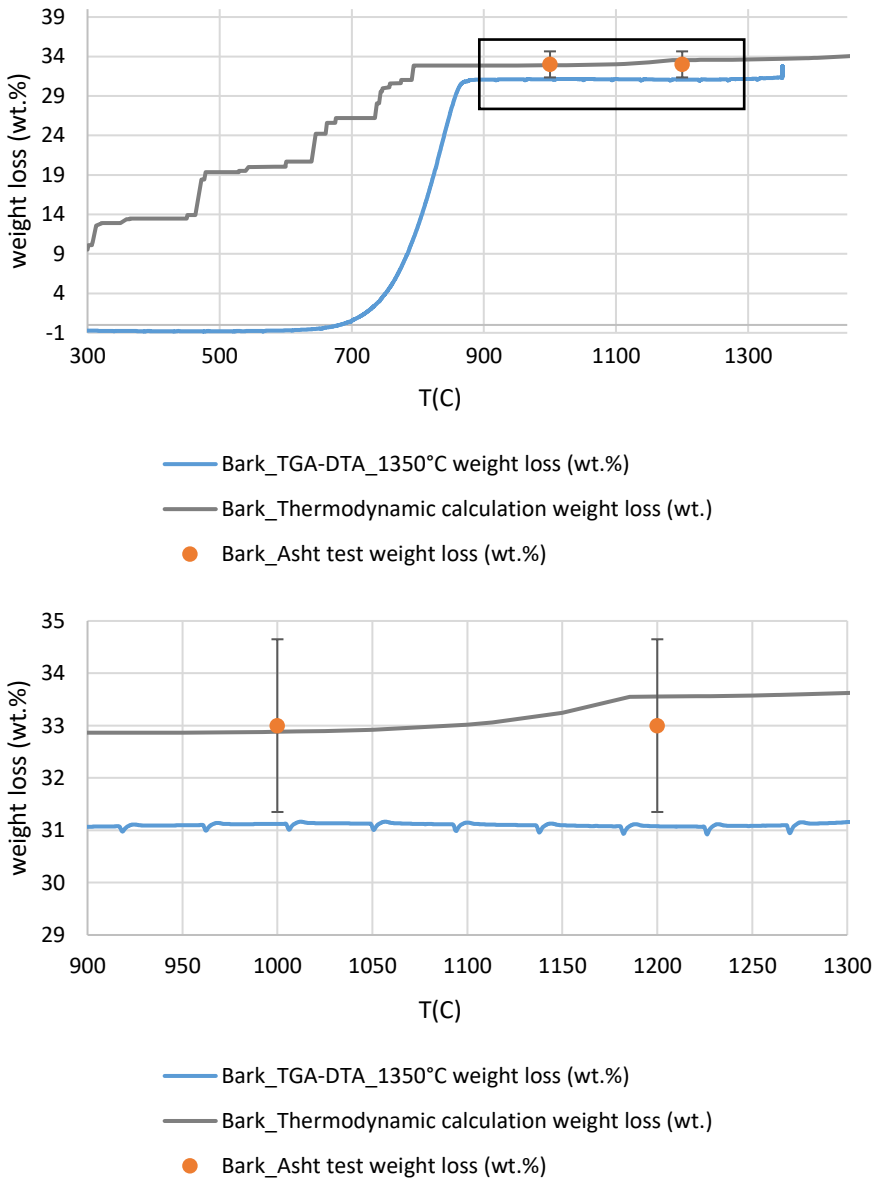

Figure 5.6: Bark ash total weight loss comparison between the predicted ash test simulation, laboratory ash test, and TGA-DTA.

In terms of elemental weight loss (Figure 5.7), partial agreement existed between the predicted (as curves) and the measured values using ICP-MS (as points) at 1000 °C. Chlorine was not measured by ICP-MS, while the predicted and measured carbon volatilization at 1000 °C were in agreement at a value of 100% and the one of sodium at 0%. In addition, negligible differences existed between the measured and the predicted values of potassium volatilization. However, at the same temperature, the only difference between the measured and predicted values was in

terms of sulfur volatilization, which was measured to be 60 wt.%, while the predicted one was negligible.

In conclusion, the global simulation approach effectively predicted the total and elemental volatilization of bark ash.

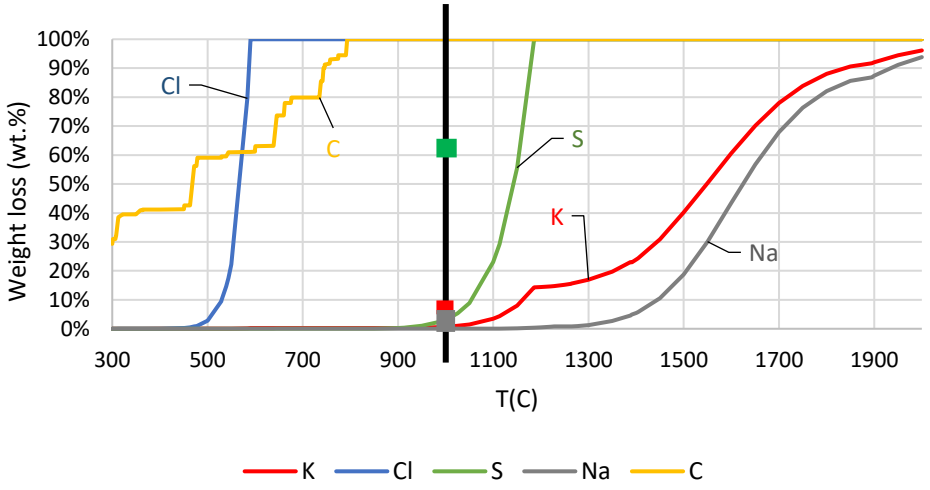

Figure 5.7 : Bark ash elemental weight loss comparison between the predicted ash test simulation and ICP-MS (points).

1.4.Bark characteristic temperatures

The prediction tool showed a very high liquidus temperature (higher than the maximum calculated temperature of 2000 °C), which can explain not attaining the fusion temperature at 1350 °C in the TGA-DTA analysis. For instance, in the results in Figure 5.4, Ca_2SiO_4 was predicted to remain stable until 1850 °C and CaO until a much higher temperature (~2570 °C). However, the solidus temperature differed between the experimental results and the predicted ones. The solidus temperature was predicted to be at 992 °C while it was never detected experimentally within the range of 1350 °C in the TGA-DTA. In a thorough review, Vassilev et al. (Vassilev, Baxter, and Vassileva 2014) reported a melting point of ash from the bark at around 1330 °C. In addition, in a recent study by Link et al. (Siim Link et al. 2022), they measured the melting point of Douglas fire wood chips at 1238 °C and pine wood pellets at 1123 °C using TGA-DTA technique. As a result, more annealing time might have been needed in the TGA-DTA analysis in this work to detect a solidus within this temperature range (i.e. until 1350 °C), as was the case in the work in Link et al. (Siim Link et al. 2022).

1.5.Straw (WC) analysis

Straw was experimentally found to melt at a very low temperature (<800 °C). Hence, the technician responsible for the TGA-DTA equipment was afraid to conduct any analysis on this

biomass to protect the instrument, which finally were not conducted. However, to further understand the straw ash behavior, thermodynamic simulation of the TGA-DTA experiments was performed in air versus temperature (Figure 5.8). The results in this Figure reported that straw ash should contain only liquid and K_2SO_4 after 924 °C (around 70 wt.% K_2SO_4 and 93 wt.% liquid). The solidus was predicted to be at 868 °C and the liquidus at around 1250 °C (Figure 5.8). Accordingly, in Figure 5.2, the three straws annealed at 1000 °C in the ash test contained around 90 wt.% of amorphous contents with a minority of K_2SO_4. The SEM-EDX in Defoort et al. (Defoort et al. 2019) supported these findings at 1000 °C. Hence, Figure 5.9 contains the SEM-EDX results for straw (WC) at 1200 °C.

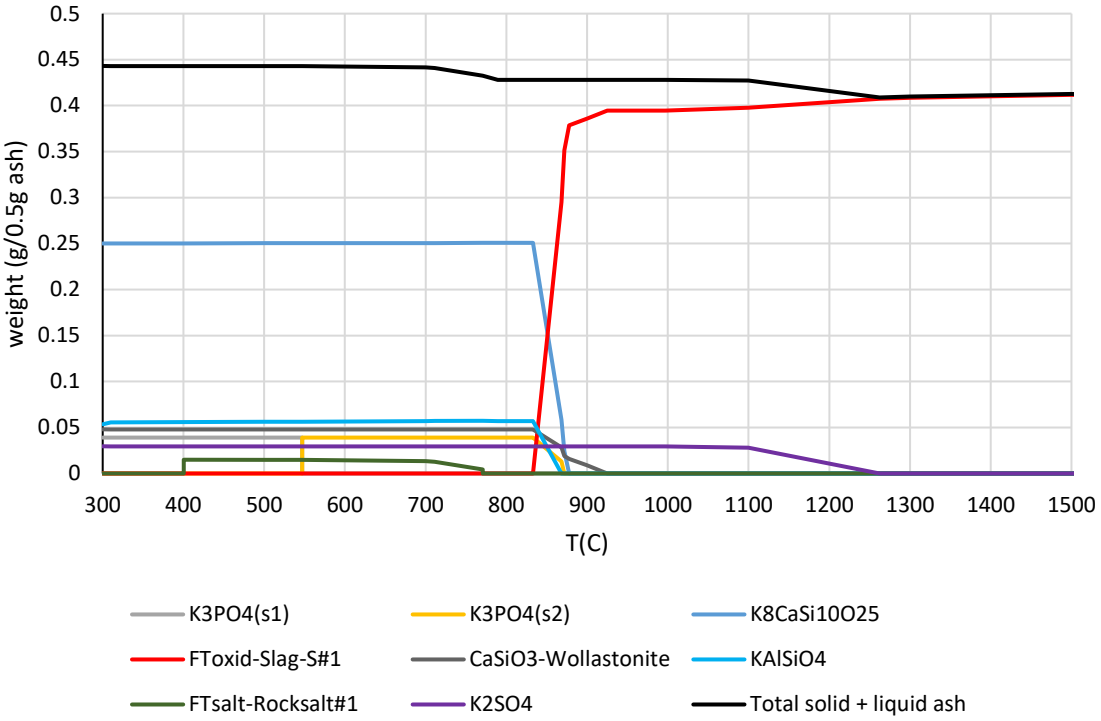

Figure 5.8: Predicted condensed composition in the straw ash with respect to temperature simulated using FToxid database set.

The results in Figure 5.9 further supported the prediction, the P-XRD measurements, and the findings of Defoort et al. (Defoort et al. 2019). Accordingly, the straw sample was highly rich in liquid, which was abundant with K and Si. In addition, traces of K_2SO_4 and KO_2 were also present in the sample. Since KO_2 is highly reactive (Tremblay et al. 1994), the shapes in Figure 5.8 reporting KO_2 might be a liquid with this composition. In all cases, the presence of KO_2 in the SEM analysis remained doubtful.

In conclusion, the SEM-EDX analysis on straw samples supported the P-XRD ones.

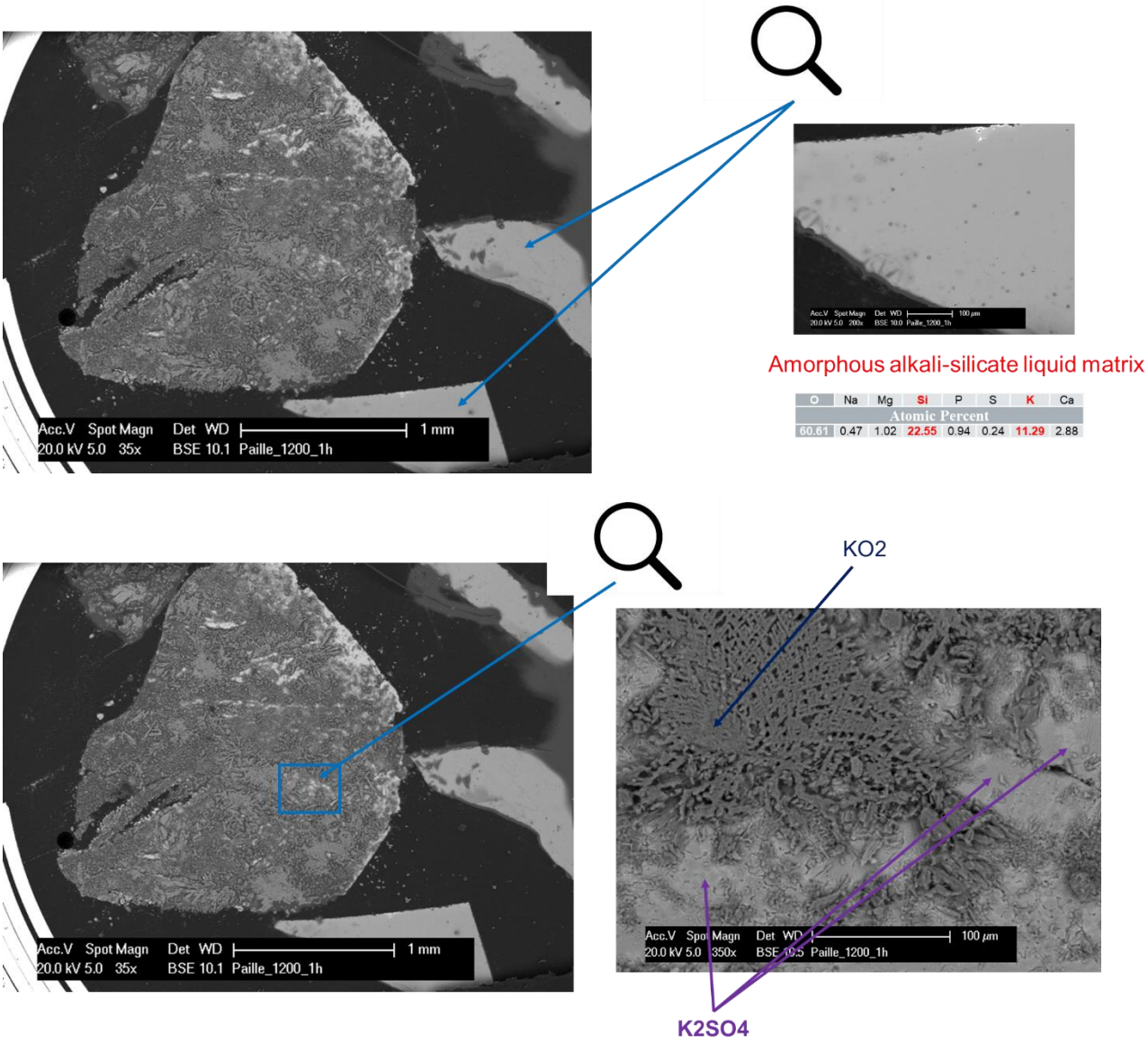

Figure 5.9 : Straw (WC) SEM-EDX results at 1200 °C.

2. Biomass ash mixtures prediction

In this section, the capabilities of the thermodynamic approaches to predict the ash state of biomass mixtures will be evaluated in detail. Calculated results will be compared against measured ones by P-XRD and TGA-DTA on ash blend samples that were shown previously to be at equilibrium.

2.1.Thermodynamic prediction approach for the condensed phases

Figure 5.10 shows the measured P-XRD results for each straw-bark ash mixture compared to those predicted by the global simulation approach using each database set at 1000 °C. Figure 5.11 shows the measured experimental P-XRD results for the BCWC ash mixture at various temperatures compared to those predicted by each database.

According to the phase diagram approach in Figure 5.1, all mixtures were positioned in the solid-liquid region, besides BCWC and BCWI. BCWI was on the border of the solid and solid-liquid region. BCWC was deep in the solid region. Accordingly, from the results in Figure 5.10, the measured P-XRD concentrations showed crystalline phases mixtures with significant amorphous contents, ranging between 40 wt.% and 60 wt.%. The lowest amorphous contents were seen in the BCWC mixture. The presence of the amorphous phase in the blends located in the solid section of the ternary diagram included the same limitations as already explained for the case of barks in section 1.1. This was a direct source of error, highlighting the need for further improvements in the thermodynamic database, especially in terms of the thermodynamic properties of the compounds located in the middle sections of the diagram. As a result, the phase diagram approach using both databases showed good prediction capabilities for the ash state (solid, liquid, or solid-liquid) in the case of the blends, with minor limitations.

According to Figures 5.10 and 5.11, global simulations using the GTOX dataset failed to predict the major ternary phases found experimentally. $K_2Ca_6Si_4O_{15}$ and $K_2Ca_2Si_2O_7$ were absent from this database (Table 3.1 in chapter 3). Besides, calculations using the GTOX dataset consistently predicted K_2CaSiO_4 and ranked it as one of the major phases. However, this phase was never found experimentally in any of the mixtures or BCWC at various reaction temperatures. This experimental finding in this work was in agreement with the work of Arroyabe et al. (Arroyabe et al. 2011).

On the other hand, in Figure 5.10, equilibrium results obtained with the FToxid dataset presented good prediction capabilities for the major ternary phases in the mixtures located in the solid section (green section in Figure 5.1) or close to it, as BCWC, BFWC, and BCWI. However, the use of the FToxid dataset failed to offer good predictions in the other samples, especially those in the solid-liquid sections, i.e. in the middle section of the diagram. Similarly, in Figure 5.11, calculation results obtained with FToxid provided better predictions for the measured major phases, especially at 1000 °C (equilibrium temperature for $K_2Ca_6Si_4O_{15}$ and $K_2Ca_2Si_2O_7$ (Atallah et al. 2022)), than those using the GTOX dataset.

Simulations using the two databases predicted the presence of the liquid phase coherently with the measurements. However, discrepancies remained between the measured composition and the predicted ones in both cases of different mixtures (Figure 5.10) and at different temperatures (Figure 5.11).

It should be noted that from the results in Figure 5.10, simulations using the GTOX dataset were able to better predict the presence of Ca_2SiO_4 than using the FToxid dataset for the mixtures in the solid section (green section in Figure 5.1) or close to it (BCWC, BFWC, and BCWI). However, further improvements are still needed for a better quantitative prediction. For the case of BCWC at different temperatures, the use of both databases failed to predict the presence of Ca_2SiO_4 at 850 °C but provided good qualitative and quantitative predictions at 1200 °C. Nevertheless, only using the GTOX dataset predicted this phase at 1000 °C. The different thermodynamic data applied in each database for this crystalline phase (Table 3.1 in chapter 3) could be the main reason behind this behavior.

$Ca_3Si_2O_7$ was predicted using the two databases but was rarely found experimentally in the various mixtures (Figure 5.10) and at different temperatures (Figure 5.11). Its absence could be due to its slow kinetic formation (ŠMIGELSKYTĖ 2019). However, its predicted appearance in the mixtures was always conjugated with the experimental $CaSiO_3$ appearance (Figure 5.10). The latter was never predicted by any database.

In terms of minor compounds, simulations using the GTOX dataset could not predict the K-rich compounds (with aluminum and sulfur) that were found experimentally according to the results in Figures 5.10 and 5.11, such as $KAlSiO_4$ and K_2SO_4. As discussed before, they were predicted to dissolve in the LIOS slag solution in the GTOX database modeling. Though simulations using the FToxid dataset were able to predict the presence of these experimental phases, they needed further improvement in terms of predicted concentrations. Furthermore, the only minor compound, $NaAlSiO_4$, predicted in certain mixtures using GTOX calculations, was never found experimentally. Hence, using the GTOX dataset for the simulations showed clear limitations for predicting the minor phases. Calculations using the FToxid dataset behaved better but still needed further improvements.

The disagreement between the measured and predicted major crystalline phases along with the liquid contents can be due to the estimated thermodynamic data of $K_2Ca_6Si_4O_{15}$ and $K_2Ca_2Si_2O_7$ in FToxid. It can also result from the thermodynamic extrapolation of the liquid phase from the binaries into the ternary. Once the missing / estimated properties are measured and added to the database, and if this system is remodeled after excluding K_2CaSiO_4, the tie lines and phase equilibria may change. This update can induce significant modifications to the predicted results, especially for the samples in the central section of the ternary diagram. This remodeling may also increase the quantitative prediction capabilities of the thermodynamic approach/database.

In conclusion, simulations using the FToxid database showed clear advantages over those using GTOX, but both databases need further improvements.

In conclusion, in the case of annealed ash of mixed biomass, the phase diagram approach provided a good qualitative ash state prediction (solid, liquid, or solid-liquid), using both databases. The global simulation approach using the FToxid database, showed decent qualitative prediction capabilities for the ash mixtures far from the central section of the ternary diagram. However, quantitative predictions using both database sets were a complete failure.

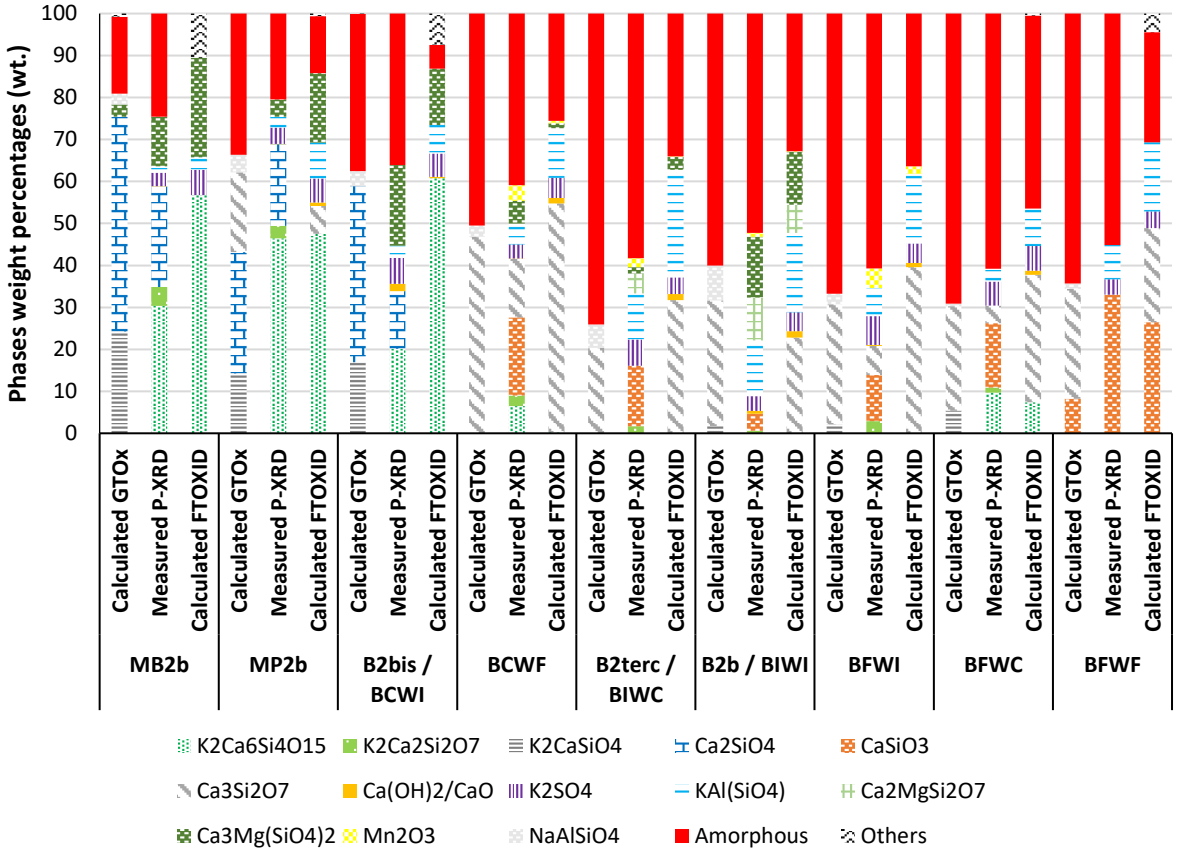

Figure 5.10: Measured (P-XRD) phases within the ash of the various mixtures VS predicted ones by the global simulation using GTOX and FToxid database sets after annealing for 6h at 1000 °C. The error for the measured P-XRD results was in the range of 2 wt.%.

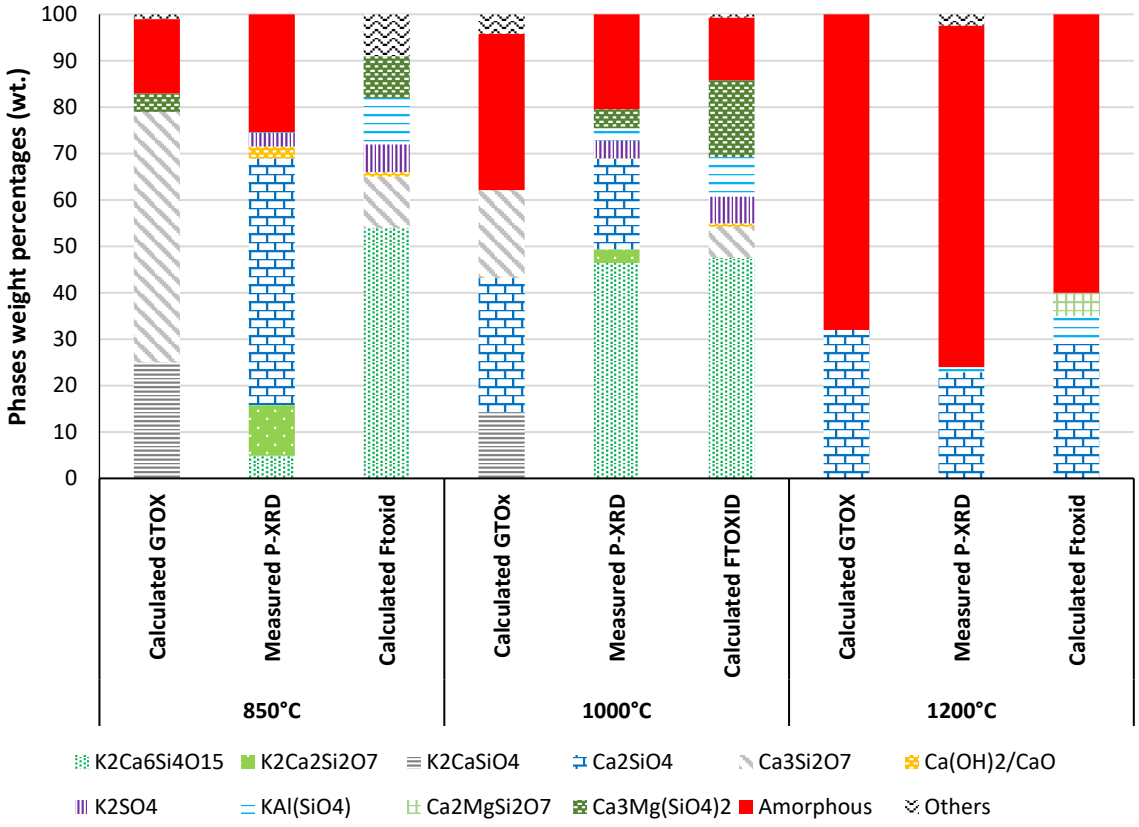

Figure 5.11: Predicted phases by the global simulation approach using GTOX and FToxid database sets VS measured (P-XRD) ones within the ash of the BCWC (MP2b) mixture after annealing for 24h at 850 °C, 6h at 1000 °C, and 6h at 1200 °C. The error for the measured P-XRD results was in the range of 2 wt.%.

2.2.TGA-DTA analysis on BCWC

Figure 5.12 depicts the ash behavior of the BCWC ash blend up to 1350 °C using TGA-DTA-MS analysis. The weight loss in green, the heat flow in blue, and the temperature in red were all measured with respect to time. Three trials using BCWC ash samples were tested: two replicate trials (straight and dotted lines) up to 1300 °C with a plateau of 1h, then a fast cooling (25 °C/min), and the third one (dashed line) up to 1350 °C with a plateau of 20 min then a slow cooling (10 °C/min). All samples gave reproducible results (error < 2%).

Figure 5.12 shows that the 50:50 mixture BCWC (MP2b) exhibited several endothermic and exothermic events corresponding to different mass losses. The first endothermic peak at 100 °C could be related to steam evaporation (mass loss 1.4 wt.%). The second exothermic peak at 420 °C is still unknown and seemed unrelated to mass loss. It might be related to a transition reaction. Link et al. (Siim Link et al. 2022) found a peak at the same position in their biomass blends. They explained it by the crystallization of some species like amorphous silicon to crystalline silicon (Siim Link et al. 2022), similar to Olanders and Steenari (Olanders and Steenari 1995). In addition, the same authors reported that this temperature could be related to

the burning of the remaining char (Siim Link et al. 2022). However, since the BCWC used in the TGA-DTA analysis was made of ash blend, the second option is not valid in this work. The third endothermic peak at 720 °C had a total mass loss of 14.2 wt.% and was related to decarbonation at 720 °C. The fourth endothermic peak could probably refer to ash fusion (solidus) that happened at 1180 °C. Negligible mass loss and no events were seen on the plateau (for both 1300 °C and 1350 °C cases). The last major exothermic peak in the case of 1300 °C was a result of the fast cooling.

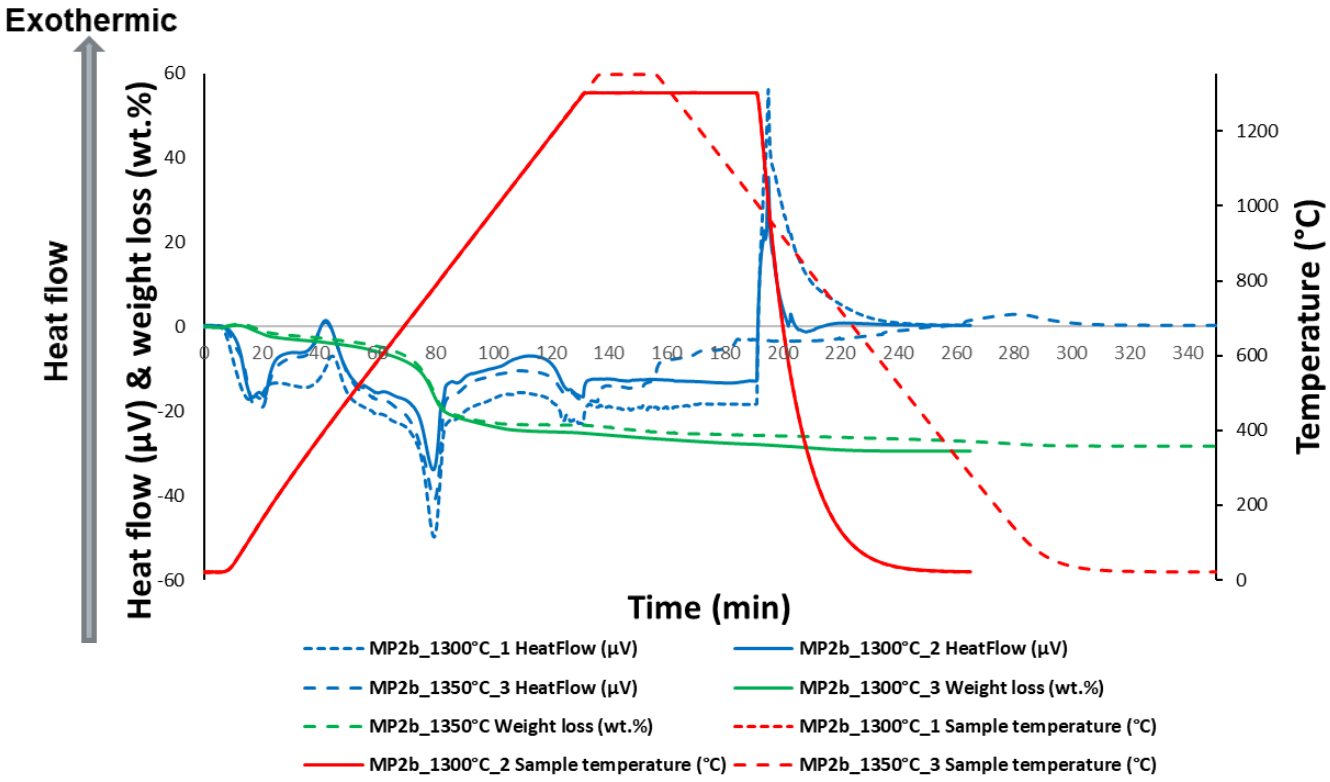

Figure 5.12: Ash BCWC (MP2b) TGA-DTA results.

Thermodynamic simulation of the TGA-DTA experiments was performed versus temperature. From section 2.1, GTOX prediction proved to be limited. Hence, it will be omitted from this comparison. The results presented in section 2.1 already proved the quantitative discrepancies between the measured condensed phases and the predicted ones using the FToxid dataset. Hence, in Table 5.2, a qualitative comparison was developed between the predicted (using FToxid dataset) and the measured BCWC phases at various temperatures. In this table the results of the ashes collected after the TGA-DTA tests at 1300 °C and 1350 °C were reported along with the results obtained in the ashes at 550 °C and in the ashes collected after the ash test at 850 °C (24 h), 1000 °C (6 h) and 1200 °C (6 h).

According with section 2.1, a partial agreement can be seen between the predicted and the measured values in Table 5.2. As explained earlier in chapter 3, the $K_2Ca_2Si_2O_7$ phase was destabilized by other elements in the simulations. Hence, it was never predicted despite its presence in all the analyzed samples by the P-XRD. A good qualitative prediction was achieved for the rest of the phases, besides minor disagreement in the case of K_2SO_4 at 1200 °C, slag at 850 °C, and Ca_2SiO_4 and $Ca_3Si_2O_7$ at 1000 °C. The predicted $KAlSiO_4$ was not measured, which was the opposite case for $Ca_3Si_2O_7$ at low temperatures. Consequently, in accord with section 2.1, the prediction tool showed limited capabilities in terms of condensed phase contents for the case of the mixture in the ash test at various temperatures.

Table 5.2: Thermodynamic calculation using FToxid dataset VS measured P-XRD results (solid & liquid) on BCWC (MP2b) ash sample at various temperatures.

	550 °C	**850 °C**	**1000 °C**	**1200 °C**	**1300 °C**	**1350 °C**
K_2SO_4	P	T P	T P	T		
$K_2Ca_6Si_4O_{15}$		T P	T P			
Slag		P	T P	T P	T P	T P
$K_2Ca_2Si_2O_7$		P	P		P	P
Carbonates (K and Ca)	T P					
Ca_2SiO_4		T P	P	T P	T P	T P
$KAlSiO_4$	T	T	T P			
$Ca_3Si_2O_7$	T	T	T			

T	Thermodynamically predicted
P	P-XRD detected

2.3.Total and elemental weight loss (volatilization)

To further assess the capabilities of the thermodynamic tool to predict the annealing experiments of ash, total and elemental volatilization (K, Na, and C) predicted by FToxid and GTOX were compared to the ones measured experimentally in Figure 5.13 for the BCWC (MP2b) ash mixture. It should be noted that the volatilization for the rest of the inorganic elements was negligible (both in the measurements and the predictions).

As shown in Figure 5.13.a, the predicted total volatilization values from the two databases were analogous. In addition, they were close to the dynamic total volatilization measured by the TGA-DTA, especially at temperatures higher than 850 °C. This temperature is considered the minimum operating temperature of any combustion process in general (Zhang and Zhang 2019; Luo and Zhou 2012). The total weight loss behavior at a temperature below 800 °C was different between the measurements and the predictions. For instance, carbon weight loss was

detected by the TGA-DTA at around 700 °C. In contrast, it was predicted to happen between 400 °C and 600 °C using both database sets. Nevertheless, the calculated total volatilization was consistent with the three static total volatilizations measured with the ash test (i.e. total experimental weight loss between the beginning and the end of the experimental test).

In parallel, from Figure 5.13.b, taking into account the relative percentage of error of the method used to calculate the elemental volatilization from the measured ICP-AES values (~15%), it can also be concluded that simulations using both databases were able to predict potassium, sodium, and carbon volatilization efficiently. The total volatilization of carbon and the significant loss of K, S, and Na into the gaseous phase, which were found experimentally, also agreed with the literature. Bostrom et al. (Boström et al. 2012) ranked the stability of oxides in the following increasing order: $K_2O<Na_2O<SO_2<H_2O/P_2O_5<CO_2<CO<SiO_2<MgO<CaO$. Hence, at a high availability of oxygen, such as in the combustion mode, carbon will be lost in the gaseous phase in the form of CO_2(g) and CO(g) (Vassilev, Baxter, and Vassileva 2013). Alkali oxides (K_2O and Na_2O) will primarily react with water vapor and volatilize fast in the form of KOH(g) and NaOH(g) (Thy et al. 2006; Boström et al. 2012). Sulfur has a lower affinity to oxygen than to carbon and hydrogen (Boström et al. 2012). Hence it will initially be released in the form of H_2S to further oxidize in the presence of excess oxygen to form SO_2 and later SO_3 in the gaseous phase (Boström et al. 2012; Vassilev, Baxter, and Vassileva 2013). Similarly, chlorine, which is considered an unstable oxide, will easily volatilize in the form of KCl(g), Cl_2(g), and HCl(g) vapor due to their low stability bonds with oxygen (Royo, Canalís, and Quintana 2020).

In conclusion, the global simulation approach effectively predicted the total and elemental volatilization of the BCWC ash blend.

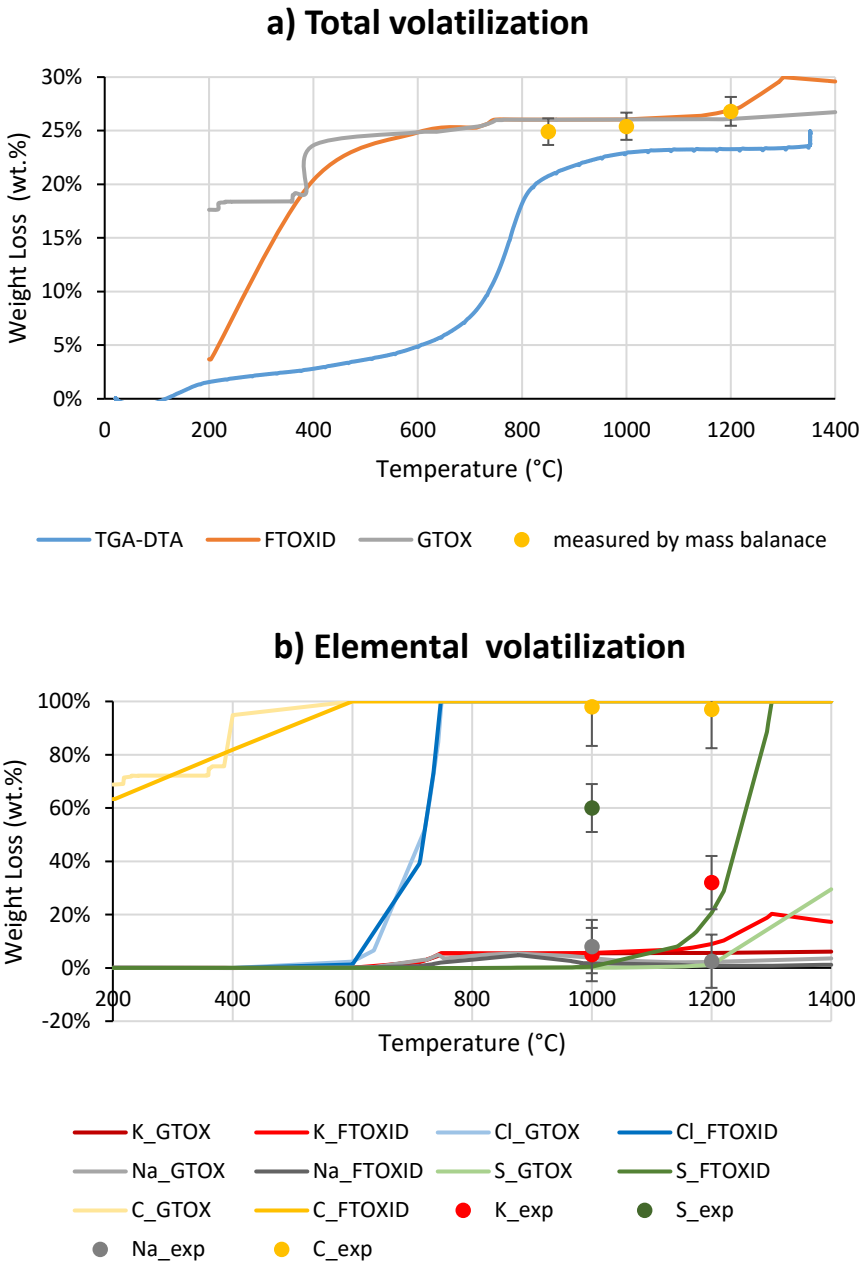

Figure 5.13: Predicted and measured total (a) and elemental (b) volatilization for the BCWC ash mixture.

2.4.Characteristic temperatures

Table 5.3 shows the solidus and liquidus temperatures for the BCWC mixture as measured by the TGA-DTA in Figure 5.12 and compared with the predicted ones in chapter 3. Calculations using the FToxid and GTOX databases predicted a close liquidus temperature of around 1400 °C while showing a 100 °C difference in solidus temperature. Though the liquidus temperature of the mixture was not able to be measured due to experimental limitations, the experimental solidus temperature was 1180 °C, significantly higher than the predicted ones.

Two main reasons can be behind this difference in the characteristic temperatures. First, this could be due to the limitation of the current thermodynamic databases and the need for corrections, especially in measuring the thermodynamic properties of the new ternary compounds of interest, $K_2Ca_6Si_4O_{15}$ and $K_2Ca_2Si_2O_7$. Second, the TGA-DTA analysis was limited and needed further annealing time for all the events to happen (Siim Link et al. 2022; S. Link et al. 2015). Furthermore, most biomass ashes are complex systems of various carbonates, phosphates, chlorides, sulfates, and silicates. Therefore, the phase-mineral transformations are highly complex and include various softening, melting, dissolution, and viscosity changes mechanisms in both the solid and liquid phases in the system (Vassilev, Baxter, and Vassileva 2014; Siim Link et al. 2022; S. Link et al. 2015). As a result, the TGA-DTA analysis lacks precision in this type of system.

The work of Berjonneau et al. (Berjonneau et al. 2009) confirmed the findings of this work. In one of the rare literature references that tried to compare the measured and predicted liquidus temperatures in the biomass ash, these authors annealed and then analyzed synthesized ash samples with close compositions to straw and miscanthus ashes, with and without K_2O contents (Berjonneau et al. 2009). They conducted their prediction using the same approach as this work and found close measured and predicted liquidus temperatures for miscanthus ash samples synthesized without K_2O. However, when K_2O was added to the ash sample, the measured liquidus temperatures drastically decreased, and the deviations between the measured and the predicted values increased (Berjonneau et al. 2009). Similar to the current work, Berjonneau et al. (Berjonneau et al. 2009) said that the lack of measured thermodynamic data for the K-compounds in the database highly affected the calculated liquidus temperatures.

In conclusion, the prediction tool failed to predict the characteristic temperatures of the BCWC blend. Nevertheless, the preliminarily measured solidus temperature of the bark BC-straw WC 50-50 mixture was reported at 1180 °C.

Table 5.3: Solidus and liquidus measured by TGA-DTA and predicted by each database for the BCWC ash mixture.

	Solidus	**Liquidus**
TGA-DTA	1180 °C	Undetected up until 1350 °C
FTOXID prediction	878 °C	1400 °C
GTOx prediction	748 °C	1436 °C

3. Pellet test prediction of both single and mixture of biomass combustion

As discussed in chapter 4, contrary to the ash test in which compressed ash chips (inorganics) were annealed at high temperature, compressed biomass pellets (organics + inorganics) were combusted in the pellet test. The latter simulates the real-life process conditions.

Figure 5.14 shows the measured P-XRD results for straw, bark, and BCWC (MP2b) ashes obtained after their pellet combustion compared to those predicted by the global simulation approach using each database set in the pellet test (i.e. on biomass pellets). In chapter 4, the pellet test was experimentally done at 850 °C (20 min and 1 h) and 1000 °C (20 min, 1 h, and 6 h) for the case of BCWC mixture. It was shown that for the mixture BCWC, there was no changes in the phase composition between 20 min and 1 h at 850 °C, and 20 min, 1 h, and 6 h at 1000 °C. Hence, the P-XRD results of BCWC in pellet test at 850 °C - 1 h and 1000 °C - 6 h were used for comparison in Figure 5.14. For the case of BC and WC single biomasses, the pellet tests were just performed at 1000 °C (1 h). Consequently, the simulations, shown in Figure 5.14, using FToxid and GTOX datasets were also conducted at 850 °C and 1000 °C.

3.1.Straw WC pellet

Similar to section 1.1, simulations using the GTOX dataset failed to predict the presence of K_2SO_4 in the straw due to a total solubility of K and S in the liquid phase LIOS. In contrast, calculations using FToxid set successfully predicted the straw behavior, but with a quantitative difference with the P-XRD measured 50% relative error values.

3.2.Bark BC pellet

For the case of bark, predictions were more different than the measured results. For instance, calculations using both databases showed good prediction capabilities for the major crystalline phases Ca_2SiO_4 and CaO along with the amorphous contents. However, their relative quantitative prediction error ranged between 20% and 50%. In addition, simulations using both databases failed to predict the existence of the measured minor phases, such as $CaSiO_3$, $KAlSiO_4$, and SiO_2. Only calculations using the FToxid dataset predicted K_2SO_4 contents close to the measured one.

On the other hand, calculations using the two databases predicted minor Ca.Mg.Si.Al phases that were never found experimentally. This might be due to their low concentration below the P-XRD detection limit, or they might be dissolved in the amorphous phase.

In conclusion, predictions using the FToxid dataset showed better capabilities than using the GTOX dataset in the case of single biomasses, still with limited predictions, especially quantitatively in the case of barks.

3.3.Mixture BCWC pellet

For the case of mixture, calculations using FToxid were able to predict the presence of $K_2Ca_6Si_4O_{15}$ and K_2SO_4 at 850 °C and 1000 °C, and liquid at 1000 °C. Those using GTOX were able to predict the presence of liquid at 850 °C and 1000 °C, and Ca2SiO4 at 1000 °C. However, the qualitative and quantitative predictions using both datasets for the rest of the minor compounds were a total failure. $CaMn_2O_4$, $Ca_3MgSi_2O_8$, $Ca_{20}Mg_3Al_{26}Si_3O_{68}$, $KMgPO_4$, and $NaAlSiO_4$ were predicted using GTOX. In comparison, $Ca_3Fe_2Si_3O_{12}$, $Ca_7Mg(SiO_4)_4$, $Ca_3Mg_5(SiO_4)_4$, $CaMn_2O_4$, $Ca_5HO_{13}P_3$, and $Ca_3MgSi_2O_8$ were foretold using FToxid. All these compounds were never found experimentally. All of these were considered minor phases. In addition, the major experimental phases, such as CaO, Ca_2SiO_4, $K_2Ca_6Si_4O_{15}$, and $K_2Ca_2Si_2O_7$, if their presence was successfully predicted, their predicted amounts were a total failure.

The main reasons behind these experimental-prediction discrepancies, as explained in Chapter 4, was the chemical reactivity in the pellet test that was significantly lower than in the ash test. The grain proximity between the inorganic elements was low due to the presence of the organic part of the biomass within the pellet. Hence, it was tough to reach the thermodynamic equilibrium in the pellet test (even at very long residence time as we have tested), which limited the thermodynamic predictions. Hence, the experimental P-XRD values, reported at 850 °C after 1 h and 1000 °C after 6 h might not even be at equilibrium. In addition, as explained in section 2.1, K_2CaSiO_4 should be omitted from the database, and $K_2Ca_6Si_4O_{15}$ and $K_2Ca_2Si_2O_7$ thermodynamic properties were estimated. This might increase the measurement-prediction discrepancies.

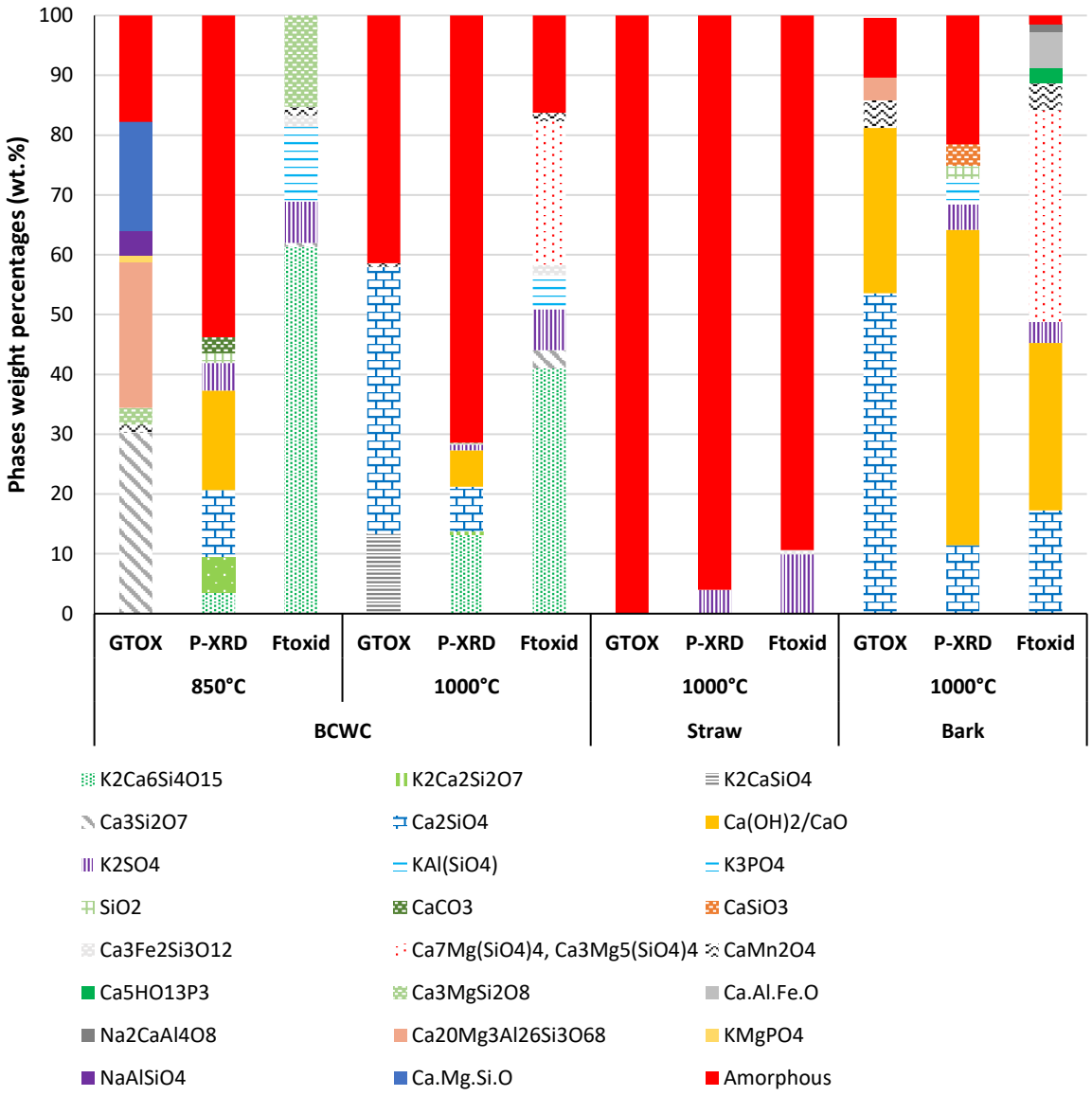

Figure 5.14: Predicted phases by the global simulation approach using GTOX and FToxid database sets VS measured (P-XRD) ones within the pellet of the BCWC mixture after annealing for 1 h at 850 °C and 6 h at 1000 °C. The error for the measured P-XRD results was in the range of 2 wt.%.

In conclusion, the pellet test predictions provided decent qualitative results for the major phases using each database set. However, the quantitative predictions using the two datasets were not compelling.

4. Conclusion

A critical assessment was carried out on two thermodynamic-based approaches to predict the interaction between the inorganic elements in the biomass ash and their mixtures. Several conclusions can be drawn out from this assessment:

- The phase diagram approach showed good capabilities in predicting the ash state (solid or liquid) using both databases, with limitations for the biomasses and blends located in the upper section (solid section) of the diagram.
- Using the global simulation approach, simulations using the FToxid dataset offered good qualitative and quantitative predictions for the single biomass ash. It also showed decent qualitative prediction capabilities for the ash mixtures far from the central section of the ternary diagram.
- Calculations using both databases showed excellent volatilization prediction capabilities. Nevertheless, they failed to forecast the characteristic temperatures for phase transitions.
- Prediction of the pellet test using both datasets was worse than with the ash test because of the lack of reactivity of the mixture. For the single biomass pellet the same prediction capability was obtained for ash or pellet tests.

Further corrections and improvements are still needed, especially in the central section of the diagram. Measuring the estimated thermodynamic properties of $K_2Ca_2Si_2O_7$ and $K_2Ca_6Si_4O_{15}$ and removing the K_2CaSiO_4 compound from this system can significantly enhance the prediction capabilities, particularly for the single biomass (ash or pellet). Afterward, the improved database can be used to reassess the capabilities of the two thermodynamic approaches to predict the ash behavior in biomass and their mixtures, not only in combustion mode but in gasification too. Furthermore, the improved database must be tested on mixtures of biomass (pellet and pilot tests). Though testing using compressed ash chips (ash test) is preferred since the ash reactivity (i.e. reaching equilibrium) was lower (chapter 4) using compressed biomass pellets (i.e. pellet and pilot tests). In addition, a preference for single biomass testing exist here since the ash reactions/interactions proved to be lower in the single biomass cases than in the blend cases.

References

Arroyabe, Erik, Richard Tessadri, Daniel M. Többens, and Volker Kahlenberg. 2011. "Does K2CaSiO4 Exist? A Phase-Analytical Study in the System K2O-CaO-SiO2 with Implications for the Characterization of Residual Materials: Does K2CaSiO4 Exist?" *Journal of the American Ceramic Society* 94 (8): 2652–55. https://doi.org/10.1111/j.1551-2916.2011.04397.x.

Atallah, Emile, Françoise Defoort, Matthieu Campargue, Alexander Pisch, and Capucine Dupont. 2022. "Will Mixing Rule or Chemical Reactions Dominate the Ash Behavior of Biomass Mixtures in Combustion Processes on Laboratory and Pilot Scales?" *Fuel* 308 (January): 122050. https://doi.org/10.1016/j.fuel.2021.122050.

Berjonneau, Jérôme, Laetitia Colombel, Jacques Poirier, Michel Pichavant, Françoise Defoort, and Jean-Marie Seiler. 2009. "Determination of the Liquidus Temperatures of Ashes from the Biomass Gazification for Fuel Production by Thermodynamical and Experimental Approaches." *Energy & Fuels* 23 (12): 6231–41. https://doi.org/10.1021/ef900738c.

Boström, Dan, Nils Skoglund, Alejandro Grimm, Christoffer Boman, Marcus Öhman, Markus Broström, and Rainer Backman. 2012. "Ash Transformation Chemistry during Combustion of Biomass." *Energy & Fuels* 26 (1): 85–93. https://doi.org/10.1021/ef201205b.

Defoort, Françoise, Matthieu Campargue, Gilles Ratel, Hélène Miller, and Capucine Dupont. 2019. "Physicochemical Approach To Blend Biomass." *Energy & Fuels* 33 (7): 5820–28. https://doi.org/10.1021/acs.energyfuels.8b04169.

Kim, Donggeum. 2017. "Coupled Experimental Study and Thermodynamic Optimization of the K2O-Na2O-CaO-MgO-Al2O3-SiO2 System." Canada: McGill University, Montreal, Quebec, Canada.

Link, S., U. Kask, J. Krail, and H. Plank. 2015. "Combustion Tests of Reed Pellets." *Proceedings of the 23rd European Biomass Conference and Exhibition* 1-4 June 2015: 5 Pages. https://doi.org/10.5071/23RDEUBCE2015-2BV.2.17.

Link, Siim, Patrik Yrjas, Daniel Lindberg, Andres Trikkel, and Valdek Mikli. 2022. "Ash Melting Behaviour of Reed and Woody Fuels Blends." *Fuel* 314 (April): 123051. https://doi.org/10.1016/j.fuel.2021.123051.

Luo, Zhongyang, and Jingsong Zhou. 2012. "Thermal Conversion of Biomass." In *Handbook of Climate Change Mitigation*, edited by Wei-Yin Chen, John Seiner, Toshio Suzuki, and Maximilian Lackner, 1001–42. New York, NY: Springer US. https://doi.org/10.1007/978-1-4419-7991-9_27.

Olanders, Birgitta, and Britt-Marie Steenari. 1995. "Characterization of Ashes from Wood and Straw." *Biomass and Bioenergy* 8 (2): 105–15. https://doi.org/10.1016/0961-9534(95)00004-Q.

Rebbling, Anders, Peter Sundberg, Jonathan Fagerström, Markus Carlborg, Claes Tullin, Dan Boström, Marcus Öhman, Christoffer Boman, and Nils Skoglund. 2020. "Demonstrating Fuel Design To Reduce Particulate Emissions and Control Slagging in Industrial-Scale Grate Combustion of Woody Biomass." *Energy & Fuels* 34 (2): 2574–83. https://doi.org/10.1021/acs.energyfuels.9b03935.

Royo, Javier, Paula Canalís, and David Quintana. 2020. "Chemical Study of Fly Ash Deposition in Combustion of Pelletized Residual Agricultural Biomass." *Fuel* 268 (May): 117228. https://doi.org/10.1016/j.fuel.2020.117228.

ŠMIGELSKYTĖ, AGNĖ. 2019. "SYNTHESIS, PROPERTIES, AND APPLICATION OF RANKINITE IN THE PRODUCTION OF CO2 CURED CONCRETE." Lithuania: KAUNAS UNIVERSITY OF TECHNOLOGY. ISBN 978-609-02-1650-7.

Thy, Peter, Bryan M. Jenkins, Charles E. Lesher, and Sidsel Grundvig. 2006. "Compositional Constraints on Slag Formation and Potassium Volatilization from Rice Straw Blended Wood Fuel." *Fuel Processing Technology* 87 (5): 383–408. https://doi.org/10.1016/j.fuproc.2005.08.015.

Tremblay, Benoît, Laurent Manceron, Pascale Roy, Anne-Marie LeQuéré, and Denis Roy. 1994. "Vibrational Spectra and Structure of the KO2 Complex in Solid Argon. A Far-Infrared Study." *Chemical Physics Letters* 228 (4): 410–16. https://doi.org/10.1016/0009-2614(94)00962-7.

Vassilev, Stanislav V., David Baxter, and Christina G. Vassileva. 2013. "An Overview of the Behaviour of Biomass during Combustion: Part I. Phase-Mineral Transformations of Organic and Inorganic Matter." *Fuel* 112 (October): 391–449. https://doi.org/10.1016/j.fuel.2013.05.043.

———. 2014. "An Overview of the Behaviour of Biomass during Combustion: Part II. Ash Fusion and Ash Formation Mechanisms of Biomass Types." *Fuel* 117 (January): 152–83. https://doi.org/10.1016/j.fuel.2013.09.024.

Zhang, Jiajun, and Xiaolei Zhang. 2019. "15 - The Thermochemical Conversion of Biomass into Biofuels." In *Biomass, Biopolymer-Based Materials, and Bioenergy*, edited by Deepak Verma, Elena Fortunati, Siddharth Jain, and Xiaolei Zhang, 327–68. Woodhead Publishing Series in Composites Science and Engineering. Woodhead Publishing. https://doi.org/10.1016/B978-0-08-102426-3.00015-1.

6. Chapter 6: Contribution to the thermodynamic database improvements

As highlighted in chapter 5, further corrections and updates are still needed to improve the thermodynamic database. From the results in chapter 3, using the FToxid database, four main ternary compounds exist in the calculated $CaO\text{-}K_2O\text{-}SiO_2$ ternary phase diagram in the temperature range between 850 °C and 1200 °C: $K_2Ca_2Si_2O_7$ (1:2:2), $K_2Ca_6Si_4O_{15}$ (1:6:4), $K_4CaSi_3O_9$ (2:1:3), and K_2CaSiO_4 (1:1:1). The thermodynamic properties of $K_2Ca_2Si_2O_7$ and $K_2Ca_6Si_4O_{15}$, which were added to FToxid and found experimentally as major phases (chapter 4), were based on estimations (D. Kim 2017). Hence, in section 1, the synthesis of $K_2Ca_2Si_2O_7$ (1:2:2), $K_2Ca_6Si_4O_{15}$ (1:6:4), and $K_4CaSi_3O_9$ (2:1:3) will be presented in detail, highlighting the optimum synthesis conditions to obtain the purest compounds. Then, in section 2, their measured melting point and enthalpy of formation will be shown. In parallel, according to chapter 5, K_2CaSiO_4 was never found experimentally and should be omitted from this system according to literature (chapter 1). Hence, in section 3, a set of synthesis and investigations, which were conducted to assess the presence of this phase, will be presented. Finally, in section 4, the thermodynamic modeling of the stoichiometric compounds in the binary $K_2O\text{-}SiO_2$ will be elaborated. This section will be a part of the ongoing work on remodeling the binary diagram $K_2O\text{-}SiO_2$ with the latest data and calculations.

1. Ternary compounds synthesis

The synthesis methods used by Arroyabe et al. (Erik Arroyabe et al. 2011; E. Arroyabe et al. 2009) and Santoso et al. (Santoso et al. 2020) were initially tried in this work for $K_2Ca_2Si_2O_7$ and $K_2Ca_6Si_4O_{15}$, respectively. They will be discussed at the beginning of each following synthesis section. $K_4CaSi_3O_9$ initial synthesis conditions were adapted from another work of Arroyabe et al. (Erik Arroyabe, Kaindl, and Kahlenberg 2009). Then, the temperature and residence time were varied depending on the produced crystalline phases to optimize the synthesis conditions to achieve the highest compound purity. In this section, the synthesis of each ternary compound of interest under the various combinations of temperatures and residence times will be presented in detail.

CaO was used in the synthesis instead of $CaCO_3$ (i.e. calcined $CaCO_3$) to reduce the total gas loss during the reaction. Hence, the total weight loss included carbon loss from K_2CO_3 in the form of CO_2 along with potassium loss in the form of K (g). In a recent study, Sergeev et al. (Sergeev et al. 2019) studied the vaporization behavior of K_2CO_3 in a Knudsen Effusion Mass Spectrometer between 600 °C and 880 °C. They have found that K_2CO_3 vaporized congruently below 750 °C (Sergeev et al. 2019). However, above this temperature, the vapor pressure of CO_2 disproportionally increased, and Sergeev et al. (Sergeev et al. 2019) observed incongruent vaporization. As a result, since the synthesis temperatures of all the compounds were above 750 °C in this work, CO_2 in K_2CO_3 was assumed to volatilize totally. Consequently, after calculating the CO_2 weight loss by mass balance from each reaction in section 3.2 in chapter 2, the additional potassium weight loss was calculated by a simple difference between the measured total weight loss and the CO_2 calculated weight loss.

Once the optimum synthesis conditions were found, 5g of each compound were synthesized and stored in a glove box for further measurements. More details about the synthesis apparatus and procedure are shown in section 3.2 in chapter 2.

1.1. $K_2Ca_2Si_2O_7$ synthesis

Arroyabe et al. (Erik Arroyabe et al. 2011) were able to synthesize pure $K_2Ca_2Si_2O_7$ (O7) starting from K_2CO_3, SiO_2, and $CaCO_3$ at 900 °C for 78 h under atmospheric conditions (in the air). However, the setup used in the current work applies argon to decrease K-loss by hindering its reaction with humidity in the air to produce KOH. Figure 6.1.a shows the total and potassium weight loss under each set of operating conditions, while Figure 6.1.b shows the corresponding produced crystalline compound and their concentrations.

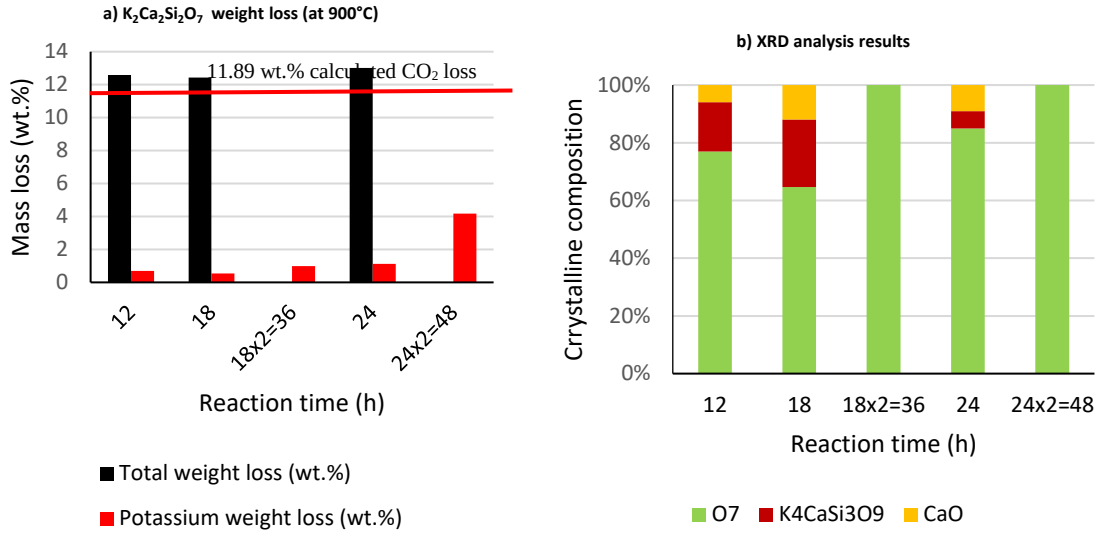

Figure 6.1: Total and K weight loss (a) and (b) XRD analysis under each set of operating conditions for $K_2Ca_2Si_2O_7$ synthesis.

CO_2 theoretical loss was calculated by mass balance from the theoretical reaction (A) in chapter 2 and was found to be 11.89 wt.%. The rest is potassium loss, calculated by the mass difference between the total measured mass loss and the CO_2 calculated weight loss. Besides, K loss at 36 h was cumulative from the one at 18 h, similarly to the case of 24 h and 48 h. From Figure 6.1.a, K loss increased with the increase in reaction time; hence the stoichiometry that should be theoretically over the pure $K_2Ca_2Si_2O_7$ point in the phase diagram was shifting. From Figure 6.1.b, no K_2CO_3 and SiO_2 were detected in the XRD analysis (totally reacted), and pure $K_2Ca_2Si_2O_7$ was obtained after 36 h and 48 h at 900 °C. The former was adopted as the optimum condition due to less K loss, around 1 wt.% at 36 h compared to 4.17 wt.% at 48 h. The results were reproducible.

1.2.$K_4CaSi_3O_9$ synthesis

$K_4CaSi_3O_9$ (O9) synthesis was not complicated at all. Arroyabe et al. (Erik Arroyabe, Kaindl, and Kahlenberg 2009) were able to synthesize pure $K_4CaSi_3O_9$ (O9) starting from K_2CO_3, SiO_2, and $CaCO_3$ at 900 °C for 4 days under atmospheric condition (in the air). Figure 6.2.a shows the total and potassium weight loss under each set of operating conditions, while Figure 6.2.b shows the corresponding produced crystalline structures and their concentrations. The optimum temperature found in the work of Arroyabe et al. (Erik Arroyabe, Kaindl, and Kahlenberg 2009) worked well here (i.e. 900 °C). However, due to the application of argon atmosphere in this work instead of air in the aforementioned work, less potassium loss was noticed, and hence pure $K_4CaSi_3O_9$ was obtained at a shorter residence time. CO_2 total loss was calculated by mass

balance from reaction (2) and was found to be 17.2 wt.%, close to the total weight loss. Hence, potassium loss was negligible in all cases (Figure 6.2.a). From Figure 6.2.b, traces of CaO were always present in the first two sets of operating conditions (18 h - 800 °C & 18 h – 900 °C), while pure $K_4CaSi_3O_9$ was found at 24 h – 900 °C without any K loss. Hence, this was assumed to be the optimum condition.

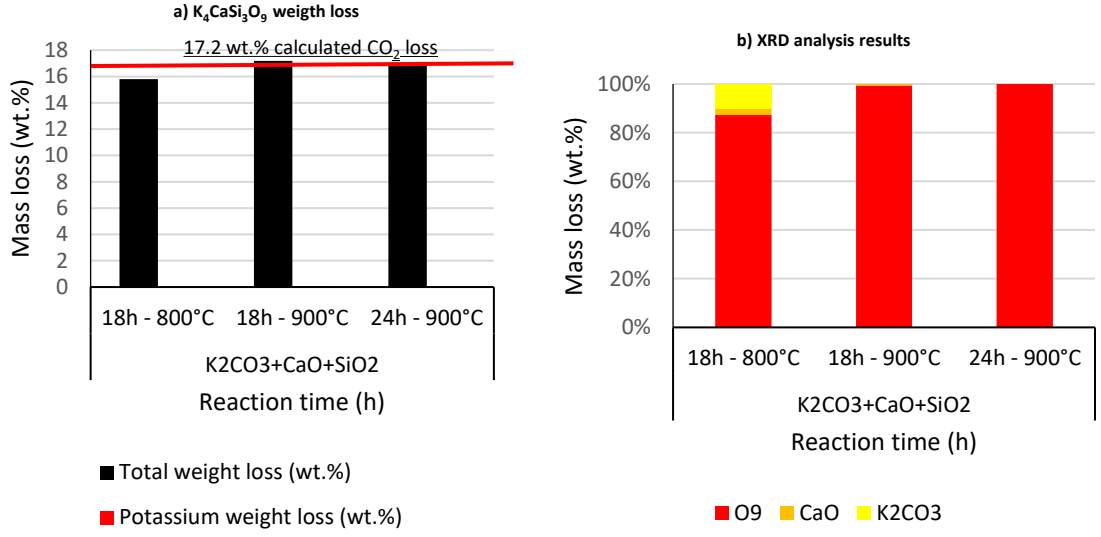

Figure 6.2: Total and K weight loss (a) and crystalline composition under each set of operating conditions for $K_4CaSi_3O_9$ synthesis.

1.3.$K_2Ca_6Si_4O_{15}$ synthesis

$K_2Ca_6Si_4O_{15}$ (O15) synthesis was the most challenging. Arroyabe et al. (E. Arroyabe et al. 2009) synthesized O15 in air at 1000 °C for 7 days, while Santoso et al. (Santoso et al. 2020) started to see O15 with liquid at 1100 °C after 43 h (sample hung by a 0.5 mm Pt wire in the air with various K_2CO_3, SiO_2, and $CaCO_3$ composition). Figure 6.3.a shows the total and potassium weight loss under each set of operating conditions, while Figure 6.3.b shows the corresponding produced crystalline compound and their concentrations. CO_2 theoretical loss was calculated by mass balance from reaction (3) and was 6.16 wt.%. The rest is potassium loss was calculated by the mass difference between the total measured mass loss and the CO_2 calculated mass loss. From Figure 6.3.a, potassium loss increased with residence time and temperature. Hence, the optimum condition was defined as the highest purity of O15 with the lowest K loss possible.

Contrary to Arroyabe et al. (E. Arroyabe et al. 2009), from Figure 6.3.b, O15 in the current work was less stable at 1000 °C, reaching a maximum of 30% after 6 days. In addition, it was decomposing at 1100 °C with an increase in residence time from 72% after 2 days to 68% after 4 days. Hence, the optimum synthesis conditions should be in-between. Though, the main

phases present with O15 were O7 and Ca_2SiO_4. K loss at high temperature and longer residence time shifted the synthesized point into a region richer in O7 and Ca_2SiO_4. Nevertheless, at a synthesis temperature of 1050 °C, O15 reached a very high value of 87% after 2 days. 99% O15 was reached under the same temperature after 4 days. Equilibrium was reached at this temperature after 4 days since a further increase in time decreased O15 contents due to the K loss that caused a point shift. Hence, 1050 °C and 4 days were found to be the optimum synthesis conditions. Under these same conditions, the total K loss was around 1 wt.%, the lowest compared with the other temperatures.

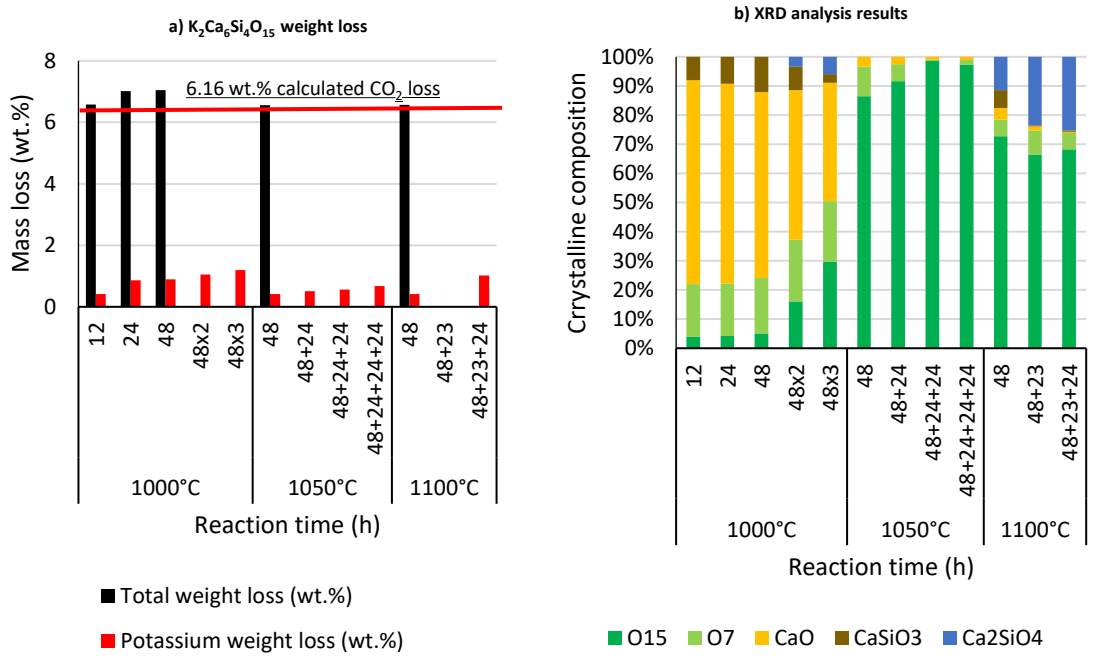

Figure 6.3: Total and K weight loss (a) and crystalline composition under each set of operating conditions for $K_2Ca_6Si_4O_{15}$ synthesis.

In conclusion, the optimum synthesis temperature and residence time for each compound along with its K loss are summarized in Table 6.1

Table 6.1: Summary of the optimum synthesis conditions of $K_2Ca_2Si_2O_7$, $K_2Ca_6Si_4O_{15}$, $K_4CaSi_3O_9$.

Compound	Temperature (°C)	Annealing time (h)	K loss (wt.%)
$K_2Ca_2Si_2O_7$	900	18+18	1
$K_4CaSi_3O_9$	900	24	0
$K_2Ca_6Si_4O_{15}$	1050	48+24+24	1

2. Ternary compounds properties measurements

As shown earlier, the three ternary phases of interest were successfully synthesized with high purity (99%). The main aim was to measure their thermodynamic properties. Hence, in this

section, the measured melting point and enthalpy of formation of each synthesized compound will be presented.

2.1.Melting point measurements

Table 6.2 shows the melting point measurement of each synthesized ternary compound. The measurements were conducted using a TGA-DSC instrument, as described in section 4.6 in chapter 2.

The melting points of the three compounds in FToxid were based on estimations (D. Kim 2017), similar to GTOX. $K_2Ca_2Si_2O_7$ and $K_2Ca_6Si_4O_{15}$ were absent from GTOX. $K_2CaSi_3O_9$ estimated values in FToxid and GTOX were slightly different due to different estimation sources. However, the new measured melting point value of $K_2Ca_2Si_2O_7$ in this work (Figure 6.4) was close to the estimated one (25 °C difference). Nevertheless, due to time constraints and measurement problems, the melting point measurements of $K_2Ca_6Si_4O_{15}$ and $K_2CaSi_3O_9$ are still in progress.

Table 6.2: TGA-DSC melting point measurements for each synthesized ternary compound compared to calculated ones using FToxid and GTOX thermodynamic databases.

	Melting point (°C)		
	Measured by the TGA-DSC	Calculated using FToxid	Calculated using GTOX
$K_2Ca_2Si_2O_7$	1255 °C ± 5 °C	1275	-
$K_2Ca_6Si_4O_{15}$	In progress	1212	-
$K_4CaSi_3O_9$	In progress	997	1013

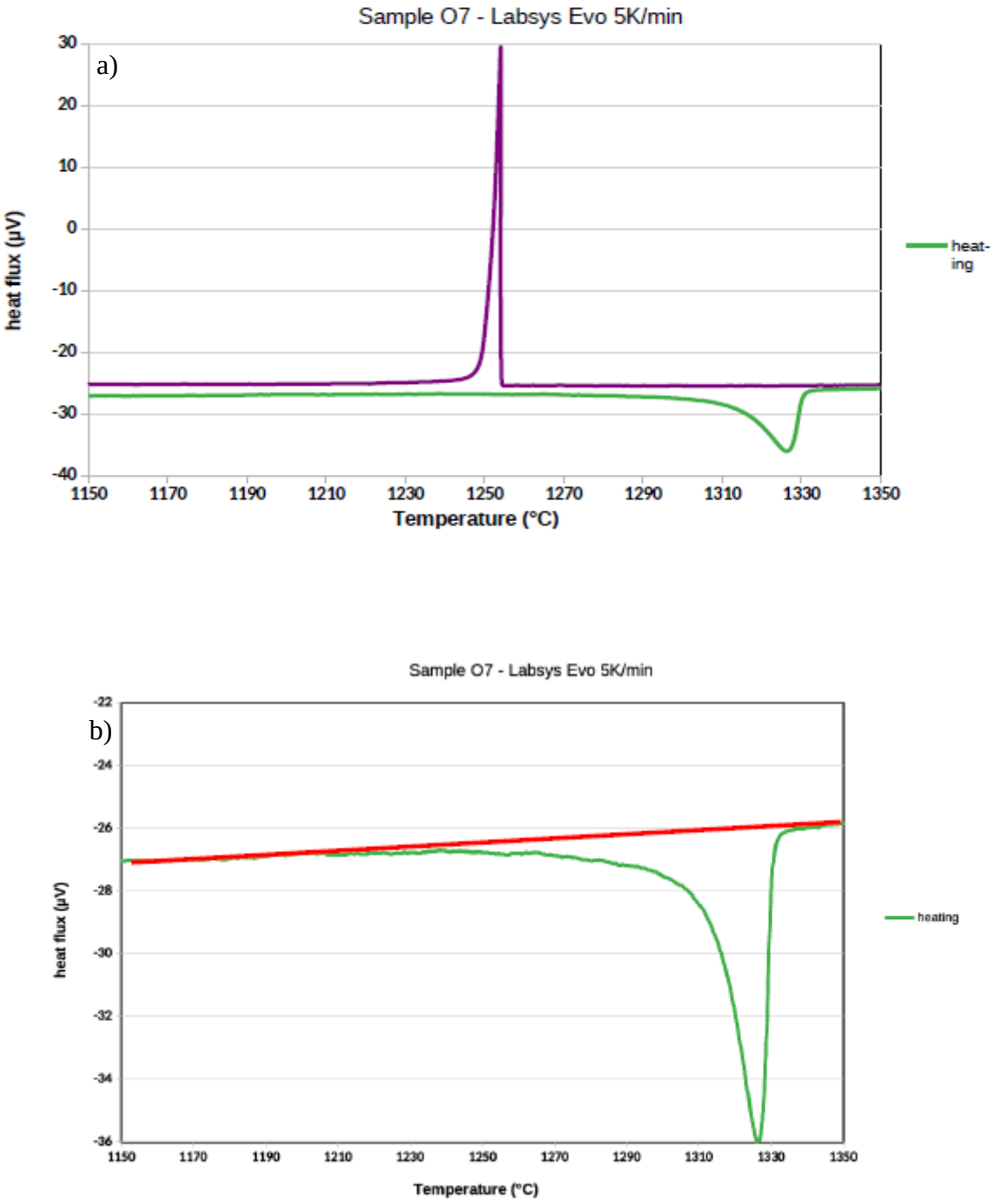

Figure 6.4: K2Ca2Si2O7 melting point measurements by DSC a) heating curve and b) cooling curve.

2.2.Enthalpy of formation

The enthalpy of formation was calculated from oxides based on Kozin et al. (Kozin et al. 2020). The drop solution enthalpy at 800 °C for each synthesized compound was measured by solution calorimetry in Lead Borate, as described in section 4.7 in chapter 2. The general pathway is as follow (x → K atoms, y → Ca atoms, z → Si atoms):

Eq. #	Equation	ΔH
1	$K_xCa_ySi_zO_{x/2+y+2z}$ (s, 298K) → (x/2).K_2O (sol, 1073K) + y.CaO (sol. 1073K) + z.SiO_2 (sol, 1073K)	measured by solution calorimetry
2	$K_xCa_ySi_zO_{x/2+y+2z}$. w.H_2O (s, 298K) → $K_xCa_ySi_zO_{x/2+y+2z}$. w.H_2O (s, 1073K) + w.H_2O (g, 1073K)	Zero → dry basis
3	$K_xCa_ySi_zO_{x/2+y+2z}$. w.H_2O (s, 298K) → $K_xCa_ySi_zO_{x/2+y+2z}$. w.H_2O (s, 1073K)	
4	K_2CO_3 (s, 298K) → K_2O (sol, 1073K) + CO_2 (g, 1073K)	Converted to eq. 11 later on
5	K_2O (s, 298K) + CO_2 (g, 298K) → K_2CO_3 (s, 298K)	
6	CO_2 (g, 298K) → CO_2 (g, 1073K)	
7	CaO (s, 298K) → CaO (sol, 1073K)	-7.08±2.31 kJ/mol (Cheng and Navrotsky 2005)
8	SiO_2 (s, 298K) → SiO_2 (sol, 1073K)	47.79±0.32 kJ/mol (Navrotsky 2014)
9	H_2O (l, 298K) → H_2O (g, 1073K)	72.84 kJ/mol ("Data From NIST Standard Reference Database 69" 2020)
10	(x/2).K_2O (s, 298K) + y.CaO (s, 298K) + z.SiO_2 (s, 298K) + w.H_2O (l, 298K) → $K_xCa_ySi_zO_{x/2+y+2z}$. w.H_2O (s, 298K)	ΔH10f = - ΔH1 - ΔH2 - ΔH3 + y. ΔH7 + z. ΔH8 + …

The samples were assumed to be dry before the analysis. Hence, the enthalpy of reactions 2 and 3 were not measured. Hence, w was taken to be zero then the enthalpy of reaction 9 was not needed anymore. Consequently, reaction 10, on a dehydrated basis (i.e. without H_2O part), becomes as follow:

(x/2).K_2O (s, 298K) + y.CaO (s, 298K) + z.SiO_2 (s, 298K) → $K_xCa_ySi_zO_{x/2+y+2z}$. (s, 298K)

$$\Delta H10_f = - \Delta H1 + y.\ \Delta H7 + z.\ \Delta H8 + (x/2).\ \Delta H_{(K2O)}$$

Equations 4, 5, and 6 can be reduced to:

11. K_2O (s, 298K) → K_2O (sol, 1073K)

$\Delta H_{(K2O)}$ (at 700 °C) was derived in the work of Navrotsky et al. (Navrotsky 2014) based on the enthalpies of reactions 4 and 5 measured by solution drop calorimetry in a molten Lead Borate solution in Kiseleva et al. (Kiseleva et al. 1996). $\Delta H_{(K2O)}$ (at 700 °C) was found to be -193.68 ± 1.10 kJ/mol. However, the drop in the current work happened at 800 °C and not 700 °C. Hence, the formula below was used to calculate $\Delta H_{drop\ (K2O)}$ at 800 °C:

$$H_{drop\ (800\ °C)} = H_{drop\ (700\ °C)} + H_{0\ K2O\ (800\ °C)} - H_{0\ K2O\ (700\ °C)}$$

$$\text{where } H_0 = H(T)-H(0)$$

Data for $H_{0\ K2O\ (800\ °C)}$ and $H_{0\ K2O\ (700\ °C)}$ were calculated using the Lagrange interpolation polynomial from the tabulated values taken from (Gurvich and Veyts 1990) (document in paper form → does not exist online). Using FactSage software equipped with FactPS, $H_{0\ K2O\ (800\ °C)} - H_{0\ K2O\ (700\ °C)}$ was found to be equal to 10.117 kJ/mol. This value was very close to the 10 kJ/mol value found in the tables of Gurvich et al. (Gurvich and Veyts 1990).

After a thorough review, just these two publications for the enthalpy of drop of K_2O were found in literature. Then, $\Delta H11 = -183.68$ kJ/mol.

In conclusion, $\Delta H10_f = -\Delta H1 + y.\ \Delta H7 + z.\ \Delta H8 + (x/2).\ \Delta H11$

As a result, the equations of the enthalpy of formation for each synthesized ternary compound is as follows:

$K_2Ca_2Si_2O_7$: $\Delta H_f = -\Delta H1 + 2.\ \Delta H7 + 2.\ \Delta H8 + \Delta H11$

$K_2Ca_6Si_4O_{15}$: $\Delta H_f = -\Delta H1 + 6.\ \Delta H3 + 4.\ \Delta H4 + \Delta H11$

$K_4CaSi_3O_9$: $\Delta H_f = -\Delta H1 + \Delta H3 + 3.\ \Delta H4 + 2.\ \Delta H11$

Table 6.3 summarizes all the final measured-calculated enthalpy of formation with respect to the ones in the FToxid and GTOX database. It should be noted that the enthalpy of formation in each database was calculated from the oxides (i.e. CaO, K_2O, and SiO_2) at 25 °C (298 K).

Table 6.3: Calculated enthalpy of formation at 298K of each synthesized ternary compound based on the solution calorimetry measurements at 800 °C in lead borate compared to calculated ones using FToxid and GTOX thermodynamic databases.

All in kJ/mol	**K_2O**	**CaO**	**SiO_2**	**Measured solution drop enthalpy**	**Enthalpy of formation calculated in this work from the measured values**	**Enthalpy of formation calculated using FToxid**	**Enthalpy of formation calculated using GTOX**
drop enthalpy 800 °C	-183.68	-7.08	47.79				
$K_2Ca_2Si_2O_7$	1	2	2	294.9	-397.1	-430.9	
$K_2Ca_6Si_4O_{15}$	1	6	4	569.5	-604.5	-740.2	
$K_4CaSi_3O_9$	2	1	3	462.6	-693.7	-654.8	-906.8

3. K_2CaSiO_4 (O4) investigation

The presence of K_2CaSiO_4 in the CaO-K_2O-SiO_2 system was always debatable in the literature. This compound was first reported in the work of Morey et al. (Morey, Kracek, and Bowen 1930) in 1930. Morey et al. (Morey, Kracek, and Bowen 1930) reported that this compound had a hexagonal structure and melted congruently at 1630 °C. On the other hand, Hughes et al. (Hughes 1966) synthesized this compound at 1100 °C for 48 h in air. They reported a cubic structure for this compound with a = 8.008 Å (Hughes 1966). This structure is used in the ICDD crystalline database, with a PDF number 00-065-0002. Later on, Berezhnoi et al. (Berezhnoi et al. 1976) formulated this compound by annealing the oxide mixture three to four times at 950 °C - 1100 °C in air with intermediate grinding. They proposed an orthorhombic structure for the same compound, with a = 8.324 Å, b = 9.273 Å, and c = 12.634 Å (Berezhnoi et al. 1976).

In recent work, Arroyabe et al. (Erik Arroyabe et al. 2011) tried to synthesize K_2CaSiO_4 in a platinum crucible covered with a lid in air. The samples were heated in a furnace from 300 °C to 1000 °C with a ramp of 50 °C/h for three different holding times at 1000 °C (1 day, 3.5 days, and 7 days) (Erik Arroyabe et al. 2011). The authors also conducted a fourth trial in which they heated the sample from 300 °C to 850 °C within 21 h, followed by a hold time of 29.5 h to volatilize the CO_2 (Erik Arroyabe et al. 2011). Then, they sealed the sample in a gold tube and annealed it at 1000 °C for 7 days (Erik Arroyabe et al. 2011). Similar to the previously reported authors (Hughes 1966; Berezhnoi et al. 1976), Arroyabe et al. (Erik Arroyabe et al. 2011) starting materials were stoichiometric mixtures of $CaCO_3$, K_2CO_3, and SiO_2.

In the open system experiments (i.e. the three experiments in air in a platinum crucible covered with a lid), Arroyabe et al. (Erik Arroyabe et al. 2011) reported a significant K-loss ranging between 45% and 53%. Hence, they stated the absence of K_2CaSiO_4 (1:1:1) and the presence of $K_2Ca_2Si_2O_7$ (1:2:2) with minor amounts of $K_2Ca_6Si_4O_{15}$ (1:6:4). In the closed system experiment (the one sealed in a gold tube), Arroyabe et al. (Erik Arroyabe et al. 2011) found an

insignificant mass loss. They reported the presence of $K_2Ca_2Si_2O_7$ with traces of K_2CO_3 x 1.5 H_2O. As a result, K_2CaSiO_4 was never found, and the authors argued that this phase was mistaken for $K_2Ca_2Si_2O_7$.

Arroyabe et al. (Erik Arroyabe et al. 2011) also reported a measured melting point at 1170 °C in the sample in the closed system (trial 4). This melting point is 100 °C different from the one estimated in the FToxid database and 80 °C lower than the value measured (on pure compound) in this work for $K_2Ca_2Si_2O_7$ (Table 6.2). The traces of K_2CO_3 x 1.5 H_2O might be the source of this difference. Nevertheless, this finding also supported Arroyabe et al. (Erik Arroyabe et al. 2011) claim that their synthesized 1:1:1 (O4) molar ratio led to the 1:2:2 (O7) ratio.

Comparing their P-XRD results to Hughes et al. (Hughes 1966) and Berezhnoi et al. (Berezhnoi et al. 1976), Arroyabe et al. (Erik Arroyabe et al. 2011) argued that the cubic cell of Hughes et al. (Hughes 1966) explained the most intense reflections (i.e. vertical lines) but left a very large number of the medium and low intensity lines unindexed. In addition, the orthorhombic cell reported by Berezhnoi et al. (Berezhnoi et al. 1976) predicted a larger number of the observed medium and low intensity peaks, but with a very low matching. Furthermore, given that Morey et al. (Morey, Kracek, and Bowen 1930) stated that K_2CaSiO_4 could form hexagonal bipyramids with optically uniaxial character, Arroyabe et al. (Erik Arroyabe et al. 2011) argued that Morey et al. (Morey, Kracek, and Bowen 1930) actually obtained single crystals of $K_2Ca_2Si_2O_7$ that indeed belonged to the hexagonal crystal system, but failed to report it due to the limited experimental techniques at that time. Finally, comparing their synthesis work on K_2CaSiO_4 (1:1:1) with a previous one on $K_2Ca_2Si_2O_7$ (1:2:2) (Erik Arroyabe and Kahlenberg 2011), Arroyabe et al. (Erik Arroyabe et al. 2011) reported a close match between the two diffractograms.

Since all the experiments mentioned before were conducted in natural air (Morey, Kracek, and Bowen 1930; Hughes 1966; Berezhnoi et al. 1976; Erik Arroyabe et al. 2011), doubts always remain due to the constant occurrence of the K-loss or its reaction with water, even in sealed crucibles. Hence, synthesis experiments were repeated in this work according to the method described in section 3.2 of chapter 2. A CaO, K_2CO_3, and SiO_2 mixture with a 1:1:1 molar ratio was annealed at 900 °C for 18 h under a constant argon flow. From its P-XRD analysis in Figure 6.5, CaO disappeared (so the mixture reached equilibrium), and $K_2Ca_2Si_2O_7$ was the major crystalline structure. Nevertheless, several major peaks at 2Θ 32°, 32.5°, and 33°, and minor ones 2Θ 40°, 46°, and 47°, were impossible to explain using the most recent ICDD 2022 crystalline database. Therefore, these unexplained peaks will be assumed to form a single

structure, absent from the most recent crystalline database. This phase will be called “phase U” in this work.

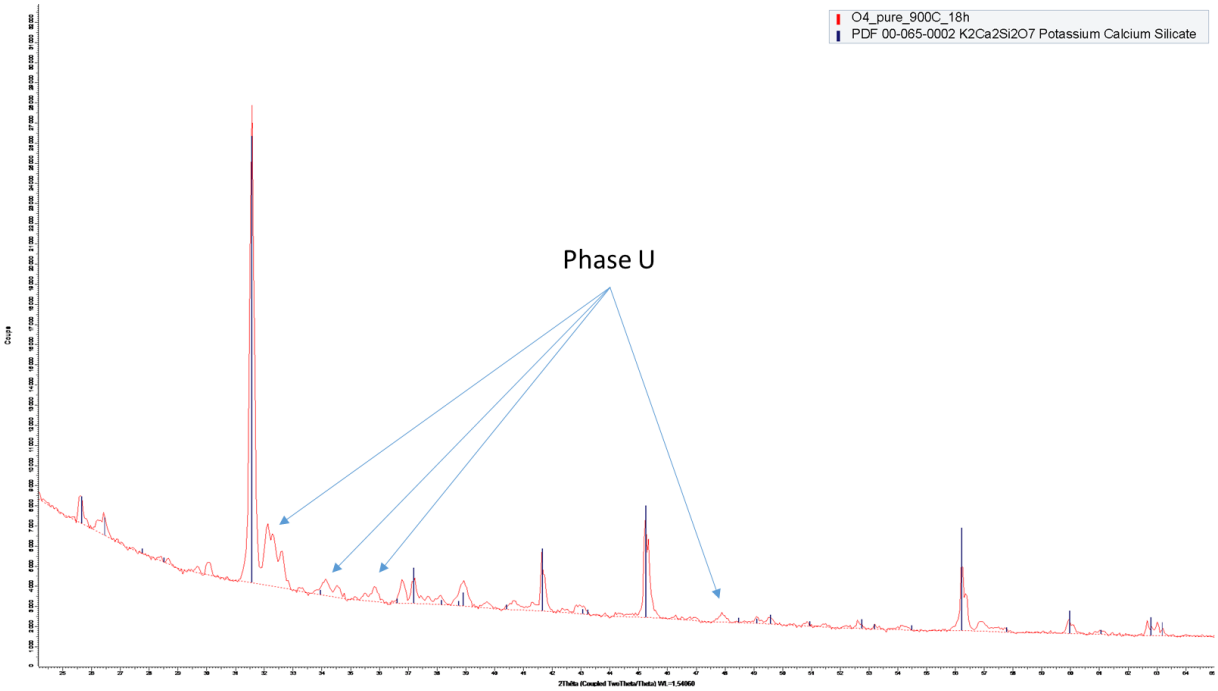

Figure 6.5: P-XRD pattern of K2CaSiO4 synthesized using a 1:1:1 CaO-K2O-SiO2 molar ration and annealed at 900 °C for 18h.

To further investigate the stability of K_2CaSiO_4, more mixtures were formed and annealed at 900 °C and 1050 °C. A mixture of CaO and the synthesized $K_2Ca_2Si_2O_7$ (in section 1.1 in this chapter) was formed, called M1 and denoted by “x” in the following Figures. The annealing results of this mixture aimed to validate the presence of the tie line between CaO and $K_2Ca_2Si_2O_7$. Next, K_2CO_3 was added to M1 to form a second mixture M2, denoted by “*”. Then, more CaO was added to the M2 mixture to form M3 mixture, denoted by “+”. Table 6.4 summarizes the P-XRD results of the various mixtures annealed under various temperatures and residence times.

Table 6.4: P-XRD results of the various synthesized mixtures, positioned in the middle section of the ternary diagram, annealed under the various temperatures and residence times.

Compound	Position on the diagram			Synthesis conditions			P-XRD results			K loss (wt.%)
	CaO Mol%	SiO_2 Mol%	K_2O Mol%	T (°C)	t (h)	Atm	O7	CaO	Phase U	
Theoretical K_2CaSiO_4	33.33	33.33	33.33	900	18	Ar	yes	no	yes	2.56
M1 (O7+CaO)	47.14	35.23	17.61	900	20	Ar	yes	yes	Yes (traces)	0
M1 (O7+CaO)	47.14	35.23	17.61	1050	20	Ar	yes	yes	yes	0
M2 (O7+CaO+K2CO3)	44.13	32.99	22.88	900	24	Ar	yes	yes	yes	0.38
M3 (O7+CaO+K2CO3+CaO)	49.54	29.79	20.66							0.15
M2 (O7+CaO+K2CO3)	44.13	32.99	22.88	1050	24	Ar	no	Yes	yes	1.97
M3 (O7+CaO+K2CO3+CaO)	49.54	29.79	20.66							1.38
M4 & M4* (CaO+SiO2+K2CO3)	57.11	24.52	18.37	1050	24	Ar	no	yes	yes	1.15 & 1.08
M5(CaO+SiO2+K2CO3)	42.25	30.42	27.32	1050	24	Ar	some peaks of O7 (maybe it is a solution)	yes	yes	0.77
M5* (CaO+SiO2+K2CO3)	42.93	30.91	26.16	1050	24	Ar	yes	no	no	2.2

Figure 6.6.a shows a CaO-K_2O-SiO_2 ternary phase diagram calculated at 900 °C using the FToxid database. From the P-XRD results in Table 6.4 at 900 °C, M1 mainly contained CaO and $K_2Ca_2Si_2O_7$, with traces of phase U. This was similar to M2 and M3 mixtures. Consequently, summing all the aforementioned results, Figure 6.6.b shows a proposed CaO-K_2O-SiO_2 ternary phase diagram calculated at 900 °C using the FToxid 8.1 database without adding K_2CaSiO_4. The tie line between K_2CaSiO_4 and $K_2Ca_2Si_2O_7$ should not exist, affecting the equilibrium in the middle-lower section of the diagram. The new tie lines were added in red. L1 referred to the new tie line between CaO and phase U, l2 between phase U and $K_2Ca_2Si_2O_7$, l3 between $K_2Ca_2Si_2O_7$ and the liquidus, l4 between the liquidus and phase U, and l5 between K_4SiO_4 and the liquidus. The phase U was estimated to correspond to $K_2Ca_2Si_{1.5}O_6$.

In addition, the liquidus should be shifted slightly higher to validate the tie lines that confirm the experimental results.

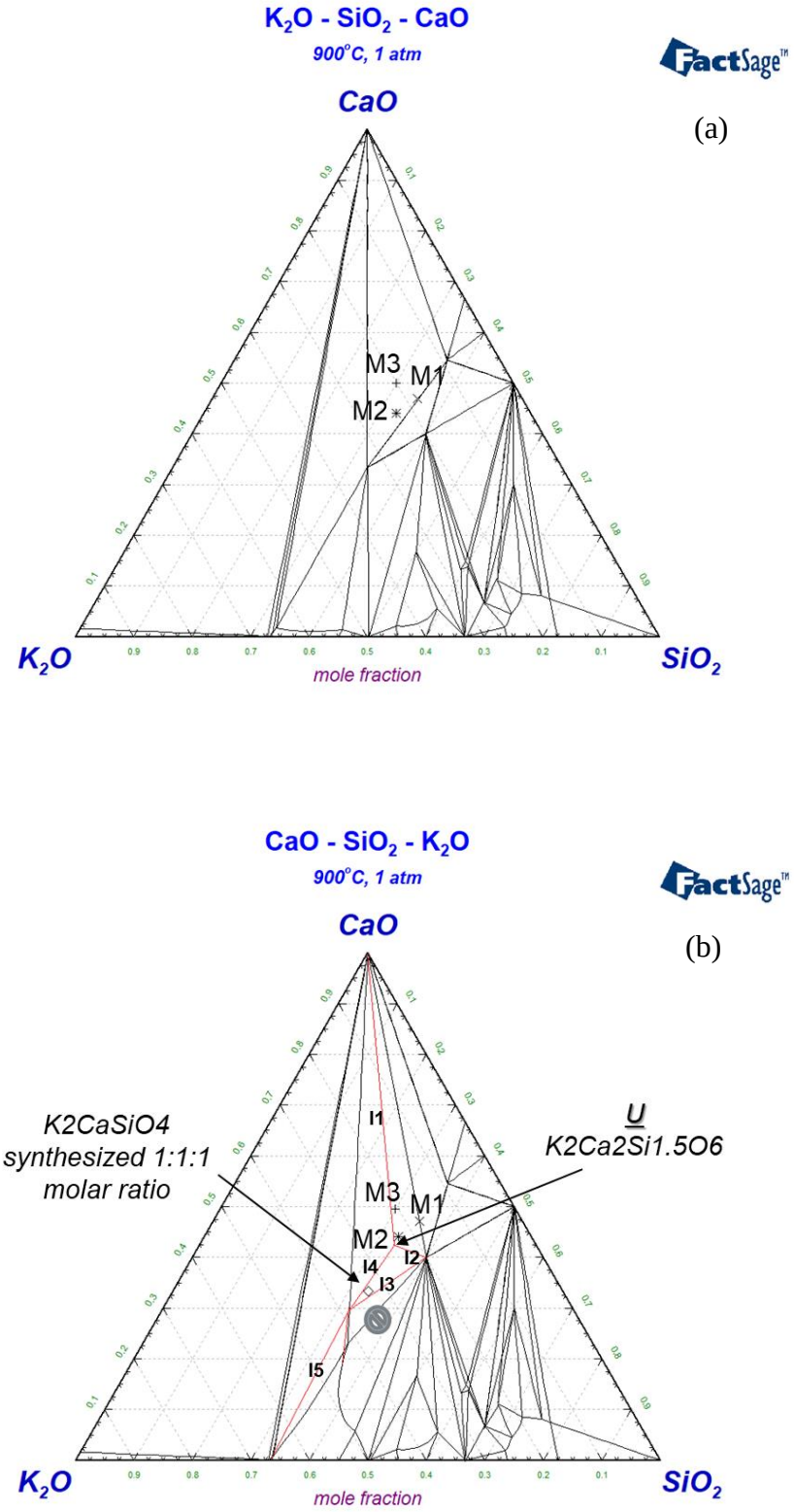

Figure 6.6: Calculated (a) VS Proposed (b) (updated tie lines in red) CaO-K_2O-SiO_2 ternary phase diagram at 900°C using FToxid 8.1.

Though M1 at 900 °C and M1 at 1050 °C contained CaO and $K_2Ca_2Si_2O_7$, the first major peak (2Θ=32°) in phase U disappeared in the case of M1 at 1050 °C. Consequently, the CaO-$K_2Ca_2Si_2O_7$ was validated. However, doubts initiated concerning the possibility that the peaks of phase U corresponded, in fact, to two compounds and not just one. For instance, the first phase was stable at 1050 °C but the second decomposed at this temperature.

To verify the behavior of phase U depicted by its peaks, M2 and M3 were annealed at 1050 °C for 24h. In addition, a fourth mixture M4, denoted by "▲" in Figure 6.6, was formed using a molar ratio of 3.11CaO:1.33SiO2:K2O. A fifth mixture M5, denoted by "▼", was also formed according to a molar ratio of 1.64CaO:1.18SiO2:K2O. M4 and M5 were also annealed twice (M4, M4*, M5, and M5*) at 1050 °C for 24 h using CaO, SiO_2, and K_2CO_3 as initial raw materials.

From the P-XRD results in Table 6.4, M4 and M4* were reproducible. In addition, at 1050 °C, M2, M3, and M4 diffractograms were identical, containing CaO and the peaks of the phase U. However, $K_2Ca_2Si_2O_7$ was absent from the three samples. As a result, another possibility was that M2 and M3 were not at equilibrium at 900 °C, which affected the peaks of the single-phase U. M2 and M3 reached equilibrium at 1050 °C. Consequently, the actual position of the phase U in the ternary phase diagram would slightly shift to the right, introducing significant changes to the equilibrium regions.

M5 Sample was not reproducible. 0.77 wt.% K-loss was measured in trial 1 (M5), compared to 2.2 wt.% K-loss in trial 2 (M5*), despite the equilibration conditions being controlled and kept the same. This will shift the ▼ point in the phase diagram. In parallel, from experimental observations, M5* trial 2 melted more than M5 trial 1. After annealing, the M5* ash chip was tough to break, supporting the claim that important contents of a liquid phase were present in the trial 2 sample. Furthermore, from the P-XRD results in Table 6.4, M5* trial 2 contained $K_2Ca_2Si_2O_7$, while CaO was absent. On the other hand, M5 trial 1 did not contain $K_2Ca_2Si_2O_7$ at the expense of the presence of CaO. In M5, just two peaks belonging to $K_2Ca_2Si_2O_7$ existed, including its major one. Hence, maybe this sample was already on the boundary of a $K_2Ca_2Si_2O_7$ dissolved in the liquid solution region.

In terms of the peaks of phase U in M5 and M5*, all its peaks were present in M5 trial 1, while just one of its peaks were seen in M5* trial 2. In addition, the unidentified peaks at 2Θ 33°, 33.75°, 35.5°, 38°, 41.25°, 44.25°, 46.25°,47°, 50.25°, 51.5°, and 57.5° were present in M5 trial 1 and not present in M5* trial 2. On the other hand, unidentified peaks at 2Θ 40°, 43°, and 55°

were seen in M5* trial 2 and not present in trial 1. In conclusion, the choice of point M5, by chance, might have been very close to the liquidus point. As more K was lost in trial 2 compared to trial 1, M5 mixture moved from a three-phase region (liquid, CaO, and phase U) to a two-phase region ($K_2Ca_2Si_2O_7$ and liquid → $K_2Ca_2Si_2O_7$ dissolved in the liquid solution). Nevertheless, more experiments should be done with a longer residence time to ensure that M5 and M5* results were at equilibrium.

To verify the CaO-Ca_2SiO_4-$K_2Ca_6Si_4O_{15}$ equilibrium section, a sixth mixture M6, denoted by "■" in Figure 6.8, was formed using a molar ratio of 32.03CaO:13.8SiO2:K2O. According to its P-XRD results in Figure 6.7, CaO, Ca_2SiO_4 Larnite, and $K_2Ca_6Si_4O_{15}$ were the only phases found in this sample. Consequently, this equilibrium section was validated.

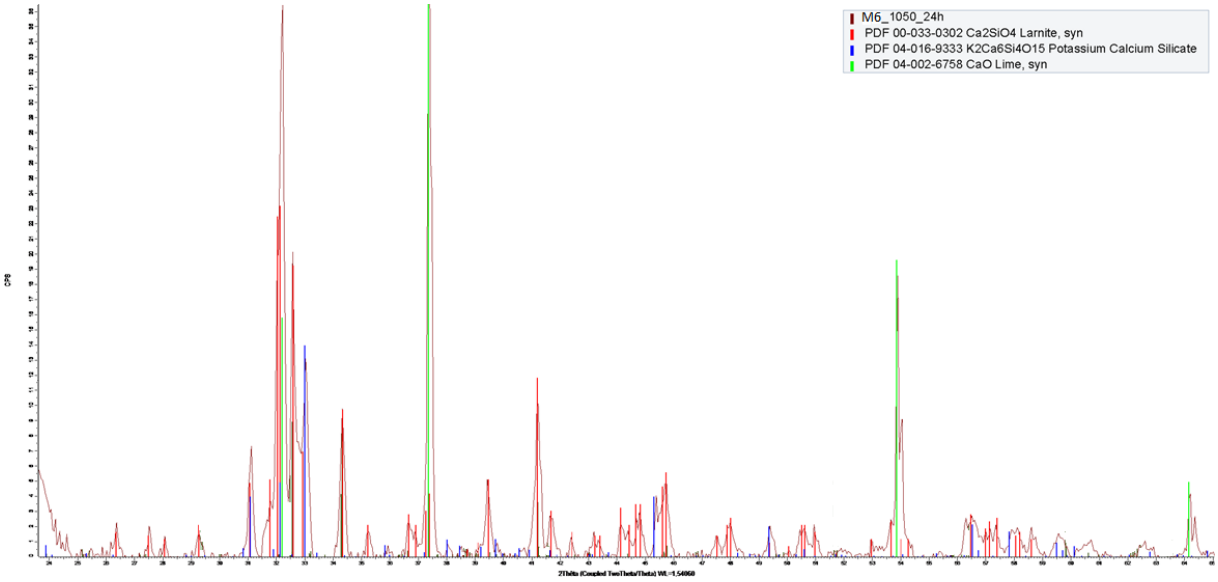

Figure 6.7: P-XRD results of M6.

In conclusion, Figure 6.8.a shows the ternary phase diagram CaO-K_2O-SiO_2 at 1050 °C as calculated using FToxid and without adding K_2CaSiO_4. The new tie lines were added in red in Figure 6.8.b. The phase U was re-estimated and slightly shifted in the diagram. However, it still closely corresponded to $K_2Ca_2Si_{1.5}O_6$. In addition, the liquidus was shifted a little higher to validate the experimental results. L1 referred to the tie line between CaO and phase U, l2 between CaO and the new liquidus, l3 between $K_2Ca_2Si_2O_7$ and phase U, l4 between $K_2Ca_2Si_2O_7$ and the new liquidus, l5 between the new liquidus and phase U, and l6 between K4SiO4 and the new liquidus.

Despite the thorough work that was presented, this section needs further investigation. All the annealing should be repeated at longer residence times to validate that each case's experimental

equilibrium was reached. In addition, more points should be analyzed in the CaO, $K_2Ca_2Si_2O_7$, and phase U proposed equilibrium section to validate it. Furthermore, the liquidus area (close to M5) should be further investigated. Unfortunately, all these ideas were not done due to the thesis time constraints.

Hence, several conclusions can be drawn out from this section:	
1.	K_2CaSiO_4 was never found.
2.	A new unidentified phase is present.
3.	CaO-Ca_2SiO_4-$K_2Ca_6Si_4O_{15}$ equilibrium section was confirmed over its original stability range.
4.	CaO- $K_2Ca_2Si_2O_7$ tie line was validated.

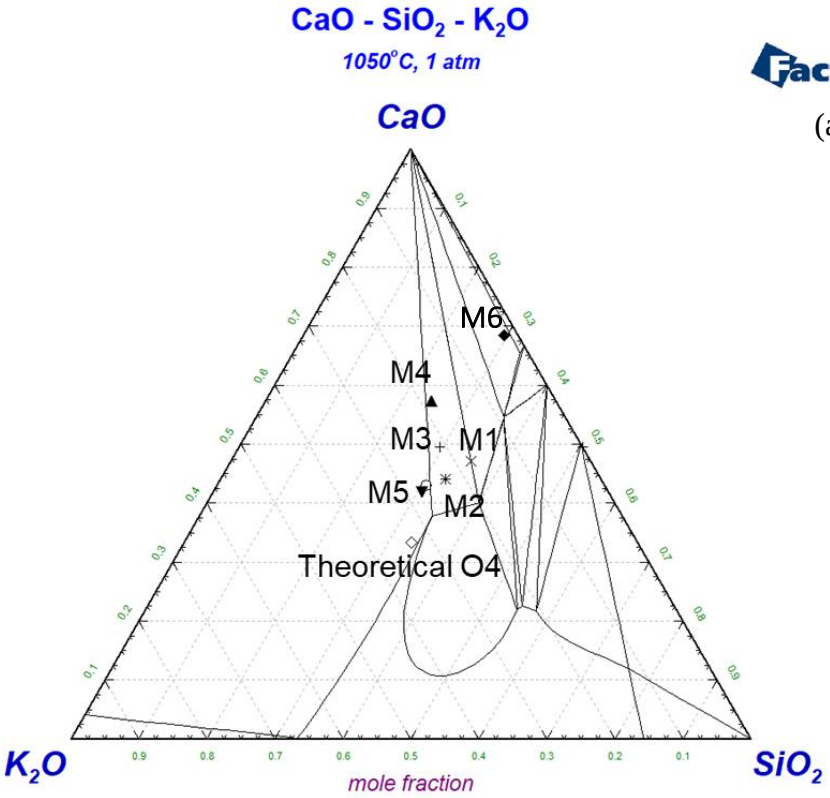

(a)

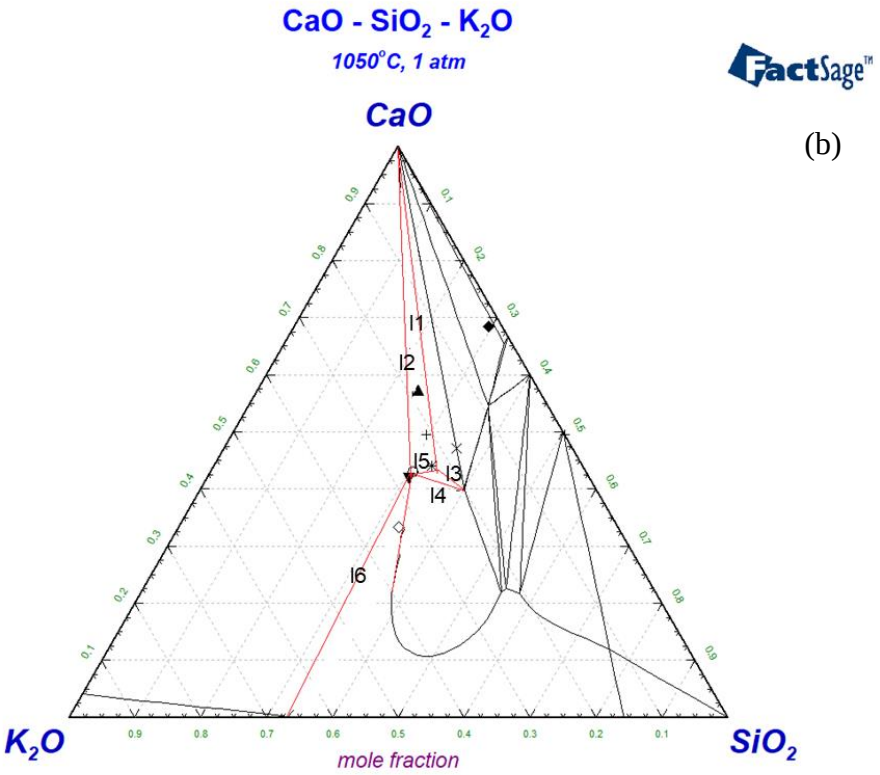

(b)

Figure 6.8: Calculated vs proposed (updated) CaO-K_2O-SiO_2 ternary phase diagram at 1050 °C using FToxid 8.1.

4. Binary K_2O-SiO_2

A contribution to the thermodynamic modeling of the binary phase diagram K_2O-SiO_2 will be presented in this section. Due to time constraints, the liquid modeling will not be performed and will remain out of scope. However, the stoichiometric compounds' phase diagram and thermodynamic properties will be critically reviewed. The reliable experimental data used in the Gibbs minimization will be thoroughly criticized.

According to the most recent literature, K_2O-SiO_2 binary system contains 7 stoichiometric compounds: K_2O, $K_6Si_2O_7$, K_4SiO_4, K_2SiO_3, $K_2Si_2O_5$, $K_2Si_4O_9$, and SiO_2. In the work of Meshalkin et al. (Meshalkin and Kaplun 2005), they defended the presence of two more intermediate compounds $K_{10}Si_3O_{11}$ and $K_8Si_3O_{10}$. However, their existence was based on viscosity measurements, and they were never checked or reported by other authors. In addition, no crystalline structure exists in the literature for them. Hence, they were omitted from this work.

K_2O, $K_6Si_2O_7$, K_4SiO_4, and K_2SiO_3 have one crystalline structure each. $K_2Si_2O_5$ has three crystalline structures (α, β, and γ), while $K_2Si_4O_9$ has two (α and β), and SiO_2 has four (α-quartz, β-quartz, β-tridymite, and β-cristobalite). Table 6.5 shows the characteristic temperature of each stoichiometric compound, while Table 6.6 presents their measured crystalline structures, as reported in the literature and calculated by the density functional theory (DFT) in a private communication by A. Pisch. Table 6.7 shows the invariant points in this binary. Table 6.8 summarizes all the measured enthalpy and entropy of formation at 298.15K, along with the transitional enthalpy (when applied) for each intermediate stoichiometric compound and SiO_2. All data reported in this work were based on measurements. Therefore, though several estimated data were found in the literature, they were not reported unless no equivalent measurements were found (as in the case of K_4SiO_4).

Based on the crystalline structure of each compound, shown in Table 6.6, DFT method was used to calculate the enthalpy of formation at 298.15K and the Cp from 0K to 300K. This theory is based on quantum mechanics (ab initio) and the minimization of the Hamiltonian and Schrodinger equations. Softwares are usually used for such calculations (Khvan et al. 2019).

The crystalline phase description used in the CalPhad modeling provides an improved physical meaning than the usual polynomial description for the temperature dependence of the heat capacity by an extended Debye or Einstein model (Chase et al. 1995). In addition, using CalPhad model allows to model the thermodynamic properties of the phases down to 0K

(Bigdeli, Chen, and Selleby 2018; Deffrennes et al. 2020). Consequently, better data integration from first-principles calculations is allowed (Deffrennes et al. 2020; Khvan et al. 2018). In parallel, the two-state model performed better than the traditional polynomial in the liquid phase modeling. While the extrapolation beyond the stability range of the phases may lead to spurious predictions (such as artificial phase stability (Agren et al. 1995)) in the latter, the former models the liquid phase as amorphous-like or liquid-like (Li et al. 2017; Bigdeli, Chen, and Selleby 2018; Becker et al. 2014; Chen and Sundman 2001).

The heat capacity (Cp) of the solid phases was modeled using the 3rd generation CalPhad Einstein model with multiple Einstein temperatures and an-harmonic corrections (Deffrennes et al. 2020), as follows:

$$C_p(T) = 3R\sum_i \alpha_i \left(\frac{\theta_i}{T}\right)^2 \frac{e^{\frac{\theta_i}{T}}}{\left(e^{\frac{\theta_i}{T}}-1\right)^2} + \sum_{n\geq 1} a_n T^n$$

for one mole of atoms, $\sum_i \alpha_i = 1$ (additional constraint, not always verified)

Since Cp model is for compounds made of three types of atoms K, Si, and O; then, the model was expanded using maximum three temperature and four an-harmonic parameters, as follow:

Cp = $24.9432*a_1*(t_1/t_k)^2*(\exp(t_1/t_k)/(\exp(t_1/t_k)-1)^2) + 24.9432*a_2*(t_2/tk)^2 *(\exp(t_2/t_k)/(\exp(t_2/t_k)-1)^2) + 24.9432*(n_{atom}-a_1-a_2)*(t_3/t_k)^2*(\exp(t_3/t_k)/(\exp(t_3/t_k)-1)^2) + b_1*t_k$

The enthalpy equation is the integral of Cp in terms of temperature. Hence, its expanded equation became as follow:

H = $24.9432*a_1*t_1/(\exp(t_1/t_k)-1)+24.9432*a_2*t_2/(\exp(t_2/t_k)-1) + 24.9432*(n_{atom}-a_1-a_2) *t_3/(\exp(t_3/t_k)-1) + b_1/2*(t_k^2) + C$

Where c is an integration constant that refers to the heat of formation.

Most importantly, the entropy equation is the integral of Cp/T in terms of temperature. Hence, its expansion was as follow (the integration constant at 0K is zero since S(0K)=0):

$$S = 24.9432*a_1*(t_1\text{^}2)*[(\exp(t_1/t_k)/(t_1*t_k*\exp(t_1/t_k)-t_1*t_k))-(\ln(\exp(t_1/t_k)-1)/(t_1\text{^}2))] + 24.9432*a_2*(t_2\text{^}2)*[(\exp(t_2/t_k)/(t_2*t_k*\exp(t_2/t_k)-t_2*t_k))-(\ln(\exp(t_2/t_k)-1)/(t_2\text{^}2))] + 24.9432*(n_{atom}-a_1-a_2)*(t_3\text{^}2)*[(\exp(t_3/t_k)/(t_3*t_k*\exp(t_3/t_k)-t_3*t_k))-(\ln(\exp(t_3/t_k)-1)/(t_3\text{^}2))] + b_1*t_k$$

To optimize the parameters a1, a2, t1, t2, t3, and b1, measured Cp values from the literature were used. If absent in the literature, the Cp values calculated by DFT were applied individually or combined with the measured literature values to cover the whole temperature range. The optimized parameters are shown in Table 6.9. Then, these values were plugged in the equation of S to calculate the standard entropy reported in Table 6.10 at 298.15K.

4.1.K_2SiO_3

Kroger and Fingas (Kroger and Fingas 1933) reported $\Delta H_{298.15K}°$ by calculating the enthalpy through the partial CO_2 pressure in the reaction $K_2CO_3 + SiO_2 = K_2SiO_3 + CO_2$ from 808K to 898K measured by gas equilibration technique. Takashi and Yohio (K. Takahashi and Yoshio 1970) and Brown et al. (Brown and Bennington 1987) determined $\Delta H_{298.15K}°$ by solution calorimetry. Their reported values were very close. Besides, solution calorimetry is more reliable than gas equilibration since the latter uses some estimations. Hence, any of the last two values are proposed to be used in the new modeling.

Stull et al. (Stull et al. 1970) used adiabatic calorimetry to measure Cp at low temperatures (15K-298.15K). Then, they calculated $S_{298.15K}°$ based on these values. It should be noted that the purity of the starting materials of Stull et al. (Stull et al. 1970) was around 97.3%. This is considered to be a low value. However, this was the only source in the literature that reported measured Cp values for K_2SiO_3 below 298.15K. Beyer et al. (Beyer 1980) measured the enthalpy using drop calorimetry between 298.15K and 1249K. Then, they derived Cp from these values. The Cp values from Stull et al. (Stull et al. 1970) and Beyer et al. (Beyer 1980) were used to optimize the continuous Cp function using the 3rd generation CalPhad Einstein model, shown in Figure 6.9.

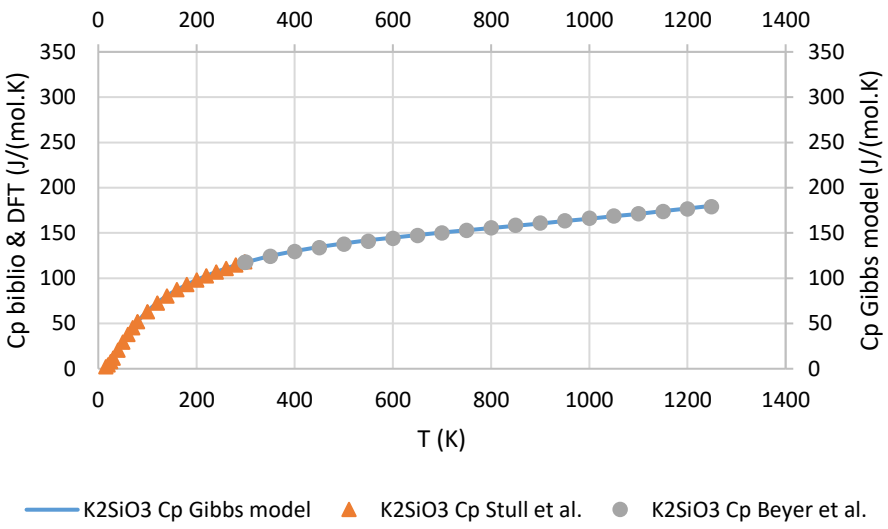

Figure 6.9: Reported literature and optimized heat capacity of K_2SiO_3.

4.2.$K_2Si_2O_5$

Several standard enthalpies of formation were reported in this work. Kroger and Fingas (Kroger and Fingas 1933) reported $\Delta H_{298.15K}°$ by calculating the enthalpy through the partial CO2 pressure in the reactions $K_2O + SiO_2 = K_2SiO_3$, $K_2Si_2O_5 + K_2CO_3 = 2.K_2SiO_3 + CO_2$, $K_2CO_3 = K_2O + CO_2$, and $2.K_2O + 2.SiO_2 = 2.K_2SiO_3$ from 808K to 898K measured by the gas equilibration technique. Kracek et al. (Kracek et al. 1953) measured the standard enthalpy of formation using HF solution calorimetry, similarly to Takahashi and Yoshio (K. Takahashi and Yoshio 1970) and Borisova and Ushakov (Borisova and Ushakov 1998).

The transition enthalpies from α to β and β to γ were measured using copper-block drop calorimetry by Beyer et al. (Beyer 1980). Another measurement for the transition enthalpy from β to γ was reported by Kracek et al. (Kracek, Bowen, and Morey 1937) using DTA, which was less accurate than the first one due to DTA technical limitations compared to drop calorimetry.

The fusion enthalpy was calculated by Takahashi and Yoshio (Katsuaki Takahashi and Yoshio 1973) and Beyer et al. (Beyer 1980) using the same method. First, both authors used drop calorimetry measurements to obtain Cp. Then, they combined these values with the crystalline transition enthalpies (Table 6.8) along with the transition enthalpy from crystal to glass at 298.15K determined by HF solution calorimetry (14.2 kJ/mol (Kracek 1932)) to report the value shown in Table 6.8. Boivin et al. (Boivin et al., n.d.) also reported the fusion enthalpy measured using DTA. All three values were close.

Similar to section 4.1, Beyer et al. (Beyer 1980) reported Cp using adiabatic calorimetry between 5K and 300K and drop calorimetry between 298.15K and 1600K. They calculated the

standard entropy from the Cp value derived by the adiabatic calorimetry measurements. In addition, Takahashi and Yoshio (Katsuaki Takahashi and Yoshio 1973) reported Cp using drop calorimetry from 298K to 1273K. However, the error in their values reached 12% (D.-G. Kim et al. 2017). Hence, they were omitted from this work. As a result, the Cp values in Beyer et al. (Beyer 1980) were used in this work to optimize the continuous Cp function using the 3rd generation CalPhad Einstein model over the whole temperature range, as shown in Figure 6.10.

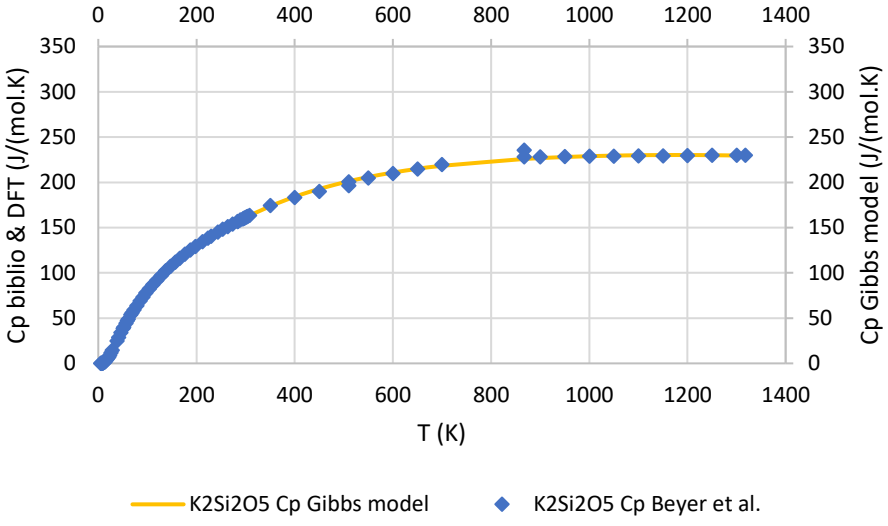

Figure 6.10: Reported literature and optimized heat capacity of $K_2Si_2O_5$.

4.3.$K_2Si_4O_9$

Geisinger et al. (Geisinger et al. 1987) conducted a thorough study on $K_2Si_4O_9$. Using vibrational modeling based on the data from Raman spectroscopy and powder infrared (IR) spectroscopy, they reported the enthalpy of formation and standard entropy of the wadeite $K_2Si_4O_9$ along with the transition and fusion enthalpies (Table 6.8). Kracek et al. (Kracek et al. 1953) reported a close enthalpy of formation measured by solution calorimetry. In his review, Spencer et al. (Spencer 1973) reported a similar standard entropy value to the one in Geisinger el al. (Geisinger et al. 1987). In addition, Goranson et al. (Goranson and Kracek 1932) and Kracek et al. (Kracek, Bowen, and Morey 1937) reported using DTA very close transition enthalpy value to Geisinger et al. (Geisinger et al. 1987). Goranson et al. (Goranson and Kracek 1932) also reported a similar fusion enthalpy value using drop calorimetry to Geisinger et al. (Geisinger et al. 1987).

The only measured Cp values in literature were reported on $K_2Si_4O_9$-Wadeite by Fasshauer et al. (Fasshauer et al. 1998) using a DSC between 195K and 598K. Hence, DFT calculations for Cp between 0K and 300K were conducted using the crystalline structure presented in Table 6.6. Then, two Cp functions were optimized using the 3rd generation CalPhad Einstein model over

the whole temperature range. The first optimized Cp function used the DFT wadeite values coupled with those of Fasshauer et al. (Fasshauer et al. 1998), and the second used the DFT sheet values. The calculated Cp values by DFT, the ones measured by Fasshauer et al. (Fasshauer et al. 1998), and each optimized Cp model are all shown in Figure 6.11.

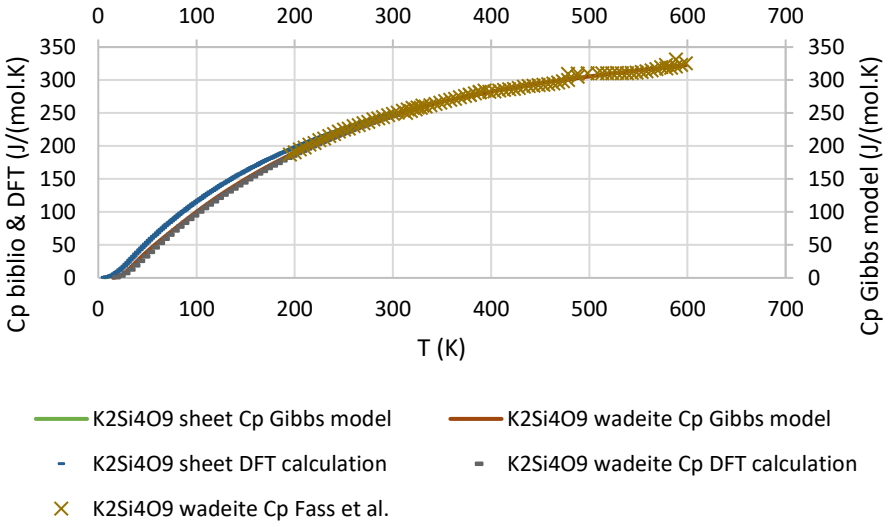

Figure 6.11: Reported literature and optimized heat capacity of $K_2Si_4O_9$.

4.4.K_4SiO_4

The crystalline structure of K_4SiO_4 was reported in the work of Bernet et al. (Bernet and Hoppe 1990), Stebbins et al. (Stebbins, McMillan, and Dingwell 1995), and O'Keeffe et al. (O'Keeffe and Hyde 1984). Slough et al. (Slough, n.d.) and Kroger et al. (Kroger and Fingas 1933) also mentioned that this compound should be stable in the K_2O-SiO_2 binary diagram. Kroger et al. (Kroger and Fingas 1933) reported the enthalpy of formation of this compound by measuring the equilibrium pressure of CO_2 from the reaction $K_2CO_3+K_2SiO_3=K_4SiO_4+CO_2$ using the gas equilibration technique in the temperature range of 1128 to 1248 K. Slough (Slough, n.d.) also estimated $\Delta H_{298.15K}°$ from potential ionic relationships. Furthermore, using the thermodynamic data of Na_2O-SiO_2 and Li_2O-SiO_2 systems, Kim et al. (D.-G. Kim et al. 2017) estimated the enthalpy of formation of K_4SiO_4. Using NKR data based on the constituents' oxides K_2O and SiO_2, Kim et al.

(D.-G. Kim et al. 2017) also estimated the standard entropy. All estimates of Kim et al. (D.-G. Kim et al. 2017) were presented in Table 6.8. Cp data using DFT were reported in this work using the crystalline structure of this compound measured by Bernet et al. (Bernet and Hoppe 1990). Then, as shown in Figure 6.12, these values were used to optimize the Cp Einstein model.

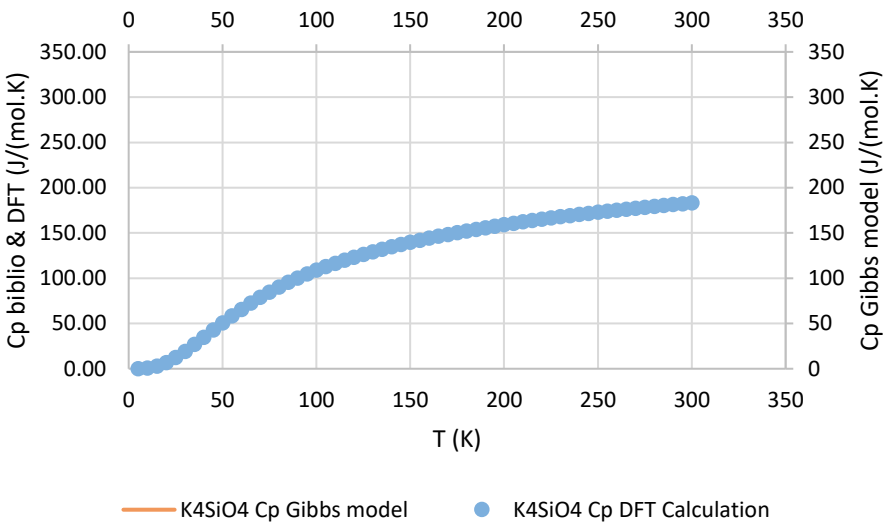

Figure 6.12: Reported DFT and optimized heat capacity of K_4SiO_4.

4.5.$K_6Si_2O_7$

The crystalline structure of K_6SiO_7 was reported in Janssen et al. (Jansen 1982). DFT calculations showed that this is one of the most stable structures in the K_2O-SiO_2 binary (had the most negative calculated enthalpy of formation in Table 6.9). However, thermodynamic data for this compound are absent in the literature. Hence, Cp data using DFT were reported in this work. Then, as shown in Figure 6.13, these values were used to optimize the Cp Einstein model.

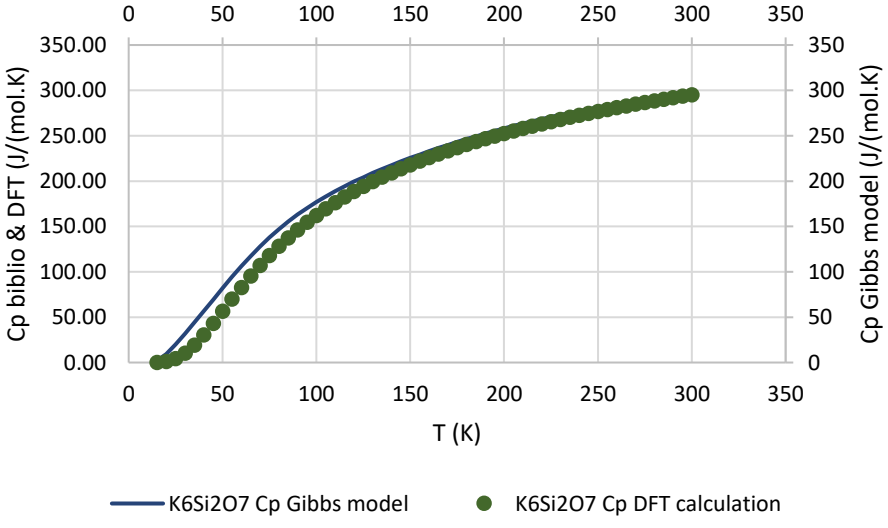

Figure 6.13: Reported literature and optimized heat capacity of $K_6Si_2O_7$.

Table 6.5: Characteristic temperatures of the intermediate stoichiometric compounds and SiO2.

Phase	Temperature (°C)	References
SiO_2 (α-Quartz)	<573	[1917Mor](Morey 1917)
SiO_2 (α-Quartz)--> SiO_2 (β-Quartz)	573	[1930Kra](Kracek 1930), [1937Kra](Kracek, Bowen, and Morey 1937)
SiO_2 (β-Quartz)	575-870	[1917Mor](Morey 1917)
SiO_2 (β-Quartz) <-> SiO_2 (β-tridymite)	870	[1937Kra](Kracek, Bowen, and Morey 1937)
SiO_2 (β-tridymite)	870-1470	[1917Mor](Morey 1917)
SiO_2 (β-tridymite) <-> SiO_2 (β-Cristobalite)	1470	[1937Kra](Kracek, Bowen, and Morey 1937)
SiO_2 (β-Cristobalite)	1470-1625	[1917Mor](Morey 1917)
SiO_2 (β-Cristobalite) --> Liquid	1638	[1930Kra](Kracek 1930)
SiO_2 (β-Cristobalite) --> Liquid	1713	[1937Kra](Kracek, Bowen, and Morey 1937)
SiO_2 (β-Cristobalite) --> Liquid	1544	[1930Kra](Kracek 1930)
α-$K_2Si_4O_9$_Wadeite	<592	[1930Kra](Kracek 1930)
α-$K_2Si_4O_9$_Wadeite --> β-$K_2Si_4O_9$_Sheet	592	[1930Kra](Kracek 1930) , [1937Kra](Kracek, Bowen, and Morey 1937)
β-$K_2Si_4O_9$_Sheet	592-765	[1930Kra](Kracek 1930)
β-$K_2Si_4O_9$_Sheet --> Liquid	765	[1930Kra](Kracek 1930)
β-$K_2Si_2O_5$	<594	[1930Kra](Kracek 1930), [1937Kra](Kracek, Bowen, and Morey 1937)
β-K_2Si_2O5 -> a-$K_2Si_2O_5$	594	[1937Kra](Kracek, Bowen, and Morey 1937)
α-$K_2Si_2O_5$	594-1041	[1917Mor](Morey 1917)
α-$K_2Si_2O_5$ --> Liquid	1045	[1917Mor](Morey 1917), [1937Kra](Kracek, Bowen, and Morey 1937)
K_2SiO_3	0-976	[1917Mor](Morey 1917)
K_2SiO_3 --> Liquid	976	[1937Kra](Kracek, Bowen, and Morey 1937)
K_4SiO_4	0-1031	[2017Kim](D.-G. Kim et al. 2017)
K_4SiO_4 --> Liquid	1031	[2017Kim](D.-G. Kim et al. 2017)

Table 6.6: Crystalline structures of each stoichiometric intermediate compound in literature and used in the DFT calculations.

Phase	Space group	Lattice Parameters (Å)	References
$K_6Si_2O_7$	$P2_1/c$	a = 6.458 Å	[1982Jan](Jansen 1982)
		b = 8.887 Å	
		c = 10.879 Å	
		β = 125°	
		a = 6.39358 Å	DFT (Pisch, private communication)
		b = 8.8461 Å	
		c = 10.879 Å	
		β = 125°	
K_4SiO_4	$P2_1/c$	a = 10.37 Å	[1990Ber](Bernet and Hoppe 1990)
		b = 6.392 Å	
		c = 10.366 Å	
		β = 112.83°	
		a = 10.27774 Å	DFT (Pisch, private communication)
		b = 6.3744 Å	
		c = 10.24311 Å	
		β = 112.572°	
K_2SiO_3	$P2_1/c$	a = 16.23539 Å	DFT (Pisch, private communication)
		b = 12.69444 Å	
		c = 15.6467 Å	
		β = 107.336°	
		a = 13.269 Å	[1981Wer](Hoppe and Werthmann 1981)
		b = 6.330 Å	
		c = 15.952 Å	
		α = 72.085°	
		β = 90.000°	
$K_2Si_2O_5$	monoclinic Cc	a = 9.72 Å	

		b = 25.26 Å	[1972Sch](Schweinsberg and Liebau 1972)
		c = 14.24 Å	
		β = 90°	
$K_2Si_2O_5$ (1058K)	Monoclinic Cc	a=16.3224 Å	[1998Jon](Jong et al. 1998)
		b=11.243 Å	
		c = 9.919 Å	
		β = 115.972°	
		a=16.35627 Å	DFT (Pisch, private communication)
		b=11.21018 Å	
		c = 9.91083 Å	
		β = 116.153°	
α-$K_2Si_4O_9$_Waseite_low T	$P6_3/m$	a = 6.6124 Å	[1983Swa](Swanson and Prewitt 1983) [1987Gei](Geisinger et al. 1987)
		c = 9.5102 Å	
		a = 6.58848 Å	DFT (Pisch, private communication)
		c = 9.50818 Å	
β-$K_2Si_4O_9$_Sheet_high T	P-1	a = 12.32 Å	[1974Sch](Schweinsberg and Liebau 1974) [1987Gei](Geisinger et al. 1987)
		b = 4.943 Å	
		c = 8.369 Å	
		α = 90.8°	
		β = 111.19°	
		γ = 89.69°	
		a = 4.92791 Å	DFT (Pisch, private communication)
		b = 8.27909 Å	
		c = 12.0939 Å	
		α = 39.986°	
		β = 89.812°	
		γ = 89.143°	

Table 6.7: Invariant reaction (points) in the binary K_2O-SiO_2 [L denotes liquid].

Reaction	T (°C)	Type	Phase	K2O mol%	SiO2 mol%	References
L <-> SiO_2 (β-quartz) + $K_2Si_4O_9$	769	eutectic	L, SiO_2 (β-quartz), $K_2Si_4O_9$	27.5	72.5	[1937Kra](Kracek, Bowen, and Morey 1937)
L <-> $K_2Si_2O_5$ + $K_2Si_4O_9$	744	eutectic	L, $K_2Si_2O_5$, $K_2Si_4O_9$	32.4	67.6	[1937Kra](Kracek, Bowen, and Morey 1937)
L <-> K_2SiO_3 + a-$K_2Si_2O_5$	775	eutectic	L, K_2SiO_3, $K_2Si_2O_5$	56.5	43.5	[1917Mor](Morey 1917)
L <-> K_2SiO_3 + a-$K_2Si_2O_5$	780	eutectic	L, K_2SiO_3, $K_2Si_2O_5$	54.5	45.5	[1937Kra](Kracek, Bowen, and Morey 1937)
L <-> K_4SiO_4 + K_2SiO_3	714+-6	eutectic	L, K_4SiO_4, K_2SiO_3	59	41	[2017Kim](D.-G. Kim et al. 2017)

Table 6.8: $\Delta H_{298.15K}°$, $S_{298.15K}°$, transition enthalpy, and fusion enthalpy of the stoichiometric compounds and SiO_2.

Phases	**Temperature (°C)**	**$\Delta H_{298.15K}°$ & $S_{298.15K}$ °**	**References**	**Technique**
K_2O	25	$\Delta H_{298.15K}°$ = -361.498 kJ/mol	[2016Bale] (Bale et al. 2016)	
		$S_{298.15K}$ ° = 102.006 J/K/mol		
SiO_2 (α-Quartz)	25	$\Delta H_{298.15K}°$ = -910.7 kJ/mol	[2016Bale] (Bale et al. 2016)	
		$S_{298.15K}$ ° = 41.467 J/K/mol		
SiO_2 (β-Quartz)	25	$\Delta H_{298.15K}°$ = -908.627 kJ/mol	[2016Bale] (Bale et al. 2016)	
		$S_{298.15K}$ ° = 44.207 J/mol/K		
SiO_2 (β-tridymite) low	25	$\Delta H_{298.15K}°$ = -907.752 kJ/mol	[1988Ber](BERMAN 1988)	
		$S_{298.15K}$ ° = 43.774 J/mol/K		
SiO_2 (β-tridymite) high	25	$\Delta H_{298.15K}°$ = -907.045 kJ/mol	[2016Bale] (Bale et al. 2016)	
		$S_{298.15K}$ ° = 45.524 J/mol/K		
SiO_2 (α-Cristobalite)	25	$\Delta H_{298.15K}°$ = -907.753 kJ/mol	[1988Ber](BERMAN 1988)	
		$S_{298.15K}$ ° = 43.394 J/mol/K		
SiO_2 (β-Cristobalite)	25	$\Delta H_{298.15K}°$ = -906.377 kJ/mol	[2016Bale] (Bale et al. 2016)	
		$S_{298.15K}$ ° = 46.029 J/mol/K		
SiO_2 aqueous	25	$\Delta H_{298.15K}°$ = -881.359kJ/mol		

		$S_{298.15K}$ ° = 62.63/mol/K	[1988Ber](BERMAN 1988)	
α-$K_2Si_4O_9$_Wadeite	25	$\Delta H_{298.15K}$° =-309.36 kJ/mole from oxides = -4306.06 kJ/mol from elements	[1953Kra](Kracek et al. 1953)	Solution calorimetry
		$\Delta H_{298.15K}$° =-314.08+-3.66 kJ/mole from oxides = -4310.78 kJ/mol from elements	[1987Gei](Geisinger et al. 1987)	Vibrational modeling
		$S_{298.15K}$ ° =265.684 J/mole/K	[1973Spe](Spencer 1973)	Estimation
		$S_{298.15K}$ ° =223.72 J/mole/K	[1987Gei](Geisinger et al. 1987)	Vibrational modeling
α-$K_2Si_4O_9$_Wadeite --> β-$K_2Si_4O_9$_Sheet	592	ΔH_{tr} = 3.219 kJ/mol	[1932Gor] (Goranson and Kracek 1932), [1937Kra] (Kracek, Bowen, and Morey 1937)	DTA
		ΔH_{tr} (combined with Kracek study) = -3.17 KJ/mol	[1987Gei](Geisinger et al. 1987)	Vibrational modeling
β-$K_2Si_4O_9$_Sheet --> L	765	ΔH_{fus} = 49 kJ/mol	[1932Gor](Goranson and Kracek 1932)	Drop calorimetry
	770	ΔH_{fus} = 43 KJ/mol	[1987Gei](Geisinger et al. 1987)	Vibrational modeling
α-$K_2Si_2O_5$	25	$\Delta H_{298.15K}$° = 321.45 kJ/mol from oxides = 2496.75 kJ/mol from elements	[1933Kro](Kroger and Fingas 1933)	Gas equilibration
		$\Delta H_{298.15K}$° =-324.34 kcal/mole from oxides = -2499.64 kJ/mol form elements	[1953Kra](Kracek et al. 1953)	Solution calorimetry
		$\Delta H_{298.15K}$° = 2418.352 kJ/mole from elements	[1970Tak1](K. Takahashi and Yoshio 1970)	Solution calorimetry
		$\Delta H_{298.15K}$° = 2470.898 kJ/mole from elements	[1998Bor](Borisova and Ushakov 1998)	Solution calorimetry
		$S_{298.15K}$ ° = 190.581 J/K/mol	[1980Bey](Beyer 1980)	Adiabatic calorimetry
α-$K_2Si_2O_5$ --> β-$K_2Si_2O_5$	237	ΔH_{tr} = 1.213 ± 0.004 kJ/mol	[1980Bey](Beyer 1980)	Drop calorimetry
β-$K_2Si_2O_5$ -> γ-$K_2Si_2O_5$	594	ΔH_{tr} = 1.075 ± 0.045 kJ/mol	[1937Kra](Kracek, Bowen, and Morey 1937)	DTA
		ΔH_{tr} = 1.590 ± 0.005 kJ/mol	[1980Bey](Beyer 1980)	Drop calorimetry

γ-$K_2Si_2O_5$ --> Liquid	1045	ΔH_{fus} = 31.7984 kJ/mol	[1973Tak](Katsuaki Takahashi and Yoshio 1973)	Drop calorimetry
		ΔH_{fus} = 31.2 kJ/mol	[1980Bey](Beyer 1980)	Drop calorimetry
		ΔH_{fus} = 31.3 kJ/mol	[Boivin](Boivin et al., n.d.)	DTA
		ΔH_{fus} = 24.35 kJ/mol	[1973Tak](Katsuaki Takahashi and Yoshio 1973)	Drop calorimetry
K_2SiO_3	25	$\Delta H_{298.15K}$° = -263 kJ/mol from oxides = -1528.24 kJ/mol from elements	[1933Kro](Kroger and Fingas 1933)	Gas equilibration
		$\Delta H_{298.15K}$° = -1522.976 kJ/mole	[1970Tak1](K. Takahashi and Yoshio 1970)	Solution calorimetry
		$\Delta H_{298.15K}$° = -271.065 kJ/mol from oxides = -1522.415 kJ/mol from elements	[1987Bro](Brown and Bennington 1987)	Solution calorimetry
		$S_{298.15K}$ ° = 146.147 kJ/mol	[1970Stu](Stull et al. 1970)	Adiabatic calorimetry
K_4SiO_4	25	$\Delta H_{298.15K}$° = -365.68 kJ/mol from oxides = -1984.18 kJ/mol from elements	[1933Kro](Kroger and Fingas 1933)	Gas equilibration
		$\Delta H_{298.15K}$° = -2064.614 kJ/mol from elements	[1973Slo](Slough, n.d.)	Estimation
		$\Delta H_{298.15K}$° = -2065.22 kJ/mol from elements	[2017Kim](D.-G. Kim et al. 2017)	Estimation
		$S_{298.15K}$ ° = 233.198 J/mol/K	[2017Kim](D.-G. Kim et al. 2017)	Estimation

Table 6.9: Optimized Einstein Cp model parameters for each stoichiometric compound using literature and DFT Cp data.

	K4SiO4	**K6Si2O7**	**K2Si4O9_Wadeite**	**K2Si4O9_Sheet**	**K2Si2O5**	**K2SiO3**
a1=	2.5307956	3.76329642	3.5642931	5.5476009	1.970957	2.571
a2=	2.3378067	6.767400769	4.3801107	5.8959553	3.3501574	2.508
a3=	4.1313977	4.469302811	7.0555962	3.5564438	3.6788856	0.921
t1=	118.89116	114.7269942	1517.6585	1255.2076	113.26108	157.4
t2=	966.2579	269.8904078	179.71002	429.07301	336.3784	584.9
t3=	291.93126	847.6540862	603.86703	126.8549	1076.1517	3094
b1=	0	-0.04181816	-0.002693229	-0.001319027	0.012078152	0.03101

4.6. Thermodynamic data proposed in this work for the K_2O-SiO_2 binary phase diagram re-modelling

As discussed in chapters 3 and 5, predictions using the FToxid database set were more effective than those using the GTOX database set. However, FToxid needed further improvements. Hence, Table 6.10 offers a detailed comparison between the data proposed to be used in this work to remodel the K_2O-SiO_2 diagram with the ones used in the recent modeling by Kim et al. (D.-G. Kim et al. 2017), on which the FToxid database was based upon. Data from FactPS were also included in this comparison.

4.6.1. Proposed K_2SiO_3 properties

For K_2SiO_3, Brown et al. (Brown and Bennington 1987) and Takahashi et al. (K. Takahashi and Yoshio 1970) reported close enthalpy of formation values (Table 6.8). The one calculated from the gas equilibration data in Kroger et al. (Kroger and Fingas 1933) was also close, similar to the one calculated by DFT in Table 6.10. Hence, the experimental value of Brown et al. (Brown and Bennington 1987) is proposed to be used in this work. This value was far from the one used in FactPS but somehow close to the value of Kim et al. (D.-G. Kim et al. 2017). Concerning the standard entropy, the value calculated in this work from the Einstein model, the one used in FactPS, and the one reported by Kim et al. (D.-G. Kim et al. 2017) were all similar. Consequently, any of these values, preferably the one calculated by DFT, is proposed to be used in this work.

4.6.2. Proposed $K_2Si_2O_5$ properties

For $K_2Si_2O_5$, the enthalpy of formation value measured by Kracek et al. (Kracek et al. 1953) using solution calorimetry was close to the one reported by Kroger et al. (Kroger and Fingas 1933) using the data of gas equilibration. However, the DFT calculated value was less while the one used in FactPS was higher. In parallel, the enthalpy of formation optimized by Kim et al. (D.-G. Kim et al. 2017) was similar to the one measured by Kracek et al. (Kracek et al. 1953). Hence, The value reported by Kracek et al. (Kracek et al. 1953) was proposed to be used in this work. Concerning the standard entropy, the value calculated in this work from the Einstein model was similar to that reported by Kim et al. (D.-G. Kim et al. 2017) but significantly different from the value used in FactPS. Consequently, the entropy value calculated using the Einstein model is proposed in this work.

4.6.3. Proposed $K_2Si_4O_9$ properties

For $K_2Si_4O_9$, the enthalpy of formation value measured by Kracek et al. (Kracek et al. 1953) using solution calorimetry was close to the one reported by Geisinger et al. (Geisinger et al. 1987) using the vibrational model, similarly with the DFT calculated value. However, these

values differed from the modified one in Kim et al. (D.-G. Kim et al. 2017) and the one used in FactPS. Hence, Kracek et al. (Kracek et al. 1953) or the DFT value was considered more accurate and was proposed to be used in this work. Concerning the standard entropy, the value calculated in this work from the Einstein model was similar to the one adopted in FactPS but different from the one reported by Kim et al. (D.-G. Kim et al. 2017). Kim et al. (D.-G. Kim et al. 2017) value was adopted from the estimation of Spencer et al. (Spencer 1973). Hence, it is considered less accurate than DFT or measurements. Consequently, the entropy value calculated using the Einstein model is proposed in this work.

4.6.4. Proposed K_4SiO_4 properties

For K_4SiO_4, the value calculated by DFT (-1991.07kJ/mol) was in the middle of the value estimated by Slough et al. (Slough, n.d.) (-2064.614 kJ/mol) and the one calculated by Kroger et al. (Kroger and Fingas 1933) (-1984.18 kJ/mol). The one estimated by Kim et al. (D.-G. Kim et al. 2017) was very close to the one of Slough et al. (Slough, n.d.). Nevertheless, the enthalpy value calculated by DFT was based on a well-defined crystalline structure in the literature. In addition, DFT calculation is a trustworthy method. Hence, the DFT value is proposed to be used in this work. Concerning the standard entropy, the one calculated using the Einstein model based on Cp values by DFT was in the middle between the one adapted in FactPS and the one estimated by Kim et al. (D.-G. Kim et al. 2017). Consequently, the DFT entropy value is also proposed by this work.

4.6.5. Proposed $K_6Si_2O_7$ properties

For $K_6Si_2O_7$, experimental thermodynamic properties are absent from the literature. Consequently, the enthalpy of formation and the standard entropy were reported for the first time in this work using calculated DFT values.

As shown in Figures 6.9 to 6.13 in sections 4.1 to 4.5, the Einstein Cp model matched the measured and DFT calculated Cp values. Hence, this model is proposed to be adapted to calculate the Cp of each stoichiometric compound.

Finally, the solid section of the binary phase diagram K_2O-SiO_2 was recalculated, and the final results show all the compounds discussed before as stable ones.

Table 6.10: Applied thermodynamic data (enthalpy of formation and standard entropy) in this work compared to Kim et al. (D.-G. Kim et al. 2017), FactPS, and FToxid.

	$\Delta H_f°$(kJ/mol) at 298.15K									
	Proposed in this work				From Kim et al. (D.-G. Kim et al. 2017)		FactPS		FToxid	
	reference	elements	oxides	Calculated by DFT (in oxides)	value	reference	value	reference	value	reference
K_2SiO_3	Brown 1987(Brown and Bennington 1987) *HF calorimeter in 20% HF at 74.7 °C* ***± 4.605 kJ/mol***	-1522.00	-257.39	-254.22	-1543.80	optimized from elemental reference state	-1560.36	Barin, Pelton, and Berman (Barin, Knacke, and Kubaschewski 1977; Pelton, Eriksson, and Wu 1992; Berman and Brown 1985)	same as Kim	
$K_2Si_2O_5$	Kracek 1953(Kracek et al. 1953) *HF calorimeter in 20% HF at 74.7 °C* *± 1.452 kJ/mol*	-2499.64	-324.34	-288.78	-2503.70	optimized = value of Kracek et al.	-2522.54	Pelton and Berman (Pelton, Eriksson, and Wu 1992; Berman and Brown 1985)	same as Kim	
$K_2Si_4O_9$	Kracek 1953(Kracek et al. 1953) *HF calorimeter in 20% HF at 74.7 °C* *± 1.452 kJ/mol*	-4306.06	-309.36	-313.25	-4342.00	initially taken from Kracek et al. (-4313.7kJ/mol) then modified	-4335.34	Pelton and Barin (Barin, Knacke, and Kubaschewski 1977; Pelton, Eriksson, and Wu 1992)	same as Kim	

K_4SiO_4				-372.57	-2065.22	estimated based on similar system Na and Li	-2045.90	Optimized in the Centre for Research in Computational Thermochemistry (CRCT), Montreal.	same as FactPS
$K_6Si_2O_7$				-668.80	does not exist in the database				

	S° (J/(mol.K)) at 298.15K						
	this work	Kim		FactPS		FToxid	
	value from Einstein model	value	reference	value	reference	value	reference
K_2SiO_3	145.318	146.100	calculated from Cp by adiabatic calorimetry in Stull et al.	146.147	Barin, Pelton, and Berman (Barin, Knacke, and Kubaschewski 1977; Pelton, Eriksson, and Wu 1992; Berman and Brown 1985)	same as Kim	
$K_2Si_2O_5$	190.342	190.600	calculated from Cp by adiabatic calorimetry in Beyer et al.	182.004	Pelton and Berman (Pelton, Eriksson, and Wu 1992; Berman and Brown 1985)	same as Kim	
$K_2Si_4O_9$	247.592	265.700	from the review of spencer et al.	265.684	Pelton and Barin (Barin, Knacke, and Kubaschewski	same as Kim	

					1977; Pelton, Eriksson, and Wu 1992)	
K_4SiO_4	241.323	233.198	estimated using NKR	245.472	Optimized in the Centre for Research in Computational Thermochemistry (CRCT), Montreal.	same as FactPS
$K_6Si_2O_7$	389.177	does not exist in the database				

5. Conclusion

In this chapter, the contribution to the improvement of the database was presented. The optimum synthesis conditions of the ternary compounds $K_2Ca_2Si_2O_7$, $K_2Ca_6Si_4O_{15}$, and $K_4CaSi_3O_9$ were discussed in detail. Their enthalpy of formation using drop calorimetry and melting points measurements were also presented. A thorough investigation of the stability of the fourth ternary compound in the CaO-K_2O-SiO_2 phase diagram between 800 °C and 1200 °C, K_2CaSiO_4, was discussed. Several conclusions can be drawn out from this section:

1. K_2CaSiO_4 was never found.
2. A new unidentified phase should be present.
3. CaO-Ca_2SiO_4-$K_2Ca_6Si_4O_{15}$ equilibrium section was confirmed.
4. CaO- $K_2Ca_2Si_2O_7$ tie line was validated.

In addition, all the phase diagrams and thermodynamic properties of the intermediate stoichiometric compounds in the K_2O-SiO_2 binary phase diagram were critically reviewed. Reliable experimental data were used for Gibbs minimization using the 3rd generation CalPhad Einstein model with multiple Einstein temperatures and an-harmonic corrections. For the first time in literature without estimated values, a combination of measured (in literature) and calculated (by DFT) was proposed to re-model the stoichiometric compounds in this binary. In addition, for the first time in literature, accurate thermodynamic properties of K_4SiO_4 and $K_6Si_2O_7$ were provided instead of estimations.

In terms of perspectives, the heat capacity of the three synthesized ternary compounds should be measured to determine their Cp over the whole temperature range. In addition, K_2CaSiO_4 stability needs further investigations. Furthermore, the liquid section of the binary diagram K_2O-SiO_2 is still missing in this work and needs further study and examination.

References

Agren, J., B. Cheynet, M.T. Clavaguera-Mora, K. Hack, J. Hertz, F. Sommer, and U. Kattner. 1995. "Workshop on Thermodynamic Models and Data for Pure Elements and Other Endmembers of Solutions: Schloβ Ringberg, Febr. 21, to March 3, 1995." *Calphad* 19 (4): 449–80. https://doi.org/10.1016/0364-5916(96)00003-X.

Arroyabe, E., R. Kaindl, D.M. Többens, and V. Kahlenberg. 2009. "K2Ca6Si4O15—Structural and Spectroscopical Studies on a Mixed Tetrahedral–Octahedral Framework." *Journal of Solid State Chemistry* 182 (12): 3254–61. https://doi.org/10.1016/j.jssc.2009.09.013.

Arroyabe, Erik, and Volker Kahlenberg. 2011. "Structural Investigations on the Fertilizer Component K2Ca2Si2O7." *European Journal of Mineralogy* 23 (1): 101–10. https://doi.org/10.1127/0935-1221/2011/0023-2080.

Arroyabe, Erik, Reinhard Kaindl, and Volker Kahlenberg. 2009. "Structural and Raman Spectroscopic Investigations of K4BaSi3O9 and K4CaSi3O9." *Zeitschrift Für Anorganische Und Allgemeine Chemie* 635 (2): 337–45. https://doi.org/10.1002/zaac.200800398.

Arroyabe, Erik, Richard Tessadri, Daniel M. Többens, and Volker Kahlenberg. 2011. "Does K2CaSiO4 Exist? A Phase-Analytical Study in the System K2O-CaO-SiO2 with Implications for the Characterization of Residual Materials: Does K2CaSiO4 Exist?" *Journal of the American Ceramic Society* 94 (8): 2652–55. https://doi.org/10.1111/j.1551-2916.2011.04397.x.

Bale, C.W., E. Bélisle, P. Chartrand, S.A. Decterov, G. Eriksson, A.E. Gheribi, K. Hack, et al. 2016. "FactSage Thermochemical Software and Databases, 2010–2016." *Calphad* 54 (September): 35–53. https://doi.org/10.1016/j.calphad.2016.05.002.

Barin, Ihsan, Ottmar Knacke, and Oswald Kubaschewski. 1977. *Thermochemical Properties of Inorganic Substances. Suppl*. Berlin: Springer.

Becker, Chandler A., John Ågren, Marcello Baricco, Qing Chen, Sergei A. Decterov, Ursula R. Kattner, John H. Perepezko, Gernot R. Pottlacher, and Malin Selleby. 2014. "Thermodynamic Modelling of Liquids: CALPHAD Approaches and Contributions from Statistical Physics." *Physica Status Solidi (b)* 251 (1): 33–52. https://doi.org/10.1002/pssb.201350149.

Berezhnoi, A. S., N. V. Lapina, E. V. Lifshits, and E. P. Shevyakova. 1976. "Characteristics of Multicomponent High-Basic Silicates in the System Na2O–K2O– CaO–MgO–SiO2." *Neorg. Mater.*, 1976, 12.

BERMAN, R. G. 1988. "Internally-Consistent Thermodynamic Data for Minerals in the System Na2O-K2O-CaO-MgO-FeO-Fe2O3-Al2O3-SiO2-TiO2-H2O-CO2." *Journal of Petrology* 29 (2): 445–522. https://doi.org/10.1093/petrology/29.2.445.

Berman, RG, and TH Brown. 1985. *Heaat Capacity of Minerals in the System Na2O-K2O-CaO-MgO-FeO-Fe2O3-Al2O3-SiO2-TiO2-CO2: Representation, Estimation, and High Temperature Extrapolation.* 89th ed. Contrib. Miner. Petrol.

Bernet, K., and R. Hoppe. 1990. "Zur Kristallstruktur von K4[SiO4]." *Zeitschrift für anorganische und allgemeine Chemie* 589 (1): 129–38. https://doi.org/10.1002/zaac.19905890115.

Beyer, R. P. 1980. *Thermodynamic Properties of Potassium Metasilicate and Disilicate / by R.P. Beyer [and Others]*. Report of Investigations - Bureau of Mines ; No. 8410. Washington: Dept. of the Interior, Bureau of Mines.

Bigdeli, Sedigheh, Qing Chen, and Malin Selleby. 2018. "A New Description of Pure C in Developing the Third Generation of Calphad Databases." *Journal of Phase Equilibria and Diffusion* 39 (6): 832–40. https://doi.org/10.1007/s11669-018-0679-3.

Boivin, P., J. C. Berthelay, Y. Blanc, A. Coulet, and R. Castanet. n.d. “Determination of Temperature and Enthalpy of Melting of Alkali Disilicates by Differential Calorimetric Analysis.” *J. Mater. Sci.*, 28.

Borisova, N.V., and V.M. Ushakov. 1998. “High-Temperature Calorimetry of Glasses and Crystals in the K2O-SiO2 System.” *Glas. Phys. Chem.*, 1998, 24.

Brown, R. R., and K. O. Bennington. 1987. “Thermodynamic Properties of Potassium Metasilicate (K2SiO3).” *Thermochimica Acta* 122 (2): 289–94. https://doi.org/10.1016/0040-6031(87)87048-X.

Chase, M.W., I. Ansara, A. Dinsdale, G. Erikson, G. Grimvall, L. Hoglund, and H. Yokokawa. 1995. “Workshop on Thermodynamic Models and Data for Pure Elements and Other Endmembers of Solutions: Schloβ Ringberg, Feb. 26 to March 3, 1995.” *Calphad* 19 (4): 437–47. https://doi.org/10.1016/0364-5916(96)00002-8.

Chen, Qing, and Bo Sundman. 2001. “Modeling of Thermodynamic Properties for Bcc, Fcc, Liquid, and Amorphous Iron.” *Journal of Phase Equilibria* 22 (6): 631–44. https://doi.org/10.1007/s11669-001-0027-9.

Cheng, Jihong, and Alexandra Navrotsky. 2005. “Energetics of La1−xAxCrO3−δ Perovskites (A=Ca or Sr).” *Journal of Solid State Chemistry* 178 (1): 234–44. https://doi.org/10.1016/j.jssc.2004.11.028.

“Data From NIST Standard Reference Database 69.” 2020. NIST Chemistry WebBook. http://webbook.nist.gov/cgi/cbook.cgi?ID=C7732185&Units=SI.

Deffrennes, Guillaume, Noël Jakse, Cecilia M. S. Alvares, Ioana Nuta, Alain Pasturel, Alexandra Khvan, and Alexander Pisch. 2020. “Thermodynamic Modelling of the Ca–O System Including 3rd Generation Description of CaO and CaO2.” *Calphad* 69 (June): 101764. https://doi.org/10.1016/j.calphad.2020.101764.

Fasshauer, Detlef, Bernd Wunder, Niranjan Chatterjee, and Günther Höhne. 1998. “Heat Capacity of Wadeite-Type K2Si4O9 and the Pressure-Induced Stable Decomposition of K-Feldspar.” *Contributions to Mineralogy and Petrology* 131 (April): 210–18. https://doi.org/10.1007/s004100050389.

Geisinger, Karen L., Nancy L. Ross, Paul F. McMillan, and Alexandra Navrotsky. 1987. “K2Si4O9: Energetics and Vibrational Spectra of Glass, Sheet Silicate, and Wadeite-Type Phases.” *American Mineralogist* 72 (9–10): 984–94.

Goranson, R. W., and F. C. Kracek. 1932. “An Experimental Investigation of the Phase Relations of K2Si4O9 under Pressure.” *J. Phys. Chem.*, 1932, 36.

Gurvich, L. V., and I. Veyts. 1990. “Thermodynamic Properties of Individual Substances: Elements and Compounds (Vol. 2).” CRC press.

Hoppe, R., and R. Werthmann. 1981. “Ueber K2 Si O3 - Das Erste Cyclotrisilicat Eines Alkalimetalls - Sowie Rb2 Si O3, Cs2 Si O3, Rb2 Ge O3 Und Cs2 Ge O3.” *Revue de Chimie Minerale*, 1981, 18.

Hughes, H. 1966. “Formation of Alkali Silicates and Alumino-Silicates and Their Occurrence in Blast Furnaces.” *Trans. Br. Ceram. Soc.*, 1966, 65.

Jansen, M. 1982. “Zur Struktur von Kaliumdisilicat.” *Journal Door Crystallography*, 1982, 160.

Jong, B. H. W. S. de, H. T. J. Supèr, A. L. Spek, N. Veldman, G. Nachtegaal, and J. C. Fischer. 1998. “Mixed Alkali Systems: Structure and ^{29} Si MASNMR of Li $_2$ Si $_2$ O $_5$ and K $_2$ Si $_2$ O $_5$.” *Acta Crystallographica Section B Structural Science* 54 (5): 568–77. https://doi.org/10.1107/S0108768198001062.

Khvan, A. V., T. Babkina, A. T. Dinsdale, I. A. Uspenskaya, I. V. Fartushna, A. I. Druzhinina, A. B. Syzdykova, M. P. Belov, and I. A. Abrikosov. 2019. “Thermodynamic Properties of Tin: Part I Experimental Investigation, Ab-Initio Modelling of α-, β-Phase and a Thermodynamic Description for Pure Metal in Solid

and Liquid State from 0 K." *Calphad* 65 (June): 50–72. https://doi.org/10.1016/j.calphad.2019.02.003.

Khvan, A. V., A. T. Dinsdale, I. A. Uspenskaya, M. Zhilin, T. Babkina, and A. M. Phiri. 2018. "A Thermodynamic Description of Data for Pure Pb from 0K Using the Expanded Einstein Model for the Solid and the Two State Model for the Liquid Phase." *Calphad* 60 (March): 144–55. https://doi.org/10.1016/j.calphad.2017.12.008.

Kim, Donggeum. 2017. "Coupled Experimental Study and Thermodynamic Optimization of the K2O-Na2O-CaO-MgO-Al2O3-SiO2 System." Canada: McGill University, Montreal, Quebec, Canada.

Kim, Dong-Geun, Marie-Aline Van Ende, Pierre Hudon, and In-Ho Jung. 2017. "Coupled Experimental Study and Thermodynamic Optimization of the K2O-SiO2 System." *Journal of Non-Crystalline Solids* 471 (September): 51–64. https://doi.org/10.1016/j.jnoncrysol.2017.04.029.

Kiseleva, Irina, Alexandra Navrotsky, Igor A. Belitsky, and Boris A. Fursenko. 1996. "Thermochemistry of Natural Potassium Sodium Calcium Leonhardite and Its Cation-Exchanged Forms." *American Mineralogist*, 1996, 81.

Kozin, N.Yu., A.L. Voskov, A.V. Khvan, and I.A. Uspenskaya. 2020. "Thermodynamic Properties of Synthetic Zeolite – Mordenite." *Thermochimica Acta* 688 (June): 178600. https://doi.org/10.1016/j.tca.2020.178600.

Kracek, F. C. 1930. "The Cristobalite Liquidus in the Alkali Oxide-Silica Systems and the Heat of Fusion of Cristobalite." *J Am Chem Soc*, 1930, 52, 1436–1442.

Kracek, F. C., N. L. Bowen, and G. W. Morey. 1937. "EQUILIBRIUM RELATIONS AND FACTORS INFLUENCING THEIR DETERMINATION IN THE SYSTEM IK2SiO3-SiO2." *Journal of Physical Chemistry*, 1937, 41, 1183–1193.

Kracek, F. C., G. Neuvonen, G. Burley, and R. J. Gorden. 1953. "Contributions of Thermochemical and X-Ray Data to the Problem of Mineral Stability." *52 Carnegie Inst., Washington, Ybk.*, 1953, 69-75.

Kracek, F.C. 1932. "The Ternary System: K2SiO3-Na2SiO3-SiO2." *J. Phys. Chem.*, 1932, 36, 2529-2542.

Kroger, C., and E. Fingas. 1933. "Action of Quartz and Alkali Silicates upon Alkali Carbonates." *Z. Anorg. Allg. Chem.*, 1933, 213, 12-57.

Li, Zhou, Sedigheh Bigdeli, Huahai Mao, Qing Chen, and Malin Selleby. 2017. "Thermodynamic Evaluation of Pure Co for the Third Generation of Thermodynamic Databases." *Physica Status Solidi (b)* 254 (2): 1600231. https://doi.org/10.1002/pssb.201600231.

Meshalkin, Arkadiy B., and Alexander B. Kaplun. 2005. "The Complex Investigation of the Phase Equilibria and Melt Characteristics in Borate and Silicate Systems." *Journal of Crystal Growth* 275 (1–2): e115–19. https://doi.org/10.1016/j.jcrysgro.2004.10.136.

Morey, G. W. 1917. "THE TERNARY SYSTEM H2O-K2SiO3-SiO2." *Contribution from the Geophysical Laboratory, Carnegie Institution of Washington.*, 1917.

Morey, G.W., F.C. Kracek, and N.L. Bowen. 1930. "The Ternary System K2O-CaO-SiO2." *Journal of the Society of Glass Technology* 14: 149–87.

Navrotsky, Alexandra. 2014. "Progress and New Directions in Calorimetry: A 2014 Perspective." Edited by D. J. Green. *Journal of the American Ceramic Society* 97 (11): 3349–59. https://doi.org/10.1111/jace.13278.

O'Keeffe, M., and B. G. Hyde. 1984. "Stoichiometry and the Structure and Stability of Inorganic Solids." *Nature*, 1984, 309, 411-414.

Pelton, A. D., G. Eriksson, and P. Wu. 1992. "Coupled Optimization of Thermodynamic and Phase Diagram Data." thesis, Ecole Polytechnique, Montreal.

Santoso, Imam, Pekka Taskinen, Ari Jokilaakso, Min-Kyu Paek, and Daniel Lindberg. 2020. "Phase Equilibria and Liquid Phase Behavior of the K2O-CaO-SiO2 System for Entrained Flow Biomass Gasification." *Fuel* 265 (April): 116894. https://doi.org/10.1016/j.fuel.2019.116894.

Schweinsberg, H., and F. Liebau. 1972. "Darstellung und kristallographische Daten von K2Si2O5, KHSi2O5I und K2Si4O9." *Zeitschrift für anorganische und allgemeine Chemie* 387 (2): 241–51. https://doi.org/10.1002/zaac.19723870211.

———. 1974. "Die Kristallstruktur des K4[Si8O19]: ein neuer Silikat-Schichttyp." *Acta Crystallographica Section B: Structural Crystallography and Crystal Chemistry* 30 (9): 2206–13. https://doi.org/10.1107/S0567740874006753.

Sergeev, D., E. Yazhenskikh, D. Kobertz, and M. Müller. 2019. "Vaporization Behavior of Na2CO3 and K2CO3." *Calphad* 65 (June): 42–49. https://doi.org/10.1016/j.calphad.2019.02.004.

Slough, W. n.d. "Comparison of Methods Available for the Estimation of Enthalpies of Formation for Double Oxide Systems." *Nat. Phys. Lab. (1973) (U. K.), Div. Chem. Stand., Rep., No. 25 (12 Pp).*

Spencer, P. J. 1973. "Thermodynamic Properties of Silicates." *Natl. Phys. Lab.*, 1973.

Stebbins, J. F., P. F. McMillan, and D. B. Dingwell. 1995. "Structure, Dynamics and Properties of Silicate Melts." *Mineralogical Society of America*, 1995, 32.

Stull, D. R., D. L. Hildenbrand, F. L. Oetting, and G. C. Sinke. 1970. "Low-Temperature Heat Capacities of 15 Inorganic Compounds." *Journal of Chemical & Engineering Data* 15 (1): 52–56. https://doi.org/10.1021/je60044a035.

Swanson, Donald K., and Charles T. Prewitt. 1983. "The Crystal Structure of K 2 Si VI Si 3IV O 9." *American Mineralogist* 68 (5–6): 581–85.

Takahashi, K., and T. Yoshio. 1970. "Thermochemical Investigations of Glasses. II. Oxygenalkali Metal Bond Energy in Alkali Silicates. (R2O-SiO2)." *Yogyo Kyokai Shi*, 1970, 78.

Takahashi, Katsuaki, and T. Yoshio. 1973. "Thermodynamic Quantities of Alkali Silicates in the Temperature Range from 25°C to Melting Point." https://doi.org/10.2109/JCERSJ1950.81.940_524.

Conclusion

The main aim of this work was to study the ash behavior of biomass and their mixtures to limit their operational problems in combustion reactors. Biomass blending showed good possibility in controlling the problematic ash behavior. However, a chemical reaction within the ash should take place to form new phases in the mixture and reduce the percentage of the problematic phase. Hence, the first objective of this work was to assess the presence of such a chemical reaction compared to a phase dilution (mixing without interactions) within the ash of biomass blends. This assessment was conducted with varying reactor scale, reactor type, and operating conditions. In addition, three different wheat straws and oak barks along with their mixtures were used. After analyzing the produced ash, several conclusions were drawn out, as follows:

1. Chemical reactions effect was dominant when ash mixtures (i.e. ash test) were used.
2. Mixing rule influence was the most important when biomass mixtures were applied; still a minor reaction effect remained.
3. Chemical interactions decreased as the furnace scale increased, contrary to phase dilution.
4. Chemical reactions were more complex in the fluidized bed reactor in gasification and combustion modes. The inorganic elements reacted with the bed materials instead of each other.
5. The ash reactivity of the BCWC mixture (similar to the operating conditions effects rank) was ranked in the decreasing order: ash test > pellet test > pilot burner.
6. The temperature then residence time had higher effects on the ash reactivity than cooling and pellet compression rates.
7. $K_2Ca_6Si_4O_{15}$ and $K_2Ca_2Si_2O_7$ were the main products of the chemical reactions in 50-50 bark (BC)-straw (WC) biomass and ash mixtures. They were absent in the single feedstock but highly stable at 1000 °C and 6 h in the blend in the ash test, conditions at which equilibrium was experimentally reached. Their appearance along with their increasing proportions, led to a decrease in the amorphous proportion.
8. The laboratory pellet test was able to predict the pilot burner behavior in terms of crystalline and amorphous proportions along with agglomeration distribution for both individual biomasses and biomass mixtures.

Afterward, the second objective was to assess the use of a tool based on thermodynamic equilibrium calculations and simulations (maximized ash interactions/reactions) to predict the ash behavior in real-life processes. Such a tool can help adapt the blend type and proportions to

the applied reactor. FactSage software was used, equipped with FToxid, FactPS, FTsalt, and GTOX databases. Two approaches were proposed. The first was based on predicting the state of the ash based on the thermodynamic phase equilibria of the calculated ternary phase diagram $CaO\text{-}K_2O\text{-}SiO_2$ after localizing the biomasses on it. The second was based on process equilibrium simulations based on the global composition of the biomass ash. Consequently, in the first part of the second objective, these two approaches were assessed in terms of the improvements in thermodynamic databases. The conclusions were:

1. FToxid provided a phase diagram containing more ternary compounds compared to GTOX, especially the addition of $K_2Ca_6Si_4O_{15}$ and $K_2Ca_2Si_2O_7$ to its database.
2. Phase diagram and ash test global simulations approaches exhibited the same behavior.
3. Apparent differences between the phase diagram approach (=ash test simulation) and the pellet test simulation were present, especially as the mixture became richer in bark.
4. In the global simulation approach, significant differences were evident in the predicted condensed phases and volatilizations between the two database sets at varying temperatures and bark weight fractions in the blends.
5. Several factors affected the prediction results using the FToxid database set:
    - P, Cl, and Mg destabilized $K_2Ca_2Si_2O_7$.
    - Insignificant effect for adding the FTsalt database to the FToxid database set 2.
    - Slag B application destabilized several major K-rich phases.

To further elaborate on the assessment of the prediction capabilities of this tool, the second part of the second objective was to assess the prediction capabilities using each database and each approach with respect to experimental results. It was found that:

1. The phase diagram approach showed good capabilities in predicting the ash state (solid or liquid) using both databases, with limitations for the biomasses and blends located in the upper section (solid section) of the diagram.
2. Using the global simulation approach on the ash test, simulations using the FToxid dataset offered good qualitative and quantitative predictions for the single biomass ash. It also showed decent qualitative prediction capabilities for the ash mixtures far from the central section of the ternary diagram.
3. Prediction of the pellet test using both datasets was worse than with the ash test due to the lack of reactivity of the mixture.
4. In the case of the single biomass, the same prediction capability was obtained for ash or pellet tests.

5. Calculations using both databases showed excellent volatilization prediction capabilities. Nevertheless, they failed to forecast the characteristic temperatures for phase transitions.

From the results of the second objective, further corrections and improvements were found to be still needed in the thermodynamic database. Hence, the third objective of this work consisted of a contribution to the thermodynamic database improvements.

1. Ternary section improvements:
    a. $K_2Ca_2Si_2O_7$, $K_2Ca_6Si_4O_{15}$, and $K_4CaSi_3O_9$ were synthesized, and their enthalpy of formation and melting points were measured.
    b. Several equilibrium regions of the phase diagram were experimentally checked using various synthesized CaO, K_2O, and SiO_2 mixtures. The main conclusions from this investigation were:
        1. K_2CaSiO_4 was never found.
        2. A new unidentified phase should be present.
        3. CaO-Ca_2SiO_4-$K_2Ca_6Si_4O_{15}$ equilibrium section was confirmed.
        4. CaO- $K_2Ca_2Si_2O_7$ tie line was validated.
2. Binary section improvements (K_2O-SiO_2 remodeling-solid section):
    a. A thorough literature review of the thermodynamic properties of the compounds in this system was conducted, and measured values were chosen rather than estimations.
    b. DFT Cp calculation (0-300K) was done, and the Einstein model was used to model Cp, enthalpy, and entropy.
    c. From the DFT calculation, $K_6Si_2O_7$ was found to be stable.

Perspectives

After the thorough discussions and clear findings shown in this work, several perspectives can be proposed for each objective.

Objective 1 (ash reactivity vs phase dilution):

1. Study the ash reactivity of the same mixture in an entrained flow reactor. The liquid phase ash will be more preferred in this case. So, the blend type and proportions should be adapted accordingly.
2. Assess the ash reactivity in gasification mode (fixed and fluidized bed). The oxygen shortage, in this case, might change the whole inorganic interactions.

3. Conduct the same study on other types of biomasses. Biomass located in the K-rich region is highly advised since this region is rarely investigated in literature.
4. Conduct the same study on other wheat straw and oak bark blend fractions. For instance, in a previous study, the 80wt.% bark blend produced more ash in the solid phase than the 20wt.% bark blend. A more thorough investigation of the ash behavior in these two blends is still needed.
5. Check if the boiler efficiency in terms of unburnt char will have an effect on the ash reactivity.

Objective 2 (thermodynamic tool prediction assessment):

1. Test the addition of a 4th oxide (MgO, Al_2O_3, P_2O_5) into a synthetic ash composition made with only the three major oxides CaO-SiO_2-K_2O («ash test»). The choice of the fourth element will depend on the ash composition of the chosen biomass.
2. Study the addition of a 4th oxide (MgO, Al_2O_3, P_2O_5) to the ternary phase diagram K_2O-CaO-SiO_2 using FactSage and the latest databases.

Objective 3 (improving the thermodynamic database):

1. Measure the heat capacity of the three synthesized ternary compounds to determine their Cp over the whole temperature range. Some Cp measurements were already done (maybe those of $K_2Ca_2Si_2O_7$) by other research teams in Europe, so collaboration/contact with them is advised.
2. Measure the melting point of $K_2Ca_6Si_4O_{15}$ and $K_4CaSi_3O_9$. K volatilization might pose certain measurement problems in the case of $K_4CaSi_3O_9$ and should be taken into account. $K_2Ca_6Si_4O_{15}$ already gave incoherent results, and the measurement technique should be checked again.
3. K_2CaSiO_4 stability needs further investigations. Experiments in this region were challenging, and the presence of the unknown phase U needs a crystallographic experience.
4. The liquid section of the binary diagram K_2O-SiO_2 is still missing in this work and needs further study and examination. The liquid model should be chosen based on agreements between the colleagues that will conduct the thermodynamic modeling.

Appendix A

A.1. Biomass organic contents

Biomass is mainly formed of organic elements that consist of 70 wt.% to 95 wt.% of its total weight and include C, O, H, N, and S. Table A1 shows the volatile matter (VM), fixed carbon (FC), moisture contents (M), ash contents (A) along with carbon (C), oxygen (O), hydrogen (H), nitrogen (N), and sulfur (S) weight percentages in typical biomasses and coals. According to this table, the proportion of elements vary depending on the biomass type, source, and organic structure. The main organic structures of biomass are hemicellulose, cellulose, and lignin (Figure A1). Hemicellulose are branched amorphous polymeric carbohydrates in the form of glycoside linkage between the monomeric sugars (Sun, Zhang, and Wang 2021). Cellulose is an organic unbranched polysaccharide molecule formed of linear polymers of glucose with an iterative molecular formula $(C_6H_{10}O_5)_n$ (Bakri, Rahman, and Chowdhury 2022). Lignin is a polyophenol made up of the primary monolignols coumaryl, coniferyl, and sinapyl alcohol (Sinha Ray and Banerjee 2022).

Table A1: Typical biomass and various coal ultimate and proximate analyses (Vassilev et al. 2010).

[VM=volatile matter, FC=fixed carbon, M=moisture contents, A=Ash contents]

	VM	**FC**	**M**	**A**	**C**	**O**	**H**	**N**	**S**
	Wt.%				***Wt.% on ash free basis***				
woody biomass	62.9	15.1	19.3	2.7	52.1	41.2	6.2	0.4	0.1
Herbaceous and agricultural biomass	66.0	16.9	12.0	5.1	49.9	42.6	6.2	1.2	0.2
Animal biomass	52.5	12.8	5.9	28.8	58.9	23.1	7.4	9.2	1.5
Grass	69.0	14.1	12.6	4.3	49.2	43.7	6.1	0.9	0.1
Straw	66.7	15.3	10.2	7.8	49.4	43.2	6.1	1.2	0.2
Biomass mixture	63.3	16.5	8.8	11.4	56.7	33.1	6.6	2.7	0.9
Wood-agricultural residue	54.7	12.7	30.3	2.3	52.4	41.2	6.0	0.4	0.0
Wood-almond residue	59.7	12.3	22.7	5.3	50.9	42.5	5.9	0.6	0.1
Wood-straw residue	69.6	15.5	7.3	7.6	51.7	41.5	6.3	0.4	0.1
Coal	30.8	43.9	5.5	19.8	78.2	13.6	5.2	1.3	1.7
Lignite	32.8	25.7	10.5	31.0	64.0	23.7	5.5	1.0	5.8
Sub-bituminous coal	33.4	34.1	8.2	24.3	74.4	17.7	5.6	1.4	0.9
Bituminous coal	29.1	52.6	3.1	15.2	83.1	9.5	5.0	1.3	1.1

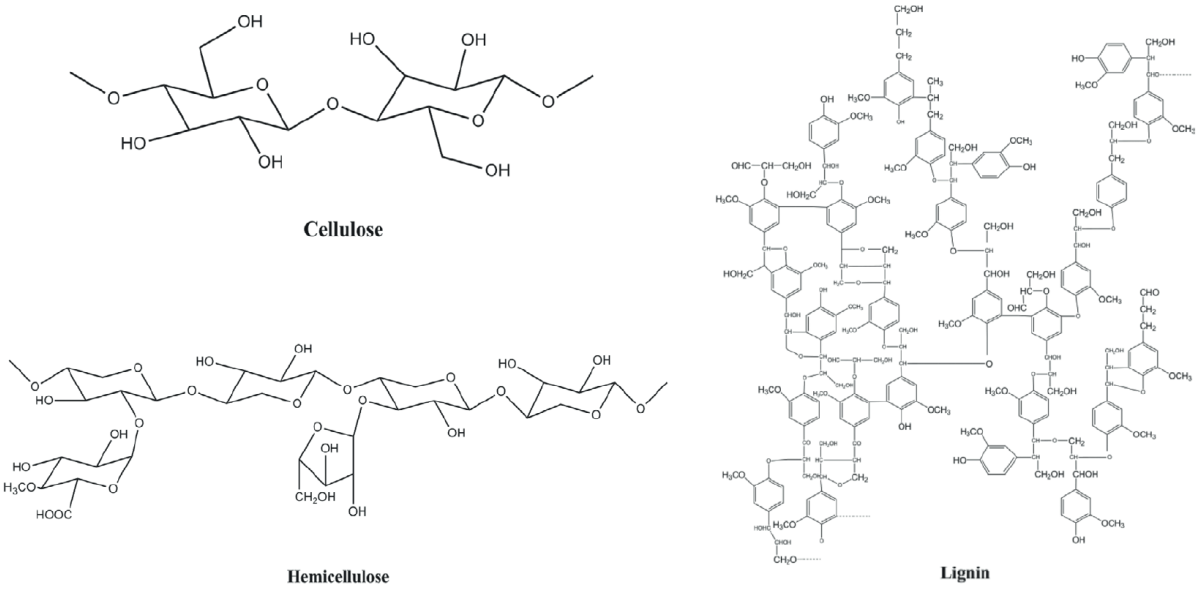

Figure A1: Biomass organic structural composition (Ilham 2022).

A.2. Biomass VS Coal

Coal is considered the origin of all fossil fuels in earth after a long sedimentation period of biomass residues (Altawell 2021). It is a combustible black or brownish-black sedimentary rock, formed as rock strata called coal seams (Kopp 2022; Altawell 2021). Coal contains mostly carbon (between 60 wt.% and 80 wt.%) with variable amounts of other elements, such as hydrogen, sulfur, oxygen, and nitrogen (Vassilev et al. 2010; Kopp 2022). The volatile matter and oxygen contents of biomass is double the ones of coal at the expenses of significantly higher fixed carbon and carbon contents for the latter (Table A1). Sulfur contents is generally higher in coal compared to biomass (Table A1), which explains the higher SO_x emissions when coal is burnt. Generally, coal presents a higher ash contents then biomass (Table A1). Coal ash consists mainly, in terms of oxides, of SiO_2, Al_2O_3, and CaO while biomass ash consists mainly of SiO_2, K_2O, and CaO (Table A2). Differences between biomass and coal can be summarized in Table A2.

Table A2: Biomass VS coal key points comparison.

	Biomass	Coal
Volatile matter	High	Low
Oxygen contents	High	Low
Carbon contents	Low	High
Sulfur contents	Low	High
Heating values	Low	High

Fractional heat contribution by volatiles	70%	36%
Ash contents concentration	High	Low
Ash contents composition	Wide	Less variable
Key oxide difference	Rich in K_2O	Rich in Al_2O_3

A.3. Combustion reaction and products

Combustion process is an overall exothermic set of reactions in which the carbon is oxidized into carbon dioxide and the hydrogen into water. The simplified combustion reaction is as follow:

$$C_nH_mN_kO_l + (n+m/4-l/2)O_2 \text{ or Air} \rightarrow nCO_2 + (m/2)H_2O + (k/2)N_2 + \text{heat} \quad (1)$$

The major products of combustion are heat, H_2O, and CO_2. However, this formula is incomplete since it does not account for the inorganic metals in the ash, nor the moisture contents in the feedstock, neither the numerous pollutants, such nitrous oxides (NO_x).

In combustion, the fuel burns at a temperature ranging between 800 °C and 1000 °C with excess oxygen. It has three main requirements to happen: fuel, air, and heat. If any of these factors is absent, burning can stop or can be incomplete. The excess air ratio, denoted by lambda (λ), is a key factor for any combustion process. Its formula is as follow:

$$\lambda = \frac{real\ air\ or\ O2\ pumped\ into\ the\ system}{stoichiometric\ air\ or\ O2} \quad (2)$$

In most cases, the excess air ratio is higher than the stoichiometric amount and the locally available combustion air, with a value ranging between 1 and 2.3 (Royo et al. 2019). When λ is less than 1, oxygen is the limiting reactant, and hence the increase in oxidant flow will accelerate the propagation of the combustion front and the temperature goes up (Royo et al. 2019). However, as the amount of oxygen inside the reactor further increases and leads to a λ higher than 1, fuel bed temperature started to decrease with the increase in air flow due to convective cooling effect (Royo et al. 2019). Oxidant preheating leads to an increase in the ignition rate, which behave against convective cooling and improves drying (Royo et al. 2019). Hence, λ is considered one of the most important factors that should be controlled and adapted in a combustion process depending on the required outputs.

A.3.1. Combustion mechanism

The combustion of solid fuels occurs via a sequence of steps that take place in parallel or sequentially. Figure A2 depicts the typical combustion pathways.

It starts by heating or drying the fuel to get rid of all the moisture contents. In this step, the majority of the necessary heat is coming from the radiating wall. The drying step takes place at low temperature (<100°C) where all the moisture exits from the fuel pores and surface in the form of water vapor. Fuel with high moisture contents is problematic for combustion since it can lead to poor ignition and reduction of the combustion temperature (Abuelnuor et al. 2014). This in turn hinders the combustion of the reaction products and consequently affects the combustion efficiency (Abuelnuor et al. 2014).

In the second step, after the fuel is totally dried, the fuel temperature rises quickly to 260 °C and the organic materials that already exist in the fuel start to volatilize (Strzalka, Erhart, and Eicker 2013). This step depends on the heating rate, final temperature, fuel composition, particle size and pressure. The fuel loses a significant amount of its weight (losing more than 90 wt.% of its volatile matter) and approximately 30% of its heating value (Strzalka, Erhart, and Eicker 2013).

In the third step, thermal degradation of the carbonaceous particles occurs at around 800 °C. Volatile gases containing H_2O, CO_2, CO, CH_4, hydrocarbons, and other gaseous components are released. In this step, volatilization and carbonization occur at the same time. In parallel to the thermal decomposition, fragmentation/cracking occurs because of both the thermal shock and the release of volatile matter. Thermal efficiency and carbon conversion decrease due to particles exiting the combustion chamber (Abuelnuor et al. 2014; Nunes, Matias, and Catalão 2014). Abrasion also happen due to the collision of particles between themselves and the wall of the reactor (Nunes, Matias, and Catalão 2014).

The final and forth step is char oxidization and ash behavior. This stage is much slower than its previous and encompasses for around 20% of the combustion total time (Strzalka, Erhart, and Eicker 2013). It is considered as the most complicated and fuel dependent step. Ash behavior during combustion will be discussed in details in the coming sections.

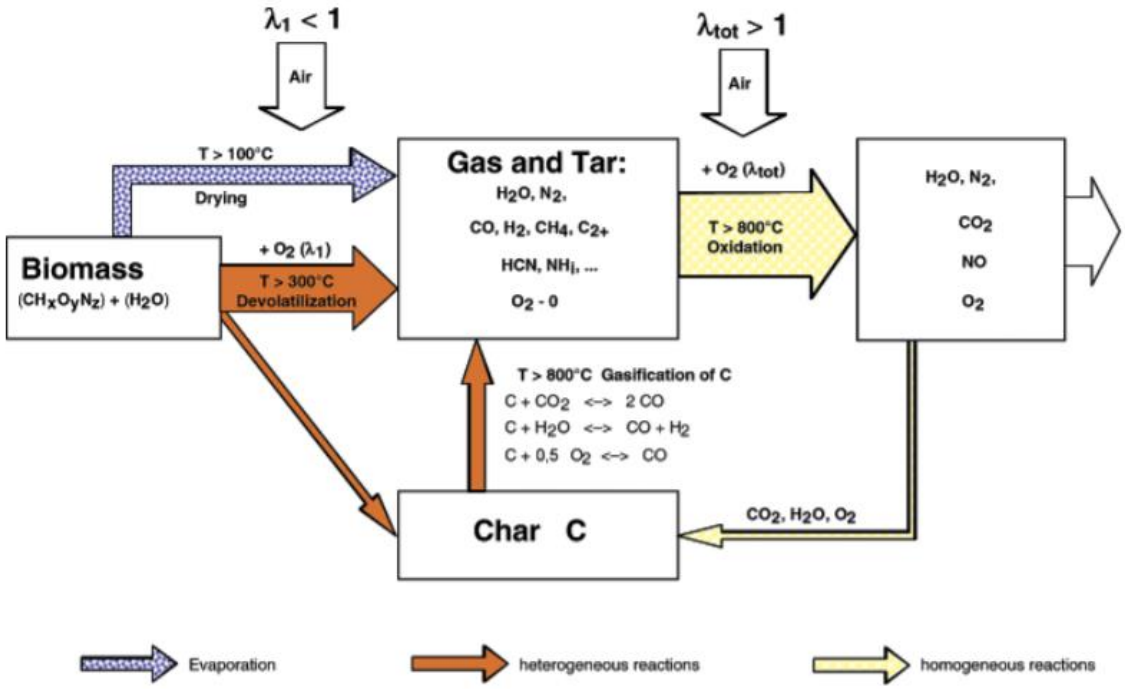

Figure A2: Biomass combustion reactions, products, and stages (EAGRI, n.d.).

A.4. Gasification

Gasification is an old technology and is very similar to combustion. The key difference between the two techniques is related to the oxidizing agent. Excess ($\lambda>1$) O_2 (or air) is used in combustion while limiting O_2 ($\lambda<1$), steam and CO_2 are used in the gasification mode. Hence, gasification can be called incomplete combustion, from which CO and H_2 (called syngas or synthetic gas) are the main products instead of CO_2 and H_2O.

Gasification received major boost in the mid-1940s when it was used to produce hydrocarbons to power vehicles in Europe (Huber, Iborra, and Corma 2006). Generally, gasification has a higher energy efficiency (proportional to the carbon recovery) than combustion (Luo and Zhou 2012). It is still under continuous research, especially in the case of biomass gasification (Luo and Zhou 2012). Similar to the previous section, gasification mechanism will be presented. Then, the various oxidizing agent (oxidizer) types that can be used in gasification will be shown. The effect and importance of each one of them on the gasification products will be presented.

A.4.1. Gasification mechanism

Similar to combustion, gasification starts by drying the waste. Then, fast pyrolysis occurs at 300 °C – 500 °C where the volatile matter volatilize; and Char, condensable hydrocarbons, tars, and gases are released.

Afterwards, char gasification takes place. It converts the pyrolyzed products (i.e. volatiles, char, tar, etc.) to a combustible gas mixture through partial oxidation (i.e. incomplete combustion) at high temperature of 600 °C – 900 °C (Luo and Zhou 2012; Richardson et al. 2015). The remaining chars and tars are then converted back to syngas in a reductive atmosphere. Hence, the produced syngas quality depends on : the raw material composition, the water content of the fuel, the temperature of the reactor, the heating rate, the type of the gasifier, and the oxidation of pyrolysis products (Luo and Zhou 2012). The reaction mechanism can proceed as follow (Gómez-Barea and Leckner 2010):

Reactions	Heat of Reaction ΔH^0 (kJ mol^{-1})	Name	Number
Biomass → char + tars + H_2O + light gases ($CO + CO_2 + H_2 + CH_4 + C_xH_yO_z + N_2 + \cdots$)	>0	Pyrolysis or devolatilization	R1
Char combustion			
$C + \frac{1}{2}O_2 \rightarrow CO$	−111	Partial combustion	R2
$C + O_2 \rightarrow CO_2$	−394	Total combustion	R3
Char gasification			
$C + CO_2 \rightleftarrows 2CO$	+173	Boudouard reaction	R4
$C + H_2O \rightarrow CO + H_2$	+131	Steam gasification	R5
$C + 2H_2 \rightleftarrows CH_4$	−75	Hydrogene gasification	R6
Homogeneous reactions			
$CO + \frac{1}{2}O_2 \rightarrow CO_2$	−283	CO oxidation	R7
$H_2 + \frac{1}{2}O_2 \rightarrow H_2O$	−242	H_2 oxidation	R8
$CH_4 + 2O_2 \rightarrow CO_2 + 2H_2O$	−283	CH_4 oxidation	R9
$CO + H_2O \rightleftarrows CO_2 + H_2$	−41	Water-gas shift (WGS)	R10
$CO + 3H_2 \rightleftarrows CH_4 + H_2O$	−206	Methanation	R11
Tar conversion reactions			
$C_nH_m + (n/2)O_2 \rightarrow nCO + (m/2)H_2$		Partial oxidation	R12
$C_nH_m + nH_2O \rightarrow (m/2 + n)H_2 + nCO_2$	Highly endothermic	Steam reforming	R13
$C_nH_m + nCO_2 \rightarrow 2nCO_2 + (m/2)H_2$		Dry reforming	R14
$C_nH_m \rightarrow (m/4)CH_4 + (n - m/4)C$		Thermal cracking	R15

Gasification is an overall endothermic reaction, in which some of the minor reactions are exothermic. The heat can be indirectly provided, where it is generated outside the reactor then transferred to it generally by the oxidant gas. It can also be supplied by direct gasification, where the heat is generated by the exothermic combustion and partial combustion reactions inside the gasifier (Richardson et al. 2015).

A.4.2. Oxidizing agent types in gasification

Gasification, as a partial oxidation, uses less than the stoichiometric ratio required for complete combustion. Lambda, λ, (Eq.2) generally ranges between 0.3 and 0.6 (Richardson et al. 2015).

The oxidant can be air (Zainal et al. 2002), CO_2 (Luo and Zhou 2012), pure O_2 (Luo and Zhou 2012), and steam (Rapagnà 2000). According to Table A3 (compiled based on the references mentioned just before), each has its own advantages and limitations. Hence, their application depends on the desired plant design. Nevertheless, a mixture of air-steam, a mixture of O_2-steam, a mixture of CO_2-steam, and a mixture of air-CO_2 are usually adapted in the industry (Luo and Zhou 2012).

Table A3: Advantages and disadvantages of each oxidant type used in gasification.

	Advantages	**Disadvantages**
Air	simple equipment	rich in N_2 low syngas HHV
	easy operation	
	simple maintenance	
	low cost	
O2	high syngas HHV	high operational cost
H2O (v)	syngas rich in H2 high syngas HHV	require an external heating source
		high cost
		corrosion
		high tar contents
CO2	lower CO2 emissions	low efficiency
		medium syngas HHV
		complicated reactor design

A.5. Applied reactors

In this section, the various types of reactors that are used in the thermochemical conversion techniques, specifically combustion, are presented in details. Each type of reactor is defined and its operational mode is discussed.

A.5.1. Furnace / Grate / Fixed bed

Grates reactors (fixed and moving beds) were the first combustion structures used to valorize solid fuel due to their simple design, easy operation, and reliable performance (Luo and Zhou 2012; Richardson et al. 2015). Reaction conditions can be easily controlled when a grate is used (Royo, Canalís, and Quintana 2020). They are considered very good candidate in the industry to burn fuel with high moisture contents, non-homogeneous particle size, and high ash contents (Luo and Zhou 2012). However, low and non-uniform heat and mass transfers lead to large quantities of tars and chars in the products. This increases the system complexity and investment needed for subsequent processing. Therefore, small-scale reactors are preferred in this system (Luo and Zhou 2012).

A.5.1.1. Horizontal reactor

According to Figure A3, a grate reactor has four main components: the fuel supply, the grate, the primary and secondary air feeder, and the ash discharger. Fuel is fed to the grate through the feeder. The grate is always at the bottom of the combustion chamber and is used to distribute the fuel. Grate is classified as stationary (i.e. fixed bed) or mechanical, which can be reciprocal (i.e. with downward or upward moving grid), vibrating, oscillating, mobile, or drum. The air required for combustion usually comes from the bottom through the grate, and is called primary air. Secondary air is always above the grid, and is applied to ensure complete burnout of the combustible gas and flying particles. Preheating air helps reach an efficient combustion at a lower temperature (Royo, Canalís, and Quintana 2020). The remaining ash fall down below the grate into the pit air at the tail.

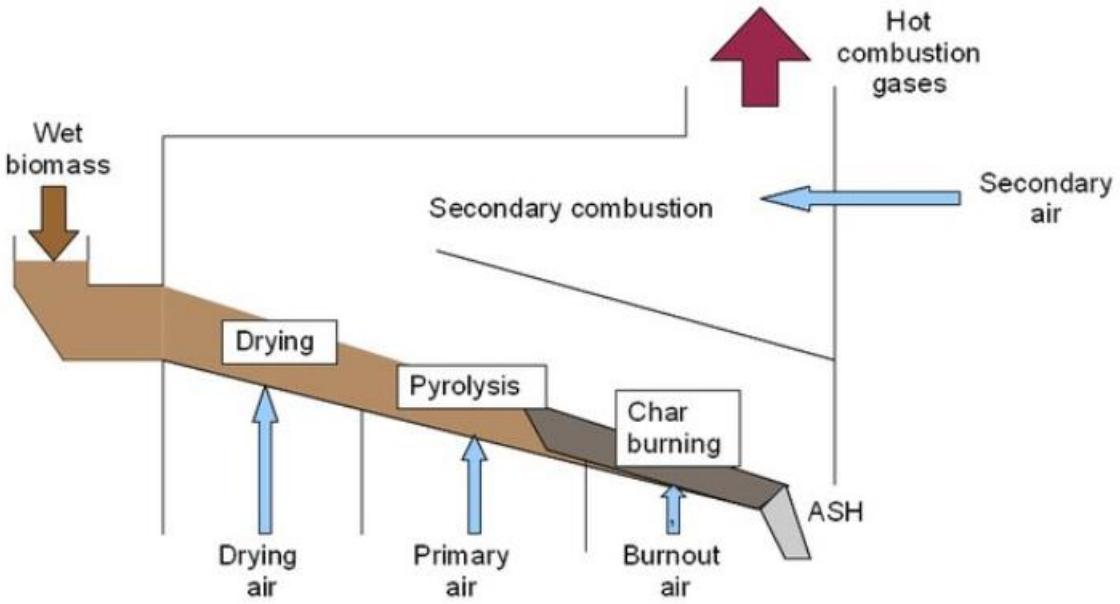

Figure A3*: Combustion chamber of the biomass grate furnace (Strzalka, Erhart, and Eicker 2013).*

Horizontal fixed and moving bed reactors (i.e. grates) are used in the systems that do not require high capital cost and investment (Nunes, Matias, and Catalão 2014). A secondary combustion chamber is usually inserted in this type of reactor to ensure the complete burnout of the fuel since some of it may remain as unburnt particles exiting from the primary chamber (Strzalka, Erhart, and Eicker 2013). Its capacity varies between 2 kW and 50 MW. The combustion time can be controlled by the movement or vibration of the grate.

A.5.1.2. Vertical reactor

A grate reactor can also take a vertical shape which can be classified as downdraft and updraft (Richardson et al. 2015). They are simple to construct and easy to operate. They provide high

thermal efficiency and they require minimal pretreatment. The vertical shape grate reactors are usually applied at small scale (i.e. <10MW).

As in Figure A4, in both updraft and downdraft vertical reactors, the fuel is fed from the top of the reactor and is dried afterwards. The dried fuel moves downward the reactor to the upper-middle zone where pyrolysis occurs at higher temperature to produce tars along with some gases. The tars and gases then evolve towards the oxidation zone, where gasification or combustion take place depending on the lambda (i.e. the amount of oxidant pumped into the reactor). The ash-formed chemical species move through the reduction zone where H_2 and CO contents are enriched.

Both updraft and downdraft vertical reactors have the same shape; one difference is in the location of the oxidant feed and the exit gas (Richardson et al. 2015). For instance, in the updraft reactor (Figure A4.a), the gaseous product exits from the top of the reactor to provide a countercurrent flow with the fuel. On the other hand, in the downdraft reactor (Figure A4.b), the gaseous product exits from the bottom of the reactor to provide a co-current flow with the fuel. Consequently, in an updraft setup, the condensation of the tars in the vapor is significant as they pass over a relatively cold drying region before reaching the reactor exit. As a result, this setup is rarely used in industry. Nevertheless, it has a low gas exit temperature and a low sensitivity to ash problems since the highest temperature is achieved at the far bottom of the reactor close to the ash discharge point. Consequently, the risk of ash fusion, sticky ash, or solidification of slag and reactor clogging when proceeding to the zone of lower temperature is insignificant.

On the other hand, the oxidant is pumped through a downdraft setup by a nozzle or a throat in the combustion/gasification zone (Figure A4.b). Hence, the highest temperature is around the throat leading to an increase in the ash problems risks (i.e. slag, fusion, etc.). This poses various limitations of scale up related to the throat size (Siedlecki, De Jong, and Verkooijen 2011). It also adds difficulties in handling fuels with high moisture and ash contents (Richardson et al. 2015). In addition, it has low overall thermal efficiency (Richardson et al. 2015). Nevertheless, this type of fixed bed reactors is widely applied due to its clean gas, and low tars and particles contents since the exit gas is in the bottom of the reactor (Richardson et al. 2015).

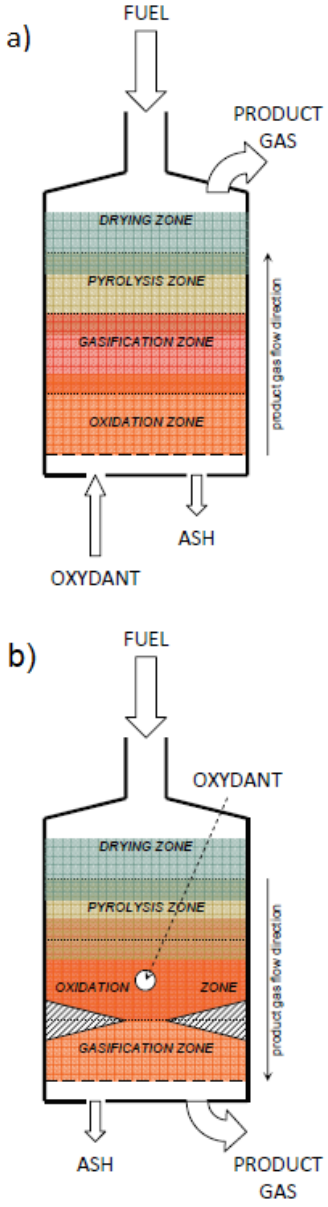

Figure A4: Fixed bed updraft (a) and downdraft (b) reactors (Siedlecki, De Jong, and Verkooijen 2011).

A.5.2. Fluidized bed

Fluidized bed reactors are proving to be one of the best types of reactors that can be used for combustion and gasification for large scale applications due to their flexibility, stability, and efficiency (Luo and Zhou 2012; Richardson et al. 2015).

Figure A5 depicts a scheme of fluidized bed reactor. It is a vessel with a grid at the bottom through which the oxidation agent enters the reactor. Above this grid, the fuel is introduced and mixed with the bed materials. The temperature inside the reactor is controlled by controlling the air/fuel ratio. The high velocity of the oxidation agent drives the fuel upward through a bed of functional materials that consist generally of sand or catalysts. The fuel, the oxidant, and the bed materials are all mixed intensely in a hot circulation zone, hence enhancing the reactions.

Combustion and gasification reactions (i.e. drying, pyrolysis, combustion/gasification, reduction, etc.) happen in the same zone of the reactor. The fuel is pyrolized in the hot bed where chars and gaseous compounds along with tars are formed. The tar further decomposes into gaseous compounds, sometimes in the presence of a catalyst, within the hot bed materials. Hence, the bed not only plays a core role in the reactions but also ensures a homogeneous distribution of temperature inside the reactor which gives the fluidized bed a huge advantage over the fixed bed, especially on large scales (Luo and Zhou 2012). In addition, reactions between the particles in the fluidized bed are more enhanced than in the furnace due to the higher surface contact in the former than the latter (Porbatzki, Stemmler, and Müller 2011).

At the end, the solid particles that exits the reactor mixed with the gas are separated by a cyclone. The former are recycled back to the bottom of the reactor for further reaction. The clean syngas exists from the top of the cyclone.

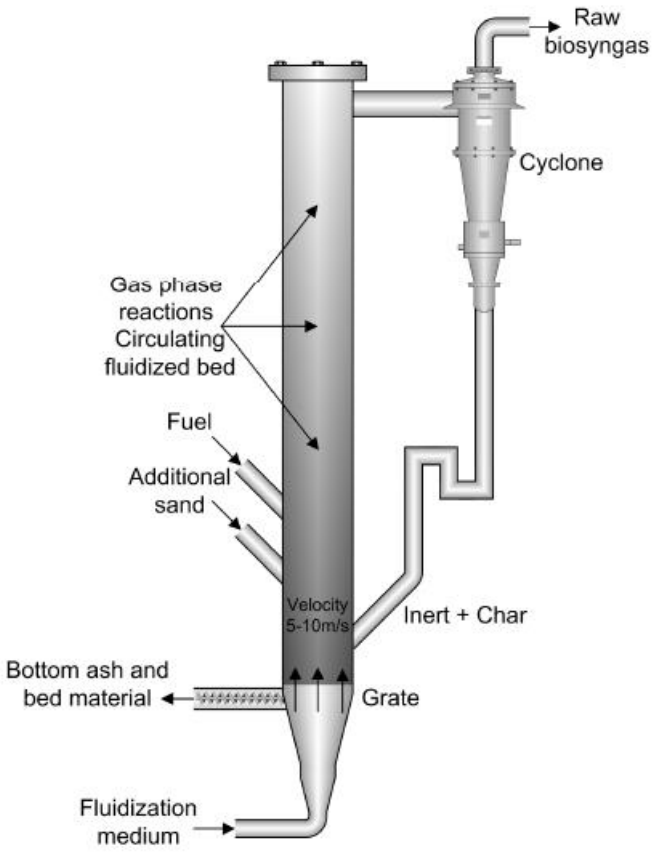

Figure A5: fluidized bed reactor schematic (Siedlecki, De Jong, and Verkooijen 2011).

Depending on the fluidization rate, fluidized bed reactors can be divided into bubbling fluidized bed and circulating fluidized bed. Bubbling bed operates at a relatively low gas velocity (< 1

m/s) while the circulating fluidized bed operates at a higher gas velocities (3-10 m/s) (Siedlecki, De Jong, and Verkooijen 2011).

Flexible feed rate and composition can be applied to a fluidized bed and it can accept fuels with high ash content (Nunes, Matias, and Catalão 2014). It is able to sustain high pressures and has a high volumetric capacity along with easy temperature control (Luo and Zhou 2012). In terms of blended fuel feedstock, fluidized bed reactors were more able to face the ash problems. The presence of bed materials absorbs the agglomeration effect of the ashes and protect the reactor against sintering and corrosion (Miles and Miles 1996). At the same time, it provides uniform mixing (Miles and Miles 1996).

Nevertheless, this type of reactor suffers from several problems. For instance, operating temperature is limited by ash clinkering and bed agglomeration (Balland et al. 2017; Öhman et al. 2000). The output gas is also rich in tars and fine particles and it has a very high temperature (>800 °C) (Luo and Zhou 2012). The carbon content in the fly ash is also high (Luo and Zhou 2012). The presence of chlorine can further enhance corrosion (Luo and Zhou 2012; Siedlecki, De Jong, and Verkooijen 2011).

Catalysts can be applied to faster reach equilibrium in a fluidized bed reactor (Siedlecki, De Jong, and Verkooijen 2011). Due to their geometry and excellent mixing properties, fluidized bed reactors are also very suitable for scaling up and for pressurized operation (Siedlecki, De Jong, and Verkooijen 2011). Additives can be easily applied in these types of reactors and intense mixing allows the application of a wide particle size range (Siedlecki, De Jong, and Verkooijen 2011). Fluidized bed can provide good opportunity for contact between the particles, and hence enhancing the ash reactivity leading to a possible decrease in agglomeration degree (Boström et al. 2012).

A.5.3. Dual fluidized bed

Dual fluidized bed, also called indirectly heated fluidized bed, is an emerging technology that has already been implemented on a demonstration scale and is attracting many researches. Dual fluidized bed is a promising gasification technology for the production of high-quality syngas. According to Figure A6, the dual fluidized bed is basically composed of two fluidized beds. The first is an endothermal fluidized bed gasifier that uses steam as the gasifying agent. The second is an exothermic combustion fluidized bed that provides the heat for the first gasifier bed. The original fuel is gasified in the first bed, from which the ungasified char are circulated to the second bed. These chars are burnt in the second bed in a combustion media, and the

released heat is used to heat up the bed materials and recycle it back to the first gasification chamber. Generally, a bubbling fluidized bed is used in the first gasification bed while a circulating fluidized bed is applied in the second combustion bed (Siedlecki, De Jong, and Verkooijen 2011).

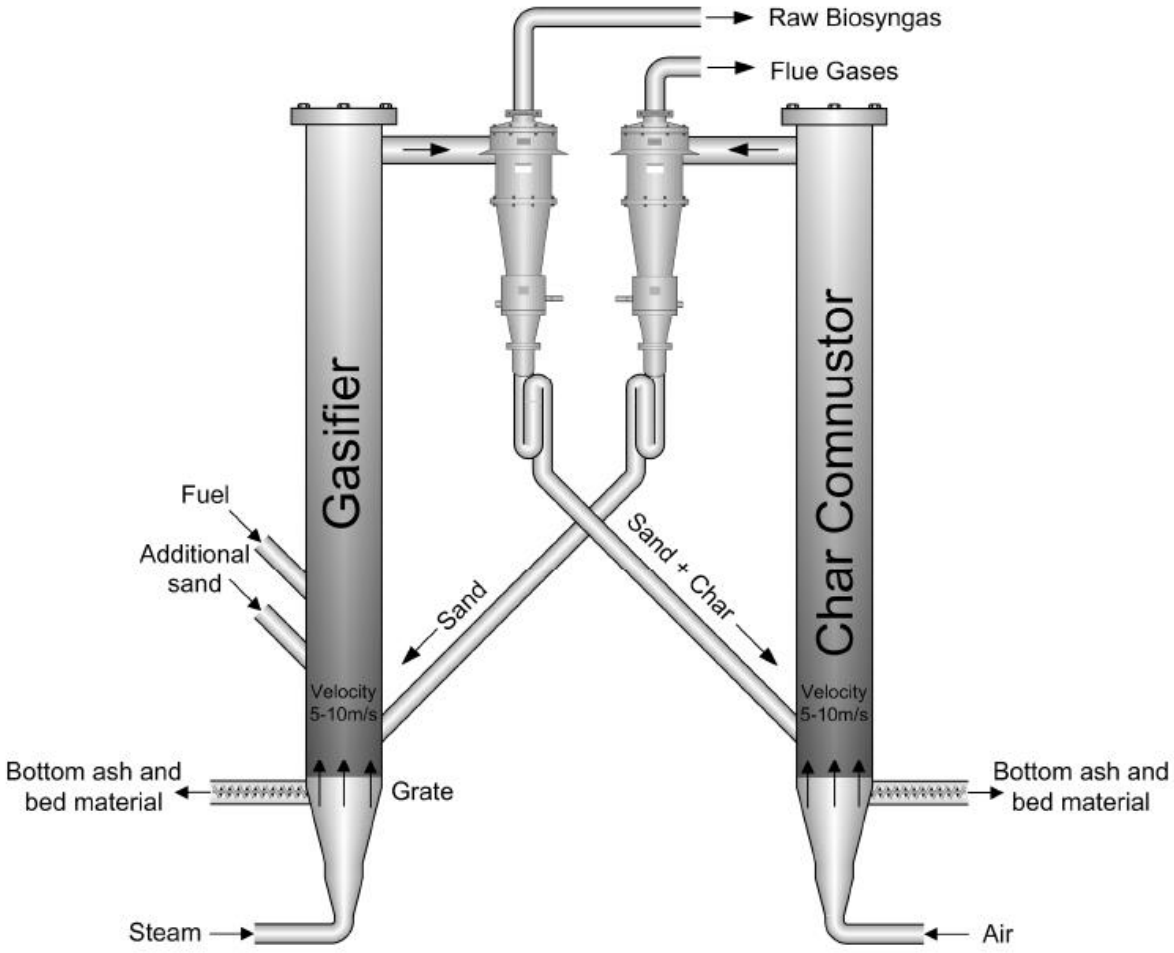

Figure A6: Dual fluidized bed schematic (Siedlecki, De Jong, and Verkooijen 2011).

A.5.4. Entrained flow reactor

Entrained flow reactor (EFR) is the most successful and widely used reactor for large-scale industrial gasification (i.e. >50 MWth) of coal, petroleum coke, and refinery residues (Basu 2010b). EFR generally operates at a temperature of 1400℃ and a pressure ranging from 20 to 70 bar (Basu 2010a). Due to the short residence time (i.e. a few seconds) in the EFR, the fuel need to be very fine and low in moisture contents (Basu 2010b). Hence, the reactor is characterized by a very high fluidization speed that fully entrains the fuel particles (Basu 2010a).

EFR works in a sub-stoichiometric supply of oxygen (Basu 2010b). Hence, as shown in Figure A7, combustion reaction takes place at the entry point of the oxidant where all the fuel particles

start to degrade. Then, it is followed by gasification of the gas and tars since the excess oxygen at the entrance is used up fast at the high temperature of at least 1400℃ (Basu 2010a). This allows the production of high purity gas with nearly tar-free and very low methane contents (Basu 2010b). A very high carbon conversion rate close to 100% can be reached in this type of reactors (Basu 2010b; 2010a). The very hot product gas is generally cooled down in heat exchangers that produce the superheated steam required for gasification.

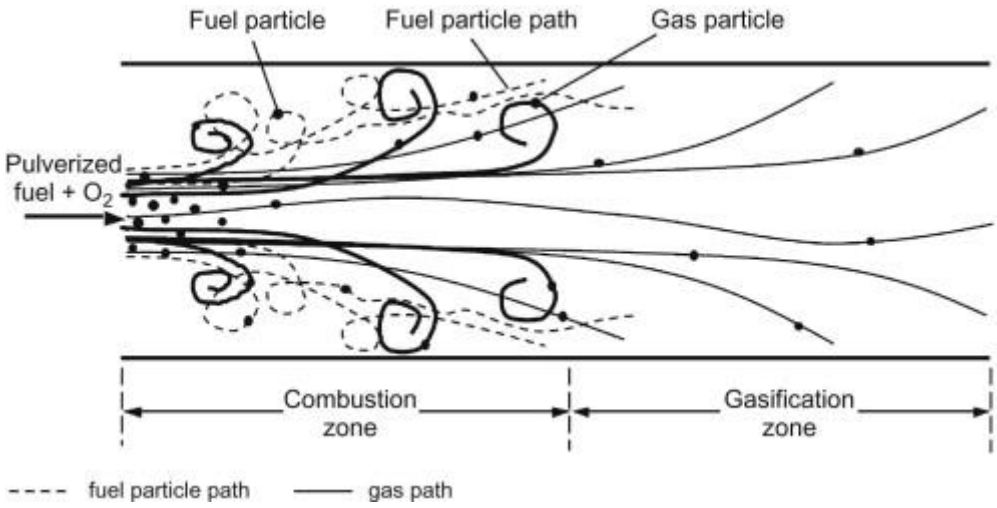

Figure A7: Simplified sketch of gas-solid flow in an entrained flow reactor (Basu 2010b).

In general, two EFR mediums can be used, depending on how and where the fuel is injected into the reactor: side-Fed gasifier (Figure A8) and top-fed gasifier (figure A9) (Basu 2010b). In the side-fed EFR, the powdered fuel and the oxidant are injected through perpendicular nozzles in the lower section of the reactor (Basu 2010b). The two are highly mixed inside the reactor and both flow upwards until they reach the exit. In the upper section of the reactor, the highly available oxygen triggers a rapid exothermic reaction that raises the gas temperature well above the melting point of the ash (i.e.>1400℃) and separate them from the fuel. Consequently, the ash cools down on the walls of the reactor to form of slags.

On the other hand, the top-fed reactor uses a vertical cylinder vessel, in which the fuel is fed with the oxidant from the top. The vessel is a vertical furnace with a downdraft burner (Basu 2010b). Most of the reaction takes place in the upper part of the reactor. The slag ash cools down while flowing on the reactor walls along with the gas. They both exit from the bottom of the reactor.

The gas in the side-fed EFR always exists at lower temperature than the one in the top-fed EFR. The top-fed EFR has several advantages over the side-fed EFR (Basu 2010b):

1. Its axisymmetric construction reduces the equipment cost.

2. Reactants flow from one burner, which reduces the number of burners to be controlled.
3. The product gas and the slag flow in the same direction, which reduces any potential blockage in a slag trap.

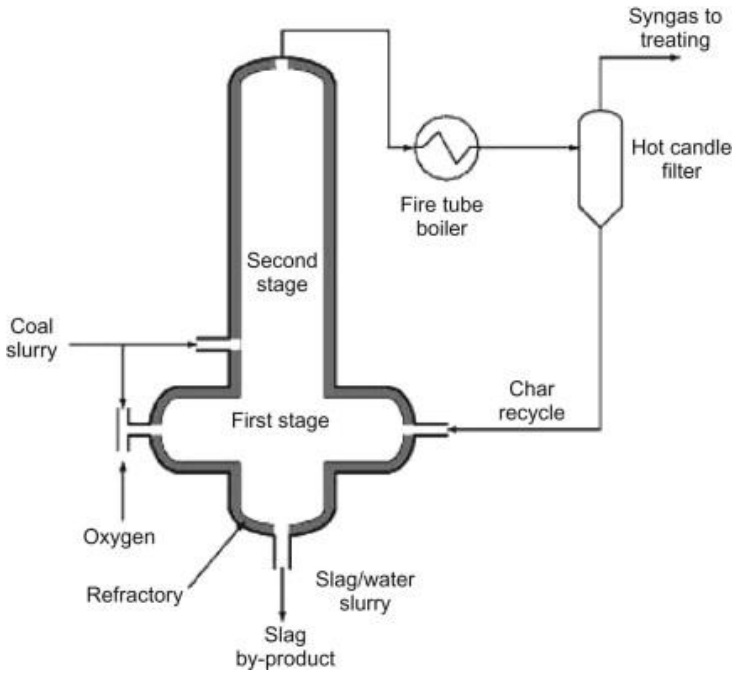

Figure A8: Side-fed entrained flow reactor (Basu 2010b).

.

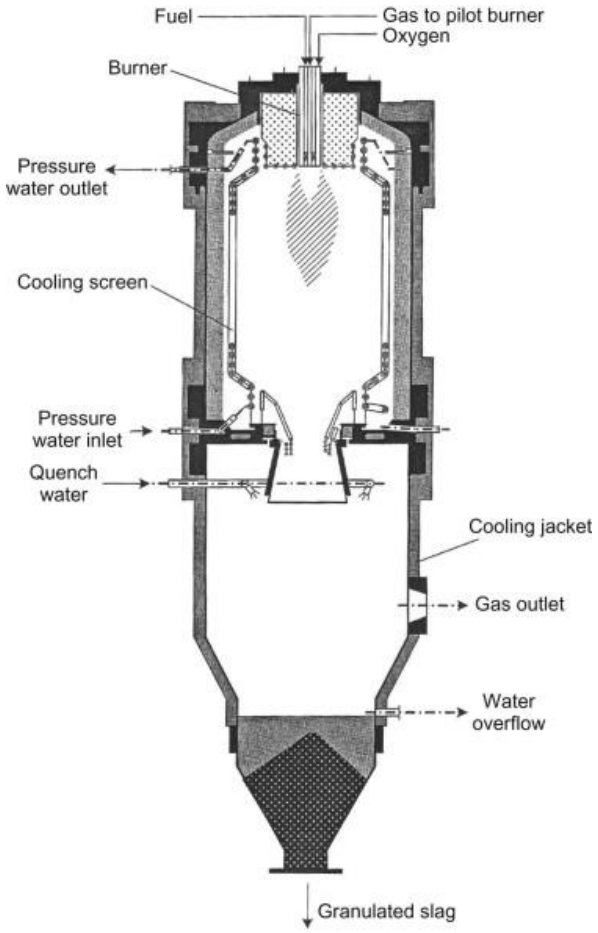

Figure A9: Top-fed entrained flow reactor (Basu 2010b).

In both EFR mediums, the ash behavior can critically affect the EFR performance. As particles impact the wall, they adhere to it in the liquid phase form (molten phase also called slags) to provide smooth particles flow (Troiano et al. 2020; Basu 2010b). The wall can be electrically heated, hence more reaction will take place between the ash and the wall materials (Shannon et al. 2008; Troiano et al. 2020). The wall can also be cooled, hence the oxidizing agent temperature should be close to the liquidus of the ash to provide a smooth flow and minimal ash-wall interactions (Marra et al. 2017). When the thickness of the slag layer reaches a critical value, the fully developed slag layer starts to incorporate some char particles (Troiano et al. 2020; Ma et al. 2016). The latter are trapped but not fully incorporated in the slag (due to interfacial forces), gradually forming a carbon-rich refractory coverage of the slag layer (Montagnaro and Salatino 2010). The formed refractory layer can affect the particles flow and lead to poor reaction.

The main advantages of an EFR over the other types of reactors (Basu 2010b):

1. Low tar production.
2. Accept a wide range of feed (compositions, particle sizes, etc.).

3. Produce ash in the form of slags in both setups.
4. High pressure and temperature operation.
5. Higher carbon conversion.
6. Low methane contents.

The main disadvantages of an EFR over the other types of reactors (Basu 2010b):

1. Residence time is very short so incomplete reactions can easily take place.
2. Biomass application is limited due to their fibrous contents that makes their pulverization hard. Their molten ash is also highly aggressive on the reactor's refractory and metal lining due to their high alkali-metals contents.

A.6. Effect of atmosphere on the ash behavior (combustion versus gasification)

As previously discussed in section 2.1.1., the excess air to fuel ratio (λ) plays a key role in any combustion or gasification processes. When λ is lower than 1 (gasification mode), O_2 is the limiting reactant. Hence, increasing the airflow increases both lambda and ash entrainment effect. The increase in λ will accelerate the combustion front. Consequently, the temperature inside the reactor chamber rises, increasing the ash volatility with it (Royo et al. 2019). As a result, the increased ash entrainment and volatility will decrease the available K, Cl, S, and Na that react with the silicate matrix and the alkaline earth metals inside the reactor chamber. This leads to a decrease in sintering and slagging effect (Royo et al. 2019). However, it can increase corrosion and fly ash deposition.

In contrast, for lambda higher than 1 (combustion mode), O_2 is in surplus. Hence, as lambda increases, ash entrainment effect will still increase due to the velocity increase. However, the ash volatility decreases. This is due to the increase in convective cooling that decreases the reactor temperature (Royo et al. 2019). As a result, entrainment and volatility will counteract. Nevertheless, ash volatility overcomes entrainment in the case of fuels rich in K, Na, and Si (herbaceous fuels) (Royo et al. 2019). In this case, sintering and slagging will overall increase due to the decrease in volatility effect.

The atmosphere plays a crucial role on the oxidation/reduction reactions. In an oxidizing atmosphere (i.e. combustion), the formation of sulfates, carbonates, and silicates is enhanced (Zeng et al. 2016; Boström et al. 2012; Lamberg et al. 2013; Garcia-Maraver et al. 2014). Hence, K and S, for example, will be found more in the bottom ash than in the emissions. However, in the gasification mode, less oxygen is available for inorganic oxidation to happen. Consequently,

more H_2S, SOx, and KCl will be formed and emitted with the syngas (Arvelakis et al. 1999; Porbatzki, Stemmler, and Müller 2011).

A.7. Coal and coal-biomass ash combustion behavior

Coal was one of the earliest main sources of heat and energy in the world. It was discovered and firstly used in china 3000 years ago (coal education 2007). Coal industry boomed in the 18th century in Europe due to the industrial revolution (coal education 2007). Due to its low cost and high abundance, it was widely used for engines and electricity. By the late 20th century, and after the Second World War, coal was widely replaced with fossil fuels and natural gas (coal education 2007). By 2010, coal provided fourth the needed energy, and is expected to provide its third by 2050 (Speight 2011; Suárez-Ruiz and Ward 2008). However, here again, the application of this type of feedstock highly depends on its ash behavior. Consequently, in this section, the combustion ash behavior of coal and its blends with biomass (wood and straw) will be presented, with a minor focus that the section before.

A.7.1. Coal ash behavior

The major oxides found in coal ashes are SiO_2, Al_2O_3, SO_3, CaO, and Fe_2O_3, while the remaining oxides are below 10% in total (Alam et al. 2021). Coal ash is specifically rich in alumina-silicates (Vassilev, Baxter, and Vassileva 2013). Al_2O_3 can increase the ash fusion temperature more than SiO_2 (Niu et al. 2014; Li et al. 2013). Hence, the ash-sintering effect in coal combustion is minimal compared to biomass (Alam et al. 2021). Though, when it happens, the liquid phase ash becomes rich in sulfuric acid and chlorides (Chadwick, Highton, and Lindman 1987). The melting tendencies of coal are simple and well-studied in the literature (Chadwick, Highton, and Lindman 1987). Coal ash combustion melting temperature usually varies between 1100 °C and 1500 °C, depending on the type of coal (Vassilev, Baxter, and Vassileva 2014). The coal ash can be a low-melting temperature ash if the coal has high Ca, Mg, S, Fe, and Na concentrations, as is the case for low-rank brown coal and lignite (Chadwick, Highton, and Lindman 1987). In contrast, it can be categorized as high-melting temperature ash if the concentrations of the same elements are low, as is the case for anthracite and bituminous coal (Chadwick, Highton, and Lindman 1987). The first category ash is generally rich in carbonate, oxides, sulphates, montmorillonite, sulfides, and feldspars (Chadwick, Highton, and Lindman 1987). The second one is rich in illite, kaolinite, quartz, and rutile (Chadwick, Highton, and Lindman 1987).

Despite its low sintering problematics, coal combustion generates a range of dangerous gaseous emissions and particles. Instead of being trapped within the sintered ash, S, Cl, NO_x rich

compounds will escape into the gaseous phase. Hence, coal combustion emissions are rich in acid gases, organic compounds, and particulate matter, such as HCl, H_2S, SO_x, and NO_x (Suárez-Ruiz and Ward 2008; Finkelman et al. 2018). These compounds are detrimental to the reactors and, most importantly, human health and the environment. Furthermore, coal combustion/gasification emits harmful elements such as arsenic, fluorine, selenium, mercury, and lead (Finkelman et al. 2018). Most importantly, due to its high carbon contents, coal combustion emits substantial concentrations of CO_2 (Altawell 2021; Chadwick, Highton, and Lindman 1987). As a result, nowadays, it is becoming a common practice to burn 100% biomass or to co-fire coal with biomass to decrease CO_2 emission and meet the emerging environmental limitations (Xing et al. 2016).

A.7.2. Coal-biomass blend ash behavior

Since the early 1990s, cofiring of coal and biomass was attracting a lot of attention (Miles and Miles 1996). However, this field boomed in 2005 and onwards (Jing et al. 2016). The increasing biomass application in the industry, and the increasing limitations on the coal applications due to its environmental complications, played a crucial factor in this boom (Jing et al. 2016). Co-firing coal with biomass has a crucial effect on diluting sulfur, hence decreasing SO_x emissions (Xing et al. 2016; Fryda et al. 2010). Similarly, mixing biomass with coal decreases the total carbon in the fuel since biomasses are poorer in carbon than coal (Vassilev, Baxter, and Vassileva 2013). As a result, the potential of CO_2 emissions decreases (Jing et al. 2016; Fryda et al. 2010). The blend can also reduce the investment cost since most used biomasses are already wastes (Jing et al. 2016).

However, cofiring coal with biomass has several disadvantages. Biomass has a higher alkali-silicate metals concentration than coal (Vassilev, Baxter, and Vassileva 2013). Hence, mixing coal with biomass lowers the ash melting temperature (Luan, You, and Zhang 2014). This induces several ash-related problems, such as slagging, sintering, deposition, corrosion, and erosion (Xing et al. 2016; Jing et al. 2016). Nevertheless, this ash behavior is highly dependent on the type of the applied biomass, i.e. its ash composition and concentration (Jing et al. 2016). Jing et al. (Jing et al. 2016) found that the sintering temperature decreased with the increase in the percentage of biomass in the blend, irrespective of the type of biomass. This was mainly due to the addition of alkali and alkaline earth metals to the feedstock (Jing et al. 2016). In the biomass, both Ca and K react with aluminosilicates in the coal to form low-temperature eutectics (Jing et al. 2016). Nevertheless, biomass with the highest K and Cl concentrations and the lowest Ca contents always presents the lowest sintering temperature (Jing et al. 2016).

Cofiring coal with wood presented several advantages. After cofiring coal with wood, straw, and miscanthus in a laboratory-scale gasification furnace, Blasting et al. (Bläsing, Hasir, and Müller 2015) found that mixing wood with coal decreased H_2S emissions while keeping KCl and HCl releases low. This is directly related to the low potassium and sulfur concentrations in woody biomasses (Vassilev, Baxter, and Vassileva 2013). Wet wood, which is low in sulfur, can further help reduce the emissions from coal when blended since the former can cool down the fire at the grate. Coal simply raises the temperature in the boiler and thus increases alkali volatilization and the potential for deposits problems (Miles and Miles 1996). On the other hand, the sintering effect is enhanced, and the sintering temperature is lowered as the wooden biomass percentage in the mixture increases (Xing et al. 2016; Yao et al. 2020). For instance, Yao et al. (Yao et al. 2020) measured the sintering temperature in various fractions of wood-coal blends. They have found that 30 wt.% was the limiting wood fraction in the blend to prevent ash-related problems (Yao et al. 2020). When combusted in a bubbling fluidized bed, Wander et al. (Wander et al. 2020) went further down to 15 wt.% of wood in the blend. Mixing sawdust wood with coal also decreased the ash deposition and made the deposit structure looser and easily removable (Wander et al. 2020). This was mainly due to the high contents of silicon and aluminum in the sawdust that have a lower capacity to adhere to surfaces (Wander et al. 2020).

Mixing coal with agricultural residues is more problematic than wood-coal blends. Coal is rich in sulfur and alumina-silicates, while agricultural residues are rich in alkali-silicates (Vassilev, Baxter, and Vassileva 2013). Consequently, mixing agricultural residues, such as miscanthus and wheat straws, with coal will enhance the sintering effect, especially as the agricultural residue fraction increases in the blend (Jing et al. 2016; Bläsing, Hasir, and Müller 2015). Due to the increased sintering effect, more K and S will be retained in the slag, decreasing the KCl, SOx, and H_2S emissions (Bläsing, Hasir, and Müller 2015). Blasing et al. (Bläsing, Hasir, and Müller 2015) reiterated that the ash behavior using mixed feedstock is quite complex and can never be just explained by dilution effects, especially for coal-straw and coal-miscanthus mixtures, i.e. coal-agricultural waste mixtures (Bläsing, Hasir, and Müller 2015). A coal fraction threshold always exists in this type of blends. This threshold plays a major key role on sintering and emissions behavior, and it depends on the coal and biomass ash compositions. Depending on this threshold, the behavior of sintering and emissions can act in the same or the opposite ways. Below this threshold, the slag can retain a significant amount of the emitted particles. However, when this threshold is attained, the slag becomes saturated, and the excess K, Cl, and S compounds will be emitted in the fly ash or TPM.

Appendix B: Thermodynamic databases

In this work, four different thermodynamic databases were equipped with FactSage to conduct the thermodynamic calculations and simulations: FactPS, FToxid, FTsalt, and GTOx. The contents of each database are extracted from FactSage documentation module and the work of Jung et al. (Jung and Van Ende 2020), Bale et al. (Bale et al. 2016), and Lindberg et al. (Lindberg et al. 2013) for the FACT databases, and from the work of Hack et al. (Hack et al. 2012) for GTT database.

B.1. FactPS

FactPS database was used in this work to provide thermodynamic data for all stoichiometric compounds. It contains thermodynamic data of over 4900 stoichiometric phases in solid, liquid, gas, and ionic states (Jung and Van Ende 2020). Their main sources are from JANAF ("NIST-JANAF Table," n.d.) and Barin et al. (Barin 1995) thermodynamic compilations. FactSage team also revised some of the thermodynamic data and stored them in the database after critical evaluation and optimization (Jung and Van Ende 2020; Bale et al. 2016; Lindberg et al. 2013).

B.2. FToxid

FToxid database (also called FACT oxide database) contains thermodynamic data for pure oxides and oxide solid solutions formed by 23 elements (as well as for dilute solutions of S, SO_4, PO_4, H_2O/OH, CO_3, F, Cl, and I in the molten slag phase). In addition, the FToxid database contains the molten slag phase, numerous extensive ceramic solid solution phases, and all available stoichiometric compounds containing SiO_2-CaO-MgO-Al_2O_3-FeO-Fe_2O_3-MnO-TiO_2-Ti_2O_3-CrO-Cr_2O_3-ZrO_2-NiO-CoO-Na_2O-K_2O-Li_2O-B_2O_3-P_2O_5-Cu_2O-As_2O_3-GeO_2-PbO-SnO-ZnO (Jung and Van Ende 2020; Bale et al. 2016; Lindberg et al. 2013).

Al_2O_3-CaO-FeO-Fe_2O_3-MgO-MnO-SiO_2 system has been fully optimized from 25 C to above liquidus temperatures at all compositions and oxygen partial pressures (Jung and Van Ende 2020). Components like B_2O_3, K_2O, Na_2O, Li_2O, CoO, CrO, Cr_2O_3, P_2O_5, Cu_2O, NiO, PbO, SnO, TiO_2, Ti_2O_3, ZnO, and ZrO_2 were added to this core seven-component system, and the relevant subsystems were optimized over composition ranges important for industrial applications (Jung and Van Ende 2020). The molten slag phase is described using the modified quasichemical model (MQM) (Jung and Van Ende 2020; Bale et al. 2016; Lindberg et al. 2013). The S and F content in molten oxide slag is extended up to pure sulfide and fluoride using the new two-sublattice MQM (Jung and Van Ende 2020; Bale et al. 2016; Lindberg et al. 2013). The dilute solubility of gaseous species such as SO_4, H_2O, OH, C, CO_3, CN, Cl, and I are also modeled using the Blander-Reddy Model (Jung and Van Ende 2020). The extensive solid

solutions such as spinel, olivine, melilite, pyroxenes, monoxide, perovskite, wollastonite, etc. are modeled in the framework of the CEF, taking into account the crystal structure of each solution (Jung and Van Ende 2020). Over 80 solid oxide solutions are available in the FToxid database (Jung and Van Ende 2020; Bale et al. 2016; Lindberg et al. 2013).

B.3. FTsalt

The FTsalt databases was used to add data for pure salts and salt solutions of 27 main cations (Li^+, Na_+, K_+, Rb_+, Cs_+, Mg_{2+}, Ca_{2+}, Sr_{2+}, Ba_{2+}, Mn_{2+}, Al_{3+}, Fe_{2+}, Fe_{3+}, Co_{2+}, Ni_{2+}, Zn_{2+}, Pb_{2+}, La_{3+}, Ce_{3+}, Th_{4+}, U_{3+}, U_{4+}, Pu_{3+}, Pu_{4+}, Cr_{2+}, Cr_{3+}, Mo_{5+}) and 9 main anions (F, Cl, Br, I, NO_3, NO_2, OH, CO_3^2, SO_4^2) (Jung and Van Ende 2020; Bale et al. 2016; Lindberg et al. 2013). The salts are widely found in biomass ash and can lead to corrosion in combustion reactors. Dilute amounts of O^2 and OH are also allowed in the molten salt phase (Jung and Van Ende 2020; Bale et al. 2016; Lindberg et al. 2013). A wide range of F and Cl systems are covered (Jung and Van Ende 2020). Systems made with a certain combination of F and Cl with Br, I, NO_3, OH, CO_3^2, and SO_4^2 are available (Jung and Van Ende 2020; Bale et al. 2016; Lindberg et al. 2013). Recent molten salt nuclear reactor is also covered with a specialized liquid solution of Li_+, Th_{4+}, U_{3+}, U_{4+}, Pu_{3+}, Pu_{4+}, Cr_{2+}, Cr_{3+}, Ni_{2+}, Mo_{5+} // F (Jung and Van Ende 2020; Bale et al. 2016; Lindberg et al. 2013).

B.4. GTOX

GTOX database was used in this work as an alternative for the FToxid database. The first was developed by the GTT team in Jülich in Germany in 2018 (Hack et al. 2012) while the Canadian FACT team established the second based on the recent Ph.D. thesis of Kim in 2017 (D.-G. Kim et al. 2017; D. Kim 2017). According to Hack et al. (Hack et al. 2012), FToxid lacks in the accessibility of the Gibbs energy parameters and shows remarkable deviation from experimental information, especially for systems with K_2O.

GTOX thermodynamic database contains calculated phase diagrams and thermodynamic properties for any composition and temperature for the system CaO-MgO-Al_2O_3-CrOx-FeO_x-K_2O-Na_2O-SiO_2 (Hack et al. 2012). More details for the solution (LIOS) and the compounds contained in this database are provided below.

GTOX	LIOS: Slag (Na_2O, Al_2O_3, K_2O, $K_4Si_2O_6$, $K_2Si_2O_5$, $K_2Si_4O_9$, Si_2O_4, P_2O_5, Ca $(PO_3)_2$, $Ca_2O_7P_2$, $Ca_3(PO_4)_2$, KPO_3, K_3PO_4, $K_4P_2O_7$, $CaKP_3O_9$, $KPMgO_4$, $KMgP_3O_9$) MeO: (Al^{3+},Ca^{2+},Fe^{2+},Fe^{3+},Mg^{2+},Va, Cr^{3+},Na^{+1},Mn^{+2},Mn^{+3},Zn^{2+})1(O^{2-})1 WOLL: Wollastonite (Ca^{2+}, Fe^{2+}, Mg^{2+}, Mn)1(Si)1(O)3 CLIN: CLINO_PYROXENE (Ca^{2+}, Fe^{2+}, Mg^{2+})1(Fe^{2+}, Mg^{2+})1(Si^{4+})2(O^{2-})6 NEKS: Nepheline NaAlSiO4-LT with solubility for K_2O.

	Al^{3+}:Va:Na^{1+}:O^{2-}, Al^{3+}:Va:Va:O^{2-}, Si^{4+}:Va:Na^{1+}:O^{2-}, Si^{4+}:Va:Va:O^{2-}, Si^{4+}:Va:K^{1+}:O^{2-}, Al^{3+}:Va:K^{1+}:O^{2-} GARN: Garnet Al^{+3}:Ca^{+2}:Si^{+4}:O^{-2}, Fe^{+3}//Ca^{+2}//Si^{+4}//O^{-2} OLIV: Olivine Ca^{+2}:Ca^{+2}:Si^{+4}:O^{-2}, Ca^{+2}:Fe^{+2}:Si^{+4}:O^{-2}, Ca^{+2}:Mg^{+2}:Si^{+4}:O^{-2}, Fe^{+2}: Ca^{+2}:Si^{+4}:O^{-2}, .. K3PM: K3P_MT K_3PO_4-MT with solubility for CaO and MgO. $(K_2O)_2(P_2O_5)(K_2O,CaO,K_2CaO_2,MgO,K_2MgO_2)$ FSPA Feldspar in Al2O3- K_2O -Na_2O-Fe_2O_3-SiO_2 system. $(Al^{3+},Fe^{3+})_1(K^{+1},Na^{+1})_1(Si^{+4})_3(O^{-2})_8$ HEXA: Hexagonal $(Ca^{+2},K^{+1},Mg^{+2},Na^{+1},Va)(S^{-2},SO_4^{-2})$

Appendix C

All the experimental simulation conducted in the appendix were done using just the mixture BCWC (called sometimes MP2b). This decision was made to simplify the discussion. The behavior of the other mixtures was the same.

C.1. The effects of each elements on the results of the global simulations ($K_2Ca_2Si_2O_7$ destabilization)

In chapter 3, some differences were observed when comparing the global simulation results in Figures 2.b and 2.d (using three oxides) against those in Figure 4.c and 4.g (using all elements) in the pellet test. $K_2Ca_2Si_2O_7$ was present among the phases predicted by the simulations in Figure 2.b (using only 3 oxides), while it was absent from the predicted results using all elements (Figure 4.c) at the expense of more liquid and Ca_2SiO_4 contents. This was similar in the ash test simulations (Figures 2.a vs 4.d). In parallel, the overall K volatilization was higher in the pellet test simulations using full elements simulations (Figure 4.g) than using the three oxides case (Figure 2.d). However, K volatilization in the three elements simulation in the ash test was negligible (Figure 2.c) compared to a minor one in the case of the full elements simulations (Figure 4.h). As a result, it was clear that another inorganic element (i.e. S, Cl, Na, Mg, P, Fe, or Mn) was affecting K volatility and destabilizing $K_2Ca_2Si_2O_7$.

To further investigate this effect, simulations were repeated, adding one element X (X denoted Mn, Na, Fe, Al, S, Mg, Cl, and P) to the combination C, H, O, N, Ca, K, and Si. FToxid oxide solution Slag A was always used. From the results in Appendix A.1, the addition of each new element X led to the addition of crystalline solids and solutions linked to it, like $KAlSiO_4$ and $KAlO_2$ in the case of Al (i.e. for the CHNOCaKSiAl system), $Ca_3Fe_2Si_3O_{12}$ in the case of Fe (CHNOCaKSiFe), etc. (Figure C1). Nevertheless, this single addition kept $K_2Ca_2Si_2O_7$ stable and K volatility immovable. Hence, additional elements were added simultaneously, and the results are shown in Figures C2 to C5. To simplify the comparison of these results, Table C1 was set in place. This Table showed the comparison between the individual addition of Na, P, Cl, and Mg to the set of elements (called best_O7) that consisted of Ca, K, Si, S, Fe, Al, and

Mn. In this set (i.e. best_O7), the main phases (i.e. Ca_2SiO_4, Slag, $K_2Ca_2Si_2O_7$, and $K_2Ca_6Si_4O_{15}$) were all present and stable in the experimental simulations at 1000 °C.

From Figure C2, the addition of Na did not disturb the equilibrium. The results were identical to the one without Na. However, Na presence added four solid solutions that consisted mainly of Na compounds, as elaborated in the legend of Table C1.

However, from the results in Figures C3 to C5, the individual addition of P or Cl or Mg disequilibrate the ternary phase $K_2Ca_2Si_2O_7$ (O7) and the $CaAl_6O_{10}$ - $CaFe_6O_{10}$ single solid solution. The addition of Mg further destabilized the FTOXID-Mel_A solid solution consisting of $Ca_2MgSi_2O_7$, $Ca_2FeSi_2O_7$, $Ca_2Al_2SiO_7$, $Ca_2ZnSi_2O_7$, $Pb_2ZnSi_2O_7$ (Figure C3). The addition of Mg also added the SPINB phase, $Ca_3MgSi_2O_8$(s), and FTOXID-Bred that consists of $Ca_7Mg(SiO_4)4$ and $Ca_3Mg_5(SiO_4)4$ (Figure C3).

The addition of P or Cl added $K_4Ca_3Al_{10}O_{20}$(s) and the FToxid-WOLLA that contains $MgSiO_3$, $FeSiO_3$, $CaSiO_3$, $MnSiO_3$. The addition of P also added $Ca_5HO_{13}P_3$(s) and K_3PO_4(s2) (Figure C4), while the addition of Cl added the FToxid-SPINB that contains Mn, Fe, Al, Mg, and Cr oxides in addition to the two previous phases (Figure C5). Furthermore, in these two cases, the destabilization of the O7 phase occurred in parallel with the appearance of $CaSiO_3$ and the suck of K into the $K_4Ca_3Al_{10}O_{20}$.

It should be noted that the addition of Mn kept Ca_2SiO_4 but shifted its structure from b2C2SC that contains K and Li to bC2SA that contains Mn.

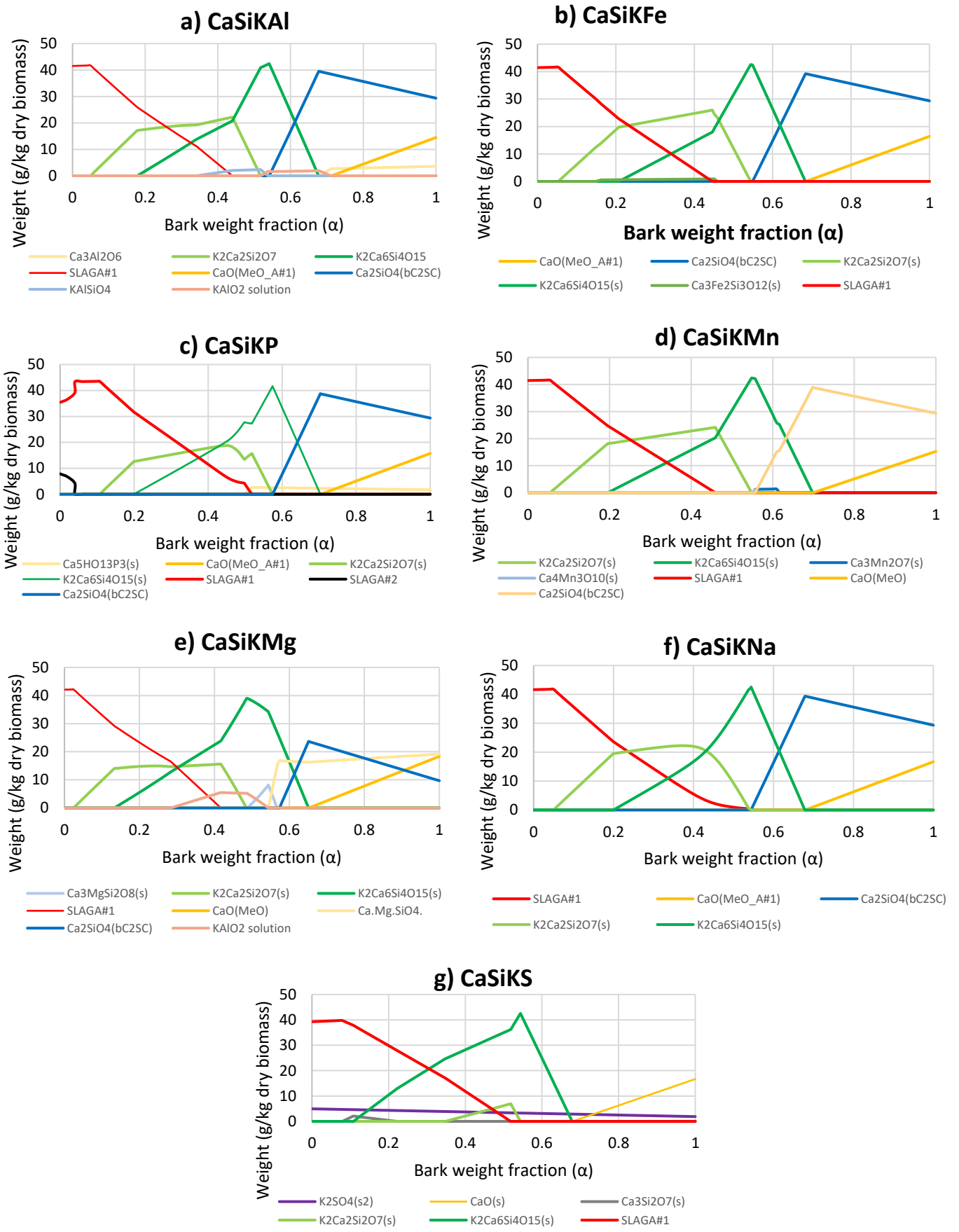

Figure C1: Global simulation results using Ca, K, and Si in addition to one element at a time a) Al, b) Fe, c) P, d) Mn, e) Mg, f) Na, g) S.

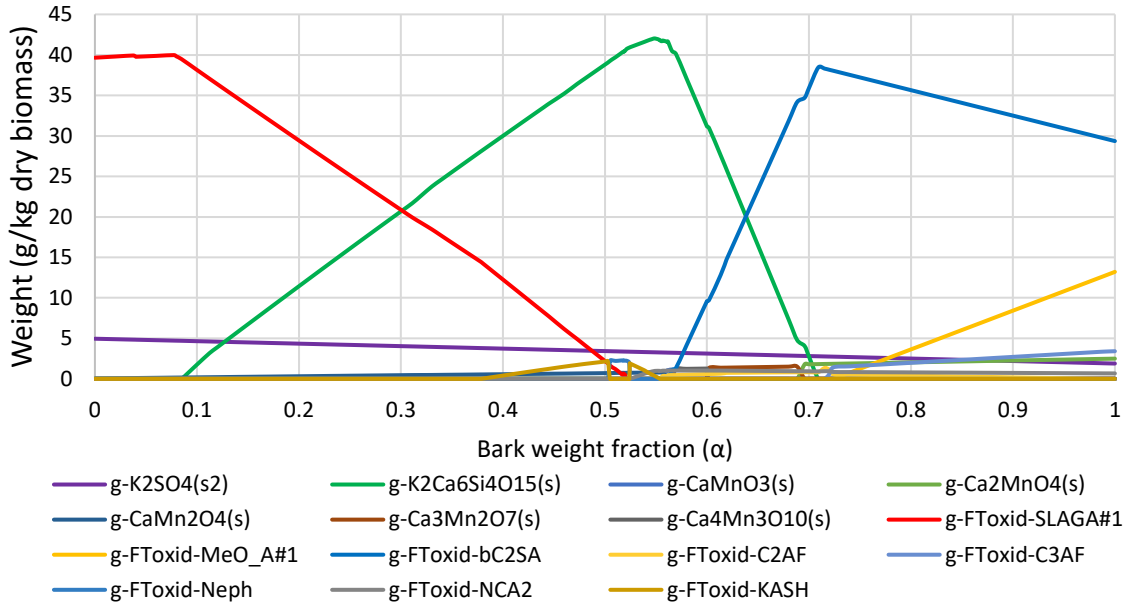

Figure C2: Crystalline phases and solutions weight versus Alpha (bark weight fraction) using Ca, K, Si, S, Al, Fe, Mn, and Na in the experimental simulations.

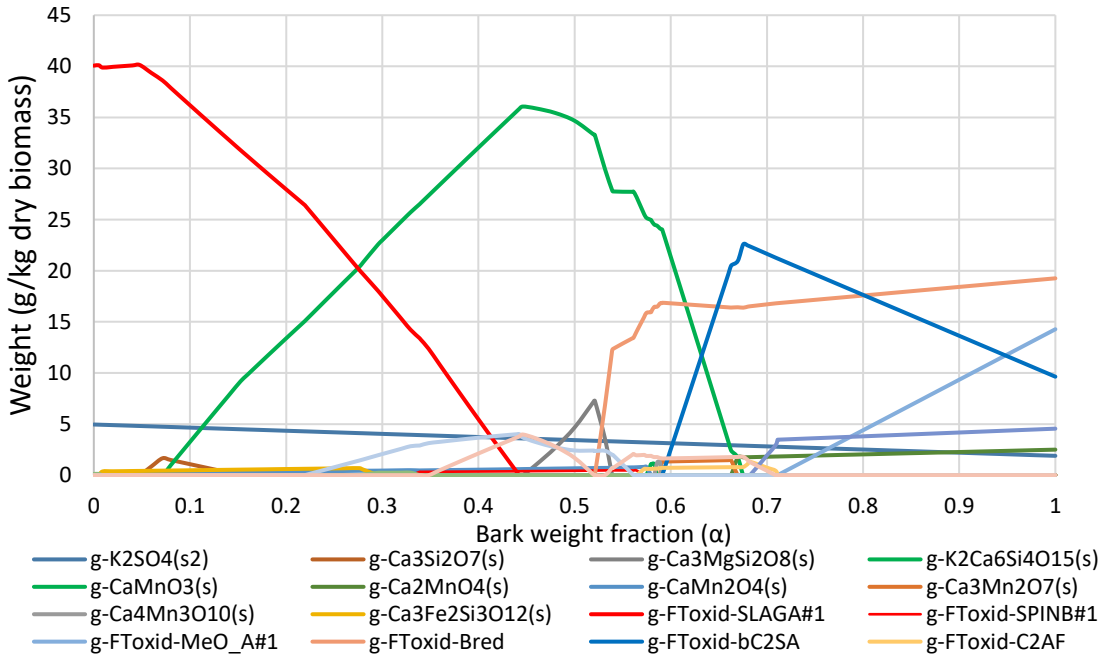

Figure C3: Crystalline phases and solutions weight versus Alpha (bark weight fraction) using Ca, K, Si, S, Al, Fe, Mn, and Mg in the experimental simulations.

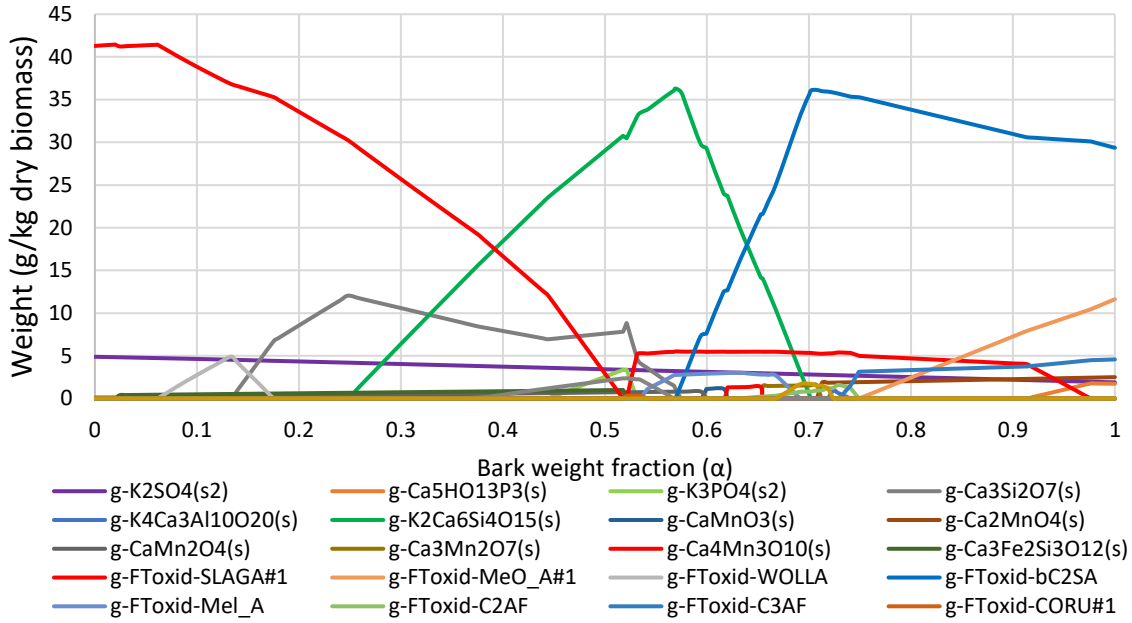

Figure C4: Crystalline phases and solutions weight versus Alpha (bark weight fraction) using Ca, K, Si, S, Al, Fe, Mn, and P in the experimental simulations.

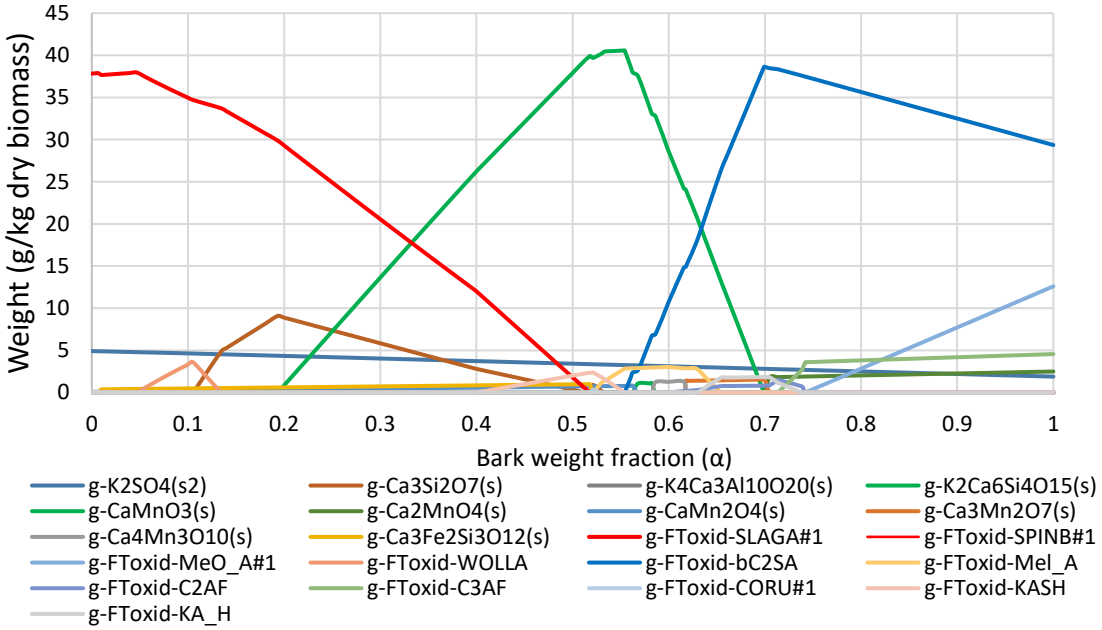

Figure C5: Crystalline phases and solutions weight versus Alpha (bark weight fraction) using Ca, K, Si, S, Al, Fe, Mn, and Cl in the experimental simulations.

Table C1: Crystalline phases and solutions present in the produced ash in the process simulation with respect to each elemental combination.

Ca, K, Si	Ca, K, Si, Al, S, Fe, Mn	Ca, K, Si, Al, S, Fe, Mn, and Na	Ca, K, Si, Al, S, Fe, Mn, and P	Ca, K, Si, Al, S, Fe, Mn, and Cl	Ca, K, Si, Al, S, Fe, Mn, and Mg	Full Elements
	g-K2SO4(s2)	g-K2SO4(s2)	g-K2SO4(s2)	g-K2SO4(s2)	g-K2SO4(s2)	g-K2SO4(s2)
	g-Ca3Si2O7(s)	g-Ca3Si2O7(s)	g-Ca3Si2O7(s)	g-Ca3Si2O7(s)	g-Ca3Si2O7(s)	g-Ca3Si2O7(s)
g-K2Ca2Si2O7(s)	g-K2Ca2Si2O7(s)	g-K2Ca2Si2O7(s)				
g-K2Ca6Si4O15(s)	g-K2Ca6Si4O15(s)	g-K2Ca6Si4O15(s)	g-K2Ca6Si4O15(s)	g-K2Ca6Si4O15(s)	g-K2Ca6Si4O15(s)	g-K2Ca6Si4O15(s)
	g-CaMnO3(s)	g-CaMnO3(s)	g-CaMnO3(s)	g-CaMnO3(s)	g-CaMnO3(s)	g-CaMnO3(s)
	g-Ca2MnO4(s)	g-Ca2MnO4(s)	g-Ca2MnO4(s)	g-Ca2MnO4(s)	g-Ca2MnO4(s)	g-Ca2MnO4(s)
	g-CaMn2O4(s)	g-CaMn2O4(s)	g-CaMn2O4(s)	g-CaMn2O4(s)	g-CaMn2O4(s)	g-CaMn2O4(s)
	g-Ca3Mn2O7(s)	g-Ca3Mn2O7(s)	g-Ca3Mn2O7(s)	g-Ca3Mn2O7(s)	g-Ca3Mn2O7(s)	g-Ca3Mn2O7(s)
	g-Ca4Mn3O10(s)	g-Ca4Mn3O10(s)	g-Ca4Mn3O10(s)	g-Ca4Mn3O10(s)	g-Ca4Mn3O10(s)	g-Ca4Mn3O10(s)
	g-Ca3Fe2Si3O12(s)	g-Ca3Fe2Si3O12(s)	g-Ca3Fe2Si3O12(s)	g-Ca3Fe2Si3O12(s)	g-Ca3Fe2Si3O12(s)	g-Ca3Fe2Si3O12(s)
g-FToxid-SLAGA#1	g-FToxid-SLAGA#1	g-FToxid-SLAGA#1	g-FToxid-SLAGA#1	g-FToxid-SLAGA#1	g-FToxid-SLAGA#1	g-FToxid-SLAGA#1
g-CaO(s)	g-FToxid-MeO_A#1	g-FToxid-MeO_A#1	g-FToxid-MeO_A#1	g-FToxid-MeO_A#1	g-FToxid-MeO_A#1	g-FToxid-MeO_A#1
g-FToxid-bC2SC	g-FToxid-bC2SA	g-FToxid-bC2SA	g-FToxid-bC2SA	g-FToxid-bC2SA	g-FToxid-bC2SA	g-FToxid-bC2SA
	g-FToxid-Mel_A	g-FToxid-Mel_A	g-FToxid-Mel_A	g-FToxid-Mel_A		g-FToxid-Mel_A
	g-FToxid-CAF3	g-FToxid-CAF3				g-FToxid-CAF3
	g-FToxid-C2AF	g-FToxid-C2AF	g-FToxid-C2AF	g-FToxid-C2AF	g-FToxid-C2AF	g-FToxid-C2AF
	g-FToxid-C3AF	g-FToxid-C3AF	g-FToxid-C3AF	g-FToxid-C3AF	g-FToxid-C3AF	g-FToxid-C3AF
	g-FToxid-CORU#1	g-FToxid-CORU#1	g-FToxid-CORU#1	g-FToxid-CORU#1	g-FToxid-CORU#1	g-FToxid-CORU#1
	g-FToxid-KASH	g-FToxid-KASH	g-FToxid-KASH	g-FToxid-KASH	g-FToxid-KASH	g-FToxid-KASH
	g-FToxid-KA_H	g-FToxid-KA_H	g-FToxid-KA_H	g-FToxid-KA_H	g-FToxid-KA_H	g-FToxid-KA_H
		g-FToxid-NAF6				g-FToxid-NAF6
		g-FToxid-Neph				
		g-FToxid-NAShA				
		g-FToxid-NCA2				g-FToxid-NCA2

			g-Ca5HO13P3(s) g-K3PO4(s2) **g-K4Ca3Al10O20(s)** **g-FToxid-WOLLA**	**g-K4Ca3Al10O20(s)** **g-FToxid-WOLLA**		g-Ca5HO13P3(s) g-FToxid-WOLLA
				g-FToxid-SPINB#1	g-FToxid-SPINB#1	
					g-Ca3MgSi2O8(s) g-FToxid-Bred	g-Ca3MgSi2O8(s) g-FToxid-Bred
						g-FToxid-SLAGA#2

List of solutions compositions:

- [FToxid-bC2SC] {C-a'(Ca,Sr,Ba)2SiO4} : OXIDE solution alpha-prime (Ca,Sr,Ba)2SiO4 Ca2SiO4 + (Mg2SiO4, Fe2SiO4, K4SiO4, Li4SiO4, Ca3B2O6 in dilute amounts). Ca2SiO4 must be present. End-members in pure compound database FToxidBase.cdb: Ca2SiO4(S2).
- [FToxid-bC2SA] {A-a'(Ca,Sr,Ba)2SiO4}: OXIDE solution alpha-prime (Ca,Sr,Ba)2SiO4 Ca2SiO4 - Sr2SiO4 - Ba2SiO4 solution + (Mg2SiO4, Fe2SiO4, Mn2SiO4, Pb2SiO4, Zn2SiO4, Ca3B2O6 in dilute amounts). Ca2SiO4, Sr2SiO4 or Ba2SiO4 must be present. End-members in pure compound database FToxidBase.cdb: Ca2SiO4(S2), Sr2SiO4(S2) and Ba2SiO4(S1).
- KASH: KAlSiO4
- KA_H: KAlO2

- [FToxid-NAF6] : Na2Al12O19 with Na2Fe12O19 in solution (Na2Al12O19-rich)
- [FToxid-Neph] Nepheline: Non-stoichiometric low-temperature NaAlSiO4 - KAlSiO4 solid solution, dissolving excess SiO2, Ca and Fe. Miscibility gap below ~1000 °C.
- [FToxid-NAShA] A-(Na,Li)(Al,Fe)O2-HT: Non-stoichiometric high-temperature (Na)(Al,Fe)O2 with excess SiO2. End-members in pure compound database FToxidBase.cdb: NaAlO2(S2) and NaFeO2(S2).
- [FToxid-NCA2] Na2CaAl4O8: Na2CaAl4O8 solid solution Na2(Na2,Ca)Al4O8.

- [FToxid-CAF3] {Ca(Al,Fe)6O10}: OXIDE solution CaAl6O10 - CaFe6O10 solid solution. The pure end-member components are not stable. This solution only exists as a stable phase when both Al and Fe are present.

- [FToxid-WOLLA]: MgSiO3, FeSiO3, CaSiO3, MnSiO3.

- [FToxid-SPINB] B-Spinel {OXIDE Spinel (Cubic)}: AB2O4 cubic spinel containing Mn(II)-Mn(III)-Mn(IV)-Fe(II)-Fe(III)-Cr(II)-Cr(III)-Mg(II)-Al(III)-O

  Mineralogical names: Magnetite (Fe3O4), Manganoferrite (MnFe2O4), Manganochromite (MnCr2O4), Chromite (FeCr2O4), Galaxite (MnAl2O4).

  Oxides of elements other than Mn, Fe, Cr, Mg and Al are not components of FToxid-SPINB, and so the calculated contents of any other oxides will always be zero if you use FToxid-SPINB. For systems containing other oxides, use FToxid-SPINA. Evaluated and optimized over all compositions. FToxid-SPINB replaces FToxid-AlSp, which has been eliminated in FactSage 7.3.

- [FToxid-Mel_A] {A-Melilite}OXIDE solution melilite: End-members in pure compound database FToxidBase.cdb: Ca2MgSi2O7, Ca2FeSi2O7, Ca2Al2SiO7, Ca2ZnSi2O7, Pb2ZnSi2O7.

- [FToxid-Bred]: Ca7Mg(SiO4)4, Ca3Mg5(SiO4)4

- [FTsalt-B1] Rocksalt {ROCKSALT SOLID SOLUTION}
  (Rocksalt Strukturbericht : FCC_B1; Pearson : cF8; Space group : Fm-3m (225); prototype : NaCl)
  (Li,Na,K,Rb,Cs,Cu(I),Ag,Mg,Ca,Sr,Ba,Mn,Fe(II),Co,Ni,Cu(II),Zn,Fe(III),Al,Va){H[-], F,Cl,Br,I,C2[2-],O,OH,NO3}
  Important : Possible 2- and 3-phase miscibility gaps. Use J option.
  This Rocksalt-FCC-B1 solid solution was previously divided into many differently named solution models without common intersolubility. This new solid solution includes the hydrides, fluorides, chlorides, bromides, iodides, acetylides, hydroxides and nitrates (with several oxides) of Li, Na, K, Rb, Cs, with solubilities of Mg, Ca, Sr and Ba. Minor solubility of the transition metals and Ag have also been added. Not all binary and ternary sub-systems have been evaluated and optimized. Sub-systems which have not been evaluated and optimized have been approximated.

- [FTsalt-hP22] alpha-K2SO4
  A SOLID SOLUTION WITH THE alpha-K2SO4 STRUCTURE
  (alpha-K2SO4 Pearson : hP22; Space group : P63/mmc (194); prototype : K2SO4)
  (Li,Na,K,Ag,Va,Ca,Ba,Mg)2{SO4,CO3,S[2-],CrO4}
  Important : Possible miscibility gaps. Use I option.
  This solid solution contains the sulfates, carbonates, sulfides and chromates of Li, Na, K, Ag, Ca, Ba and Mg. Not all binary and ternary sub-systems have been evaluated and optimized. Sub-systems which have not been evaluated and optimized have been approximated.

- Salg A: all oxides +S
  Solution Phase FToxid-SLAG
  -Slag-liq oxide Al,As,B,Ba,Ca,Co,Cr,Cu,Fe,Ge,K,Li,Mg,Mn,Na,Ni,P,Pb,Si,Sn,Sr,Ti,Zn,Zr+
  dilute S and F (Mis.gap at high SiO2, use [I] option).
  The components in FToxid-SLAGA for the current calculation are: Na2O, K2O, Al2O3, SiO2, NaAlO2, KAlO2, CaO, FeO, Fe2O3, MgO, MnO, Mn2O3, Na2S, K2S, Al2S3, SiS2, NaAlS2, KAlS2, CaS, FeS, Fe2S3, MgS, MnS, Mn2S3, NaFeO2, P2O5, NaFeS2, P2O3S2, KFeO2, KFeS2, K2MgSiO4, K2MgSiS4

- Salg B with SO4
  Solution Phase FToxid-SLAG
  -Slag-liq oxide Al,As,B,Ca,Co,Cr,Cu,Fe,Ge,K,Mg,Mn,Na,Ni,Pb,Si,Sn,Ti,Zn,Zr.+dilute
  S,SO4,PO4,H2O/OH,CO3,F,Cl,I,C,N,CN (Mis.gap at high SiO2, use [I] option).
  The components in FToxid-SLAGB for the current calculation are: MgO, MnO, Na2O, SiO2, CaO, Al2O3, K2O, Fe2O3, MnSO4, Fe2(SO4)3, Na2SO4, K2SO4, CaSO4, MgSO4

C.2. FTSalt addition to FToxid and FactPS in the experimental simulations

From Figure C6, adding FTsalt database to the ash test simulation at 1000 °C introduced two differences in the predicted results, without affecting the condensed phases:

1. K_2SO_4 existed as a single compound without FTSALT while it was present in a solid solution called FTsalt-hP22-1 when FTsalt was added.
2. CaO in no FTsalt was replaced by FTsalt-B1-1 solid solution that contains CaO, lime as a major component.

The exact composition of each solid solution is shown in Table C1. From Figures C6.a and C6.c, K_2SO_4 and FTsalt-hP22-1 were superposed, the same case for CaO and FTsalt-B1-1. No differences were also found in terms of volatilization with and without FTsalt.

In conclusion, there is no important effect of taking into account for adding the FTsalt database. This is normal because most of the FTsalt phases are stable at lower temperature (carbonates, chlorides and sulphates). It is therefore advisable to use FTsalt for calculations at lower temperatures or for calculations versus temperature.

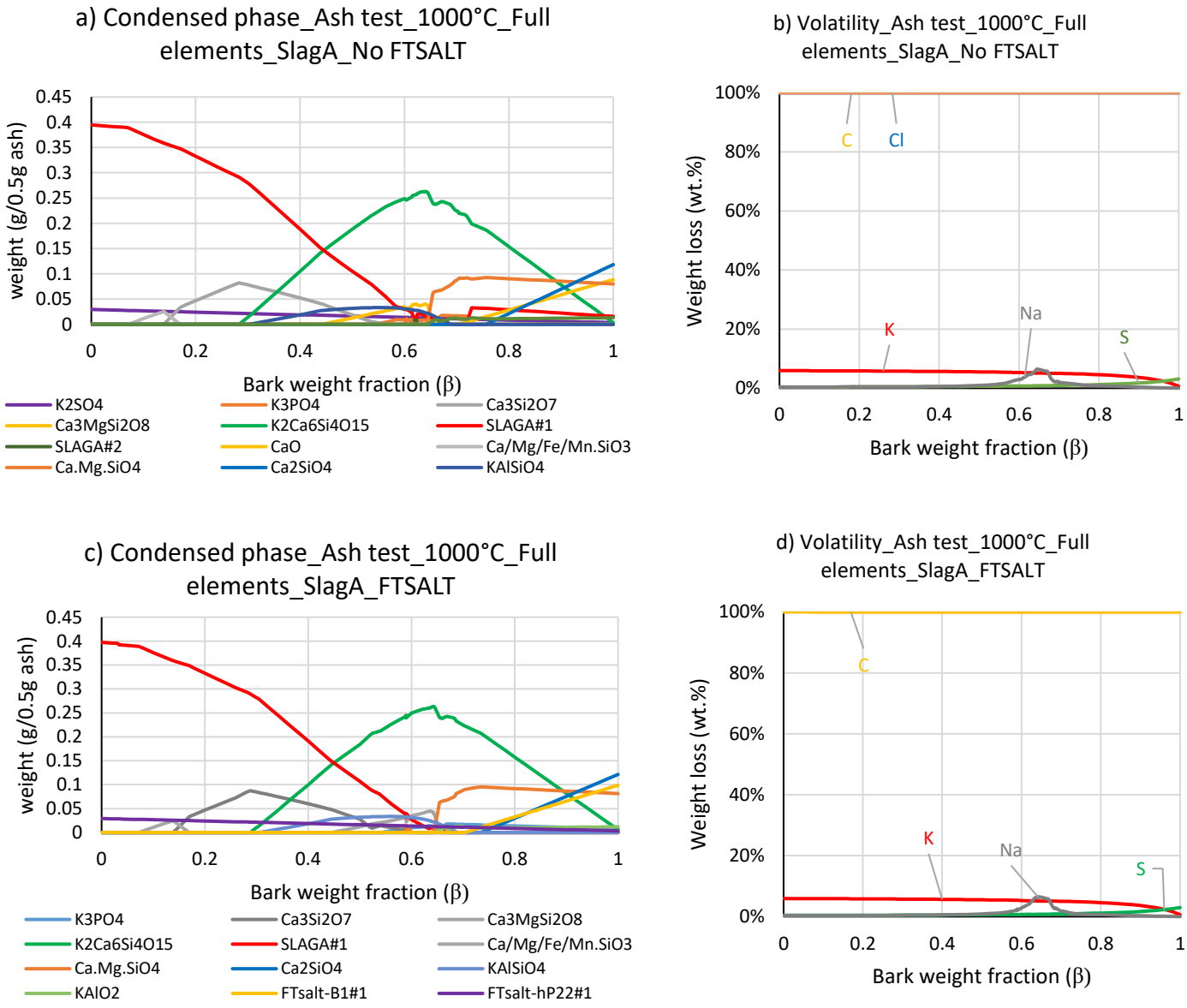

Figure C6: Predicted condensed phases and volatility for the ash test in terms of α without FTsalt (a & b) and with FTsalt (c & d).

C.3. Effects of adding Slag A or Slag B in FToxid on the experimental simulations

Several potential liquid solution descriptions are available in FToxid 8.1 database called Slag A or Slag B. According to the documentation file of the FToxid database, slag A is a liquid solution of various oxides that can dissolve sulfur as sulfides. It is wider used in literature than slag B [4–6]. In contrast, the FactSage description of Slag B says that it is a liquid solution of various oxides that can dissolve sulfur as sulfates as a dilute solution with a maximum concentration of 10 wt.%. Sulfates, especially in the form of K_2SO_4, rather than sulfides, are generally found in biomass ash. Hence, Slag B is usually chosen for feedstock rich in sulfur due to its ability to handle both silicates and sulfates interactions with various positively charged ions [7] and accommodate for SO_3 dissolution [8]. However, according to the documentation file of the FToxid database, slag B was never optimized for the system CaO-K_2O-SiO_2.

As shown in section C.1, the choice of elements in the simulation affected the appearance of one of the ternary phases of interest ($K_2Ca_2Si_2O_7$). In addition, from the predicted results in section C.2, the ash test prediction results presented higher contents of the ternary compounds rich in K than those of the pellet test. Hence, the experimental simulations in this section were conducted without P, Cl, and Mg. Consequently, the simulation results using Slag A (Figures C7.a and C7.b) and Slag B (Figures C7.c and C7.d) were shown in Figure C7 for BCWC and at varying temperatures between 500 °C and 2000 °C in ash test.

Comparing the results in Figure C7.a with those in Figure C7.c, slag B destabilized $K_2Ca_2Si_2O_7$ and $KAlSiO_4$ at the expense of producing $Ca_3Si_2O_7$. In addition, more Ca_2SiO_4 were present in the case of slag B at the expense of less $K_2Ca_6Si_4O_{15}$. Here again, potassium behavior played a vital role in the predicted results. Slag A dissociated potassium in the form of K_2S compared to the more stable K_2SO_4 in slag B (Table C1). Hence, more potassium was dissociated in the liquid phase in the presence of slag B leading to increasing destabilization of the solid crystalline structures rich in this element. This was clear by comparing the results between Figure C7.a and C7.c: first, slag B1 existed over the whole temperature range compared to slag A1, which appeared at 850 °C; second, another slag B2 was present while slag A1 was absent. In terms of volatilization, more potassium was volatilized at high temperature (>1700 °C) in the case of slag B (Figures C7.b vs C7.d). This also played a role in destabilizing the K-rich ternary phases. Similar results were found in the predicted results in the pellet test at 1000 °C using CHON with CaKSiAlSFeMnNa (the elements stabilizing O7) using slag A (Figure C8.a and C8.b) and slag B (Figures C8.c and C8.d).

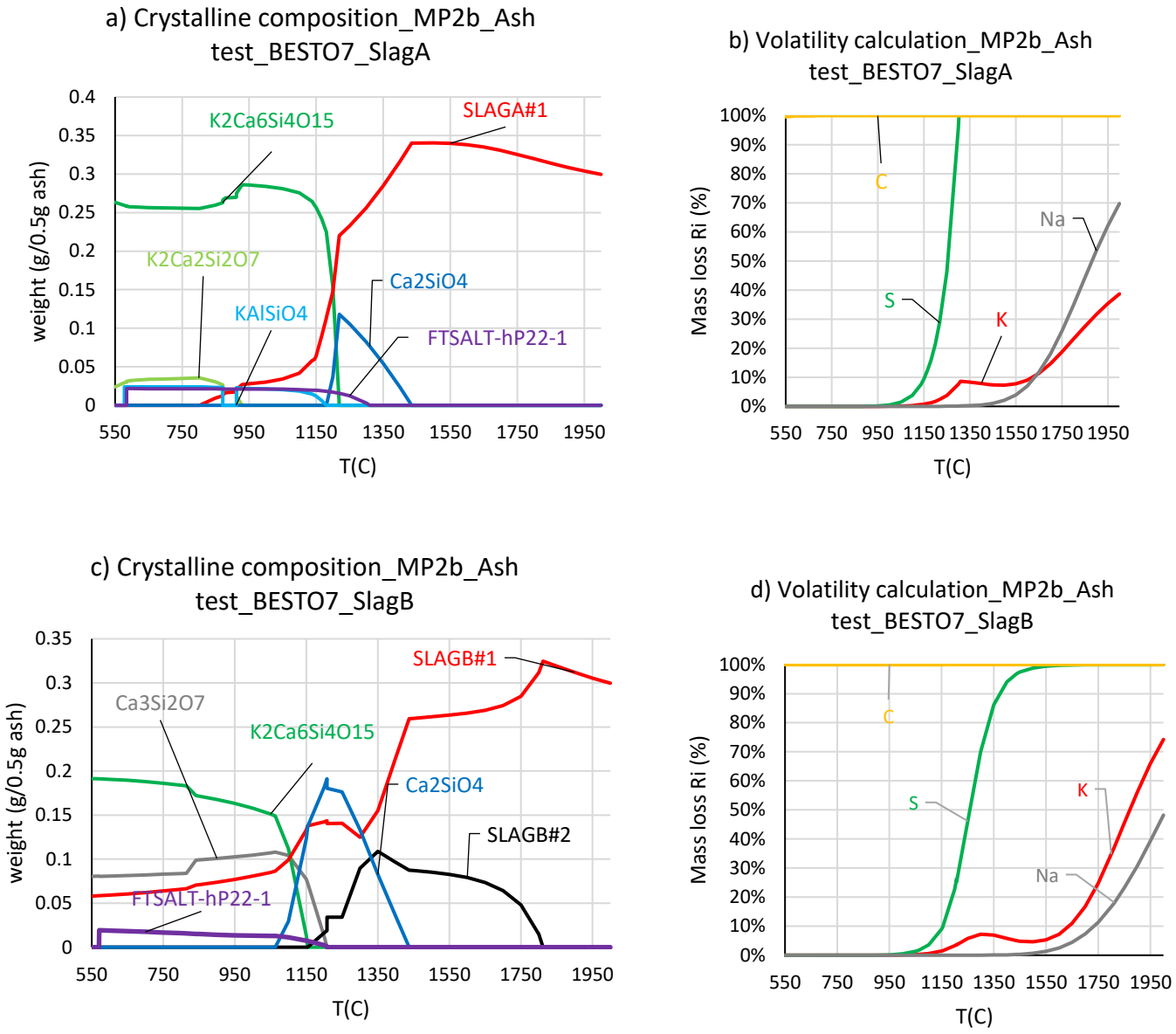

Figure C7: Predicted crystalline composition and volatility in terms of temperature for both slag A (a1 & a2) and slag B (b1 &b2).

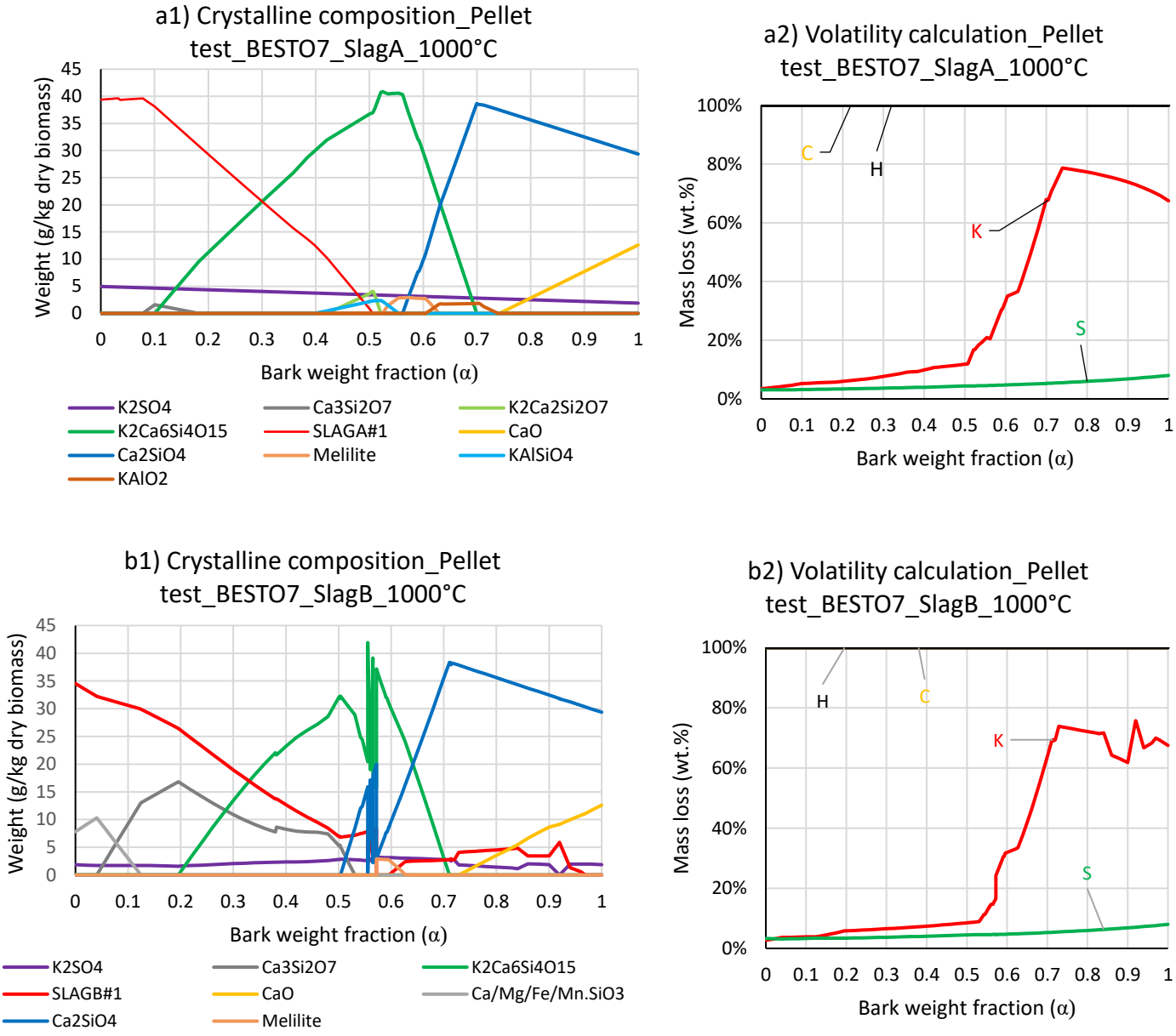

Figure C8: Predicted crystalline composition and volatility in terms of α in pellet test using the elements that stabilize the phase O7 (CHNOS CaSiK AlFeMn) at 1000 °C for slag A (a1 & a2) and slag B (b1 &b2).

Appendix D

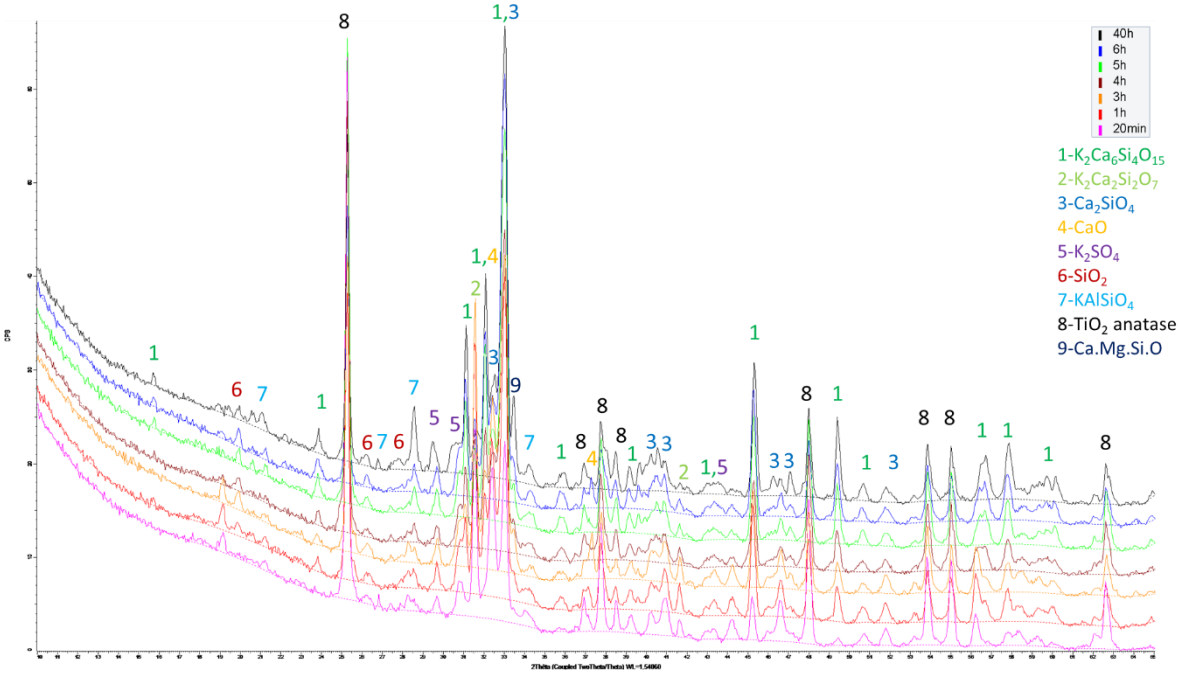

Figure D1: Measured Diffractograms for the bark-straw mixture (BCWC) in ash test at 1000 °C.

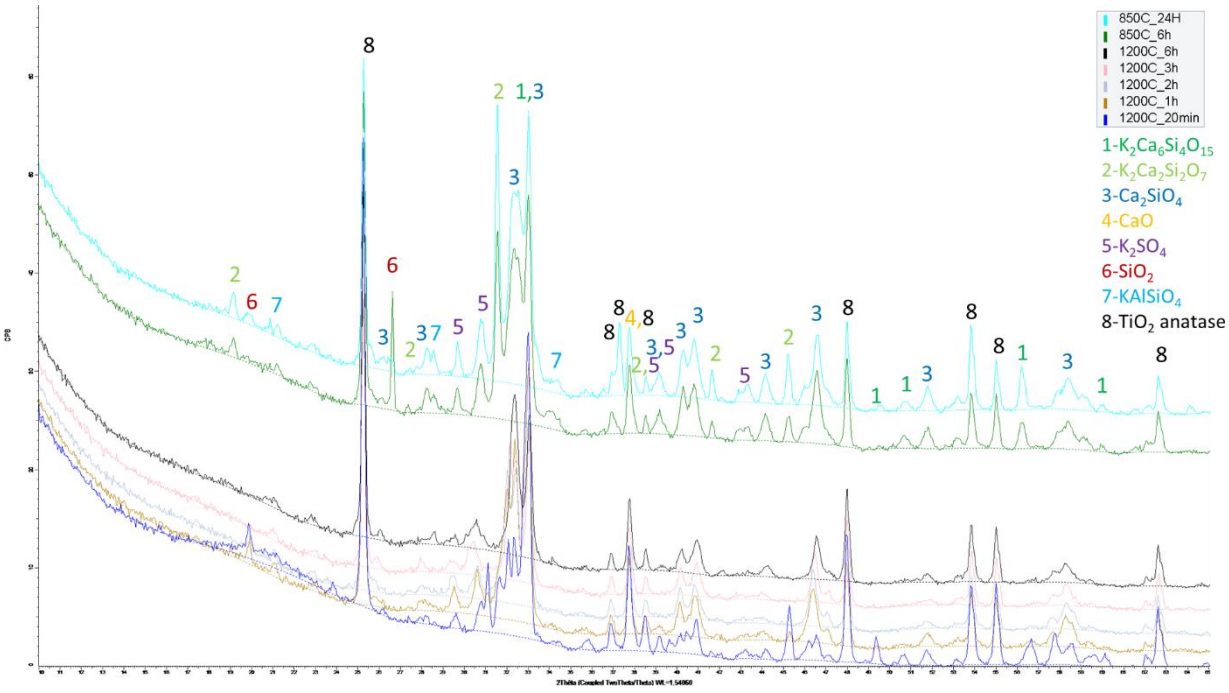

Figure D2: Measured Diffractograms for the bark-straw mixture (BCWC) in ash test at 850 °C and 1200 °C.

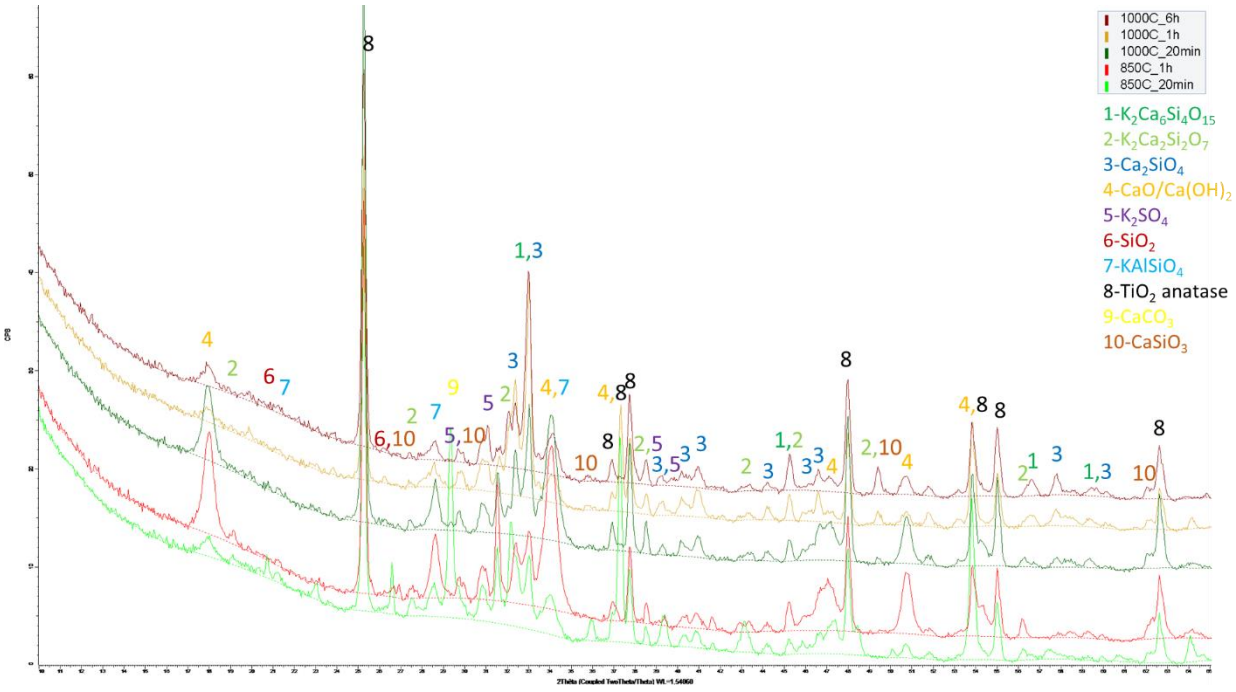

Figure D3: Measured Diffractograms for the bark-straw mixture (BCWC) in pellet test at 850 °C and 1000 °C.

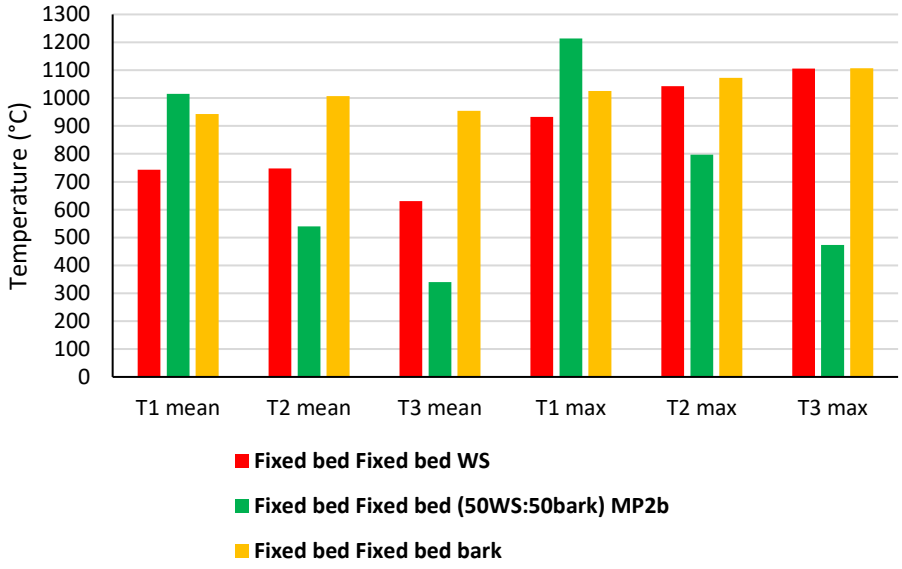

Figure D4: Temperature distribution in the fixed bed pilot reactor.